

# MALAYSIAN JOURNAL OF SCIENCE

**Vol. 43 • No 2 • June 2024**

MALAYSIAN JOURNAL OF SCIENCE

**M J S**

**ISSN 1394-3065**

MJS is indexed in Scopus, Google Scholar, Chemical Abstracts Service Database, ASEAN Citation Index (ACI), and MYCite.

# MOLECULAR ANALYSIS OF SOME FORENSICALLY SIGNIFICANT DIPTERANS ASSOCIATED WITH DECOMPOSING PIG (*SUS SCROFA*) CARCASS IN IWO SOUTH-WESTERN NIGERIA USING THE COI GENE

Iyabo Victoria OLATUBI<sup>1a\*</sup>, Wasiu Adesola MUSE<sup>2b</sup>, Olusesan Adeyemi ADELABU<sup>3c</sup>, Olufemi Micheal AWODIRAN<sup>4b</sup>, Anthony Ifeanyi Okoh<sup>5c</sup>

**Abstract:** Identification of many forensically important insects has been achieved using morphological keys with only a few relying on molecular techniques. Yet, information regarding the molecular identification of Dipteran flies from sub-Saharan Africa is scarce. Therefore, this study used the COI gene to analyze fly specimens collected from decomposing pig (*Sus scrofa*) carcasses in Iwo South-Western Nigeria. Several batches of eggs from carcasses were reared to adults and preserved in 75% ethanol for subsequent identification using molecular techniques in triplicate. A total of 450 bp sequences was obtained from BLAST analysis of the samples from the population, which has led to the identification of four families consisting of five species with the following breakdown: *Sarcophaga africa* (95.4%), *Chrysomya putoria* (99.1%), *Chrysomya inclinata* (98.3%), *Tricogena rubricosa* (89.6%), and *Chirosia flavipennis* (88.8%). The phylogenetic analysis identified *Chrysomya chloropyga* (AY139694) as the same as *C. putoria* and *S. africa* as the same as *Sarcophaga cruentata*, suggesting them as sister species. This study concluded that *T. rubricosa* and *C. flavipennis* are implicated in carrion decomposition, which provides crucial insights for forensic investigations.

**Keywords:** Carrion flies, COI gene, decomposition, forensic entomology, identification.

## 1. Introduction

Fly communities are crucial biological indicators of time elapsed since the death of an organism (Sharma & Gaur, 2015). Calliphorids (blowflies), Sarcophagids (fleshflies), and Muscids (houseflies) are among the first insects to colonize corpses (Oliveira-Costa, 2003; Reibe & Madea, 2010) as they feed on soft tissues of fresh carcasses. Thus, these species have been included in most forensic investigations. However, accessibility to identification tools has been a significant obstacle to the progression of forensic entomology in most African countries, particularly Nigeria, where the incidence of kidnap, banditry, rape, and other societal vices continues to rise (Ngwama, 2014). It is disheartening that medico-legal investigations, particularly involving the adoption of a forensic entomology approach, remain at its rudimentary stage despite the recent events in the country. Therefore, it is imperative to take steps to produce evidence

conducive to swift and accurate prosecution to curb these social vices. The first step in this undertaking involves the accurate identification of these flies, whether they are in the egg, larval, pupal, or adult stage, to the species level. Morphological keys remain the main component in most methods for the identification of insects, whose effectiveness extends only to the family level. Improvements have been seen in these morphological approaches with further identification of key features of adult fly species by Carvalho & Mello-Patiu (2008) in South America, and later certain blowflies by Lutz *et al.* (2018) in Africa. However, similarities between species remain a crucial challenge to morphological identification. Recent advances in research have explored the use of molecular methods in identifying forensically important flies. These methods offer a precise, rapid, and reliable identification of different developmental stages of flies (Sperling, Anderson & Hickey, 1994; Marlgor & Coquoz, 1999; Oliveira *et al.*, 2011). Research has identified the COI gene (Cytochrome Oxidase subunit I) as a suitable marker for the identification of insect species (Harvey, Dadour, & Gaudieri 2003; Nelson, Wallman, and Dowton, 2007; Tuccia *et al.*, 2016). Recently, Sontigun *et al.* (2018) identified 16 species of blowflies in Thailand using the COI and COII genes. Similarly, several other studies have adopted molecular techniques to identify numerous fly species, particularly those with medico-legal significance (Sperling, Anderson & Hickey,

### Authors information:

<sup>a</sup>Pure and Applied Biology Programme, College of Agriculture Engineering and Science, Bowen University Iwo Osun State, NIGERIA. E-mail: [olatubivictoria@gmail.com](mailto:olatubivictoria@gmail.com)<sup>1</sup>

<sup>b</sup>Department of Zoology, Obafemi Awolowo University Ile-Ife Osun State, NIGERIA. E-mail: [Wmuse2002@yahoo.com](mailto:Wmuse2002@yahoo.com)<sup>2</sup>; [michfemi@yahoo.com](mailto:michfemi@yahoo.com)<sup>4</sup>

<sup>c</sup>SAMRC Microbial Water Quality Monitoring Centre, University of Fort Hare, Alice 5700, SOUTH AFRICA. E-mail: [oluseanadelabu@gmail.com](mailto:oluseanadelabu@gmail.com)<sup>3</sup>; [aokoh@ufh.ac.za](mailto:aokoh@ufh.ac.za)<sup>5</sup>

\*Corresponding Author: [olatubivictoria@gmail.com](mailto:olatubivictoria@gmail.com)

Received: May 30, 2022

Accepted: March 10, 2023

Published: June 30, 2024

1994; Marlgorn & Coquoz, 1999; Ames, Turner & Daniel, 2006; Oliveira *et al.*, 2011). However, this identification has been limited to temperate regions, prompting the need to identify forensically important fly species native to the tropical region, particularly sub-Saharan Africa. Therefore, this study sought to identify some forensically significant fly species from decomposing carcasses in two South-Western Nigeria using molecular techniques.

## 2. Materials and Methods

### Specimen Collection and Preparation

Egg deposits and larvae present on different parts (eyes, nostril, mouth, ears, anus, and body folds) of six (6) pig carcasses were collected into 50-mL universal bottles. The collected samples were transported to the laboratory and transferred into rearing cages. The eggs were placed in 300-mL plastic bowls with a lid. A ventilation panel with a dimension of 20 mm x 25 mm was made on the lids, which were then covered using woven clothes with a dimension of 24 mm x 29 mm to allow air into the bowl. The pork was served as a main diet. The bowls were placed in the rearing cages in which sawdust was added to serve as bedding for the larvae to pupate before emerged. Upon the emergence of adult flies, they were collected using universal bottles and freeze-killed at -20 °C, according to a method of Lonsdale, Dixon & Gennard (2004). This step is crucial to prevent the rapid degradation of DNA before preserving the specimens in 75% ethanol for 96 h. These adult flies were then mounted and identified using the established morphological keys in Carvalho & Mello-Patiu, 2008, Szpila *et al.*, 2015, and Lutz *et al.*, 2018. These identified flies were preserved again in 75% ethanol for further molecular identification. Four of each of the fly samples were put into 20-mL universal bottles and added with 2 mL of 75% ethanol. Each bottle was labelled and sent to the Biochemistry and Microbiology Department of the University of Fort-Hare, South Africa for molecular analysis. Ethical clearance was sought from the Health Research Ethic Committee (HREC) Institute of Public Health Obafemi Awolowo University (HREC No: IPHOAU/12/1611).

### DNA Extraction

Upon the collection, ethanol was completely removed from the flies. The removal was achieved by rinsing the flies in Petri dishes containing phosphate buffer saline (PBS) three to four times. The flies were subsequently chopped using a sterile blade, removed into a 2-mL centrifuge tube, and vortexed. Then, 20 µL of Proteinase K (PK) (for the digestion of contaminating proteins) and 200 µL of cell lysis buffer (CLD) were added to the homogenized samples. The suspensions were incubated at 56 °C for 2 h, followed by centrifugation at 15,000 rpm for 1 minute, from which the supernatants were aliquoted into sterilized 2-mL centrifuge tubes. Subsequently, DNA extraction was performed using the commercial kit, Promega ReliaPrep® gDNA Tissue Miniprep System (Madison, USA) (lot number: 0000318464). The protocol provided by the manufacturer was strictly followed and the eluted DNA was preserved at -20 °C until further use.

### DNA Amplification and Sequencing

A portion (450 bp) of the COI gene of the DNA was amplified using a set of oligonucleotides: forward primer of 5'-CAGCTACTTTATGAGCTTTAGG-3'; reverse primer of 5'-CATTTC AAGCTGTGTAAGCATC-3'. The protocol by Sharma *et al.* (2015) was followed with slight modifications.

A reaction mixture of 25 µL consisting of 14 µL of master mix, 1 µL each of 10 pmol/L of the forward and reverse primers, 4 µL of RNase nuclease-free water, and 5 µL of DNA template was prepared to perform the polymerase chain reaction (PCR). The amplification was carried out under these cycling conditions; initial denaturation at 94 °C for 3 min, followed by denaturation at 93 °C for 30 sec, annealing at 50 °C for 30 sec, elongation at 72 °C for 60 sec, and a final elongation at 72 °C for 5 min. A negative control was used for the PCR to spot false positives or any likelihood of recontamination.

The transillumination method using 1.5 % agarose gel stained with ethidium bromide (EtBr) was applied to visualize the PCR products. The positive amplicons were subsequently sequenced bi-directionally using an ABI3500xl automated DNA sequencer with a 50-cm Capillary array and POP7 (all supplied by Applied Biosystems).

### Editing of Sequences, Blast Search, and Accession Numbers Allocation

The Geneious program version 11.1.5 was used to produce consensus sequences for each positive PCR product using the collected and corrected forward and reverse nucleotide sequence strands. The data produced after the editing were submitted to the BLAST program in GenBank for homology search against other curated sequences in GenBank (<http://blast.ncbi.nlm.nih.gov>) (Table 1). All the curated sequences were placed on the "highly similar sequences" parameter on the blast tool to reveal their identity. Assembled sequences were subsequently deposited to the NCBI GenBank database, and the following accession numbers OM492409-OM492417 were assigned.

### Sequence Analysis

The sequences generated were submitted to a Clustal W program in MEGA software version 11 for sequence alignment (Thompson *et al.*, 1994). Phylogenetic and molecular evolutionary analyses were subsequently performed using nine nucleotide sequences, and a neighbor-joining tree was drawn with branch lengths of the same unit as those used for evolutionary distances (Tamura *et al.*, 2011). Evolutionary distances were calculated using the Maximum Composite Likelihood method, according to Tamura *et al.* (2004). The variation in the gene within and between species was also determined using the Kimura two-parameter model.

### 3. Results

A total of 52 individuals of over 450 bp of the COI gene were sequenced. The BLAST search revealed that the analyzed flies belonged to four families (*Sarcophagidae*, *Calliphoridae*, *Anthonomyiidae*, and *Rhinophoridae*) (Table 1). A comparison between the sequences to their reference strains in the GenBank revealed a sequence similarity ranging from 99.19% to 88.85% (Table 2).

**Table 1.** Reference sequences NCBI GenBank used in this Study

Family	Species	Accession Number	COI length	Region	Author	Reference
Anthomyiidae	<i>Chirosia flavipennis</i>	DQ657040	1-743	Singapore	Kutty <i>et al.</i>	Kutty <i>et al.</i> (2007)
	<i>Chirosia cinerosa</i>	MZ625164	1 to 658	Finland	Roslin <i>et al.</i>	Roslin <i>et al.</i> (2021)
	<i>Palesisa nudioculata</i>	NC_041657	1-16476	China	Han <i>et al.</i>	Unpublished
Calliphoridae	<i>Melinda viridicyanea</i>	GQ409335	1-725	Singapore	Kutty <i>et al.</i>	Kutty <i>et al.</i> (2010)
	<i>Chrysomya putoria</i>	FJ195384	1-1256	USA	Singh <i>et al.</i>	Singh <i>et al.</i> (2011)
	<i>Chrysomya putoria</i>	MH034007	1-313	South America	Mat <i>et al.</i>	Unpublished
	<i>Chrysomya putoria</i>	MH034006	1-313	South America	Mat <i>et al.</i>	Unpublished
	<i>Chrysomya putoria</i>	EU418542	1-1167	United Kingdom	Harvey <i>et al.</i>	Harvey <i>et al.</i> (2008)
	<i>Chrysomya putoria</i>	AF295554	1-2304	USA	Wells and Sperling	Wells and Sperling (2001)
	<i>Chrysomya putoria</i>	AB112835	1-1167	Australia	Harvey <i>et al.</i>	Harvey <i>et al.</i> (2003)
	<i>Chrysomya putoria</i>	AB112831	1-1167	Australia	Harvey <i>et al.</i>	Harvey <i>et al.</i> (2003)
	<i>Chrysomya putoria</i>	AB112860	1-1167	Australi	Harvey <i>et al.</i>	Harvey <i>et al.</i> (2003)
<i>Chrysomya inclinata</i>	AB112857	1-1167	Australia	Harvey <i>et al.</i>	Harvey <i>et al.</i> (2003)	
<i>Sarcophagidae</i>	<i>Sarcophaga africa</i>	JQ582120	1-1535	Belgium	Jordaens <i>et al.</i>	Jordaens <i>et al.</i> (2013)
	<i>Sarcophaga africa</i>	KF038000	1-2305	China	Guo <i>et al.</i>	Unpublished
	<i>Sarcophaga cruentata</i>	JN604570	1-1539	China	Ling <i>et al.</i>	Unpublished

Rhinophoridae	<i>Tricogena rubricosa</i>	KP004882	1-634	Czech Republic	Ziegler and Tothova	Unpublished
	<i>Tricogena caucasica</i>	KP004881	1-736	Czech Republic	Ziegler and Tothova	Unpublished

**Table 2.** Percentage similarity index between the sequences of the collected carrion flies and the respective reference sequences from the GenBank

S/N	Specimen	Blast molecular identity	Percentage similarity
1	IWO1901.1	<i>Sarcophaga africa</i>	95.44%
2	IWO1902.1	<i>Chrysomya putoria</i>	99.19%
3	IWO1903.1	<i>Chrysomya putoria</i>	98.86%
4	IWO1904.1	<i>Chrysomya putoria</i>	94.47%
5	IWO1905.1	<i>Crysomya inclinata</i>	98.25%
6	IWO1906.1	<i>Chrysomya putoria</i>	98.91%
7	IWO1909.1	<i>Chirosia flavipennis</i>	88.85%
8	IWO1910.1	<i>Tricogen rubricosa</i>	89.60%
9	IWO1913.1	<i>Chrysomya putoria</i>	91.61%

Phylogenetic Analysis

*C. putoria*, *C. inclinata*, *S. africa*, *C. flavipennis*, and *T. rubricosa* were clustered with reference sequences to construct a phylogenetic tree according to Vogel *et al.* (2014) (Figure 1). The neighbor-joining trees of the sequences of COI genes from this study showed three distinct groups with a clear monophyletic cluster among

them. The genus *Chrysomya* was divided into two clades: one clade consists of *C. putoria* while the other consists of *C. inclinata*. The genus *Chrysomya* formed a monophyletic group with *S. africa*. Similarly, *C. flavipennis* and *T. rubricosa* formed a monophyletic group with *Musca domestica*.

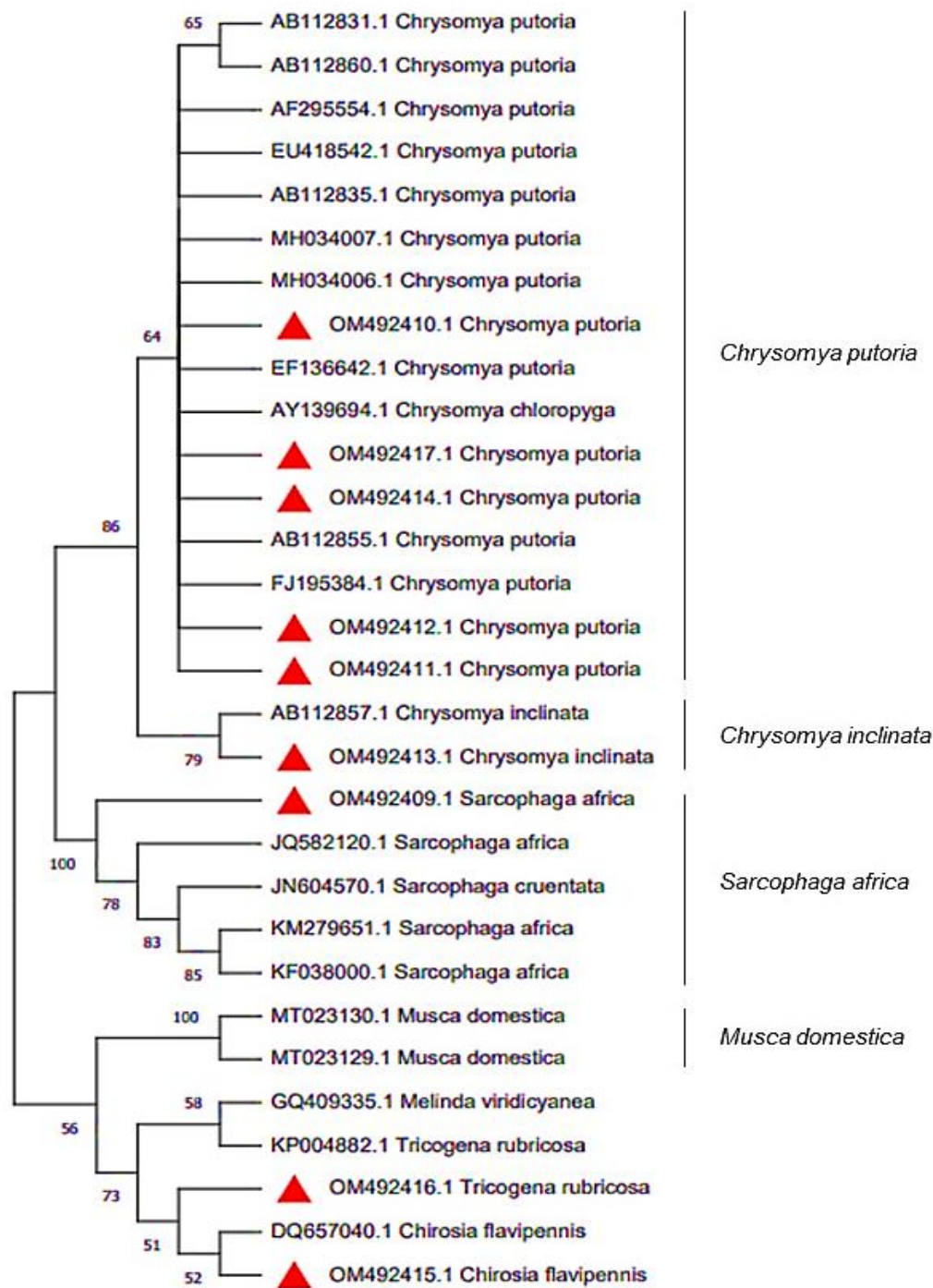


**Figure 1.** Neighbor-joining tree of COI sequences (450 bp) demonstrates evolutionary relationships among species. Genetic Distance

Based on the 450 bp of COI sequences, the mean percentage of the interspecific variation between the carrion flies collected from this study varied from 0.01% to 0.25% (Table 2). *C. putoria* and *C. flavipennis* showed the highest variation (0.25%) while the least was observed between *C. putoria* and *C. putoria* (0.01%).

Species pairs of *C. putoria*/*C. inclinata*, *C. flavipennis*/*T.*

*rubricosa*, and *T. rubricosa*/*S. Africa* was separated by 0.09%, 0.17%, and 0.22%, respectively. Similarly, the intraspecific distance values of the sequenced data varied from 0.03% to 7.33% (Table 3) with the highest value recorded in *T. rubricosa*. The calculated pairwise distance indicates that *C. Putoria* differs only by 0.01%, whereas *C. putoria* and *C. inclinata* differ only by 0.03%.

**Table 3.** Percentage mean of interspecific distances of carrion flies with their respective standard error based on 450-bp COI sequences

S/N	SPECIES	INTERSPECIFIC DISTANCE									
		1	2	3	4	5	6	7	8	9	
1	<i>Tricogena rubricosa</i>		0.03	0.04	0.03	0.03	0.04	0.04	0.03	0.03	
2	<i>Sarcophaga africa</i>	0.22		0.03	0.03	0.03	0.03	0.03	0.03	0.03	
3	<i>Chrysomya putoria</i>	0.25	0.18		0.02	0.03	0.02	0.02	0.02	0.03	
4	<i>Chrysomya putoria</i>	0.19	0.14	0.07		0.02	0.01	0.01	0.01	0.03	
5	<i>Chrysomya putoria</i>	0.21	0.23	0.16	0.08		0.02	0.03	0.02	0.03	
6	<i>Chrysomya putoria</i>	0.19	0.14	0.07	0.01	0.09		0.01	0.02	0.03	
7	<i>Chrysomya putoria</i>	0.17	0.13	0.07	0.02	0.10	0.02		0.01	0.03	
8	<i>Chrysomya inclinata</i>	0.18	0.14	0.09	0.04	0.12	0.05	0.03		0.03	
9	<i>Chirosia flavipennis</i>	0.17	0.22	0.23	0.19	0.25	0.18	0.17	0.19		

Table 4. Maximum percentage of intraspecific variation in COI sequences of Dipteran species

S/N	Species	Maximum variation within species
1	<i>Sarcophaga africa</i>	0.03±0.02
2	<i>Chrysomya putoria</i>	0.09±0.03
3	<i>Chrysomya inclinata</i>	0.05±0.01
4	<i>Chirosia flavipennis</i>	2.24±1.48
5	<i>Tricogena_rubricosa</i>	7.33±2.08

#### 4. Discussion

Cytochrome c oxidase subunit 1 (COI) sequences were used to identify fly species from the Order Diptera among which are the genus: *Chrysomya*, *Sarcophaga*, *Chirosia*, and *Tricogena*. The results are comparable with those of Sontigun *et al.* (2018), who identified 16 species of forensically significant blowflies in Thailand, the majority from the genus *Chrysomya*. In addition, Khoso *et al.* (2015) successfully used COI gene sequences and phylogenetic analysis to identify Cyclorrhaphan flies. Carvalho & Mello-Patiu (2008) used advanced morphological keys to identify 12 families of carrion flies, of which *Calliphoridae*, *Muscidae* *Fanniidae*, and *Sarcophagidae* were the most abundant genera found on carrion and cadaver in South America. *S. africa* identified in this study is comparable to that of Guo *et al.* (2013), who used a large fragment of COI and period gene to identify Sarcophagid flies in India. Harvey *et al.* (2003) conducted molecular identification of some Southern African and Australian blowflies, which led to the discovery of *C. inclinata*, the same species found in this current research. These similar findings demonstrate the vital role of the species in carrion decomposition irrespective of regional differences.

This current study was able to identify the forensically significant fly species using short fragments of 450 bp nucleotides similar to the previous studies using large fragments of ~710 bp (Mashaly *et al.*, 2017) and 1247 bp (Sontigun *et al.*, 2018) nucleotides, and complete genome. The results are also consistent with the findings of Bosly (2020) who used a partial mitochondrial cytochrome oxidase gene of 272 bp to identify *Musca domestica* from Jazan, Saudi Arabia.

The molecular approach for the identification of forensically important flies is the key to a successful species identification method alternative to the exhaustive, time-consuming, and potentially error-prone morphological method. Despite the development of sophisticated and high-quality key features for morphological identification (Lutz *et al.*, 2018) based on recent findings, the procedures remain cumbersome and unable to correctly identify down to species level. Although expensive, molecular identification can misidentify sister species; however, the method proves excellent for the accurate identification of organisms when used with other supportive analyses. Based on the tree analysis conducted in this study, *C. putoria* and *C. chloropyga* were identified as sister species. These two species had long been treated as synonymous despite being classified as distinct species (Rognes & Paterson, 2005). This finding demonstrates a case of misidentification. Similarly, *S. africa* and *S. curentata* appeared similar with just 78% bootstrap value. Additionally, *C. flavipennis* and *T. rubricosa* were implicated in carrion decomposition for the first time although with low bootstrap values. These findings provide an indication and further study is necessary to affirm their role in decomposition.

The morphological method also faces limitations when identifying the larval stages of flies that are forensically significant. In contrast, the DNA-based identification method has successfully identified different stages (first, second, third, pupa, and adult) in the life cycle of the carrion flies (Kavitha *et al.*, 2013). The previous study further used an empty puparium sampled from ten different crime scenes, which revealed a 100% similarity, demonstrating the accuracy of the molecular method in species identification.

## 5. Conclusion

Over the years, molecular techniques using the COI gene have demonstrated consistent success. Out of over two million animal sequences in the GeneBank, 75% are insects, the majority of which were identified using the COI sequences, boasting up to 100% identity similarity. This current study demonstrated a successful identification of forensically important fly species using a short fragment of the MT-CO1 gene (~450 bp). Given the effectiveness of molecular techniques, future forensic investigations may preferentially opt for the use of insects and their larvae for accurately determining the actual time, nature, and circumstances of death.

## 6. References

- Ames, C., Turner, B. & Daniel, B. (2006). The use of mitochondrial cytochrome oxidase I gene (COI) to differentiate two UK blowfly species – *Calliphora vicina* and *Calliphora vomitoria*, *Forensic Sci. Int.* 164 :179–182.
- Bosly, H. A. E. (2020). Molecular identification of *Musca domestica* L. from Jazan (KSA) based on partial mitochondrial cytochrome oxidase gene sequencing. *Journal of Entomology*, 17: 6-13.
- Carvalho, C. J. & Mello-Patiu, C. A. (2008). Key to the adults of the most common forensic species of Diptera in South America *Revista Brasileira de Entomologia* 52(3): 390-406.
- Guo, Y., Zha, L., Yan, W., Li, P., Cai, J. & Wu, L. (2013). Identification of forensically important sarcophagid flies (Diptera: Sarcophagidae) in China based on COI and period gene. *International Journal of Legal Medicine*, In press PUBMED 24101094.
- Harvey, M. L., Gaudieri, S., Villet, M. H. & Dadour, I. R. (2008). A global study of forensically significant calliphorids: implications for identification. *Forensic Science International Journal*, 177 (1): 66-76. PUBMED 18295422
- Harvey, M. L., Mansell, M. W., Villet, M. H., & Dadour, I. R. (2003). Molecular identification of some forensically important blowflies of southern Africa and Australia. *Medical and veterinary entomology*, 17(4), 363–369. <https://doi.org/10.1111/j.1365-2915.2003.00452>.
- Jordaens, K., Sonet, G., Richet, R., Dupont, E., Braet, Y. & Desmyter, S. (2013). Reliability of long vs short COI markers in identification of forensically important flies. *Int. J. Legal Med.* 127 (2), 491-504 PUBMED 22960880
- Kavitha, R., Tan, T. C., Lee, H. L., Nazni, W. A., & Sofian, A. M. (2013). Molecular identification of Malaysian *Chrysomya megacephala* (Fabricius) and *Chrysomya rufifacies* (Macquart) using life stage specific mitochondrial DNA. *Tropical biomedicine*, 30(2), 211–219.
- Khoso, F. N., Tan, M. P. I., Talib, S. M. B. & Lau, W. H. (2015). Molecular Identification and Composition of Cyclorrhaphan Flies Associated with Cafeterias. *Pakistan Journal of Zoology*, 47(6): 1743-1752.
- Kutty, S.N., Bernasconi, M.V., Sifner, F. & Meier, R. (2007). Sensitivity analysis, molecular systematics and natural history evolution of Scathophagidae (Diptera: Cyclorrhapha: Calyptratae). *Cladistics* 23 (1), 64-83.
- Kutty, S.N., Pape, T., Wiegmann, B.M. & Meier, R. (2010). Molecular phylogeny of the Calyptratae (Diptera: Cyclorrhapha) with an emphasis on the superfamily Oestroidea. *Syst. Entomol.* 35 (4), 614-635
- Lonsdale, H. L., Dixon, R. A. & Gennard, D. E. (2004). Comparison of the efficiency of mitochondrial DNA extraction and assessment in aged and modern dipteran samples. *Forensic Analysis. Royal Society of Chemistry Conference University of Lincoln* 20–22.
- Lutz, L., Williams, K.A., Villet, M. H., Ekanem, M. & Szpila, K. (2018). Species identification of adult African blowflies (Diptera: Calliphoridae) of forensic importance. *International Journal of Legal Medicine*, 132:831–842
- Marlgorn, Y. & Coquoz, R. (1999). DNA typing for identification of some species of Calliphoridae: an interest in forensic entomology, *Forensic Sci. Int.* 102 :111–119.
- Mashaly, A., Alajmi, R., Mustafa, A.E.Z., Rady, A. & Alkhedir, H. (2017). Species abundance and identification of forensically important flies of Saudi Arabia by DNA barcoding. *Journal of Medical Entomology*, 54: 837-843.
- Nelson, L.A., Wallman, J.F. & Dowton, M. (2007). Using COI barcodes to identify forensically and medically important blowflies, *Med. Vet. Entomol.* 21:44–52.
- Ngwama, J. C. (2014). Kidnapping in Nigeria: An Emerging Social Crime and the Implications for the Labour Market. *International Journal of Humanities and Social Sciences.* 4:133-145.
- Oliveira, A.R., Farinha, A. Rebelo, M.T. & Dias, D. (2011). Forensic entomology: Molecular identification of blowfly species (Diptera: Calliphoridae) in Portugal, *Forensic Science International: Genetics Supplement Series*, 3 (1): e439-e440.

- Oliveira-Costa, J. (2003). *Entomologia forense; quando os insetos são os vestígios*. Campinas: Millennium Editora.
- Reibe, S. & Madea, B. (2010) how promptly do blowflies colonise fresh carcasses? A study comparing indoor with outdoor locations. *Forensic sci. int.* 195:52-57. [crossref][PubMed]
- Rognes, K., & Paterson, H.E.H. (2005). *Chrysomya chloropyga* (Wiedemann, 1818) and *Chrysomya putoria* (Wiedemann, 1830) (Diptera, Calliphoridae) are two different species, *African Entomol.* (13) 49–70
- Roslin, T., Somervuo, P., Pentinsaari, M., Hebert, P. D. N., Agda, J., Ahlroth, P., Anttonen, P., Aspi, J., Blagoev, G., Blanco, S., Chan, D., Clayhills, T., deWaard, J., deWaard, S., Elliot, T., Elo, R., Haapala, S., Helve, E., Ilmonen, J., . . . & Mutanen, M. (2021). A molecular-based identification resource for the arthropods of Finland. *Molecular Ecology Resources.* 22(2)
- Sharma, R. & Gaur, J.R. (2015). Various methods for the estimation of the post mortem interval from calliphoridae: A review. *Egyptian Journal of Forensic Sciences*,5(1):1-12.
- Sharma, R., Kishore, A., Mukesh, M., Ahlawat, S., Maitra, A., Kumar, A. P. & Madhu Sudan Tantia M.S. (2015). Genetic diversity and relationship of Indian cattle inferred from microsatellite and mitochondrial DNA markers. *BMC Genetics* 16:73.
- Singh, B., Kurahashi, H., & Wells, J. D. (2011). Molecular phylogeny of the blowfly genus *Chrysomya*. *Medical and veterinary entomology*, 25(2), 126–134.
- Sontigun, N., Sukontason, K. L., Amendt, J., Zajac, B. K., Zehner, R., Sukontason, K., Chareonviriyaphap, T. & Wannasan, A. (2018). Molecular Analysis of Forensically Important Blowflies in Thailand. *Insects*, 9 (159)
- Sperling, F. Anderson, G. & Hickey, D. A. (1994). DNA-based approach to the identification of insect species used for post-mortem interval estimation, *J. Forensic Sci.* 39 :418–427.
- Szpila, K., Richet, R. & Pape, T. (2015). Third instar larvae of flesh flies (Diptera: Sarcophagidae) of forensic importance—critical review of characters and key for European species. *Parasitology Research*, 114:2279–2289.
- Tamura K., Nei M., & Kumar S. (2004). Prospects for inferring very large phylogenies by using the neighbor-joining method. *Proceedings of the National Academy of Sciences (USA)* 101:11030-11035.
- Tamura K., Peterson D., Peterson N., Stecher G., Nei M., & Kumar S. (2011). MEGA5: Molecular Evolutionary Genetics Analysis using Maximum Likelihood, Evolutionary Distance, and Maximum Parsimony Methods. *Molecular Biology and Evolution* 28: 2731-2739.
- Thompson, J. D., Higgins, D. G., & Gibson, T. J. (1994). CLUSTAL W: improving the sensitivity of progressive multiple sequence alignment through sequence weighting, position-specific gap penalties and weight matrix choice. *Nucleic acids research*, 22(22), 4673–4680.
- Tuccia, F., Giordani, G. & Vanin, S. (2016). A general review of the most common COI primers for Calliphoridae identification in forensic entomology. *Forensic Science International: Genetics*, 24: e9-e11.
- Vogel, H., Badapanda C., Knorr E., & Vilcinskis A. (2014). RNA-sequencing analysis reveals abundant developmental stage-specific and immunity-related genes in the pollen beetle *Meligethes aeneus*. *Insect Mol. Biol.* 23:98–112.
- Wells, J. D., & Sperling, F. A. (2001). DNA-based identification of forensically important *Chrysomyinae* (Diptera: Calliphoridae). *Forensic science international*, 120(1-2), 110–115.

## DNA BARCODING IN THE VALIDATION OF SCAD SPECIES IDENTIFICATION (GENUS: DECAPTERUS) IN AMBON

Gino V. Limmon<sup>1a,d,e\*</sup>, Ray Purnama<sup>2b</sup>, Juliaeta A. B. Mamesah<sup>3c</sup>, Gratia D. Manuputty<sup>4a,d</sup>, Rahman<sup>5a</sup>

**Abstract:** The limitations of morphology-based identification systems and the decreasing number of taxonomists necessitate a molecular approach for species recognition and identification, with DNA barcoding emerging as an efficient solution to some of taxonomy's challenges. This research aimed to identify several scad species found in the waters surrounding Ambon both morphologically and molecularly through DNA barcoding. Fish samples were collected from January to June 2018 at the Mardika fish market in Ambon, initially analyzed morphologically, and subsequently validated using the DNA barcode method. Both analyses were conducted in the Molecular Biology Laboratory at the Maritime and Marine Science Centre of Excellence of Pattimura University. Morphological identification revealed six species of scad: *Decapterus macarellus*, *D. macarellus* (suspected), *D. macrosoma*, *D. macrosoma* (suspected), *D. russelli* (suspected), and *D. kurroides*, with four samples per species collected, resulting in a total of 24 samples analyzed. DNA barcoding identified only four species: *D. macarellus*, *D. macrosoma*, *D. russelli*, and *D. kurroides*, with identification percentages ranging from 99-100%. After validation, the confirmed scad species found in Ambon's waters are *D. macarellus*, *D. macrosoma*, *D. russelli*, and *D. kurroides*, highlighting that DNA barcoding serves as a complementary method that can reinforce morphology-based identification quickly and accurately.

**Keywords:** *Decapterus*, identification, morphological, molecular.

### 1. Introduction

Ambon is a small island in Maluku Province adjacent to Banda Sea. Ambon waters are rich in marine biodiversity, where both non-fin-fish and finfish are widely found, including the small and large demersal and pelagic Fish (Rijoly 2016; Limmon et al., 2017a, 2017b). However, there is a pressing need for updated information to effectively manage these resources. The lack of primary data about the diversity of Fish in Ambon inhibits the marine resource management in the area.

Small pelagic fish such as scad (genus: *Decapterus*) are predominant species in the area. Despite the substantial catches of scad by fishermen in these waters, there has been insufficient identification of the specific varieties present due to inadequate primary data about the variations of Scad in Ambon's waters or even Maluku's waters.

The limited morphology-based identification system and the lack of taxonomists require the use of molecular approach for the

introduction and identification of an organism (Steinke et al., 2009 cited in Zhang & Hanner, 2011). Molecular identification uses DNA pattern that has been proven accurate, relatively easy, and fast compared to conventional methods (Ciardo et al., 2006). DNA barcoding using a short and standardized gene area proposed by Hebert et al. (2003) has been proven helpful in identifying ambiguous taxonomies. The DNA Mitochondria (mtDNA) is a string of DNA passed on by a female parent and is appropriate for analyzing the offspring of a species with a high rate of similarities (Wallace 1997; Syafrina 2011). One of the mtDNA segments usually used as a species marker is cytochrome oxidase I (COI), a mitochondria genome popularized by Hebert et al. (2003). mtDNA genomes are used for biogeography analysis and their systematics frequently diverges from morphology. According to Syafrina (2011) morphological characters usually show similar types of a phenomenon but are genotypically different (cryptic species). The identification of cryptic species has to undergo various taxonomy protocols based on the morphological characters which requires detailed process and longer time (Costa & Carvalho 2007).

Zhang & Hanner (2011) stated that due to high-efficiency rate in species identification, a few ichthyologists recommended using DNA barcode in the formal description of a species (Victor, 2007; Astarlon et al., 2008), since it reinforces quicker and more accurate morphological identification (Lahaye et al., 2008). Lack of information and data regarding scads variety in Ambon combine morphological analysis and DNA barcoding approach in this research. To date, the results of research conducted in Ambon and Maluku by using DNA barcode method have been applied to marine biotas such as marine fish larvae in the Banda

#### Authors information:

<sup>a</sup>Marine Science Department, Fishery and Marine Science Faculty, Pattimura University, Maluku 97233, INDONESIA. Email: [gino.limmon@gmail.com](mailto:gino.limmon@gmail.com)<sup>1</sup>;

[gd.manuputty@gmail.com](mailto:gd.manuputty@gmail.com)<sup>4</sup>; [rahmanrajaali@gmail.com](mailto:rahmanrajaali@gmail.com)<sup>5</sup>

<sup>b</sup>Marine and Fisheries Affairs, Ambon, Maluku, INDONESIA. Email: [ray.purnama@gmail.com](mailto:ray.purnama@gmail.com)<sup>2</sup>

<sup>c</sup>Departement of Aquatic Resources Management, Pattimura University, Ambon, INDONESIA. Email: [jellymamesah@gmail.com](mailto:jellymamesah@gmail.com)<sup>3</sup>

<sup>d</sup>Maritime and Marine Science Center of Excellence, Pattimura University, Ambon; Jl. Mr. Chr. Soplanit, Kampus Poka-Ambon 97233, INDONESIA. Email: [gino.limmon@gmail.com](mailto:gino.limmon@gmail.com)<sup>1</sup>; [gd.manuputty@gmail.com](mailto:gd.manuputty@gmail.com)<sup>4</sup>

<sup>e</sup>Center for Collaborative Research on Aquatic Eco system ini Eastern Indonesia, Ambon, INDONESIA.

\*Corresponding Author: [gino.limmon@gmail.com](mailto:gino.limmon@gmail.com)

Received: November 29, 2022

Accepted: July 25, 2023

Published: June 30, 2024

Sea (Wibowo et al., 2018), coral reefs fish (Limmon, et al., 2017; Limmon et al., 2019), large pelagic fish (Akbar et al., 2018), and hetero-branch (Nimbs et al., 2020). In this research, species variation of scads in Ambon waters was identified by morphological analysis and validated by DNA barcoding approach.

## 2. Method

### Sampling

Scad samples were obtained from Mardika fish market from January to June 2018. Five specimens were collected for every scad species. The samples were photographed, and the scads' body tissue extracted and inserted into a 1.5 ml microtube screw cap filled with 95% alcohol to be stored at -20°C as voucher specimens.

### Morphological Analysis

Morphological identification of all the fish specimens was conducted based on Trautman's method (1957) as cited by Lagler et al. (1977) and Rijoly (1987), including the use of morphometric or meristic calculations. The morphological characters were then compared with the identification key as determined in the reference books (Norman 1935; Genisa 1998; Carpenter & Niem 1999; Cayetano & Honebrink 2000; Golani 2006; Sakinan & Orek 2011; Abdussamad et al., 2013; Dahlan et al., 2014).

### DNA Extraction, Amplification, and Sequencing

DNA extraction was done following the Spin-Column Protocol from the Qiagen DNeasy blood and tissue kit as this method offered simpler and more efficient DNA extraction. DNA fragments of the COI gene were amplified in 50µl of PCR reaction which consisted of 25µl of Toptaq Master Mix, 10 µl DNA template, and 1µl for every primer [10pmol/µl] and 11µl of Nuclease-free water (H<sub>2</sub>O). The primer used for the amplification of the DNA fragment of the COI gene was FishF2\_t1 (5'TGTAAAACGACGGCCAGTCTCGACTAATCATAAAGATATCGGCAC3') - FishR2\_t1 (5'CAGGAAACAGCTATGACACTTCAGGGTGACCGAAGAATCAGAA3') and VF2\_t1 (5'TGTAAAACGACGGCCAGTCAACCAACCACAAAGACATTGGCAC3') - FR1d\_t1 (5'CAGGAAACAGCTATGACACCTCAGGGTGTCCGAARAAYCARAA 3'). The PCR amplification process was performed based on Steinke et al.'s (2016) theory, starting with initial denaturation (Hot Start) at 94°C (10 minutes), and the 40 cycles, which comprised of denaturation at 94°C (40 seconds), annealing of the primer at 51°C (40 seconds), elongation at 72°C (60 seconds), and final elongation for 5 minutes. The PCR was visualized on 2% agarose gel with electrophoresis. The DNA sequencing was done at Macrogen in Korea.

### DNA Sequence Analysis

The DNA sequence data obtained from the Macrogen Company in Korea were analyzed using the BLAST program at <http://BLAST.ncbi.nlm.nih.gov> to identify the similarities/alignment between the nucleotide sequence from

this research (Query). Meanwhile, the nucleotide sequences in the gene bank (Subject) were determined using Nucleotide BLAST. After the analysis, species were determined based on the "identified" percentage, with species identification relying on sequence similarity (Song et al., 2008). A higher "identified" value indicated more accurate species identification. The genetic difference value is >2% for intraspecific variation or <2% for interspecific variation, accounting for the possibility of hybridization (Victor et al., 2015).

### Genetic and Phylogenetic Distance Analysis

Genetic and phylogenetic distances were analyzed using Molecular Evolutionary Genetics Analysis - MEGA X software (Kumar et al. 2018). Analysis of genetic distance between similar specimens (intraspecific), between specimens of different species and also phylogenetic were performed using based on the Kimura 2 parameter (K2P) model (Kimura, 1980). The results of the phylogenetic analysis are described through a phylogenetic tree created using the Neighbor-Joining (NJ) method (Saitou and Nei, 1987). The branching (nodes) on the phylogenetic tree was assessed based on the appearance of bootstrapping analysis with 1000 replications/repetitions (Felsenstein, 1985 in Ran et al. 2020).

## 3. RESULTS AND DISCUSSION

### The Number of Species identified Using Morphological Approach

In the morphological analysis, six species were identified from 24 samples of scad found in Ambon waters. However, three of the six species were suspected as other species (\* sign) due to several different characteristics compared to referral material. These six species were then labeled as: *D. macarellus* (ID number RP1-RP4), *D. macarellus\** (ID number RP5-RP8), *D. macrosoma* (ID number RP9-RP12), *D. macrosoma\** (ID number RP13-RP16), *D. russelli\** (ID number RP17-RP20) and *D. kurroides* (ID number RP21-RP24). The morphological characteristics of *D. macarellus*, *D. macrosoma* and *D. kurroides* are similar to those species in the referral material. Wherea, the suspected species (*D. macarellus\**, *D. macrosoma\**, *D. russelli\**) do not resemble the reference as they have slightly different characteristics.

The difference in morphological characteristics found on *D. macarellus* (suspected) lies in the edge of the posterior upper jaw which is rather sunken compared to the references that seem flat (Figure 1). The differences in morphological characteristics that can be found in *D. macrosoma* (suspected) can be seen in the darker upper body with larger body size, pupil, and eye diameter than *D. macrosoma* (Figure 2).

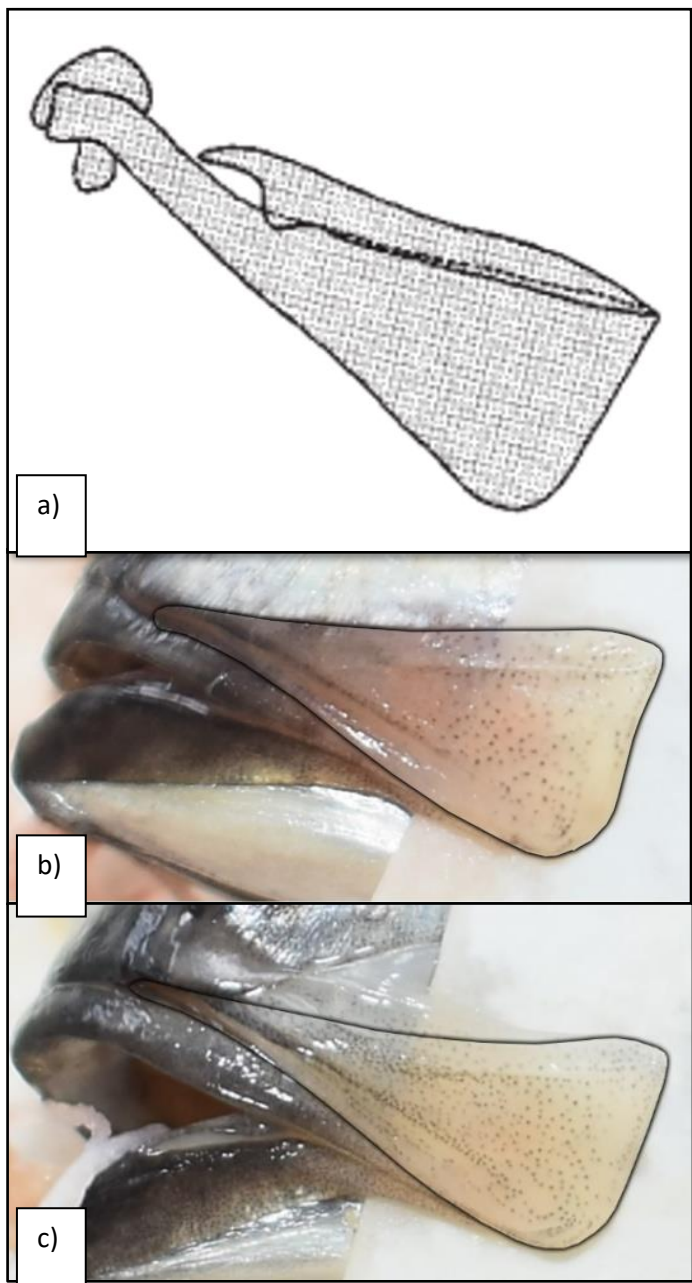


**Figure 1.** Edge of the posterior upper jaw of *D. macarellus*, a). Carpenter & Volker (1999), b). Current research (Suspected) c). Confirmed *D. macarellus*.

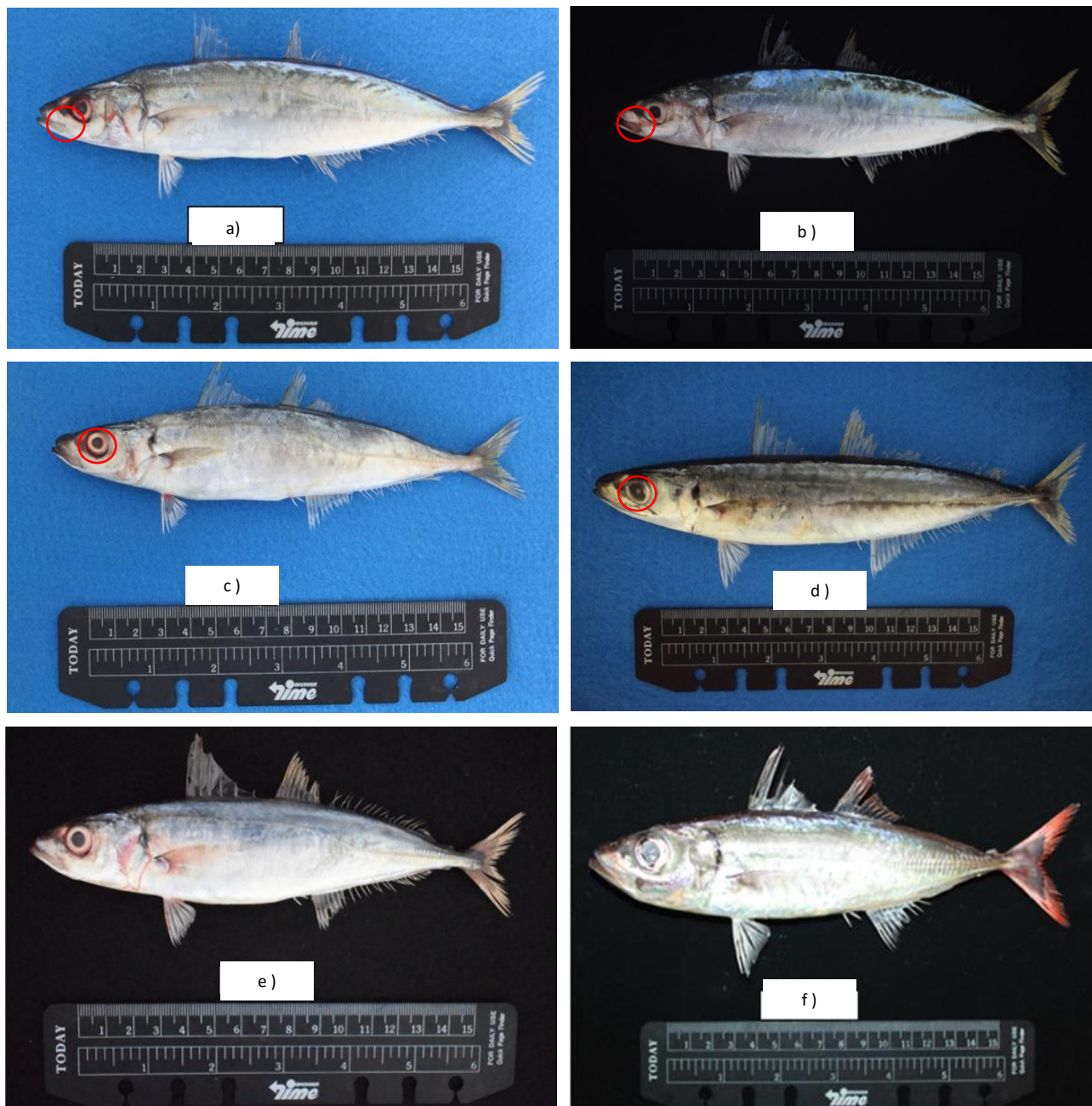


Figure 2. Body differences; a) *D. macarellus*, b) *D. macarellus\**, c) *D. macrosoma*, d) *D. macrosoma\**, e) *D. ruselli\**, and f) *D. kurroides*

The morphological differences of *D. russelli* (suspected) are in the number of filters on the lower gill that range from 26-28. Meanwhile, the reference has between 30-39 (Table 1). The morphological characters of all six species of scad (genus: *Decapterus*) are presented in Table 1.

**Table 1.** Results of the morphological identification of Scads (genus: *Decapterus*)

morphological characters	<i>D. macarellus</i>	<i>D. macarellus</i> (suspected)	<i>D. macrosoma</i>	<i>D. macrosoma</i> (suspected)	<i>D. russelli</i> (suspected)	<i>D. kurroides</i>
Dorsal Fin (D)	VIII, I 32-36	VIII, I 32-34	VIII, I 34-36	VIII, I 34-37	VIII, I 29-32	VIII, I 29-31
Anal Fin (A)	II, I 28-30	II, I 28-29	II, I 28-30	II, I 28-30	II, I 24-26	II, I 23-24
Pectoral Fin (P)	19 - 20	20	22	20	20	20
Pelvic Fin (V)	I 5	I 5	I 5	I 5	I 5	I 5
Fin Length/Head Length	59.90-65.06%	60.64- 63.24%	60.34- 72.45%	63.16- 67.51%	90.05- 95.61%	86.36- 96.62%
Scales (LL)	110 - 113	107-132	113-120	115 - 120	96 – 98	83 - 85
Scale (Curved)	50 - 62	55 – 72	60 – 62	58 - 64	56 -58	50-52
Scute (Curved)	0	0	0	0	0 – 2	0
Scale (Straight)	18 - 30	18-22	18 – 22	14 - 24	0 – 2	0
Scute (Straight)	26 -37	32 - 40	34 – 38	34 - 40	38 – 40	33 - 34
Gill Filter (Upper)	11 - 13	12 - 13	10 – 12	11 - 12	10 – 12	11 - 12
Gill Filter (Lower)	34 - 40	38 -39	34 – 35	33 - 34	26 -28	27 - 30

The presence of "suspected" status for some species of scad appears as this species could not be precisely determined due to some different morphological characters. In general, fish with broader diversity in their populations than other vertebrates and are more vulnerable to morphological variations influenced by the environment (Wimberger, 1992, cited in Sen *et al.*, 2011). Morphological structures, such as plasticity, shape, size, and colour pattern on the body can change from adaptation (Ward *et al.*, 2008; Lakra *et al.*, 2009). Species identification is usually limited based on the status of the distinctive morphological characters (Wiens & Servedio 2000).

Identifying all species shows overlapping characteristics between *D. macrosoma* and *D. Macarellus* which made the identification blurry. Carpenter and Volder (1999) stated that *D. macarellus* and *D. macrosoma* are difficult to identify. Meanwhile, *D. ruselli*\* and *D. kurroides* species have distinctive morphological characteristics.

The morphological differences are the determinant in the identification success. The "suspected" scad are other species that are not included in the identification book (Carpenter & Niem 1999). Therefore, further research need to be conducted to

precisely identify the "suspected" (ambiguous) scad. The constraint in morphological identification system and the lack of taxonomists require a more reliable approach for species identification (Steinke *et al.*, 2009) and precise results (Wong, 2011).

**The Number of Species Identified Using Molecular Approach**

DNA fragments from COI gene for 24 specimens of scads were successfully amplified using primer FishF2\_t1 - FishR2\_t1 and VF2\_t1 - FR1d\_t1 with the length of DNA fragments ranging from 700 to 800 bp. The BLAST analysis on the sequence of nucleotide base COI gene DNA fragments from 24 scad specimens resulted in four species of scads (genus *Decapterus*) whose identification percentage number ranged from 99 to 100%. The four species are *D. macarellus* with an identification percentage of 99.83-100% (mean of 99.98%), *D. macrosoma* with an identification percentage of 99.82-100 (mean of 99.97%), *D. russelli* with an identification percentage of 99.64-99.83% (mean of 99.79%), and *D. kurroides* with an identification percentage of 99.23-99.84% (mean of 99.57%).

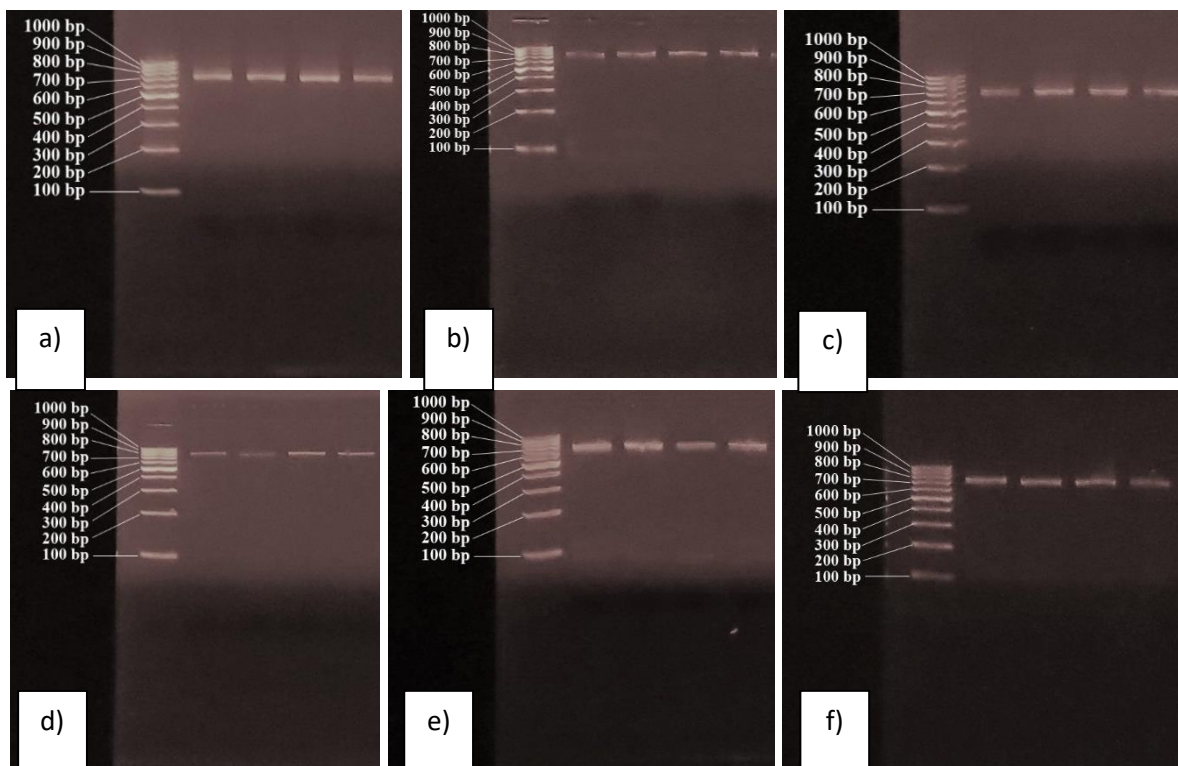


Figure 3. Gel image of PCR product; a) *D. macarellus*, b) *D. macarellus\**, c) *D. macrosoma*, d) *D. macrosoma\**, e) *D. russelli\**, and f) *D. kurroides*

Table 2. Results of DNA sequencing on the DNA fragment of the COI gene on all six species of scads (genus: *Decapterus*)

Sequence ID	Species	Query (%)	Cover	Identified (%)	Accession Number
RP1	<i>D. macarellus</i>	75		100.00	KU943796.1
RP2	<i>D. macarellus</i>	73		100.00	KU943796.1
RP3	<i>D. macarellus</i>	73		100.00	KU943796.1
RP4	<i>D. macarellus</i>	81		99.83	KY570722.1
RP5	<i>D. macarellus</i>	84		100.00	MH085884.1
RP6	<i>D. macarellus</i>	85		100.00	MH638719.1
RP7	<i>D. macarellus</i>	74		100.00	KU943796.1
RP8	<i>D. macarellus</i>	83		100.00	MH638719.1
RP9	<i>D. macrosoma</i>	74		99.82	KU943769.1
RP10	<i>D. macrosoma</i>	69		100.00	KU943769.1
RP11	<i>D. macrosoma</i>	75		100.00	KU943769.1
RP12	<i>D. macrosoma</i>	73		100.00	KU943769.1
RP13	<i>D. macrosoma</i>	74		100.00	KU943769.1
RP14	<i>D. macrosoma</i>	81		100.00	MH638663.1
RP15	<i>D. macrosoma</i>	90		100.00	HQ560948.1
RP16	<i>D. macrosoma</i>	73		100.00	KU943769.1
RP17	<i>D. russelli</i>	74		99.82	KU943718.1
RP18	<i>D. russelli</i>	75		99.82	KU943718.1
RP19	<i>D. russelli</i>	75		99.82	KU943718.1
RP20	<i>D. russelli</i>	79		99.83	JQ681458.1
RP21	<i>D. kurroides</i>	86		99.84	JN312965.1
RP22	<i>D. kurroides</i>	83		99.67	JN312965.1
RP23	<i>D. kurroides</i>	85		99.23	JN312965.1
RP24	<i>D. kurroides</i>	87		99.54	JN312965.1

All specimens have a DNA barcode (DNA fragments from the total DNA fragments of COI gene analyzed by the BLAST program) around 700-800bp in length. Savolainen et al. 2005 explained that the ideal DNA barcode is a DNA fragment with a short and uniform sequence with a length of 400-800bp that can be quickly produced and used in the identification. Every specimen has different levels of similarity in its nucleotide base sequence (identified (%) based on the DNA fragment from the COI gene being analyzed. Song et al. (2008) proposed that species identification using DNA barcoding should be based on sequence similarity. Greater percentage value of up to 100% shows more accurate the species identification. Based on the "identified" presentation, all specimens on the four species of scad have been correctly identified based on the Gene Bank with a percentage of over 99%. According to Hebert et al. 2003, species with a genetic distance of >3% are considered interspecific species.

**The Validation of The Morphological Identification Using Molecular Identification**

There is a difference in the number of species of the 24 specimens of scad morphologically identified when compared with molecular identification (DNA barcoding) (Table 3). Six species of scad are identified based on their morphological characteristics; *D. macarellus* (ID number RP1-RP4), *D. macarellus\** (ID number RP5-RP8), *D. macrosoma* (ID number RP9-RP12), *D. macrosoma\** (ID number RP13-RP16), *D. russelli\** (ID number RP17-RP20) and *D. kurroides* (ID number RP21-RP24). Furthermore, seen from the DNA barcoding, only four species of scad were successfully identified: *D. macarellus* (ID number RP1-RP8), *D. macrosoma* (RP9-RP16), *D. russelli* (ID number RP17-RP20), and *D. kurroides* (ID number RP21-RP24).

In the beginning, Scad with ID RP1-RP8 consisted of two species: *D. macarellus* dan *D. macarellus\**. However, in DNA barcoding, the Scad with ID RP1-RP8 appeared to consist of only *D. macarellus*. Similarly, Scad with ID RP11-R20 was initially identified consisting of 2 species based on the morphological analysis: *D. macrosoma* dan *D. macrosoma\**. However, the DNA barcoding confirmed that there is only one species: *D. macrosoma*. Likewise, *D. russelli\** (ID RP21-RP25) which had been falsely identified, appeared to have four Scad species: *D. macarellus*, *D. macrosoma* dan *D. russelli*. dan *D. kurroides*.

**Table 3.** The comparison of scads species based on the morphological identification with the molecular identification.

ID	Species	
	Morphological identification	Molecular identification
RP1-RP4	<i>D. macarellus</i>	<i>D. macarellus</i>
RP5-RP8	<i>D. macarellus*</i>	<i>D. macarellus</i>
RP9-RP12	<i>D. macrosoma</i>	<i>D. macrosoma</i>
/RP13-RP16	<i>D. macrosoma*</i>	<i>D. macrosoma</i>
RP17-RP20	<i>D. russelli*</i>	<i>D. russelli</i>
RP21-RP24	<i>D. kurroides</i>	<i>D. kurroides</i>
Number of Species	4	4
	*suspected to be other species	

After being validated using the results of DNA barcoding, three species of scad which were originally still "suspected" based on the morphological identification; *D. macarellus\**, *D. macrosoma\**, and *D. russelli\**, with all of the species being identified as *D. macarellus*, *D. macrosoma* dan *D. russelli*. It shows that differences in morphological characteristics of every individual vary in every Scad species yet they do not necessarily affect the genetic differences. Zhang & Hanner (2011) proposed that for fish, a large part of intraspecific diversity or interspecific overlapping in the identification process affects the accuracy of the identification. According to Bohlke & Chaplin (1993), fish in the *Carangidae* family, including scad, often show significant changes in morphology and pigmentation throughout growth, leading to incorrect identification.

The overlapping characteristics and significant genetic variation between *D. macrosoma* and *D. macarellus* represent a weakness in characteristic-based identification, as seen in Table 1 & Figure 2. Inaccuracy of fish species identification using morphological methods is common since identification keys often require a high level of expertise (Hebert et al., 2003). Several experts mentioned some factors that may interfere with the identification, including the large number of morphological characters used in identification and the variation in these characters due to geographical differences, sex differences, and character differences in each life phase (Heemstra & Randall, 1993; Blaxter, 2006; DeSalle, 2006; Victor et al., 2009) and the existence of Cryptic species (morphologically similar but

genetically different) (Hubert et al., 2012). In much research, the molecular approach has been used in the scad identification process at the species level. Furthermore, DNA Barcoding has been regarded as a suitable complementary taxonomic tool in quicker and accurate species identification.

**Genetic and Phylogenetic Distance**

Based on the results of molecular validation (DNA barcoding), four species were identified from 24 fish specimens of Momar. After the editing, 24 COI gene sequences from 24 Momar specimens resulted in a sequence length of 635 bp, which genus and species are shown in Table 4.

**Table 4.** Genetic differences (percentage of K2P distance) within taxonomic levels

% K2P Genetic Distances			
Comparison Within	Min	Max	Mean
Genus (Interspecific)	6.12	13.29	10.18
Species (Intraspecific)	0.00	1.75	0.54

The intraspecific K2P genetic of COI genes ranges from 0.00 to 1.75% (mean 0.54%); with the smallest genetic distance (0.00%) in the species *D. macarellus* and *D. macrosoma* and the most considerable genetic distance (1.75%) between specimens in the species *Decapterus russelli* (Table 5). The interspecific K2P genetic range of COI genes is between 6.12-13.29% (mean 10.18%), with the smallest genetic distance (6.12%) between specimens from *D. macarellus* species and specimens from *D. macrosoma* species and the most significant genetic distance (13.29%) between specimens from *D. russelli* species and specimens from *D. kurroides* species (Table 6). The average of interspecific K2P genetic distance, of 10.18%, is significantly greater than the average of intraspecific K2P genetic distance or about 19 times the average of intraspecific K2P genetic distance. The mean interspecific genetic distance (10.18%) is significantly higher than the

average intra-specific genetic distance (0.54%), indicating that the genetic characteristics between specimens from one species to another have quite large than the genetic characteristics between specimens of the same species.

**Table 5.** Genetic differences (percentage of K2P distance) within species (intraspecific)

% K2P Genetic Distances					
Species	Min	Max	Mean	Nearest Neighbor	Farthest Neighbor
				Species	Mean Species
<i>D. macarellus</i>	0.00	0.79	0.29	<i>D. macrosoma</i>	6.42
<i>D. macrosoma</i>	0.00	0.95	0.42	<i>D. macarellus</i>	6.42
<i>D. russelli</i>	0.47	1.75	1.03	<i>D. macarellus</i>	10.01
<i>D. kurroides</i>	0.16	0.63	0.42	<i>D. macarellus</i>	10.03

**Table 6.** Genetic differences (percentage of K2P distance) within genus (interspecific)

Comparison Within Genus	% K2P Genetic Distances		
	Min	Max	Mean
<i>D. macarellus</i> vs <i>D. macrosoma</i>	6.12	7.15	6.42
<i>D. macarellus</i> vs <i>D. russelli</i>	9.31	10.76	10.01
<i>D. macarellus</i> vs <i>D. kurroides</i>	9.56	10.46	10.03
<i>D. macrosoma</i> vs <i>D. russelli</i>	10.59	11.89	11.22
<i>D. macrosoma</i> vs <i>D. kurroides</i>	10.12	11.24	10.67
<i>D. russelli</i> vs <i>D. kurroides</i>	12.17	13.29	12.75

A phylogenetic tree (NJ) was created based on 24 DNA barcode sequences (Figure 4) which group similar specimens forms of monophyletic clusters (from the same ancestor) that are separated from each other, with the support of bootstrap values of 100%. Within the monophyletic group formed, some subgroups have bootstrap values support ranging between 40-64%. The most negligible (40%) and the largest (64%) bootstrap support was found in the subgroup nodes of the *D. russelli* species (Figure 4 (b)).

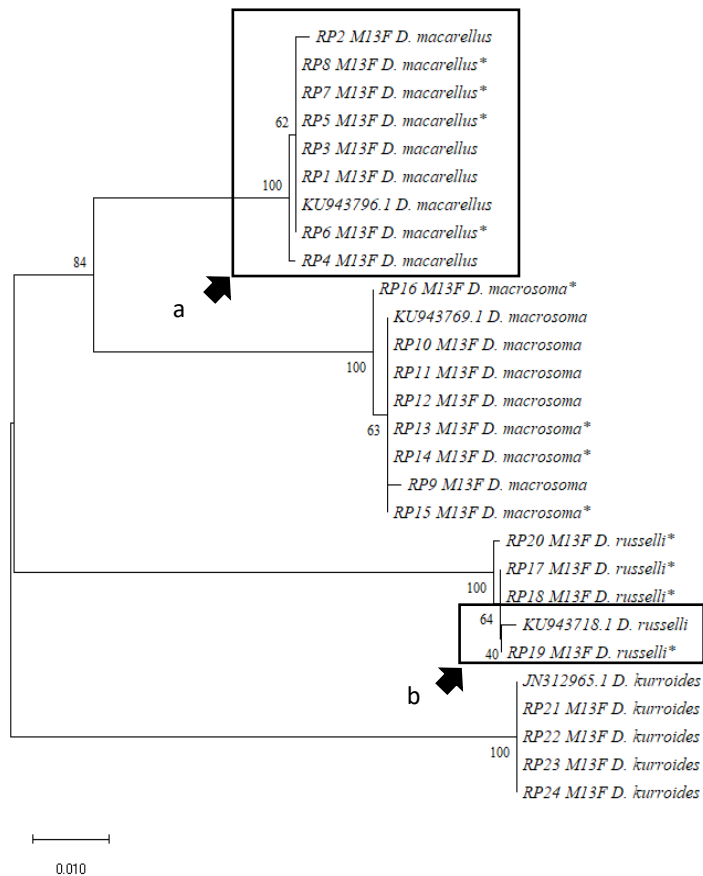


**Figure 4.** A phylogenetic tree created based on 24 DNA barcode sequences yielded a) a monophyletic group, b) a subgroup within a monophyletic group.

The mitochondrial COI gene is commonly used as a species barcode due to its distinctive pattern of genetic variation between species (Hebert et al., 2003b). The K2P model is employed in this study because it offers consistency and facilitates comparison with other studies.

Hebert et al. (2003a) suggested that DNA sequences would be more similar within species (intra-specific) than between species (inter-specific). The observed range of intra-specific genetic distance, from 0.00% to 1.75%, indicates that all specimens belong to the same four identified species. According to Hebert et al. (2003a), species with a genetic distance greater than 3% are classified as inter-specific.

Specimens were grouped based on genetic similarity, consistently resulting in the same pattern across 1000 repetitions. Identical specimens formed a monophyletic group with a 100% bootstrap value, demonstrating that COI-based DNA barcoding can accurately identify scad fish species (Ran et al., 2020). The grouping pattern remained consistent.

The formation of subgroups among similar specimens is due to their high genetic similarity. Slight differences in genetic distance between similar specimens (intra-specific) lead to the creation of subgroups within the monophyletic group (Figure 4b). Increased branching or the number of subgroups within a

monophyletic group indicates higher genetic variation among specimens within a species.

#### 4. Conclusion

Morphological identification based on morphometric and meristic calculations initially indicated six species of scads in Ambon's waters, with three of these being uncertain and suspected to be other species. However, DNA barcoding confirmed the presence of only four species: *Decapterus macarellus*, *D. macrosoma*, *D. russelli*, and *D. kurroides*.

#### 5. References

Abdussamad, E. M., Prathibha, R., Koya, K. P., Koya, S., Mohamed, H., Jeyabalan, K. 2013. Carangids (Family: Carangidae) in seas around the Indian subcontinent with a description of macro-taxonomic character for the field identification of genera and species. Kerala-India: Central Marine Fisheries Research Institute.

Akbar, N., Aris, M., Irfan, M., Tahir, I., Baksir, A., Surahman, Madduppa, H. H., Kotta, R. 2018. Filogenetik ikan tuna (*Thunnus* spp.) di Perairan Maluku Utara, Indonesia [Phylogenetic of tuna fish (*Thunnus* spp.) in North

- Mollucas Sea, Indonesia]. *Jurnal Iktiologi Indonesia*, 18(1): 1-11
- Astarloa, J.M.D., Mabragna, E., Hanner, R. 2008. Morphological and molecular evidence for a new species of longnose skate (Rajiformes: Rajidae: Dipturus) from Argentinean waters based on DNA barcoding. *Zootaxa* 1921, 35–46.
- Ausubel, F. M., Brent R., Kingston R.E., Moore D.D., Seidman J.G., Smith J.A., Struhl K. 2003. *Current Protocols in Molecular Biology*. Volume I. John Wiley and Sons, Inc., New York.
- Barry, J., Newton, M., Dodd, J.A., Hooker, O.E., Boylan, P., Lucas, M.C., Adams, C.E. 2016. Foraging specialisms influence space use and movement patterns of the European eel *Anguilla anguilla*. *Hydrobiologia* 766:333–348
- Blaxter, M., 2006. Will DNA barcoding advance efforts to conserve biodiversity more efficiently than traditional taxonomic methods? Reply. *Frontiers in Ecology and the Environmental*, 4(5), 272-272
- Bohlke, J. E., Chaplin, C.C.G. 1993. *Fishes of the Bahamas and adjacent tropical waters*. 2 ed. University of Texas press, Austin.
- Carpenter, K. E, Volker, H. N. 1999. *The Living Marine Resources Of The Western Central Pacific*. Volume 4. Bony fishes part 2 (Mugilidae to Carangidae). Department of Biological Sciences Old Dominion University Norfolk, Virginia, USA dan Marine Resources Service Species Identification dan Data Programme FAO Fisheries Department. Rome: Food dan Agriculture Organization Of The United Nations.
- Cayetano, B.J., Honebrink, R.R. 2000. A review of the biology of the family Carangidae, with emphasis on species found in Hawaiian waters. DAR Technical Report 20-01. Department of Land and Natural Resources, Hawaii, 37 p.
- Ciaro, D.E., Schaer, G., Böttger, E.C., Altwegg, M., Bosshard, P.P. 2006. Internal transcribed spacer sequencing versus biochemical profiling for identification of medically important yeasts. *J Clin Microbiol* 44, 77–84.
- Costa, F.O., Carvalho, G. R. 2007. The Barcode of Life Initiative: synopsis and prospective societal impacts of DNA barcoding of fish. *Genomics Society and Policy*, 3(2), 29–40.
- Dahlan, M.A., Nur, M., Nessa, M., Omar, B.A.S., Tresnati, J., Burhanuddin, A.I. 2014. Morphometric and Meristic Comparison of *Decapterus macrosoma* Bleeker, 1851 From Makassar Strait and Bone Bay, South Sulawesi, Indonesia. *International Journal of Plant, Animal and Environmental Science (IJAPES)*.
- DeSalle, R. 2006. What's in a character?. *J Biomed Inform* 39:6-17
- Felsenstein, J. 1985. Confidence limits on phylogenies: an approach using the bootstrap. *Evolution* 39, 783-791.
- Genisa A.S. 1998. Beberapa catatan tentang biologi ikan layang marga Decapterus. *Jurnal Genisa*, 23: 27-36.
- Golani, D. 2006. "The Indian scad (*Decapterus russelli*), (Osteichthyes: Carangidae), a new Indo-Pacific fish invader of the eastern Mediterranean". *Scientia Marina*, vol. 70(4): 603-605.
- Hebert, P.D.N., Cywinska, A., Ball, S.L., deWaard, J.R. 2003a. Biological identifications through DNA barcodes. *Proc. R. Soc. B* 270, 313–321.
- Hebert, P. D. N., Ratnasingham, S., de Ward, J. R. 2003b. Barcoding animal life: cytochrome c oxidase subunit 1 divergence among closely related species. *Proc. R. Soc. B* 270, S96-S99.
- Hubert N, Meyer C.P., Bruggemann, H.J., Guerin, F., Komeno, R.J., Espiau, B., Causse, R., Williams, J.T., Planes, S. 2012. Cryptic diversity in Indo-Pacific coral-reef fishes revealed by DNA barcoding provides new support to the centre-of-overlap hypothesis. *PloS One* 7 (3): e289287. DOI: 10.1371/journal.pone.0028987
- Heemstra, P.C., Randall, J.E. 1993. Vol.16. Groupers of the world (Family Serranidae, Subfamily Epinephelinae). FAO Species Catalogue.
- Ivanova, N.V., Zemlak, T.S., Hanner, R.H., Hebert, P.D.N. 2007. Universal primer cocktails for fish DNA barcoding. *Mol. Ecol. Notes* 7, 544–548.
- Kimura, M. 1980. A simple method for estimating evolutionary rates of base substitutions through comparative studies of a nucleotide sequence. *J. Mol. Evol.* 16, 111-120
- Kumar, S., Stecher, G., Peterson, D., Filipowski, A., Tamura, K. 2018. MEGA X: molecular evolutionary genetics analysis across computing platforms. *Molecular Biology and Evolution*, 35: 1547-1549.
- Lagler, K.F., Bardach, J.E., Miller, R.R., Passino, D.R.M. 1977. *Ichthyology*. Wiley, New York.

- Lahaye, R, Van der Bank, M., Bogarin, D., Warner, J., Pupulin, F., Gigot, G., Maurin, O., Duthoit, S., Barraclough, T.G., Savolainen, V. 2008. DNA barcoding the floras of biodiversity hotspots. *Proc. Nat. Acad. Sci.*, 105(8): 2923-2928
- Lakra, W.S., Goswami, M., Gopalakrishnan, A. 2009. Molecular identification and phylogenetic relationships of seven Indian Sciaenids (Pisces: Perciformes, Sciaenidae) based on 16S rRNA and cytochrome oxidase subunit I mitochondrial genes. *Molecular Biology Reports*, 36, 831–839.
- Limmon, G., Delrieu-Trottin, E., Pattikawa, J., Rijoly, F., Dahruddin, H. 2020. Assessing species diversity of Coral Triangle artisanal fisheries: A DNA barcode reference library for the shore fishes retailed at Ambon harbour (Indonesia). *Ecology and Evolution*, 10, 3356–3366.
- Limmon, G.V., Khouw, A.S., Loupatty, S.V., Rijoly, F., Pattikawa, J.A. 2017a. Species richness of reef food fishes in Ambon Island waters, Maluku Province, Indonesia. *AAFL Bioflux* 10(3):507-511.
- Limmon, G. V., Rijoly, F., Khouw, A. S., Manuputty, G. D., Pattikawa, J. A. 2017. The Diversity of Grouper (Epinephelinae) in Ambon Island, Maluku, Indonesia. *Occasional Papers No.58*, 23-29.
- Limmon, G.V., Rijoly, F., Ongkers, O.T.S., Loupatty, S.R., Pattikawa, J.A. 2017b. Reef fish in the southern coastal waters of Ambon Island, Maluku Province, Indonesia. *AAFL Bioflux* 10(2):234-240.
- Muschick, M., Barluenga, M., Salzburger, W., Meyer, A. 2011. Adaptive phenotypic plasticity in the Midas cichlid fish pharyngeal jaw and its relevance in adaptive radiation. *BMC Evol Biol* 11:116
- Nimbs, M. J., Wilson, N. G., Limmon, G. V., Smith, S. D. A. 2020. Redescription of the Sea Hare *Phyllaplysia Viridis* (Bergh, 1905) (Gastropoda: Heterobranchia: Aplysiida). *Malacologia*, 63 (1), 11–20
- Norman, J.R. 1935. The -carangid fishes of the genus *Decapterus* Bleeker. *Ann. Mag. nat. Hist.*, Ser. 10. 16: 252--264
- PeEnikar, Ž.F., Buzan, E.V. 2014. 20 years since the introduction of DNA barcoding: from theory to application. *J. Appl. Genet.* 55, 43-52
- Packer, L., Gibbs, J., Sheffield, C., Hanner, R. 2009. DNA Barcoding dan The Mediocrity of Morphology. *Molecular Ecology Resources* (2009) 9 (Suppl. 1), 42–50
- Radulovici, A.E., Archambault, P. Dufresne, F. 2010. DNA Barcodes for Marine Biodiversity: Moving Fast Forward? *Diversity* 2:450-472.
- Ran, K., Li, Q., Qi, L., Li, W., Kong, L. 2020. DNA barcoding for identification of marine gastropod species from Hainan island, China. *Fisheries Research* 225 (2020)105504
- Rijoly, F. 1987. “Analisa sistematika dan ekologi ikan tangkapan sampingan trawl di perairan Pantai Timur Kepulauan Aru”. Ambon: Fakultas Perikanan dan Ilmu Kelautan-Universitas Pattimura.
- Rijoly, F., Natan, Y., Pattikawa, J.A., Ongkers, O.T.S., Uneputty, P.A. 2016 Community structure of fish in inner Ambon Bay, Maluku, Indonesia. *International Journal of Fisheries and Aquatic Studies* 4(5):264-269.
- Saitou, N., Nei, M. 1987. The neighbor-joining method: A new method for reconstructing phylogenetic trees. *Molecular Biology and Evolution* 4:406-425.
- Sakinan, S, Orek, Y.A. 2011. First record of Indo-Pacific Indian scad fish, *Decapterus russelli*, on the north-eastern Mediterranean coast of Turkey. *Marine Biodiversity Records* 4, (14) 1-3.
- Savolainen, V., Cowan, R.S., Vogler, A.P., Roderick, G.K, Lane, R. 2005. Towards writing the encyclopedia of life: an introduction to DNA barcoding. *Philosophical Transactions of the Royal Society*, 360: 1805–1811.
- Sen, S., Shrinivas J., Jaiswar, A.K., Chakraborty, S.K., Sajina, A.M., Dash, G. R. 2011. Stock structure analysis of *Decapterus russelli* (Ruppell, 1830) from east and west coast of India using truss network analysis. Elsevier.
- Song, H., Buhay, J.E., Whiting, M.F., Crandall, K.A. 2008. Many species in one: DNA barcoding overestimates the number of species when nuclear mitochondrial pseudo genes are coamplified. *Proceedings of the National Academy of Sciences of the United States of America*, 105, 13486-13491.
- Steinke D., Prosser, S.W.J., Hebert, P.D.N. 2016. DNA Barcoding of Marine Metazoans. In: Bourlat S (ed), *Marine Genomics. Methods in Molecular Biology*, vol 1452. Humana Press, New York, NY.
- Steinke, D., Zemlak, T.S., Hebert, P.D.N. 2009. Barcoding Nemo: DNA-Based identifications for the ornamental fish Trade. *Plos ONE* 4, e6300.
- Syafrina, R.A. 2011. “Penggunaan DNA barcode sebagai alterative identifikasi species Udang Mantis”. Bogor:IPB-Bogor.

- Trautman, M.B. 1957. The fishes of Ohio. The Ohio State University Press. Columbus, Ohio. 638 p.
- Victor, B.C. 2007. *Coryphopterus kuna*, a new goby (Perciformes: Gobiidae: Gobiinae) from the western Caribbean, with the identification of the late larval stage and an estimate of the pelagic larval duration. *Zootaxa*, 1526, 51–61.
- Victor, B.C. Hanner, R., Shivji, M., Hyde, J., Caldow, C., 2009. Identification of the larval and juvenile stages of the Cubera Snapper, *Lutjanus cyanopterus*, using DNA barcoding. *Zootaxa*, 2215, 24-36
- Wallace, D.C. 1997. Mitochondrial DNA in Aging and Disease. New York. Scientific American. Pp 40-47.
- Ward, R. D., Holmes, B.H., Yearsley, G.K. 2008. DNA barcoding reveals a likely second species of Asian sea bass (*barramundi*) (*Lates calcarifer*). *Journal of Fish Biology*, 72, 458–463.
- Wibowo, A., Pangabean, A. S., Zamroni, A., Priatna, A., Yusuf, H. N. 2018. Using DNA Barcode to Improve the Identification of Marine Fish Larvae, Case Study Coastal Water Near Jakarta and Banda Sea, Indonesia. *Indonesian Fisheries Research Journal*, 24 (1), 23-30.
- Wiens, J.J., Servedio, M.R. 2000. Species delimitation in systematics: inferring diagnostic differences between species. *P. Roy. Soc. Lond. B. Bio* 267, 631–636.
- Wimberger, P.H. 1992. Plasticity of fish body shape-the effects of diet, development, family and age in two species of *Geophagus* (Pisces: Cichlidae). *Biol. J. Linn. Soc.* 45, 197–218.
- Wong, L.L. 2011. DNA Barcoding and Related Molecular Markers for Fish Species Authentication. Auburn: Phylogenetic Assessment and Population Studies. Auburn University.
- Zhang, J.B., Hanner, R. 2011. DNA Barcoding is A Useful Tool for the Identification of Marine Fishes from Japan. Elsevier.

## MOLECULAR APPROACH AND PRELIMINARY SCREENING OF CULTURABLE FREE-LIVING RHIZOBIUM AS PLANT GROWTH ENHANCER

Tri Ratna Sulistiyani<sup>1a\*</sup>, Siti Meliah<sup>2a</sup>, Masrukhin<sup>3a</sup>, Mia Kusmiati<sup>4a</sup>, Agus Budiyanto<sup>5b\*</sup>, Dwi Agustiyani Muslichah<sup>6c</sup>

**Abstract:** The population increase and changes in consumption are the main challenges in agriculture production related to the increase in basic needs, especially food. The high demand for food leads to fertilizer application to effectively speed up and manage plant growth. The search for alternative biofertilizers from unique microorganisms is needed to tackle this issue. *Rhizobium* is known as a plant growth enhancer. In this study, they were isolated from Aek Natonang, famous as “the lake above the lake”, located on Samosir Island, North Sumatra, at more than 1400 m. These geographical conditions offer various potential unique microorganisms. The collected free-living *Rhizobium* from the sample was identified by morphological characteristics and molecular approach through 16S rDNA sequence. They were assessed for their abilities as plant growth promoters. Based on the morphological characterization, they showed a creamy yellow colony, excessive mucus production, Gram-staining negative, and catalase positive. Through the molecular approach, they have 98-100% similarity with *Rhizobium* sp.. A combination of morphological and molecular approaches strengthens the identification results. Six *Rhizobium* sp. produced IAA, siderophore, ACC Deaminase, and ammonia. They could also solubilize phosphate tolerated to high pH and salt concentrations. All the collected *Rhizobium* were qualitatively potential to enhance the plant growth. They performed diverse abilities in vitro, and *Rhizobium radiobacter* strain DT 14.16 displayed the best features. Hence, they can be a candidate for biofertilizer. However, none of the collected *Rhizobium* could suppress the growth of *Ralstonia solanacearum*. Using quality indigenous bacteria such as *Rhizobium*, is an environmentally friendly technology to increase agricultural productivity and hopefully provide better yield.

**Keywords:** Agriculture, PGPR, *Rhizobium*, strain, Toba.

### 1. Introduction

Indonesia's population reached 270 million, becoming a big problem in every sector, including agriculture. The increase in population and changes in consumption are the main challenges in agriculture production related to the increase in basic needs, especially food. This high demand for food leads to fertilizer application to accelerate plant growth and control plant diseases. However, an extreme application of chemical fertilizers could induce severe problems for human health and environmental pollution. Furthermore, chemical fertilizers can also change the diversity of soil microorganisms essential for soil fertility (Dinca et al., 2022). Therefore, in line with human understanding of healthy food, agricultural practices changed to nature-based through eco-friendly approaches. Gradually, chemical fertilizers are replaced with biofertilizers, and microbial application is one of the strategies to fulfil the need for healthy food.

Soil microorganisms are involved in soil health and agricultural product sustainability. Besides promoting plant growth, microorganisms are considered inexpensive and environmentally safe (Dinca et al., 2022). They would reduce the need and reliance on chemical fertilizers. Studies have reported that microorganisms can increase plant growth due to their capability to generate active compounds such as growth hormones, antibiotics, and enzymes. Additionally, they are capable of performing nitrogen fixation from the environment. The genus of bacteria that are ubiquitous in the rhizosphere and widely applied in agricultural farmlands are *Rhizobium*, *Bacillus*, *Azotobacter*, *Azospirillum*, *Serratia*, *Pseudomonas*, *Burkholderia*, *Agrobacterium*, *Delftia* (Rajawat et al., 2019; Venieraki et al., 2021).

*Rhizobium* exists in the soil independently as a free-living bacteria or in symbiosis with roots in a legume nodule. *Rhizobium* can fix atmospheric nitrogen (N<sub>2</sub>) in the air and convert it into ammonia (NH<sub>3</sub>), which is further converted into amino acid used for plant growth. *Rhizobium* also produces biologically active compounds to promote plant development (Saghafi et al., 2018), directly by providing nutrients or indirectly by producing antibiotic compounds (Jaiswal et al., 2021). *Rhizobium*'s uniqueness is its symbiotic ability with Leguminosae/Fabaceae leguminosae plants by forming nodules on the roots. The *Rhizobium* characteristic is that they infect the root hairs of legumes in temperate climates or topical areas, curl the hair

#### Authors information:

<sup>a</sup>Research Center for Biosystematics and Evolution, National Research and Innovation Agency (NRIA), Cibinong, INDONESIA. E-mail: trir003@brin.go.id<sup>1</sup>; sitimeliah@gmail.com<sup>2</sup>; masrukhin21@gmail.com<sup>3</sup>; miakusmiati.charis@gmail.com<sup>4</sup>

<sup>b</sup>Research Center for Agroindustry, National Research and Innovation Agency (NRIA), Cibinong, INDONESIA. E-mail: agusbdyanto@gmail.com<sup>5</sup>

<sup>c</sup>Research Center for Applied Microbiology, National Research and Innovation Agency (NRIA), Cibinong, INDONESIA. E-mail: titinagustin@yahoo.com<sup>6</sup>

\*Corresponding Author: trilisty01@gmail.com; agusbdyanto@gmail.com

Received: June 12, 2023

Accepted: August 24, 2023

Published: June 30, 2024

roots, and, lately, produce root nodules. These processes make *Rhizobium* an intracellular symbiosis. The uniqueness and ability to generate active compounds beneficial for plants cause *Rhizobium* to be categorized as plant growth-promoting rhizobacteria (PGPR). Indonesia has the largest lake, also become the largest in the world, called Lake Toba. Aek Natonang, known as the "lake above the lake", which located on Samosir Island in the middle of Lake Toba. Being at an altitude of > 1400 m makes Aek Natonang unique regarding its geographical conditions, causing a relatively high microorganism diversity in that location. Therefore, the present study aimed to explore free-living *Rhizobium* diversity from unique conditions in the tropical rain forests around Lake Toba, screening the physiological activity of a plant-growth-promoting bacteria and their tolerance under abiotic stress conditions such as high salt levels and pH variations.

## 2. Materials and Methods

### *Rhizobium* isolation

As many as eleven rhizosphere soils were taken from the Lake Toba area, namely Aek Natonang and Eden Park 100 in North Sumatra, Indonesia, at a high altitude of >1400 m above sea level. Isolation was carried out using serial dilution and spread on Ashby Mannitol Agar media. It was followed by incubation at 28 °C for 3-7 days. The colony showing *Rhizobium* characteristics was purified and preserved using a freezing method at -80 °C for the following analysis.

### Morphology and Phenotypic Characterization

Somasegaran and Hoben (1994) refer to the morphological characterisation of bacterial colonies. The characteristics observed, i.e., size, shape, border, elevation, colour, mucosity, and transparency of colony after three days of incubation on Yeast Mannitol Agar (YMA). Gram reaction was conducted using a Gram staining reagent following the instructions provided by the manufacturer (Merck). *Rhizobium*'s ability to produce acids or bases was checked by growing on a YMA medium added with 1% Congo red or 0.025% Brom Thymol Blue (BTB). Isolate was cultured on YMA and incubated for seven days at 28 °C under dark conditions, and then the medium colour alteration was observed. As an acid-producing and fast-growing bacteria, the medium colour was changed from green to yellow. In contrast, base-producing and slow-growing bacteria were changed from green to blue.

### Molecular Identification

The DNA extract as a DNA template was collected by cell disruption at 98 °C for 5 min, as Packeiser et al. described. (2013). The bacterial DNA was amplified using primers: Forward, 27F (5'-AGAGTTTGATCCTGGCTCAG-3') and Reverse, 1492R (5'-GGTTACCTGTACGACTT-3') (Lane, 1991) with the PCR conditions: initial denaturation (95 °C, 90 sec), followed by 30 cycles of denaturation (95 °C, 30 sec); annealing (50 °C, 30 sec); elongation (72 °C, 90 sec), and final extension (72 °C, 5 min). Amplified DNA was loaded into wells on 1% agarose gel

electrophoresis, followed by DNA visualization using a UV transilluminator.

The DNA sequencing was performed in Macrogen, South Korea. The chromatogram sequence was analyzed using Chromas Pro software, and the possible identity was searched through the EzBioCloud 16S database (Yoon et al., 2017). Construction and visualization of the phylogenetic tree were executed using the MEGA 11 programme (Hall, 2013). Contig and reference sequences were aligned using Clustal W and followed by construction using the Neighbor-Joining Method (Tamura et al., 2011), Kimura 2-Parameter as a suggested model, and 1000 bootstrap replication.

### Plant Growth Promoting Ability Assay

Isolate ability to fix nitrogen was tested using Jensen-free nitrogen media. Isolates were grown on Jensen-free nitrogen media and kept at 28 °C for seven days. The growth was observed daily. Vaccination was made in two replications.

Inorganic phosphate solubilization ability was determined using Pikovskaya Agar (Jasim et al., 2013). The isolate was streaked on the Pikovskaya Agar and placed in the incubator at 28 °C. A clear zone around the colony revealed a positive result. Vaccination was made in two replications.

Indole Acetic Acid (IAA) compounds analysis followed Rahman et al. (2010) protocol. Isolates were cultured on a liquid Yeast Mineral Extract (YEM) media enriched with 0.2% (v/v) L-tryptophan and kept in a shaker incubator at 28 °C for three days. On the third day, culture centrifugation at 10000 rpm for 10 min, then 200 µL of Salkowski's reagent was put into 100 µL of supernatant and placed in the darkroom for 30 min. Finally, absorbance measurement at 530 nm. Analysis was made in two replications.

Siderophore production was evaluated using Chrome Azurol S (CAS) agar (Alexander & Zuberrer, 1991). Isolate was streaked on the CAS agar, and then placed at 28 °C for 72 hours. A circular yellow-orange around the colony indicated isolate could generate a siderophore. Vaccination was made in two replications.

Inoculated isolates checked ACC deaminase activity on Tryptone Yeast (TY) media. It was incubated for 48 ± 2 hours at 28 ± 1 °C (Beringer, 1974). Isolates possessing ACC deaminase activity were indicated by growth ability in TY media. Vaccination was made in two replications.

Ammonium production was performed by inoculating the isolate in 5 mL of Peptone water media, then incubating at 28 ± 2 °C for 72 hours. Subsequently, 0,5 mL Nessler reagent was added to the inoculated media and observed brown colour formed in the media. Vaccination was made in two replications.

### Screening for Salt and pH Tolerance

The isolate was streaked in Yeast Mannitol Broth (YMB) media containing 0.5-5.0% (w/v) NaCl, with an interval of 0.5%. Acid or alkaline tolerance was evaluated using YMB media adjusted to pH 3-9, with a rise of 1 pH unit. Cell growth in the medium indicated their salt or potential hydrogen tolerance is given.

**Biocontrol Assay Against *Ralstonia solanacearum***

The nineteen isolates were tested for antagonistic activity against *R. solanacearum*. The agar spot-on-the-lawn method carried out the antimicrobial assay with a slight modification of the agar diffusion method (van Reenen et al., 1998; Sabo et al., 2020). Prior to the assay, *R. solanacearum* was grown in the triphenyl tetrazolium chloride (TZC) agar, incubated for 48 hours, then inoculated into nutrient agar (NA) medium and incubated overnight. The concentration of *R. solanacearum* was adjusted according to the McFarland turbidity standard 0.5 and streaked to the Mueller Hinton Agar (MHA) densely. Isolates were grown in YMA medium, incubated for 72 hours, then spotted into MHA medium-containing *R. solanacearum* and incubated at 37 °C for 48-72 hours.

**3. RESULTS**

**Isolation and Morphological Characterization**

A total of 77 bacterial isolates were successfully collected from 11 rhizosphere samples. Phenotypically, 19 of 77 collected bacterial isolates showed the same characteristics as *Rhizobium*. The isolates formed circular, smooth, convex, raised, milky cream to yellow colour, opaque, and mucoid colonies. They were rod-shaped and pink in colour under Gram stains; therefore, they are considered Gram-negative bacteria. The morphological characteristics of bacterial isolates are presented in Table 1.

The notable characteristics of *Rhizobium* were that it produced catalase enzyme and mucoid texture. The mucus appeared after three days of incubation at 28°C due to exopolysaccharide production. The ability of the *Rhizobium* strain to generate acid or alkaline can be visualized by stain absorption on the YMA medium, and generally, rhizobia absorbs the dye weakly. On the other hand, 84% of the tested isolates changed medium colour from deep green to yellow. The alteration of medium colour indicates that the isolates mainly were acid-producing and fast-growing bacteria.

**Table 1.** Morphological characters of selected isolates

Isolate code	Gram stain	Cell shape	Form	Elevation	Colour	Mucosity	Transparency	CR absorption	BTB reaction (7th day)
TE 29.1	-	Rod	circular	Convex	Milky cream	Soft mucoid	Opaque	NA	R
TE 29.10	-	Rod	circular	Convex	Milky cream	Soft mucoid	Opaque	NA	R
DT 21.16	-	Rod	circular	Convex	Creamy yellow	Soft mucoid	Opaque	NA	R
DT 20.2E	-	Rod	Circular	Convex	Milky cream	Soft mucoid	Translucent	NA	R
DT 14.7	-	Rod	Small	Convex	Creamy yellow	Firm gummy	Opaque	NA	NR
DT 14.19	-	Rod	Circular	Convex	Creamy yellow	Firm	Opaque	NA	NR
DT 14.12	-	Rod	Circular	Convex	Milky cream	Soft mucoid	Translucent	NA	R
DT 14.23	-	Rod	Circular	Raised	Milky cream	Firm gummy	Opaque	NA	R
DT 14.1E	-	Rod	circular	Raised	Milky cream	Soft mucoid	Translucent	NA	R
DT 14.5	-	Rod	Circular	Convex	Milky cream	Soft mucoid	Translucent	NA	R
DT 14.16	-	Rod	Circular	Raised	Milky cream	Soft mucoid	Translucent	NA	NR
DT 14.21	-	Rod	Circular	Convex	Milky cream	Soft mucoid	Opaque	NA	R
MSP.3a.E	-	Rod	Circular	Convex	Milky cream	Soft mucoid	Translucent	NA	R
DT 14.2	-	Rod	Circular	Convex	Milky cream	Soft mucoid	Opaque	NA	R
DT 21.20	-	Rod	Circular	Convex	Milky cream	Soft mucoid	Opaque	NA	R
TE 09.2E	-	Rod	Circular	Convex	Milky cream	Soft mucoid	Opaque	NA	R
TE 29.1E	-	Rod	Circular	Convex	Milky cream	Soft mucoid	Opaque	NA	R
DT 20.1E	-	Rod	Circular	Convex	Milky cream	Soft mucoid	Opaque	NA	R
TE 09.1E	-	Rod	Circular	Convex	Milky cream	Soft mucoid	Opaque	NA	R

Note: CR: Congo Red; BTB: Brom Thymol Blue; NA: Not Absorb; R: Reacted; NR: Not reacted

**Molecular Identification**

In addition to morphological characterization, isolates were identified through the molecular approach 16S rDNA sequence. All identified bacteria belong to *Rhizobium*. The searches through the EzTaxon database generated 98.39-100% similarity value with type strain references on GenBank. This approach fully supports

the morphological characteristics of selected isolates. The closest species identity and percentage similarity are given in Table 2. The evolutionary relationship of selected isolates is shown in Figure 1.

**Table 2.** The closest identity of *Rhizobium* sp. based on the 16S rDNA.

Isolate code	The closest species identity	Homonym/ correct name	Top hit strain	Similarity (%)
TE 29.1	<i>Rhizobium leucaenae</i>	-	USDA 9039(T)	99,85
TE 29.10	<i>Rhizobium calliandrae</i>	-	CCGE524(T)	100
DT 21.16	<i>Rhizobium tropici</i>	-	CIAT 899(T)	99,84
DT 20.2E	<i>Rhizobium tropici</i>	-	CIAT 899(T)	100
DT 14.7	<i>Rhizobium altiplani</i>	-	BR10423(T)	98,87
DT 14.19	<i>Rhizobium altiplani</i>	-	BR10423(T)	99,14
DT 14.12	<i>Rhizobium grahamii</i>	-	CCGE 502(T)	99,54
DT 14.23	<i>Rhizobium smilacinae</i>	-	PTYR-5(T)	98,42
DT 14.1E	<i>Rhizobium radiobacter</i>	<i>Agrobacterium radiobacter</i>	ATCC 19358(T)	99,62
DT 14.5	<i>Rhizobium radiobacter</i>	<i>Agrobacterium radiobacter</i>	ATCC 19358(T)	99,69
DT 14.16	<i>Rhizobium radiobacter</i>	<i>Agrobacterium radiobacter</i>	ATCC 19358(T)	99,92
DT 14.21	<i>Rhizobium radiobacter</i>	<i>Agrobacterium radiobacter</i>	ATCC 19358(T)	99,92
MSP.3a.E	<i>Rhizobium radiobacter</i>	<i>Agrobacterium radiobacter</i>	ATCC 19358(T)	99,7
DT 14.2	<i>Rhizobium multihospitium</i>		HAMBI 2975(T)	100
DT 21.20	<i>Rhizobium multihospitium</i>		HAMBI 2975(T)	100
TE 09.2E	<i>Rhizobium multihospitium</i>		HAMBI 2975(T)	100
TE 29.1E	<i>Rhizobium multihospitium</i>		HAMBI 2975(T)	100
DT 20.1E	<i>Rhizobium rhizogenes</i>		NBRC 13257(T)	99,89
TE 09.1E	<i>Rhizobium miluonense</i>		HAMBI 2971(T)	100

**Physiological characterization**

*Rhizobium* strains possess several characteristics as plant-growth promoters, such as producing active compounds IAA, siderophore, ammonium, fixing nitrogen, solubilized inorganic phosphate, and also have ACC deaminase activity (Table 3). A qualitative assay for nitrogen fixation was detected in 89% of

isolates, ammonium was produced in 95% of isolates, and inorganic phosphate solubilization was exhibited in 53% of isolates. As many as 74% of isolates could produce siderophore, 79 % have ACC deaminase activity, and all bacterial isolates can produce IAA.

**Table 3.** Physiological characterization of *Rhizobium* spp.

Isolate code	Nfix activity	Inorganic Phosphate solubilization	IAA production	Siderophore activity	ACC Deaminase activity	Ammonia production
TE 29.1	+	+	+	-	+	+
TE 29.10	+	+	+	+	+	+
DT 21.16	+	-	+	-	+	+
DT 20.2E	+	+	+	+	+	+
DT 14.7	-	+	+	-	-	+
DT 14.19	-	+	+	+	+	+
DT 14.12	+	-	+	+	+	+
DT 14.23	+	-	+	+	-	-
DT 14.1E	+	-	+	+	+	+
DT 14.5	+	-	+	+	+	+
DT 14.16	+	-	+	+	+	+
DT 14.21	+	-	+	+	+	+
MSP.3a.E	+	-	+	-	-	+
DT 14.2	+	+	+	+	+	+
DT 21.20	+	+	+	+	+	+
TE 09.2E	+	-	+	+	+	+
TE 29.1E	+	+	+	+	+	+
DT 20.1E	+	+	+	+	+	+
TE 09.1E	+	+	+	-	-	+

Note: +: positive activity; -: No activity

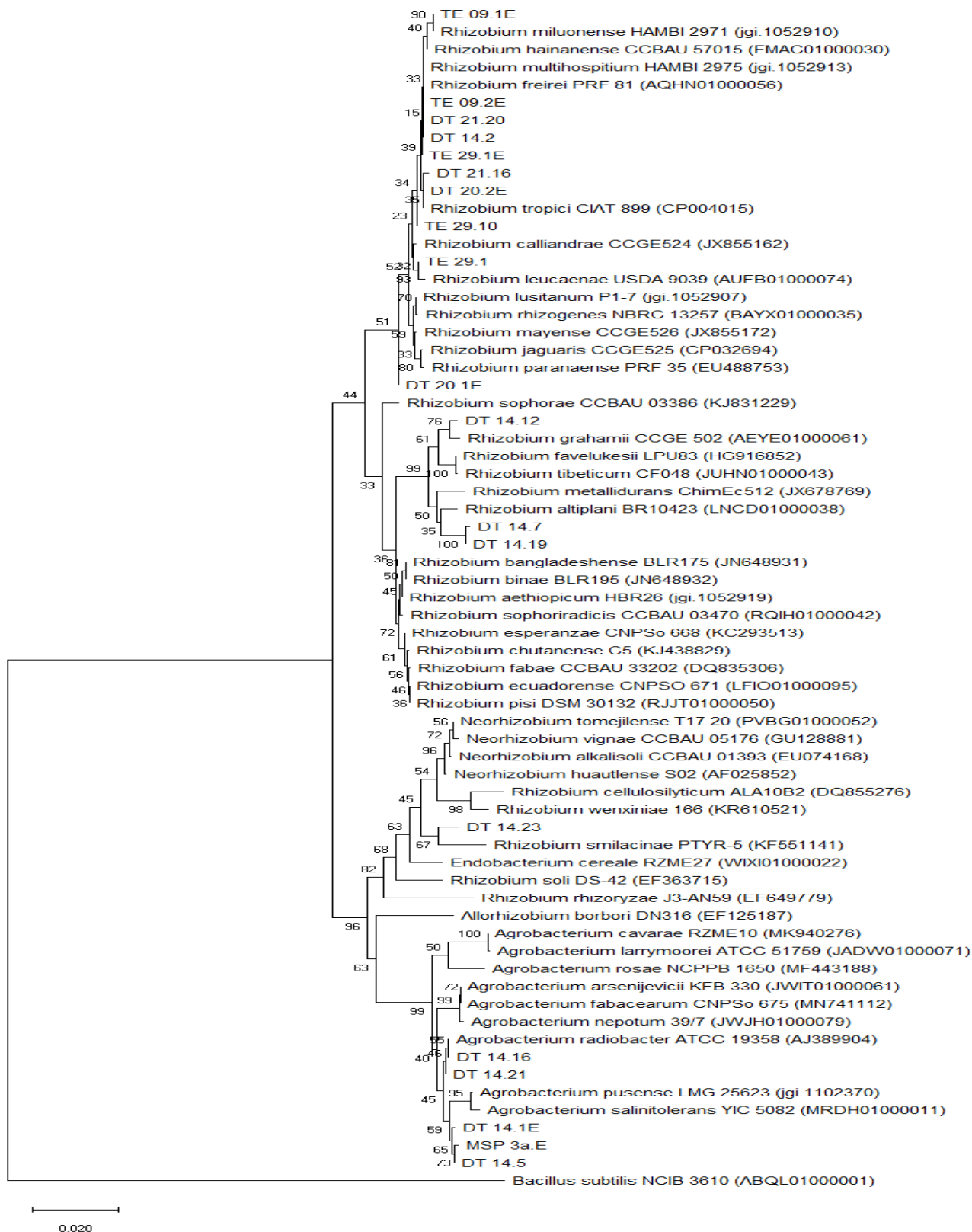


Figure 1. Phylogenetic tree of nineteen *Rhizobium* sp. using Neighbor-Joining method, Kimura-2 parameter model, and bootstrap value 1000

Amongst the *Rhizobium* strain, ten 19 isolates have a phosphate solubilization index ranging from 1,06 to 1,67, with the highest index being *R. altiplani* strain DT 14.7 (Figure 2). As many as fourteen *Rhizobium* strains can produce siderophore with index values from 1 to 14,5; *R. multihospitium* strain TE 29.1E was the highest, while the lowest was *R. multihospitium* strain DT 14.2 and *R. grahamii* strain DT. 14.12. In addition, ACC deaminase activity was also detected in fifteen *Rhizobium* strains.

Quantitatively measurement of IAA production using a spectrophotometer revealed that IAA concentration ranged from 0,792 to 30,6 ppm, with the highest IAA producer being *R. altiplani* strain DT 14.7 and *R. grahamii* strain DT 14.12, while the lowest IAA producer being *R. multihospitium* strain TE 29.1E (Figure 3).

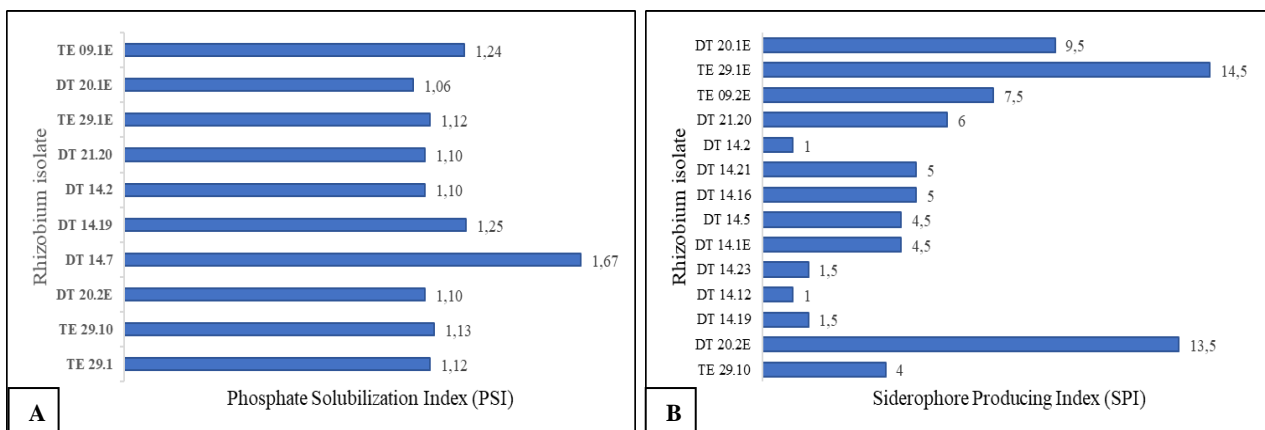


Figure 2. The capability of *Rhizobium* spp. in dissolving inorganic phosphate (A) and producing siderophore (B).

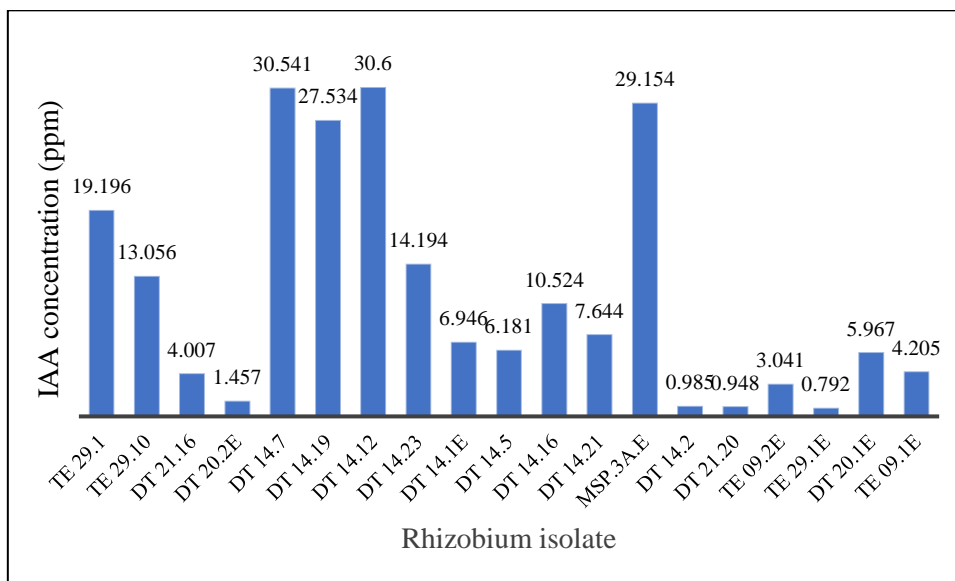


Figure 3. IAA concentration produced by *Rhizobium* spp.

**Salt and pH Tolerance**

The nineteen *Rhizobium* strains can grow in 0.5 and 1% NaCl. However, *R. radiobacter* strain DT 14.16 could grow in 0.5-5% NaCl. The optimum growth condition of *Rhizobium* was pH 7. The result of the present study showed that the nineteen *Rhizobium* spp. could grow in pH 3-9 (data not presented).

**Biological Control Against *Ralstonia solanacearum***

According to the antimicrobial assay, nineteen *Rhizobium* strains could not control *R. solanacearum* growth (data not shown). Chloramphenicol as positive control showed inhibition against *R. solanacearum*.

## 4. Discussion

Nineteen selected isolates were confirmed to be a group of rhizobia through morphology and physiology characterization as well as molecular identification, such as the creamy yellow colony, excessive mucus production, Gram-staining negative, catalase positive, and more than 98% similarity with *Rhizobium* species. Furthermore, the low absorption of Congo Red and BTB in the medium strengthens the assumption that the selected isolates belong to the rhizobia group. Kneen & Larue (1983) reported that rhizobia has white colonies or poorly absorbed dye indicators. The absorption of an indicator chemical is affected by medium composition and strain character. The colour alteration in the YMA medium containing BTB revealed that the selected bacteria was fast-growing and acid-producing, which is one of the characteristics of *Rhizobium* (Koskey et al., 2018).

Identification based on 16S rRNA gene sequence, the selected isolates showed a high similarity percentage to the reference strains. The 19 selected isolates were challenging to be identified solely based on their morphological appearance because all isolates were visually the same. However, the molecular technique was able to separate them into different species. Therefore, the combination of phenotypic and molecular approaches guaranteed that the selected isolates belonged to the genus *Rhizobium*. A point to be highlighted is *Rhizobium smilacinae* strain DT 14.23 has a slightly low percentage of similarity, 98.42%, compared to the reference species provided. Based on this value, the strain is potentially a candidate for new species. Unique locations such as Aek Natonang provide a great chance for new species discovery.

Rhizospheric microorganisms supply most of the nutrition plants require (Mendes et al., 2013). These bacteria contribute to the promotion of plant growth through both direct and indirect mechanisms. Indole acetic acid, popular as auxin, is a plant product utilized directly by plants. The IAA production highly depends on the type of bacteria and tryptophan availability in the environment (Duca et al., 2014). IAA is involved in cellular generation (Bhardwaj et al., 2014), controlling metabolite biosynthesis, and resisting environmental conditions (Rohini et al., 2018). Ul Hasan & Bano (2015) stated that L-tryptophan addition into the soil could be done to manage plant growth. Therefore, rhizospheric bacteria that could produce IAA, even in small concentrations, are necessary. The ability to utilize and produce IAA varies among bacterial strains, regardless of the presence or absence of tryptophan.

Bacteria capacity to generate IAA is also reported to have ACC deaminase with high activity (Glick, 2014). Through ACC deaminase expression, *Rhizobium* can convert 1-aminocyclopropane-1-carboxylic acid (ACC) into -ketobutyrate and NH<sub>3</sub>, then decrease plant ethylene level. Therefore, inoculating *Rhizobium* with ACC deaminase activity in plants with low ethylene content will help plants produce longer roots and avoid stress (Gopalakrishnan et al., 2015). Several *Rhizobium* species known to have ACC deaminase activity are *Rhizobium leguminosorum* Viciae., *R. hedydari*, *R. japonicum*, *R. gallicum* (Ma et al., 2003; Khan et al., 2022). In addition,

Nascimento et al., (2016) stated in their study that rhizobia with the ability to produce ACC deaminase are also effective as a nitrogen fixer.

In agriculture, diazotrophs are a possible choice for reducing the excessive use of artificial nitrogen-based fertilizers (Santi et al., 2013). Seventeen of 19 isolates (89%) could fix nitrogen, as seen from their ability to grow on Jensen's media, proving their potential as nitrogen fertilizers. Not all *Rhizobium* can fix nitrogen, such as *R. altiplani* strain DT 14.19 and *R. altiplani* strain DT 14.7. Another critical parameter in plant growth promoters is the ability to dissolve inorganic phosphate and produce siderophores. Eight *Rhizobium* strains have phosphate solubilizing activities. Most of the phosphate solubilizing obtained were *R. radiobacter*, with various strengths activity seen from the index value of the phosphate solubilization. Fifteen isolates produced siderophore, noticed by developing an orange colour surrounding the bacterial colony on blue selective media (CAS medium). *R. radiobacter* was reported to produce siderophores (Ferreira et al., 2019). This report aligns with this study that *R. radiobacter* collected from the rhizosphere can produce a siderophore. Verma et al. (2020) study revealed that *R. radiobacter* LB2 is a promising biofertilizer candidate due to its capability. It could solubilize phosphate, produce active compounds, fix nitrogen, and grow in high NaCl concentrations.

To live in symbiosis, *Rhizobium* also lives as a saprophyte by competing with others to obtain infection sites on the legume roots. Therefore, *Rhizobium* must survive in extreme conditions such as varied pH and NaCl concentrations. Abiotic factors such as acidity and salinity affect plant development. A slight change in pH affects bacterial growth in the soil. All nineteen selected isolates could grow in the pH range from 3 to 9. Seven isolates were tolerant to salt concentrations above 2.5%, including *R. smilacinae* strain DT 14.23, *R. radiobacter* strain DT 14.1E, *R. radiobacter* strain MSP.3a.E, *R. radiobacter* strain DT 14.16, *R. radiobacter* strain DT 14.21, and *R. radiobacter* strain DT 14.5. The best isolate was *R. radiobacter* strain DT 14.16 which survived at 5% salt concentration. Berrada et al. (2012) stated that the limiting aspect of the nitrogen fixation activity of *Rhizobium* is salinity. Bacteria with fast growth rates demonstrate higher tolerance to high salt concentrations and are suitable to be applied as biofertilizers in soils with high salt content. Tewari and Arora (2016) reported that exopolysaccharides contained in mucous play a role in tolerance of pH and high salinity.

## 5. Conclusion

The rhizosphere soil from tropical rain forests around Lake Toba in Sumatra, Indonesia, contains *Rhizobium*. As many as 19 bacterial isolates of *Rhizobium* collected from the unique geographical conditions are promising as plant growth enhancers and suitable for biofertilizer candidates. *R. radiobacter* strain DT 14.16 is the best candidate as a PGPR. However, none of the collected *Rhizobium* could control the *R. solanacearum* growth. Using *Rhizobium* in the consortium will provide better results, as each species or strain has different abilities. In addition, using

indigenous bacteria with such quality is an environmentally friendly technology to increase agricultural productivity.

## 6. Acknowledgement

The authors express gratitude to the Research Center for Biology, Indonesian Institute of Sciences, for the financial support provided through the "DIPA TEMATIK 2018".

## 7. References

- Alexander B., Zuberer D.A. (1991). Use of chrome azurol S reagents to evaluate siderophore production by rhizosphere bacteria. *Biology and Fertility Soils* 12:39-45.
- Berrada H., Nouioui I., Houssaini M.I., El Ghachtouli N., Gtari M. et al. (2012). Phenotypic and genotypic characterizations of rhizobia isolated from root nodules of multiple legume species native of Fez, Morocco. *African Journal of Microbiology Research* 6(25):5314-5324. DOI:10.5897/AJMR11.1505.
- Beringer J.E. (1974). R Factor transfer in *Rhizobium leguminosorum*. *Journal of General Microbiology* 84:188-198.
- Bhardwaj D., Ansari M.W., Sahoo R.K., et al. (2014). Biofertilizers function as key player in sustainable agriculture by improving soil fertility, plant tolerance and crop productivity. *Microbial Cell Factories* 13:66.
- Dinca L.C., Grenni P., Onet C., Onet A. (2022). Fertilization and Soil Microbial Community: A Review. *Applied Sciences* 12, 1198. <https://doi.org/10.3390/app12031198>.
- Duca D., Lorv J., Paten C.L., Rose D., Glick B.R. (2014). Indole-3-acetic acid in plant-microbe interactions. *Antonie van Leeuwenhoek* 106:85-125. DOI 10.1007/s10482-013-0095-y.
- Ferreira C.M., Sousa C.A., Soares H.M., Soares E.V. (2019). Comparison of five bacterial strains producing siderophores with ability to chelate iron under alkaline conditions. *AMB Express* 9(1):1-12. <https://doi.org/10.1186/s13568-019-0796-3>.
- Glick B.R. (2014). Bacteria with ACC deaminase can promote plant growth and help to feed the world. *Microbiological Research* 1699:30-39. <http://dx.doi.org/10.1016/j.micres.2013.09>.
- Hall B.G. (2013). Building phylogenetic trees from molecular data with MEGA. *Molecular Biology and Evolution* 30(5):1229-35. doi: 10.1093/molbev/mst012.
- Jaiswal S.K., Mohammed M., Ibny F.Y., Dakora F.D. (2021). Rhizobia as a source of plant growth-promoting molecules: potential applications and possible operational mechanisms. *Frontiers in Sustainable Food Systems* 4:619676. <https://doi.org/10.3389/fsufs.2020.619676>.
- Jaśim B., Jimtha C.J., Jyothis M., Radhakrishnan E.K. (2013). Plant growth promoting potential of endophytic bacteria isolated from *Piper nigrum*. *Plant Growth Regulation* 71:1-11. DOI 10.1007/s10725-013-9802-y.
- Khan N.F., Rasool A., Mansoor S., Saleem S., Baba T.R. et al. (2022). Potential Applications of Rhizobacteria as Eco-Friendly Biological Control, Plant Growth Promotion and Soil Metal Bioremediation. In VS Meena, M Choudhary, RP Yadav, & SK Meena (Eds.), *Sustainable Crop Production-Recent Advances*. IntechOpen. <https://doi.org/10.5772/intechopen.102657>.
- Kneen B.E., Larue T.A. (1983). Congo red absorption by *Rhizobium leguminosarum*. *Applied and Environmental Microbiology* 45(1):340-342. DOI.0099-2240/83/010340-03S02.00/0.
- Koskey G., Mburu S.W., Kimiti J.M., Ombori O., Maingi J.M. et al. (2018). Genetic characterization and diversity of *Rhizobium* isolated from root nodules of mid-altitude climbing bean (*Phaseolus vulgaris* L.) varieties. *Frontiers in Microbiology* 9:968. doi: 10.3389/fmicb.2018.00968.
- Lane D. (1991). 16S/23S rRNA Sequencing. In: *Nucleic Acid Techniques In Bacterial Systematics*. John Wiley and Sons, New York, pp 115-175.
- Ma W., Sebastianova S.B., Sebastian J., Burd G.I., Guinel F.C. et al. (2003). Prevalence of 1-aminocyclopropane-1-carboxylate deaminase in *Rhizobium* spp. *Antonie Van Leeuwenhoek* 83(3):285-91. doi: 10.1023/a:1023360919140. PMID: 12776924.
- Mendes R., Garbeva P., Raaijmakers J.M. (2013). The rhizosphere microbiome: significance of plant beneficial, plant pathogenic, and human pathogenic microorganisms. *FEMS Microbiology Reviews* 37(5):634-63. doi:10.1111/1574-6976.12028.
- Nascimento F.X., Brigido C., Glick B.R., Rossi M.J. (2016). The role of rhizobial ACC deaminase in the nodulation process of leguminous plants. *International Journal of Agronomy* 2016:1-10. <https://doi.org/10.1155/2016/1369472>.
- Packeiser H., Lim C., Balagurunathan B., Wu J., Zhao H. (2013). An extremely simple and effective colony PCR procedure for bacteria, yeasts, and microalgae. *Applied Biochemistry and Biotechnology* 169(2):695-700. doi:10.1007/s12010-012-0043-8.
- Rahman A., Sitepu I., Tang S., Hashidoko Y. (2010). Salkowski's reagent test as a primary screening index for functionalities of rhizobacteria isolated from wild dipterocarp saplings growing naturally on medium-strongly acidic tropical peat soil. *Bioscience, biotechnology, and biochemistry* 74(11):2202-2208. DOI. 10.1271/bbb.100360.

- Rajawat M.V.S., Singh R., Singh D., Saxena A.K. (2019). Psychrotrophs of the genus *Janthinobacterium* with potential to weather potassium aluminosilicate mineral. *3 Biotech* 9(4):142. doi:10.1007/s13205-019-1672-1.
- Rohini S., Aswani R., Kannan M. et al. (2018). Culturable endophytic bacteria of ginger rhizome and their remarkable multi-trait plant growth-promoting features. *Current Microbiology* 75:505–51. <https://doi.org/10.1007/s00284-017-1410-z>.
- Sabo S.D.S., Mendes M.A., Araujo E.D.S., Muradian L.B.D.A., Makiyama E.N. et al. (2020). Bioprospecting of probiotics with antimicrobial activities against *Salmonella* Heidelberg and that produce B-complex vitamins as potential supplements in poultry nutrition. *Scientific Reports* 10:7235. <https://doi.org/10.1038/s41598-020-64038-9>.
- Saghafi D., Ghorbanpour M., Lajayer B.A. (2018). Efficiency of *Rhizobium* strains as plant growth promoting rhizobacteria on morpho-physiological properties of *Brassica napus* L. under salinity stress. *Journal of Soil Science and Plant Nutrition* 18 (1):253-268. <http://dx.doi.org/10.4067/S0718-95162018005000903>.
- Santi C., Bogusz D., Franche C. (2013). Biological nitrogen fixation in non-legume plants. *Annals of Botany* 111(5):743–767. DOI. <https://doi.org/10.1093/aob/mct048>.
- Somasegaran P., Hoben H.J. (1994). Handbook for Rhizobia: Methods in Legumes-Rhizobium Technology. Springer-Verlag, New York. <https://doi.org/10.1007/978-1-4613-8375-8>.
- Tamura K., Stecher G., Kumar S. (2021). MEGA11: molecular evolutionary genetics analysis version 11. *Molecular Biology and Evolution* 8(7):3022–3027. <https://doi.org/10.1093/molbev/msab120>.
- Tewari S., Arora N.K. (2016). Fluorescent *Pseudomonas* sp. PF17 as an efficient plant growth regulator and biocontrol agent for sunflower crop under saline conditions. *Symbiosis* 68:99-108. DOI 10.1007/s13199-016-0389-8.
- Ul Hassan T., Bano A. (2015). The stimulatory effects of L-tryptophan and plant growth promoting rhizobacteria (PGPR) on soil health and physiology of wheat. *Journal of Soil Science and Plant Nutrition* 15:190-201.
- Van Reenen C.A., Dicks L.M.T., Chikindas M.L. (1998). Isolation, purification and partial characterization of plantaricin 423, a bacteriocin produced by *Lactobacillus plantarum*. *Journal of Applied Microbiology* 84:1131–1137. doi:10.1046/j.1365-2672.1998.00451.x. PMID: 9717299.
- Venieraki A., Chorianopoulou S.N., Katinakis P., Bouranis D.L. (2021). Multi-trait wheat rhizobacteria from calcareous soil with biocontrol activity promote plant growth and mitigate salinity stress. *Microorganisms* 9(8):1588. <https://doi.org/10.3390/microorganisms9081588>.
- Verma M., Singh A., Dwivedi D.H., Arora N.K. (2020). Zinc and phosphate solubilizing *Rhizobium radiobacter* (LB2) for enhancing quality and yield of looseleaf lettuce in saline soil. *Environmental Sustainability* 3:209-218. <https://doi.org/10.1007/s42398-020-00110-4>.
- Yoon S.H., Ha S.M., Kwon S., Lim J., Kim Y. et al. (2017). Introducing EzBioCloud: A taxonomically united database of 16S rRNA and whole genome assemblies. *International Journal of Systematic and Evolutionary Microbiology* 67:1613-1617. <https://doi.org/10.1099/ijsem.0.001755>.

## PHYTOCHEMICAL AND ANTIOXIDANT ASSESSMENT OF *ALLIUM HYPERSISTUM*, *ALLIUM PRZEWALSKIANUM* AND *ALLIUM WALLICHII*

Deepak Kumar Shrestha<sup>1a</sup>, Dr. Ajay Singh<sup>2a\*</sup>, Dr. Nishesh Sharma<sup>3c</sup>, Dr. M. Amin Mir<sup>4d</sup>, Dr. M. Waqar Ashraf<sup>5d</sup>

**Abstract:** High altitude plants are tremendously used mostly as food and traditional medicine for their role on prevention and treatment of several diseases. Thus, this study focused on comprehensive analysis of the phytoconstituents and the antioxidant activities of three plants; *Allium hypsistum*, *Allium przewalskianum*, and *Allium wallichii*. Upon analysis, the phytoconstituents such as alkaloids, terpenoids, steroidal compounds, glycosides, carbohydrates and aminoacids were identified in ethanolic, n-hexane and aqueous extracts of the plant whereas saponins and quinones were not detected at all. Other phytoconstituents like flavonoids, phenolic compound, and tannins were found in ethanolic and aqueous extracts but not in the n-hexane extract. The antioxidant activities of the plant extracts were evaluated by total phenolic content (TPC) and 2,2-diphenyl-1-picrylhydrazyl (DPPH) radical scavenging assay. TPC was assayed by Folin-Ciocalteu reagent method and significant amount of phenolic content were found in all plant extracts; however, the highest TPC was estimated in ethanolic extract of *A. hypsistum* i.e.  $172 \pm 6.53$  mg GAE/100g, the least TPC was found in n-hexane extract of *A. wallichii* ( $12 \pm 5.72$  mg GAE/100g). Similarly, DPPH assay showed that the highest DPPH free radical scavenging activity in ethanol extract of *A. hypsistum* with  $59.44 \pm 1.20$  % RSA while n-hexane extract of *A. hypsistum* showed the lowest DPPH activity with  $21.29 \pm 0.64$  % RSA. For reference, DPPH activity of ascorbic acid was estimated and found  $75.11 \pm 0.31$  % RSA. Therefore, among the plant extracts, the antioxidant activities were found to be higher in *A. hypsistum* followed by *A. przewalskianum* and *A. wallichii*. Furthermore, relationship between TPC and DPPH activity was established and found statistically to be non-significant but having weak to strong correlation. From this study, such findings may help to know chemical constituents and medicinal values of *Allium* species which may lead to develop new phytomedicines and use of these plants in herbal therapy.

**Keywords:** *Allium hypsistum*, *Allium przewalskianum*, *Allium wallichii*, phytochemicals, antioxidant activities.

### 1. Introduction

Plants are undoubtedly a major source for several therapeutic entities in the medical field. Around 80% of people prefer traditional medicine which has components extracted from medicinal plants. However, the efficacy, potency, and safety of such plants must be properly analyzed to promote their rationale use in the community (Roughani and Miri \ 2019). Plants produce various phytochemicals by primary or secondary metabolism and which in general play a key role in their growth, development, and defense against external factors. Secondary metabolites are usually bioactive molecules that comprise tannins, alkaloids, terpenoids, phenol compound, steroid compound and flavonoids. These bioactive components can elicit biological and therapeutic functions on the human body (Phan, Netzel et al. 2019).

Antioxidant properties of plants are mainly exerted by secondary metabolites like phenolics and flavonoids which are potent free radical scavengers which neutralizes free radicals and thereby inhibit the oxidative stress in the cells (Jalalvand, Zhaleh et al. 2019). Oxidative damage or stress is occurred due to an imbalance between antioxidant defense mechanism and generation of free radicals. As a result, an antioxidant decreases the harm that free radicals and reactive oxygen species do to cells (Chen, Krug et al. 2021, Chernukha, Fedulova et al. 2021). These damages include several degenerative disorders such as neuro-degenerative diseases, cancers, cardiovascular disorders, inflammation. Phenolic compounds are known to normalize oxidative stress in biological cells because of their ability to donate proton or electrons which then stabilize free radicals, delocalize the unpaired electrons and chelate metal ions. Mainly the phenol compounds found in plants are flavonoids, phenolic acids, tannins, xanthenes and tocopherols (Chanda and Dave 2009, D'Sousa' Costa, Ribeiro et al. 2015). Thus, screening of the total phenolic content of the extracts may reveal their overall antioxidant property. Similarly, another reliable method for screening the antioxidant assay is using DPPH, as it is a free radical that is typically used to assess the antioxidant molecule's capacity to scavenge free radicals, as measured by the percentage of RSA.

#### Authors information:

<sup>a</sup>Department of Chemistry, School of Applied & Life Sciences, Uttaranchal University, Dehradun, Uttarakhand, INDIA. Email: shresdeepak@gmail.com<sup>1</sup>; ajay21singh@yahoo.com<sup>2</sup>

<sup>b</sup>Department of Biotech, School of Applied & Life Sciences, Uttaranchal University, Dehradun, Uttarakhand, INDIA. Email: nishesh21@gmail.com<sup>3</sup>

<sup>c</sup>Department of Mathematics & Natural Sciences, Prince Mohammad Bin Fahd University, AlKhubar, SAUDI ARABIA. Email: mmir@pmu.edu.sa<sup>4</sup>; mashraf@pmu.edu.sa<sup>5</sup>

\*Corresponding Author: ajay21singh@yahoo.com

Received: December 31, 2022

Accepted: April 8, 2023

Published: June 30, 2024

*Allium* species are commonly used plants in households as spices and in traditional medicine as its component. Extracts of some *Allium* species have shown anti-inflammatory, antimicrobial, anticancer, antidiabetic, and also anti-HIV activities (Gross 2021). In the present study, commonly found high altitude *Allium* species such as *A. hypsistum*, *A. przewalskianum* and *A. wallichii* are chosen for phytochemical screening and *in vitro* antioxidant activity analysis. *A. hypsistum* is a popular plant that is frequently used as spice and herbal remedy in many rural Nepalese and Indian towns and villages. As a spice, it is used to flavor lentils, vegetables, salads, and pickles whereas medical uses of *A. hypsistum* include; high altitude sickness, diarrhea, stomach pain, flu, and common cold. Moreover, these are also used to cure lung and liver diseases of human as well as livestock. It is distinguished from other species by its purple color, reticulated fibrous bulb coatings, 4 to 6 narrow linear leaves, short pedicels, slightly dentate tepals, and simply combined filaments. *A. przewalskianum* is also consumed as medicinal plants to treat high altitude sickness, common cold, and diarrhea. It is bright red, regularly reticulate bulb coat, narrow leaves with tiny purple stamens. The three inner subulate filaments are present, whereas the three outer subulate filaments are broad at the base and acute on either side at the top. *A. wallichii* is popularly used in vegetables as spices and for the treatment of coughs, colds, altitude sickness, and even tuberculosis. It is a perennial plant and distributed in higher altitudes ranging from 2500 meter to 4500 meter (Bhandari, Muhammad et al. 2017).

To compute more therapeutical values of high altitude *Allium* species; *A. hypsistum*, *A. przewalskianum* and *A. wallichii*, this study emphasizes to screen their phytoconstituent and evaluate their *in-vitro* antioxidant potentials in ethanol, n-hexane and aqueous extracts.

## 2. Material and Methods

### Plant Specimen Collection and Storage

*A. hypsistum* and *A. przewalskianum* were collected from Marpha, Mustang (28.8151°N, 83.6455°E), and *A. wallichii* was collected from Palungtar, Gorkha (28.05145°N, 84.4876°E) of Nepal. The plants were taxonomically identified with flora of Nepal provided by the Department of Plant Resources, National Herbarium and Plant Laboratories, Govt. of Nepal and deposited the voucher specimens with code as mentioned in Table 1. Aerial parts of the plants were taken and cleaned with refined water. Materials were first cut off into little pieces and shade-dried in open space for fortnight at room temperature (28°C to 30°C) (Phan, Netzel et al. 2019).



*A. hypsistum*



*A. przewalskianum*



*A. wallichii*

**Figure 1.** Selected *Allium* species under the study

### Extraction

The dried materials of *A. hypsistum*, *A. przewalskianum* and *A. wallichii* were ground to get a powder which was sieved with a mesh screen. After that, Soxhlet extraction of the powdered materials with ethanol, n-hexane, and water was separately operated to get crude extract (Seino, Yamazaki et al. 2020). Then, the crude extract was fully dried and free from solvents by evaporating at 40 °C and kept in separate containers with proper labels. They were stored in the fridge at 4 °C until further use (Jeba Malar, Antonyswamy et al. 2020). Total percentage (%) extract yields were calculated for each extracts.

$$\% \text{ yield (w/w)} = x = \frac{\text{Dry weight of extract (g)}}{\text{Dry weight of a plant (g)}} \times 100$$

### Phytochemical Testing

For phytochemical testing, the extracts were first prepared as 10 % extract solution by using 0.1 % dimethyl sulphoxide (DMSO) reagent. Then, following the standard protocols, occurrence of bioactive phytoconstituent in the extracts was analyzed (Bhandari, Muhammad et al. 2017, Batiha, Beshbishy et al. 2020).

- **Test for alkaloid:** With 2 ml of 1% HCl, 5 ml of the extract was dissolved, and then it was gently warmed. After that, the mixture was treated with Wagner's reagents (iodine in potassium iodide). Finally, presence of alkaloid could be confirmed by appearance of reddish-brown precipitation.
- **Test for Terpenoid:** 5 ml of the extract were diluted with 2 ml of chloroform, and then evaporated to remove the water. To create a grayish/reddish colored precipitate as proof of terpenoid content, 2 ml of concentrated H<sub>2</sub>SO<sub>4</sub> was added to the mixture and heated for 2 minutes.
- **Tests for Flavanoid:** 5 mg of dry extract with 10 ml of ethyl acetate was heated on water bath for three minutes. After filtering, 4 ml of the filtrate was mixed with 1ml of diluted ammonia solution. A golden coloring indicated the presence of flavonoids.
- **Tests for Steroid:** Extract was combined with 2 ml of chloroform and adding concentrated H<sub>2</sub>SO<sub>4</sub> gently by sidewise. In the lower chloroform layer, a red color was appeared that confirmed the presence of steroid.
- **Tests for Phenol:** Extract was diluted with 2 ml solution of FeCl<sub>3</sub> (2 %). The presence of phenol was identified by a blue-green or black coloring solution.
- **Tests for Coumarin:** 3 ml of a 10% aqueous solution of NaOH was added to 5 ml of extract. The presence of coumarin was indicated by production of yellow color.
- **Tests for Tannin:** 5 mg dry extract was added to 20ml of water and boiled. A few drops of 0.1 % FeCl<sub>3</sub> were added to the filtrate after filtering. Brownish green or blue-black coloration revealed tannins were present by their appearance.
- **Tests for Glycoside:** 5 ml of the extract was mixed with 2 ml of each chloroform and acetic acid. Ice was used to cool the mixture and concentrated H<sub>2</sub>SO<sub>4</sub> was added cautiously. It

resulted in a color change from violet to blue to green, signifying the existence of glycone, a part of glycoside.

- **Tests for Carbohydrate:** Two drops of Molisch's reagent were added to 5 ml of extracts and mixed well. A few drops of conc. H<sub>2</sub>SO<sub>4</sub> were placed along the test tube's sidewall. Development of a violet ring indicated the presence of sugar.
- **Tests for Aminoacid:** A few drops of ninhydrin reagent were added to 5 ml of extract. For a short while, the mixture was gently heated. The appearance of purple color indicated the presence of amino acids.
- **Tests for Saponin:** 5 mg of extract was directly diluted in 5 ml of water and shaken vigorously. Then, formation of frothing was indicator for presence of saponins.
- **Tests for Quinone:** Equal volumes of the extract sample and concentrated H<sub>2</sub>SO<sub>4</sub> were mixed and observed for red color formation which indicated the presence of quinone.

### Antioxidant Analysis

#### Assay of Total Phenolic Content

Total phenolic content (TPC) in the plant extracts was estimated by Folin-Ciocalteu (FC) reagent assay (Krishnaiah, Sarbatly et al. 2011, Ravipati, Zhang et al. 2012). Initially, 50 mg of plant extract was dissolved in 50 ml DMSO (10% v/v) and centrifuged at 2000 rpm for 5 minutes. Then, 0.5 ml of 50 % FC reagent was added to 0.5 ml of supernatant of each extracts which was taken in separate, labeled test tubes. The tubes were then allowed to stand for 15 min at room temperature. Immediately, 2.5 ml of 20% sodium carbonates were added, and the tubes were left for 30 minutes in a dark place. Optical density of all test solutions was recorded at 760nm against a reagent blank in a spectrophotometer (UV-1800 Shimadzu Spectrophotometer). TPC of all tests solution of plant extracts was calculated as mg gallic acid equivalent (mg GAE/100g) with ± SEM and data was obtained by using standard calibration curve of gallic acid with the equation  $y = 0.025x + 0.006$  ( $R^2 = 0.983$ ). Gallic acid's standard calibration curve was created using successive concentrations of 2 µg/ml, 4 µg/ml, 6 µg/ml, 8 µg/ml, and 10 µg/ml, and a graph between absorbance and concentration (µg/ml) was drawn (Iqbal, Salim et al. 2015, Szerlauth, Muráth et al. 2019).

#### Assay of DPPH Scavenging Activity

The stable free radical DPPH (2,2-diphenyl -1-picrylhydrazyl) interacts with molecules that can give off a hydrogen atom. It has been extensively employed in the antioxidant assay of most compounds. This approach relies on DPPH-scavenging by adding a radical species or an antioxidant that decolorizes the purple-colored methanol solution of DPPH. Antioxidant activities of plant extracts can be assayed by the following standard protocol (Krishnaiah, Sarbatly et al. 2011, Bhandari, Muhammad et al. 2017). DPPH reagent was prepared by dissolving 10mg DPPH (2, 2-diphenyl -1-picrylhydrazyl radical) in 100ml methanol i.e. 100 µg/ml. For DPPH control, 1 ml DPPH reagent was added in 4ml methanol. Simultaneously, test samples were prepared as; 50 mg

of extracts were mixed in 50 ml methanol and further centrifuged at 2000 rpm for five minutes. After that, 2ml of supernatant of each extracts was taken in test tubes. 1ml of DPPH reagent was then added to each tube and solutions were kept in dark for exactly 30 minutes. Finally, absorbance of all test solutions and DPPH control were recorded at 517nm against reagent blank with a spectrophotometer (UV-1800 Shimadzu Spectrophotometer). Finally, DPPH free radical scavenging assay was calculated as %RSA (Radical scavenging activity).

$$\% \text{RSA} = (\text{Control absorbance} - \text{Extracts absorbance}) / \text{Control absorbance} \times 100$$

### Statistics

The obtained data were analyzed statistically in Microsoft Excel (windows 10) and SPSS (version 25). The Pearson's correlation (r) was considered to establish a relationship between TPC and DPPH activity of selected plants statistically.

## 3. Results and Discussion

### Plant Extract Yield

The yield percentage of plant extracts varied, as shown in Table 1, with aqueous extract of *A. hypsistum* (23.70%) having the greatest yield, followed by extracts of *A. wallichii* (20.77%) and *A. przewalskianum* (20.43%). While the lowest percentage of yield was found in n-hexane extract of *A. wallichii* (7.2 %).

**Table 1.** Plants under study along with their voucher code, botanical name, common name, and extract yield %.

S.N.	Voucher code	Botanical name	Common name	Extracts	Percentage yield (%)
1	SMS-001	<i>A. hypsistum</i>	Jimbu, jamboo	Ethanol	15.03
				n-hexane	9.78
				Aqueous	23.70
2	SMS-002	<i>A. przewalskianum</i>	Lambo, doona	Ethanol	16.87
				n-hexane	9.30
				Aqueous	20.43
3	SMS-003	<i>A. wallichii</i>	Banlasun, Himalayan garlic	Ethanol	12.73
				n-hexane	7.23
				Aqueous	20.77

### Phytochemical Screening

Ethanol, n-hexane, and aqueous extracts of each plant *A. hypsistum*, *A. przewalskianum* and *A. wallichii* were analyzed for the presence of twelve phytoconstituents as shown in Table 2. The alkaloids, terpenoids, steroids, glycosides, carbohydrates, and aminoacids were detected in all three plants whereas coumarin was detected only in the extracts of *A. hypsistum*. Moreover, n-hexane extraction of the plants did not contain flavanoids, phenol, or tannins as one possible explanation being they may be poorly soluble in n-hexane. Overall, ethanol and aqueous extraction of all three selected plants showed a relatively higher chance of phytochemical screening than n-hexane extracts.

The presence of phytoconstituents in a plant is known to reveal medicinal as well as biological potentials. Many previous studies have described that the phenolic compounds present in the plants show remarkable antioxidant properties which are involved in anti-inflammation, cardiovascular protection, anti-aging, anti-carcinogen, and reduces apoptosis. Similarly, alkaloids

exhibit analgesic, antispasmodic and antimicrobial properties. Likewise, glycosides are known to lower blood pressure in case of hypertension (Shrestha, Adhikari et al. 2015, B, D et al. 2016). A review by Lekshmi *et al* suggested that carbohydrates, flavonoids, saponins, steroids, and phenols are major constituents of the *Allium* species (Lekshmi, S et al. 2015) Nonetheless, our present study showed the absence of saponins and quinines in the selected plants. A similar report was made in a study by Bhandari *et al* (Bhandari, Muhammad et al. 2017), where they investigated the phytochemical composition of ethanol extracts of *A wallichii* and found the presence of flavonoids, glycosides, steroids, terpenoids but reported the absence of saponins, alkaloids, and tannins. Evidence from a previous study suggests that phytochemicals like quercetine and antioxidant activity were shown higher in fresh plant than the dried plant (Fredotović, Puizina et al. 2021, Yuasa, Kawabeta et al. 2021). Hence we can assume that the phytochemical screening might be affected by the types of solvent used and/or method chosen for plant extraction.

**Table 2** Result of phytochemical screening of selected plants

Phytochemicals	A. <i>hypsistum</i>			A. <i>przewalskianum</i>			B. <i>wallichii</i>		
	ethanol extract	n-hexane extract	aqueous extract	ethanol extract	n-hexane extract	aqueous extract	ethanol extract	n-hexane extract	aqueous extract
Alkaloid	+	+	+	+	+	+	+	+	+
Terpenoid	+	+	+	+	+	+	+	+	+
Flavanoid	+	-	+	+	-	+	+	-	+
Steroid	+	+	+	+	+	+	+	+	+
Phenol	+	-	+	+	-	+	+	-	+
Coumarin	+	+	+	-	-	-	-	-	-
Tannin	+	-	+	+	-	+	+	-	+
Glycoside	+	+	+	+	+	+	+	+	+
Carbohydrate	+	+	+	+	+	+	+	+	+
Aminoacid	+	+	+	+	+	+	+	+	+
Saponin	-	-	-	-	-	-	-	-	-
Quinone	-	-	-	-	-	-	-	-	-

(Distilled water was as taken as a negative control. The symbols +; present and -; absent)

**TPC and DPPH Free Radical Scavenging Assay**

Total phenolics content (TPC) and DPPH free radical scavenging assay in selected plants were shown in Figure 2 and Figure 3. It is evident that *A. hypsistum* had higher TPC in each of the solvent extracts compared to that of *A. przewalskianum* and *A. wallichii*. More precisely, the highest phenolics content was observed in ethanol extraction of *A. hypsistum* (172±6.53 mg GAE/100g) and moderate levels of phenolic content were estimated in ethanol extraction of *A. przewalskianum* (122±0.82 mg GAE/100g), followed by *A. wallichii* (102±0.82 mg GAE/100g). Among the extracts, remarkable phenolics content was found in ethanol extracts followed by water and n-hexane extracts of the studied plants. The order of aqueous extracts, the highest value of phenolics content was found in *A. hypsistum* (90±10.61 mg GAE/100g), followed by *A. przewalskianum* (82±13.88 mg GAE/100g) and *A. wallichii* (72±1.63 mg GAE/100g). In contrast, n-hexane extracts showed the phenolics content more in *A. przewalskianum* (44±1.63 mg GAE/100g), followed by *A. hypsistum* (42±5.72 mg GAE/100g) and lesser in *A. wallichii* (12±5.72 mg GAE/100g). Moreover, Figure 3 shows a higher DPPH activity in ethanol extract of *A. hypsistum* (59.44±1.20 % RSA), followed by *A. wallichii* (55.20±0.53 % RSA) and *A. przewalskianum* (39.53±0.43 % RSA). In the case of n-hexane extracts, DPPH activity was found higher in *A. przewalskianum*

(39.44±0.37 % RSA) than *A. wallichii* (35.02±4.31 % RSA) and *A. hypsistum* (21.29±0.64 % RSA). Subsequently, DPPH activity was found to be higher in aqueous extract of *A. hypsistum* (54.65±0.85 % RSA) than *A. wallichii* (48.11±0.05 % RSA) and *A. przewalskianum* (46.26±0.37 % RSA). While comparing with DPPH activity of reference ascorbic (75.11±0.31 % RSA), ethanol extract of *A. hypsistum* (59.44±1.20 % RSA) was found even lesser but found to be higher than that of *A. wallichii* (55.20±0.53 % RSA) and aqueous extract of *A. hypsistum* (54.65±0.85 % RSA).

The outcome presented in Figure 2 and Figure 3 from the present study are in agreement with fact from a previous study that both TPC and antioxidant activity (DPPH assay) are noticeably varied in different species of *genus Allium* like *A. cepa*, *A. sativum*, *A. schoenoprasum* and *A. ursinum*. The total polyphenols were occurred in the range 444.3 to 1591 mg GAE/Kg and DPPH assay ranging from 12.29 to 76.57 % RSA (Lenková, Bystrická et al. 2016). Another study carried out in different parts of *A. sativum* revealed that higher TPC and antioxidant activities in flowering parts rather than their bulbs. Another species *A. cepa* also showed significant antioxidant potentials in several forms (Yuasa, Kawabeta et al. 2021). Similarly, our present study also showed TPC and antioxidant activities are within the range but with variable values with specific plant extracts.

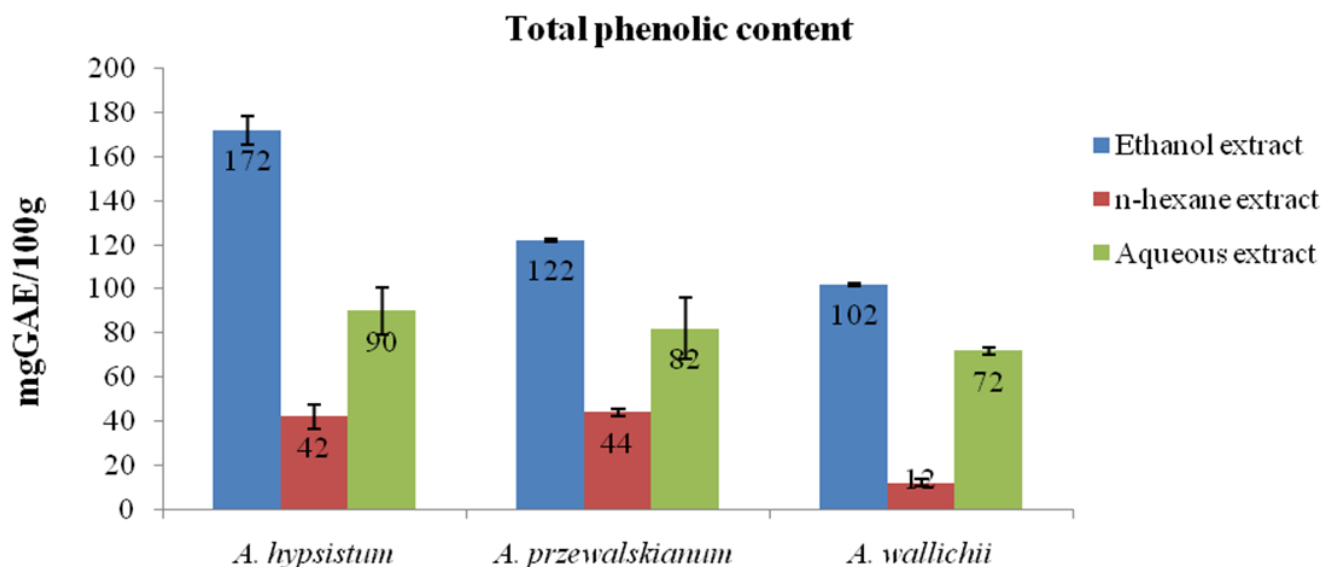


Figure 2 Total phenolic content (mg GAE/100g ± SEM) in the extracts of studied plants.

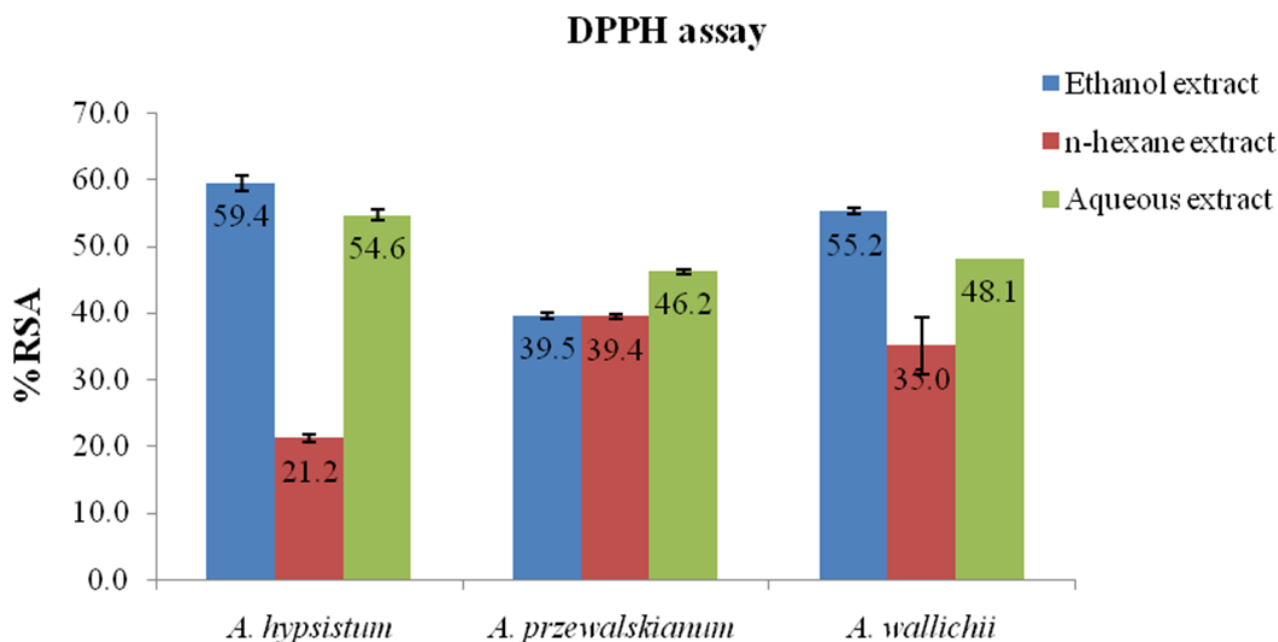


Figure 3 DPPH assay (% RSA ± SEM) of the extract of studied plants.

3.4 Correlation of TPC and DPPH free radical scavenging activity

To see whether TPC is associated with the DPPH activity, the statistical relationship between TPC and DPPH activity was established in the plant extracts by performing Pearson’s correlation which has been shown in Table 3. An association of TPC and DPPH activity in ethanol extracts ( $r= 0.431$ ) was found moderate and dependent whereas in n-hexane extracts ( $r= -0.230$ ), it was found to be weak and negative. In case of aqueous extracts ( $r= 0.697$ ), DPPH activity was found strongly and

positively associated with TPC. In contrast, Despite the observed moderate to strong correlation, no any significant correlation ( $p>0.05$ ) was seen between TPC and DPPH activity. A previous study (Ravipati, Zhang et al. 2012) on Chinese medicinal plants suggested phenolic content has a significant and strong positive correlation with DPPH scavenging activity. Similarly, a study on eight wild vegetables showed positively strong relationship between TPC and DPPH activity (Aryal, Baniya et al. 2019) and however, this study revealed no significant and found variable relationship between TPC and DPPH activity in plant extracts.

**Table 3** Correlation between TPC and DPPH activity in the following extracts of selected plants.

Plant extracts	Pearson's correlation ( <i>r</i> )	Remarks
Ethanol	0.431	Moderate and positive
n-hexane	-0.230	Weak and negative
Aqueous	0.697	Strong and positive

From above-mentioned outcome, the plant extracts varies on their phytoconstituents however most of extracts have similar phytoconstituents. Subsequently, antioxidant activities of the plant extracts were found to be higher in ethanol extracts followed by aqueous extracts and n-hexane extracts. The study even though showed strong evidence of positive correlations between the TPC and DPPH activity but was too far from establishing a significant correlation between them. The lack of significant association could be attributed to the studied plant containing lower levels of phenolic content. However, further studies need to be conducted *in vivo* model for antioxidant property and should be implementing comprehensive research to develop phytomedicine extending the scope of *Allium species* in herbal therapy.

#### 4. Conclusion

This study has demonstrated that the plant extracts under study exhibit significant *in vitro* antioxidant properties and contain promising phytochemicals. Therefore, these extracts might serve as potential antioxidant candidates which can be used to scavenge the radicals causing oxidative stress.

#### 5. Acknowledgement

The authors are thankful to Department of Plant Resources, National Herbarium and Plant Laboratories, Nepal for identifying the plants. Also, we gratefully acknowledge Department of Chemistry, SALS, Uttaranchal University, India that providing laboratory facility to conduct this study.

#### 5. References

Aryal, S., M. K. Baniya, K. Danekhu, P. Kunwar, R. Gurung and N. Koirala (2019). "Total Phenolic Content, Flavonoid Content and Antioxidant Potential of Wild Vegetables from Western Nepal." *Plants* 8(4).

B, M., J. D, C. E, N. T, N. Kundal, M. Sarma and P. Kalita (2016). "Phytochemical Analysis of Traditional Medicinal Plants and their Antimicrobial Activity: An Experience from North East India." *Open Access Journal of Pharmaceutical Research* 1: 1-7.

Batiha, G., A. Beshbishy, L. Wasef, Y. Elewa, A. Al-Sagan, M. El-Hack, A. Taha, Y. Abd-Elhakim and H. Devkota (2020). "Chemical Constituents and Pharmacological Activities of Garlic (*Allium sativum* L.): A Review." *Nutrients*.

Bhandari, J., B. Muhammad, P. Thapa and B. G. Shrestha (2017). "Study of phytochemical, anti-microbial, anti-oxidant, and anti-cancer properties of *Allium wallichii*." *BMC complementary and alternative medicine* 17(1): 1-9.

Bhandari, J., B. Muhammad, P. Thapa and B. G. Shrestha (2017). "Study of phytochemical, anti-microbial, anti-oxidant, and anti-cancer properties of *Allium wallichii*." *BMC Complement Altern Med* 17(1): 102.

Chanda, S. and R. Dave (2009). "In vitro models for antioxidant activity evaluation and some medicinal plants possessing antioxidant properties: An overview." *African Journal of Microbiology Research* 3: 981-996.

Chen, X., L. Krug, M. Yang, G. Berg and T. Cernava (2021). "The Himalayan Onion (*Allium wallichii* Kunth) Harbors Unique Spatially Organized Bacterial Communities." 82(4): 909-918.

Chernukha, I., L. Fedulova, E. Vasilevskaya, A. Kulikovskii, N. Kupueva and E. Kotenkova (2021). "Antioxidant effect of ethanolic onion (*Allium cepa*) husk extract in ageing rats." *Saudi Journal of Biological Sciences* 28(5): 2877-2885.

D'Sousa' Costa, C. O., P. R. Ribeiro, M. B. Loureiro, R. C. Simões, R. D. de Castro and L. G. Fernandez (2015). "Phytochemical screening, antioxidant and antibacterial activities of extracts prepared from different tissues of *Schinus terebinthifolius* Raddi that occurs in the coast of Bahia, Brazil." *Pharmacognosy magazine* 11(43): 607-614.

Fredotović, Ž., J. Puizina, M. Nazlić, A. Maravić, I. Ljubenkov, B. Soldo, E. Vuko and D. Bajić (2021). "Phytochemical Characterization and Screening of Antioxidant, Antimicrobial and Antiproliferative Properties of *Allium × cornutum* Clementi and Two Varieties of *Allium cepa* L. Peel Extracts." *Plants* 10(5): 832.

Gross, M. (2021). "All about *Allium*." *Current Biology* 31(22): R1449-R1452.

Iqbal, E., K. A. Salim and L. B. L. Lim (2015). "Phytochemical screening, total phenolics and antioxidant activities of bark and leaf extracts of *Goniothalamus velutinus* (Airy Shaw) from Brunei Darussalam." *Journal of King Saud University - Science* 27(3): 224-232.

Jalalvand, A. R., M. Zhaleh, S. Goorani, M. M. Zangeneh, N. Seydi, A. Zangeneh and R. Moradi (2019). "Chemical characterization and antioxidant, cytotoxic, antibacterial, and antifungal properties of ethanolic extract of *Allium Saralicum* RM Fritsch leaves rich in linolenic acid, methyl ester." *Journal of Photochemistry and Photobiology B: Biology* 192: 103-112.

Jeba Malar, T. R. J., J. Antonyswamy, P. Vijayaraghavan, Y. Ock Kim, A. A. Al-Ghamdi, M. S. Elshikh, A. A. Hatamleh, M. A. Al-

- Dosary, S. W. Na and H.-J. Kim (2020). "In-vitro phytochemical and pharmacological bio-efficacy studies on *Azadirachta indica* A. Juss and *Melia azedarach* Linn for anticancer activity." *Saudi journal of biological sciences* 27(2): 682-688.
- Krishnaiah, D., R. Sarbatly and R. Nithyanandam (2011). "A review of the antioxidant potential of medicinal plant species." *Food and Bioproducts Processing* 89(3): 217-233.
- Lekshmi, P., V. S, J. S and R. J (2015). "PHYTOCHEMICALS IN ALLIUM SPECIES AND ITS ANALYTICAL METHODS – A REVIEW." *International Journal of Institutional Pharmacy and Life Sciences* 5: 38-58.
- Lenková, M., J. Bystrická, T. Tóth and M. Hrstková (2016). "Evaluation and comparison of the content of total polyphenols and antioxidant activity of selected species of the genus *Allium*." *Journal of Central European Agriculture* 17: 1119-1133.
- Phan, A. D. T., G. Netzel, P. Chhim, M. E. Netzel and Y. Sultanbawa (2019). "Phytochemical characteristics and antimicrobial activity of Australian grown garlic (*Allium sativum* L.) cultivars." *Foods* 8(9): 358.
- Ravipati, A. S., L. Zhang, S. R. Koyyalamudi, S. C. Jeong, N. Reddy, J. Bartlett, P. T. Smith, K. Shanmugam, G. Münch, M. J. Wu, M. Satyanarayanan and B. Vysetti (2012). "Antioxidant and anti-inflammatory activities of selected Chinese medicinal plants and their relation with antioxidant content." *BMC Complement Altern Med* 12: 173.
- Roughani, A. and S. M. Miri (2019). "Plants, Organic Farming, Natural and Pharmaceutical Ingredients."
- Seino, Y., Y. Yamazaki and D. Yabe (2020). "The Asian Association for the Study of Diabetes: The first 10 years and the next 10 years." *Journal of Diabetes Investigation* 11(5): 1079-1084.
- Shrestha, P., S. Adhikari, B. Lamichhane and B. Shrestha (2015). "Phytochemical Screening of the Medicinal Plants of Nepal." *IOSR Journal of Environmental Science, Toxicology and Food Technology* 1: 2319-2399.
- Szerlauth, A., S. Muráth, S. Viski and I. Szilagyí (2019). "Radical scavenging activity of plant extracts from improved processing." *Heliyon* 5(11): e02763.
- Yuasa, M., K. Kawabeta, M. Morikawa, M. Iwami and M. Tominaga (2021). "Antioxidant and taste properties of fresh onion (*Allium cepa* L.) leaves." *Journal of Food Measurement and Characterization* 15(2): 1083-1091.

# COMPLEX OF Co(II) WITH LIGAND 2,2'-BIPYRIDINE AND ANIONIC TRIFLUOROACETATE: SYNTHESIS, PHYSICAL PROPERTY, STRUCTURAL ANALYSIS AND ITS ANTIBACTERIAL ACTIVITY

Endang Widjajanti Laksono<sup>1a</sup>, Nofianti Vivi Astuti<sup>2a</sup>, Isti Yunita<sup>3a</sup>, and Kristian Handoyo Sugiyarto<sup>4a\*</sup>

**Abstract:** The complex containing Co(II), bipyridine (*bipy*), and trifluoroacetate (TFA) was prepared and characterized. The metal content, conductance, and TGA-DTG analysis estimate the formula of  $[\text{Co}(\text{bipy})_3](\text{CF}_3\text{COO})_2 \cdot 5\text{H}_2\text{O}$ . The magnetic property shows the moment of 4.2-5.3 BM which should correspond to the three unpaired electrons with the typically strong orbital contribution in cobalt(II). The UV-VIS spectral profiles indicate the three possible spin-allowed transitions of the corresponding quartet states. The characteristic vibration modes of *bipy* and TFA confirm the complex formula. The SEM photographs support the crystalline particle size, and the corresponding EDX signifies the existence of all elemental contents. The powder XRD profile has been refined according to the Le Bail method of the Rietica program, and the result suggests being a structurally monoclinic system of space group C2/c. This complex exhibits a weak inhibition against *S. aureus* and *E. coli* bacterial activity.

**Keywords:** Synthesis, characterization,  $[\text{Co}(\text{bipy})_3](\text{CF}_3\text{COO})_2 \cdot 5\text{H}_2\text{O}$ , 2,2'-bipyridine, trifluoroacetate, antibacteria.

## 1. Introduction

Concerning the physical properties and P-XRD, the chemistry of the divalent metal complexes such as Cu(II), Ni(II), Co(II), and Mn(II) to the six coordinated bidentate, bipyridine-*bipy* (Kusumawardani, Kainastiti & Sugiyarto, 2018; Sugiyarto, Louise & Wilujeng, 2020), and phenanthroline-*phen* (Sugiyarto *et al.*, 2017; Sugiyarto *et al.*, 2018; Sutrisno *et al.*, 2018) with counterpart anions of trifluoro methanesulfonate-triflate ( $\text{CF}_3\text{SO}_3$ ) and trifluoro acetate-TFA ( $\text{CF}_3\text{COO}$ ) have been much well studied. With the help of the Le Bail method of the Rietica program, the corresponding P-XRD is an acceptable refinement for producing the lattice parameters.

Regarding the medicinal aspects, the research of metal complexes seems to apply to anti-bacterial agents (e.g. Singh *et al.*, 2017; Uddin *et al.*, 2019; Ayipo *et al.*, 2021; Beyene & Wassie, 2020; Sondavid *et al.*, 2020). A possible explanation for the toxicity of the complexes has been postulated in the light of chelation theory (Singh *et al.*, 2017).

Therefore, our research in the metal complex should now consider the extra role of an anti-bacterial agent. The two types of bacteria around human life, gram-positive and gram-negative, should be considered, and so *Staphylococcus aureus* and *Escherichia coli* are selected in this research. For these reasons, the preparation of powder Co(II) containing tris(*bipy*) with TFA anion is now a challenge, not only directed to the common physical properties associated with magnetism, IR-UV-Vis spectral

properties, and PXRD, but also to the anti-bacterial activity. The results are reported in this study.

## 2. Experimental Methods

### Chemical Materials

The main reagents,  $\text{Co}(\text{NO}_3)_2 \cdot 6\text{H}_2\text{O}$ , 2,2'-bipyridine,  $\text{CF}_3\text{COONa}$ , for the complex preparation, and  $\text{CrCl}_3 \cdot 6\text{H}_2\text{O}$ ,  $\text{Fe}(\text{NO}_3)_3 \cdot 9\text{H}_2\text{O}$ ,  $\text{CuCl}_2 \cdot 2\text{H}_2\text{O}$ ,  $\text{Ni}(\text{NO}_3)_2 \cdot 6\text{H}_2\text{O}$ ,  $\text{Co}(\text{NO}_3)_2$ ,  $\text{CuSO}_4 \cdot 5\text{H}_2\text{O}$ ,  $\text{NH}_4\text{Cl}$ , and  $\text{KCl}$ , for the conductivity measurement, were purchased from Aldrich-Sigma, and directly used without special treatment. Meanwhile, the Nutrient agar, Nutrient Broth, *Chloramphenicol*, bacteria *Staphylococcus aureus*, and bacteria *Escherichia coli*, for anti-bacterial measurement, were obtained from the laboratory of the Department of Biology, Yogyakarta State University.

### Preparation of The Complex

The Co(II) complex of tris-bipyridine was prepared according to the anionic replacement reaction as follows. To a warmed ethanolic solution of *bipy* (0.468 g; 3 mmol, ~ 4 mL), an aqueous solution of  $\text{Co}(\text{NO}_3)_2$  (0.291 g; 1 mmol, ~ 3 mL) was added. The mixture was filtered and the aqueous solution of  $\text{CF}_3\text{COONa}$  in excess (0.544 g; 4 mmol, ~ 3 mL) was added whereupon the dully greenish precipitate produced on reducing volume and scratching. It was filtered, washed with a minimum of cold water, dried in aeration, and stored in a desiccator. The preparation of the powder complex was separately done three times for reproducibility.

### Authors information:

<sup>a</sup>Department of Chemistry Education, Universitas Negeri Yogyakarta, Yogyakarta 55281, INDONESIA. Email: [endang\\_widjajanti@uny.ac.id](mailto:endang_widjajanti@uny.ac.id)<sup>1</sup>; [nofiantivivi1011@gmail.com](mailto:nofiantivivi1011@gmail.com)<sup>2</sup>; [isti\\_yunita@uny.ac.id](mailto:isti_yunita@uny.ac.id)<sup>3</sup>; [sugiyarto@uny.ac.id](mailto:sugiyarto@uny.ac.id)<sup>4</sup>

\*Corresponding Author: [sugiyarto@uny.ac.id](mailto:sugiyarto@uny.ac.id)

Received: March 25, 2023

Accepted: September 8, 2023

Published: June 30, 2024

### Physical Measurements

#### Magnetic Moment.

The MSB of Auto Sherwood Scientific 240V-AC calibrated with  $\text{CuSO}_4 \cdot 5\text{H}_2\text{O}$  was applied to measure the mass magnetic susceptibility ( $\chi_g$ ) of the complex. The powder of the complex was packed tightly in the Gouy tube. The difference in mass without and with (electro-) magnet reflecting the mass magnetic susceptibility was then recorded. It was converted into molar magnetic susceptibility ( $\chi_M$ ), and then to arrive at the corrected molar magnetic susceptibility ( $\chi_M'$ ), the corrected for diamagnetism of Pascal's constant was applied (Bain & Berry, 2008; Dalal, 2017). The effective magnetic moment ( $\mu_{\text{eff}}$ ) was obtained by the application of the general relationship,  $\mu_{\text{eff}} = 2.828 \sqrt{\chi_M' \cdot T}$  BM at temperature T of the sample (Pathshala, 2021; LibreTexts™, 2021; Lancashire, 2021).

#### UV-Vis electronic and Infrared spectra.

A spectrophotometer model of Pharmaspec UV 1700 was used to administer the UV-VIS electronic spectra. For the solid, the powder was spread on a white circle filter paper fitted to the cell holder and it was then recorded at 300-800 nm. An Infrared Spectrophotometer of the FTIR-ABB MB3000 model was used to record the IR spectrum of the complex. The powdered complex, which was mixed with KBr, was pressed on the cell holder for recording at 400-4000  $\text{cm}^{-1}$ .

#### Metal content and Electrical conductance.

An AAS of the PinAAcle 900T Perkin Elmer model was used to record the metal content. A conductometer of the Lutron CD-4301 model was used to estimate the conductance property of the complex. An aqueous solution of KCl (1 M) at 25 °C was applied in calibrating this instrument prior to use, and some known ionic solutions,  $\text{CrCl}_3 \cdot 6\text{H}_2\text{O}$ ,  $\text{Fe}(\text{NO}_3)_3 \cdot 9\text{H}_2\text{O}$ ,  $\text{CuCl}_2 \cdot 2\text{H}_2\text{O}$ ,  $\text{Ni}(\text{NO}_3)_2 \cdot 6\text{H}_2\text{O}$ ,  $\text{Co}(\text{NO}_3)_2$ ,  $\text{CuSO}_4 \cdot 5\text{H}_2\text{O}$ , and  $\text{NH}_4\text{Cl}$  were also administered for comparison.

#### TGA-DTA (Thermogravimetric and Differential Thermal Analysis).

The loss of the molecule of water and the decomposition of the complex was performed on the Diamond Perkin Elmer Instruments, and the simultaneous TGA-DTG were obtained by a NETZSCH STA 409C/CO thermal analyzer model with the rate of 10 °C/min.

#### Powder X-Ray Diffraction.

A Benchtop Diffractometer of Rigaku Miniflex 600 40 kW 15 mA (with  $\text{CuK}\alpha$ ,  $\lambda = 1.5406 \text{ \AA}$ ) was used to record the diffractogram of the complex. The sample was spread on a special glass plate and set on the cell holder. The diffractogram was then recorded in a scan mode at 2–90 degrees of  $2\theta$  within the interval of 0.04 steps per 4 sec for 2 h. It was then refined following the Le Bail method of the Rietica program within 10-60 degrees of  $2\theta$  within 30 cycles.

#### Determination of Antibacterial Property.

The antibacterial properties of the complex were tested against *Staphylococcus aureus* (ATCC 25924) as gram-positive type and *Escherichia coli* (ATCC 35218) as gram-negative type according to agar disk-diffusion method by the media of Nutrient Agar (NA) and Nutrient Broth (NB). Chloramphenicol was applied as the standard antibacterial agent (positive control), with water as the negative control. Various concentrations of the complex were performed at 125, 250, 500, and 1000  $\mu\text{g}/\text{mL}$ . The observation of the inhibition zone (in mm) was done every 3 hours during 24 hours of the incubation. The diameter of the inhibition zone was recorded and measured using a caliper (accuracy 0.02 mm) on 3 sides of the sample (Kani et al., 2016; Balouiri et al., 2016).

## 3. Results and Discussion

### Determining the Chemical Formula of the Complex

The complex should primarily contain  $\text{Co}(\text{II})$ , *bipy*, TFA, and likely molecules of  $\text{H}_2\text{O}$ . The ionic property of the complex is characterized by measuring the corresponding equivalent electrical conductance. It was estimated by comparing it with other known simple compounds, and the results are shown in **Table 1**. It falls in the range of the known ionic simple compounds consisting of three ions per molecule and therefore the stoichiometric formula,  $[\text{Co}(\text{bipy})_n](\text{CF}_3\text{COO})_2 \cdot x\text{H}_2\text{O}$ , where  $n = 3$ , is then proposed for the complex. This suggests that the formula of the complex indicates no coordinated anion is involved.

**Table 1.** The equivalent electrical conductance of the complex and several simple known compounds in an aqueous solution

Salts	Conductance, $\Lambda_c$ , ( $\Omega^{-1} \text{cm}^2 \text{mol}^{-1}$ )	The ratio number of cations to anions	The number of ions per molecule
$\text{CuSO}_4 \cdot 5\text{H}_2\text{O}$	84.5614	1:1	2
$\text{NH}_4\text{Cl}$	125.3755	1:1	2
$\text{CuCl}_2 \cdot 2\text{H}_2\text{O}$	172.0782	1:2	3
$\text{Ni}(\text{NO}_3)_2 \cdot 6\text{H}_2\text{O}$	178.2714	1:2	3
<b><math>\text{Co}(\text{NO}_3)_2 \cdot 6\text{H}_2\text{O}</math></b>	<b>226.3955</b>	<b>1:2</b>	<b>3</b>
$\text{Fe}(\text{NO}_3)_3 \cdot 9\text{H}_2\text{O}$	285.2816	1:3	4
$\text{CrCl}_3 \cdot 6\text{H}_2\text{O}$	436.4573	1:3	4
<b><math>[\text{Co}(\text{bipy})_n]</math></b>			
<b><math>(\text{CF}_3\text{COO})_2 \cdot x\text{H}_2\text{O}</math></b>	<b>217.2518</b>	<b>1:2</b>	<b>3</b>

As shown in Fig. 1 and Table 2, the loss of mass of about 11.64 % (ca. 11.61 %, giving an error of 0.25% ) in the first stage, up to 90°C, is believed to be the loss of water molecule (Paswan et al., 2019), corresponding to 5.5H<sub>2</sub>O. While the remaining stages are not analyzed in detail, it seems the DTG curve suggests that the ligand-*bipy* is lost in three stages (Czakis-Sulikowska & Czylkowska, 2003), and the residue at above 540°C (17.78%) is likely believed to be the slow conversion of metal oxides as observed for the different complexes of Co(II) (Chaudhary et al., 2015; Mir & Ashraf, 2021).

In addition, the metal content Co, being obtained from the atomic absorption spectral data, with 7.00 % (ca. 6.91 %, giving an error of 1.3%) confirms the proposed formula of  $[\text{Co}(\text{bipy})_3](\text{CF}_3\text{COO})_2 \cdot 5.5\text{H}_2\text{O}$ .

**Table 2.** The proposed formula of the complex estimated by the hydrate and metal content estimated by TGA and AAS data showing the percentage calculated error figures (in brackets \*)

Proposed complex	H <sub>2</sub> O content (%)		Co content (%)	
	calculated	TGA-DTG	calculated	AA S
$[\text{Co}(\text{bipy})_3](\text{CF}_3\text{COO})_2 \cdot 4.5\text{H}_2\text{O}$	9.70 (20.0*)		7.06 (0.85*)	
$[\text{Co}(\text{bipy})_3](\text{CF}_3\text{COO})_2 \cdot 5\text{H}_2\text{O}$	10.67 (9.09*)		6.98 (0.28*)	
<b><math>[\text{Co}(\text{bipy})_3](\text{CF}_3\text{COO})_2 \cdot 5.5\text{H}_2\text{O}</math></b>	<b>11.61 (0.25*)</b>	<b>11.6</b>	<b>6.91 (1.30*)</b>	<b>7.0</b>
$[\text{Co}(\text{bipy})_3](\text{CF}_3\text{COO})_2 \cdot 6\text{H}_2\text{O}$	12.53 (7.10*)		6.84 (2.34*)	

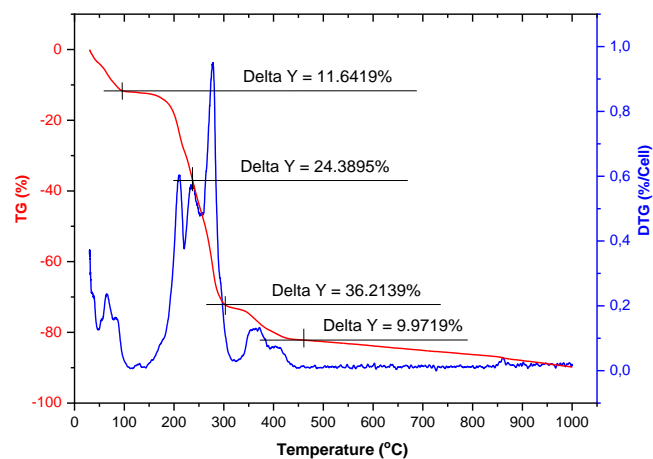


**Figure 1.** The TGA-DTG of  $[\text{Co}(\text{bipy})_3](\text{CF}_3\text{COO})_2 \cdot x\text{H}_2\text{O}$  at 30-1000°C

**Magnetism**

For the magnetic susceptibility measurement, the three samples of the Co(II) complex were prepared separately to confirm the reproducibility. The magnetic susceptibility data as shown in Table 3, produce the magnetic moments of 4.3-5.2 BM, being comparable to other reported data, e.g. 5.14 BM (Mihsen & Shareef, 2018), and 4.7 BM (Hassoon et al., 2020). The moments are significantly higher than the magnetic moment due to the spin only for the 3 unpaired electrons ( $\mu_s = 3.87 \text{ BM}$ ) in the high-spin  $3d^7$  of Co(II), which is not unusual for the strong orbital contribution to the magnetism observed in this octahedral complex (Pathshala, 2021; LibreTexts™, 2020; Lancashire, 2020; Dalal, 2017).

**Table 3.** The magnetic moment of  $[\text{Co}(\text{bipy})_3](\text{CF}_3\text{COO})_2 \cdot 5.5\text{H}_2\text{O}$

Sample	T (K)	$\chi_g$ (cgs)	$\mu_{\text{eff}}$ (BM)
1	291	$1.27112 \times 10^{-5}$	4.91
2	291	$9.41033 \times 10^{-6}$	4.20
3	291	$1.50319 \times 10^{-5}$	5.35

**Electronic Spectrum**

The magnetic data of high-spin octahedral Co(II) in the complex suggests having the triply ground state of the quartet,  $^4T_{1g}(F)$ . Therefore, following the Tanabe-Sugano diagram (Dalal, 2017), the main spin-allowed transitions of  $^4T_{1g}(F) \rightarrow ^4T_{2g}(F)$ ,  $^4T_{1g}(F) \rightarrow ^4A_{2g}(F)$ , and  $^4T_{1g}(F) \rightarrow ^4T_{1g}(P)$ , might assign to the corresponding UV-VIS spectral profiles. As displayed in Fig. 2, the powder spectrum exhibits an indicative of those transitions, the first broad ligand field band centered at  $\sim 15850 \text{ cm}^{-1}$  ( $\nu_1$ ), the second shoulder at  $\sim 18750 \text{ cm}^{-1}$  ( $\nu_2$ ), and the third shoulder at  $\sim 20500 \text{ cm}^{-1}$  ( $\nu_3$ ), respectively; the third ligand field band might overlap with the M-L charge transfer.

In the solution, the spectrum does not well resolve the ligand field bands (Fig. 2), and only their shoulders appear. The intensities, however, are to be very low with the extinction coefficient of  $3.66\text{-}11.15 \text{ Lmol}^{-1} \text{ cm}^{-1}$ , supporting the octahedral geometry of the complex (Lancashire, 2021), which is consistent with the magnetic data.

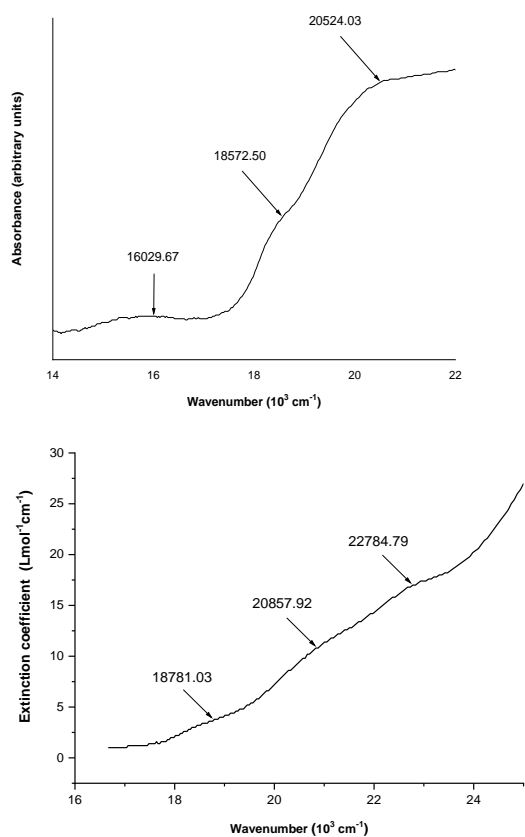


Figure 2. The electronic spectra of the powder (above), and in an aqueous solution, 0.005 M (below) for  $[Co(bipy)_3](CF_3COO)_2 \cdot 5.5H_2O$

**The Infrared Spectra**

The infrared spectrum of the complex,  $[Co(bipy)_3](CF_3COO)_2 \cdot 5.5H_2O$ , is displayed in Fig. 3, together with that of  $CF_3COONa \cdot 4H_2O$ , and thus allowing the direct assignment. The broadband (Fig. 3A-red full line) at about  $3399\text{ cm}^{-1}$  is likely due to the symmetric-/anti symmetric- stretching modes of -OH

of the  $H_2O$  lattice as indicated in the TGA-DTG data (Fig. 1) for the complex. This is comparable as observed at  $3398\text{ cm}^{-1}$  by Abebe, Kendie, & Tigineh (2022), and at  $\sim 3441\text{ cm}^{-1}$  by Shad et al. (2011), even though Kumar et al. (2014) reported that to be C-C aromatic at  $3430\text{ cm}^{-1}$ .

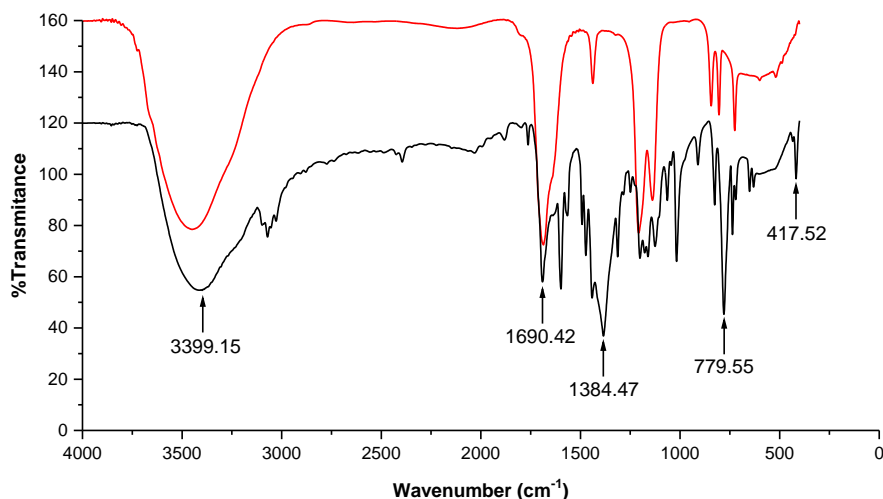


Figure 3. The IR Spectra of  $[Co(bipy)_3](CF_3COO)_2 \cdot 5.5H_2O$  (black) and  $CF_3COONa$  (red) [Note: Relative transmittance (in %) only significant for each spectrum]

A multiplet band centered at about  $3028\text{--}3097\text{ cm}^{-1}$  might be attributed to the mode of C-H of pyridine rings, being comparable to those of  $3051\text{--}3068\text{ cm}^{-1}$  (Chen et al., 2006; Tosonian et al., 2013), and of  $3100\text{ cm}^{-1}$  (Sugiyarto et al., 2020). The typical mode of bipyridine at  $\sim 1598\text{ cm}^{-1}$  is likely attributed to being  $\nu_{\text{C}=\text{C}}$  aromatic as observed by Mihsen & Shareef (2018) at  $1579\text{ cm}^{-1}$ . The mode at  $\sim 1384\text{ cm}^{-1}$  is to be  $\nu_{\text{C}-\text{N}}$  vibration as observed at  $\sim 1342\text{ cm}^{-1}$  by Sutrisno et al. (2018). That mode at  $\sim 1441\text{ cm}^{-1}$  seems to be  $\nu_{\text{C}-\text{N}}$  vibration, being close to  $1449\text{ cm}^{-1}$ , while that at  $\sim 1177\text{ cm}^{-1}$  might be due to  $\nu_{\text{C}-\text{C}}$  ring as it is relatively close to  $1257\text{ cm}^{-1}$  (Abebe, Kendie & Tigineh, 2022).

For the TFA, the very strong-sharp peaks at about  $1690$  and  $1017\text{ cm}^{-1}$  are assigned due to the mode of vibrations  $\nu_{(\text{C}=\text{O})}$  and  $\nu_{(\text{C}-\text{O})}$ , respectively, which is the same order observed by Skyranou et al. (2010) and Suzuki et al. (1978) at  $1669\text{ cm}^{-1}$ , and by Osowole et al. (2008) at  $1192\text{--}1102\text{ cm}^{-1}$ . Meanwhile, mode at about  $1442\text{ cm}^{-1}$  might be due to  $\nu_{(\text{C}-\text{C})}$  as proposed by Abdelhak et al. (2014). The sharp mode of about  $1670\text{ cm}^{-1}$  seems attributed to the C=O vibration as that observed for the sodium TFA (Fig. 3B), which was

also reported at  $1669\text{ cm}^{-1}$  by Skyranou et al. (2010). The stretching mode at  $\sim 750$  and  $848\text{ cm}^{-1}$  are assigned as the asymmetry and symmetry deformation of  $\text{CF}_3$ , respectively (Kusumawardani et al., 2017), as well as in the sodium TFA. Zhou et al. (2003) reported that the asymmetric deformations of CF might fall in the region of  $500\text{--}625\text{ cm}^{-1}$ , whereas the mode of  $700\text{ cm}^{-1}$  is to be the bending vibration of O=C-O. The relatively tiny sharp mode at  $417\text{ cm}^{-1}$  is likely evidence of the Co-N bond (Lever ABP & Mantovani, 2011).

#### SEM, EDX, and Powder XRD

The particle size as shown in the image of SEM, Fig. 4 (a), might consider the powder complex to be a relatively bulky polycrystalline rather than the amorphous type, and the presence of all the main elemental contents (carbon, nitrogen, oxygen, fluorine, and cobalt) is confirmed by the EDX-graph in Fig. 4 (b). The corresponding diffractogram profile (Fig. 5) shows no broad but sharp peaks, supporting no amorphous powders.

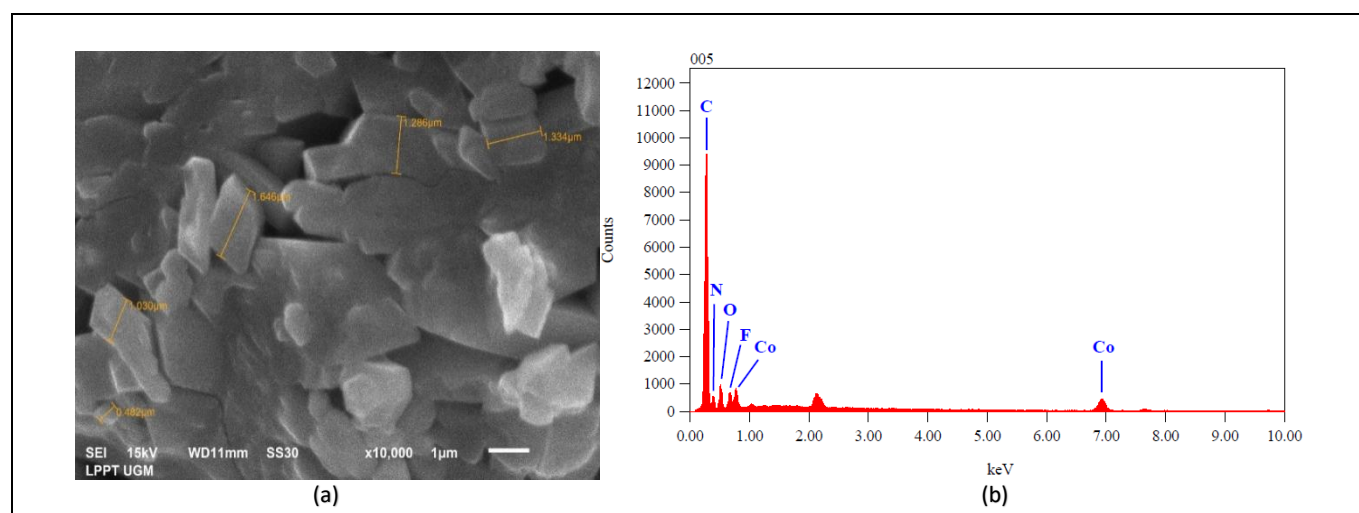


**Figure 4.** SEM photograph of  $[\text{Co}(\text{bipy})_3](\text{CF}_3\text{COO})_2 \cdot 5.5\text{H}_2\text{O}$  at a magnification of  $10,000 \times$  showing crystal size (a) and EDX showing elemental content (b)

The lattice parameters of the powder  $[\text{Co}(\text{bipy})_3](\text{CF}_3\text{COO})_2 \cdot 5.5\text{H}_2\text{O}$  were deduced from the results of the refinement of the diffractogram following the method of Le Bail with the program of Rietica, as displayed in Fig. 5 and **Table 4**. For comparison, the cell parameters of two single crystals (Yao, Ma, & Yao, 2005; Benabdallah et al., 2019) and a PXRD of cationic  $[\text{Co}(\text{bipy})_3]^{2+}$  (Sugiyarto, Kusumawardani, & Wulandari, 2018) are presented.

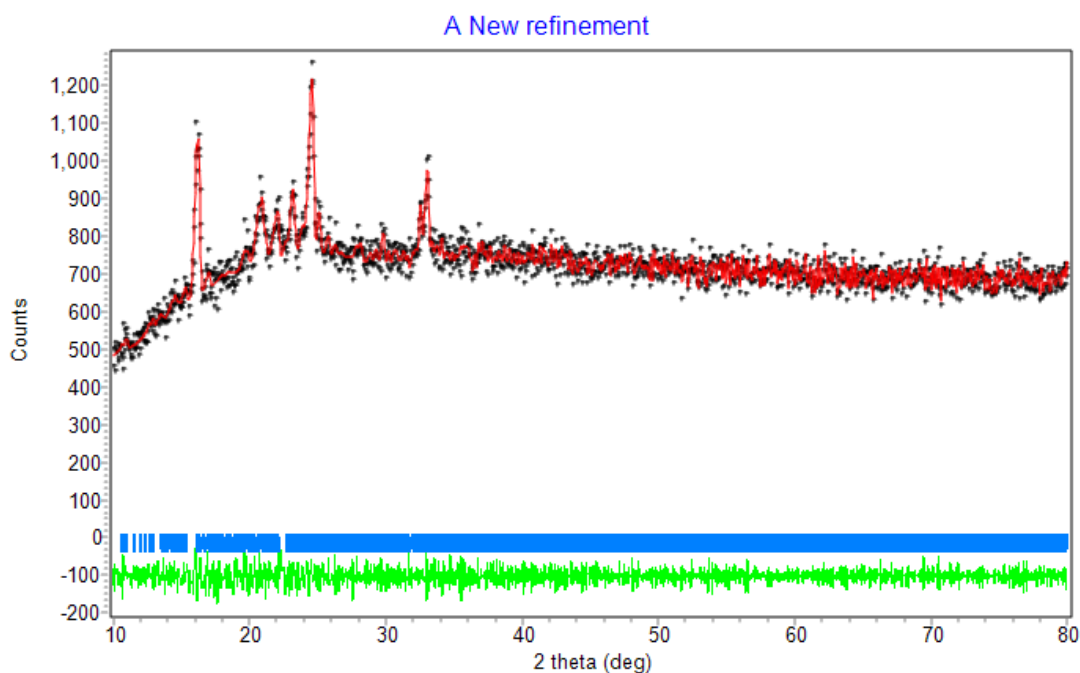


**Figure 5.** P-XRD profile of  $[\text{Co}(\text{bipy})_3](\text{CF}_3\text{COO})_2 \cdot 5.5\text{H}_2\text{O}$  (black), the monoclinic symmetry of C2/c due to the refinement (red), the position of  $2\theta$  (blue), and the difference between the two (green)

**Table 4.** Lattice parameter data of  $[\text{Co}(\text{bipy})_3]\text{X}_2^{a-d}$

$[\text{Co}(\text{bipy})_3]\text{X}_2$	$\text{X}_2 = (\text{TFA})_2 \cdot 5.5\text{H}_2\text{O}^a$	$\text{X}_2 = (\text{CF}_3\text{SO}_3)_2 \cdot 8\text{H}_2\text{O}^b$	$(\text{C}_9\text{H}_5\text{N}_4\text{O})_2^c$	$(\text{ClO}_4)_2^d$
Symmetry	Monoclinic	Monoclinic	Monoclinic	Monoclinic
Space group	C2/c	C2/c	C2/c	C12/c1
Z	4	4	4	4
a (Å)	28.5411	28.3991	22.335(4)	17.538(4)
b (Å)	13.9234	13.8964	10.9454(17)	10.897(2)
c (Å)	22.2933	22.2896	18.721(3)	16.078(3)
$\alpha$ (°)	90.0000	90.0000	90.0000	90.0000
$\beta$ (°)	86.8185	86.8444	110.691(5)	91.01(3)
$\gamma$ (°)	90.0000	90.0000	90.0000	90.0000
Volume (Å <sup>3</sup> )	8845.4824	8783.2304	4281.4(12)	3072.2
<i>The Figure of Merits</i>				
$R_p$	2.30	2.77	-	-
$R_{wp}$	3.52	6.24	-	-
$R_{exp}$	4.10	1.63	-	-
GOF	0.7366	14.79	-	-
$R-F_{Bragg}$	0.04	0.02	-	-

[<sup>a</sup>This work, <sup>b</sup> Sugiyarto, Kusumawardani & Wulandari, 2018; <sup>c</sup> Yao, Ma, & Yao, 2005; <sup>d</sup> Benabdallah et al., 2019]

As shown in **Figure 5**, the red line of the refinement passes through almost all the black points of experimental XRD data at the blue bar space group and symmetry model. The green line reflecting the difference of the model and the experimental data seems to be flat-linear. In addition, the figure of merits is to be acceptable-low. For these reasons, the refinement should satisfy the model, and hence it can be concluded that the powdered complex follows the C2/c space group, with lattice parameters,  $a = 28.5411 \text{ \AA}$ ,  $b = 13.9234 \text{ \AA}$ ,  $c = 22.2933 \text{ \AA}$ ,  $\alpha = 90^\circ$ ,  $\beta = 86.8185^\circ$ ,  $\gamma = 90^\circ$ ,  $V = 8845.4824 \text{ \AA}^3$ , and  $R-F_{Bragg} = 0.04$ .

**The Antibacterial Activity Test**

Concerning the antibacterial agent, the complex was tested against *Staphylococcus Aureus* (S.A) and *Escherichia Coli* (E.C) bacteria with chloramphenicol as a positive control according to agar disc-diffusion method in Nutrient Agar (NA) and Nutrient Broth (NB) or diffusion assay procedures (Balouiri et al., 2016; Davis & Stout, 1971). They represent the two types, gram-positive and gram-negative, respectively, which are pathogenic and easily found in humans. All numeric data of the concentration of the complex, and the zone diameter of the clear inhibition (in mm) with time (in hours) are summarized and depicted graphically in **Fig. 6** and **Fig. 7**.

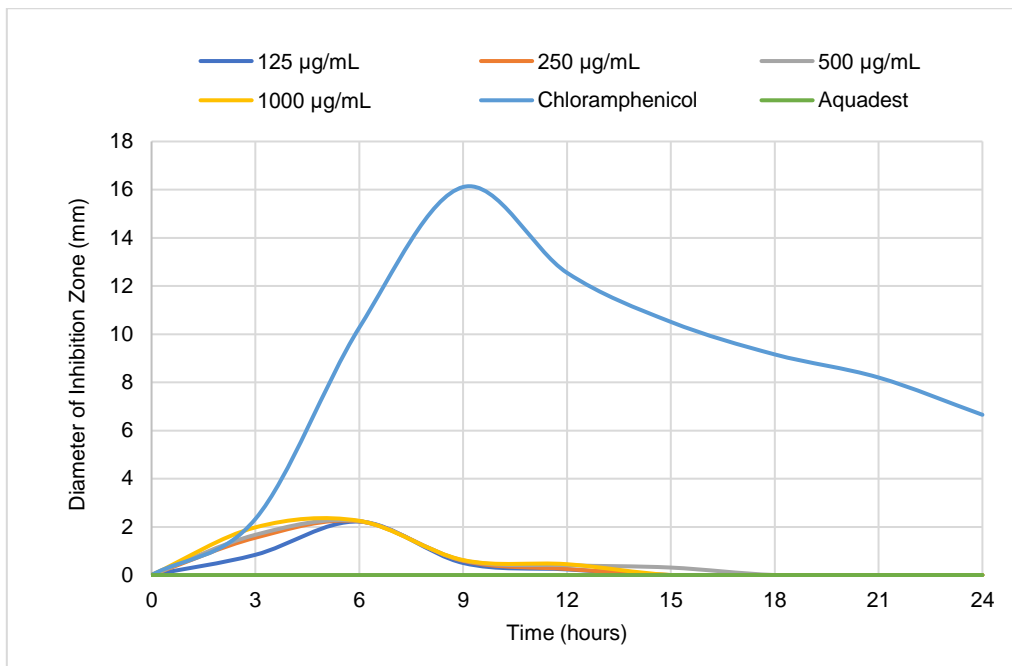


**Figure 6.** Graph of the zone diameter of the clear inhibition (in mm) at various concentrations of the complex against the time for the *S. aureus* activity

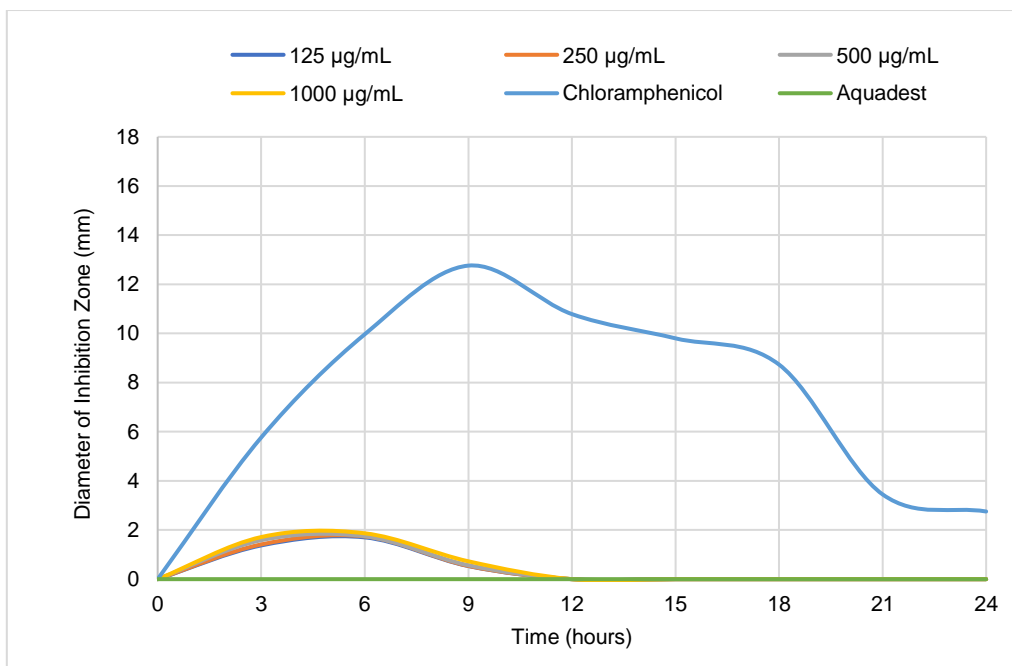


**Figure 7.** Graph of the zone diameter of the clear inhibition (in mm) at various concentrations of the complex against the time for the *E. coli* activity

Following the Kolmogorov-Smirnov test, it was found that the diameter data of the clear inhibition zone is not normally distributed ( $p = 0.000$ ;  $p < 0.05$ ), and based on the Levene's Test, it is not homogeneous ( $p = 0.000$ ;  $p < 0.05$ ). According to the next non-parametric tests, Kruskal-Wallis and Mann-Whitney tests, it can be concluded that the complex in all variant concentrations

falls statistically into 'no different' category ( $p = 0.000$ ;  $p < 0.05$ ), and a weak antibacterial agent (Davis & Stout, 1971; Rastina, Sudarwanto, & Wientarsih, 2015). **Table 5** shows the average inhibition zone of the complex at the optimum time of hour six and that of the positive-negative control, chloramphenicol-aquadest, at hour nine.

Table 11. Diameter of the average inhibition zone at various concentrations of the complex and the antibacterial power

Concentration of the complex	Diameter of the average inhibition zone (mm)		Category of Antibacterial Power
	Due to <i>S. aerous</i>	Due to <i>E. coli</i>	
125 µg/mL	2.22	1.70	Weak
250 µg/mL	2.23	1.74	Weak
500 µg/mL	2.24	1.75	Weak
1000 µg/mL	2.25	1.87	Weak
Aquadest	0.00	0.00	None
Chloramphenicol	16.11	12.76	Strong

In the light of chelation theory, the ligand *bipy* may be considered to be highly stable; however, the high-spin complex of Co(III) suggests that the tris-ligand provides significantly a weak ligand field strength, and this might cause a weak antibacterial agent, as quite recently observed for  $[Mn(bipy)_3](CF_3SO_3)_2$  (Sugiyarto et al., 2023).

#### 4. Conclusion

The powdered compound of  $[Co(bipy)_3](CF_3COO)_2 \cdot 5.5H_2O$  has been isolated and strongly confirmed by AAS, DTG-TGA, conductance, magnetism, UV-VIS, and IR spectral properties. The presence of elemental content, except for hydrogen, is confirmed by the EDX.

The corresponding cell parameters have been reviewed by Le-Bail refinement to the P-XRD diffractogram, which is found as fit as monoclinic symmetry of the C2/c space group. Its antibacterial activity against *S. aureus* and *E. coli* bacteria has been studied to show the inhibition of bacterial growth in the weak category.

#### 5. Acknowledgement

Authors greatly acknowledge the Faculty of Mathematics and Natural Sciences, Yogyakarta State University, for the financial support with a contract number of /4.57/UN/34.21/PT.01.03/2021

#### 6. References

- Abdelhak, J., Cherni, S. N., & Zid, M. F. (2014). Synthesis, characterization, and crystal structure of new cobalt(III) complex: [Tris(1,10-phenanthroline-κ2N,N') cobalt(III)] trinitrate monohydrate  $[Co(C_{12}H_8N_2)_3](NO_3)_3 \cdot H_2O$ , *Mediterranean Journal of Chemistry*, 3 (1), 738–745. DOI: 10.13171/mjc.2014.26.03.22.
- Abebe, A., Kendie, M., & Tigineh, G.T. (2022). Mono-and Binuclear Cobalt(II) Mixed Ligand Complexes of 2,2'-Bipyridine and Ethylenediamine: Synthesis, Characterization and Biological Application. *Biointerface Research in Applied Chemistry*, 12, 1962-1973. <https://doi.org/10.33263/BRIAC122.19621973>
- Ayipo, Y. O., Osunniran, W. A., Badeggi, U. M., Saheed, I. O., Jimoh. A. A., Babamale, H. F., & Olaide, E. O., (2021). Synthesis, characterization and antibacterial study of Co(II) and Cu(II) complexes of mixed ligands of piperazine and diclofenac. *JOTCSA, Journal of the Turkish Chemical Society Chemistry*, 8(2):633–50. DOI: <https://doi.org/10.18596/jotcsa.8985235>
- Bain, G. A., & Berry, J. F. (2008). Diamagnetic Corrections and Pascal's Constants. *Journal of Chemical Education*, 85(4): 532-536. DOI:10.1021/ed085p532.
- Balouiri, M., Sadiki, M., & Ibsouda, S. K. (2016). Methods for in vitro evaluating antimicrobial activity: A review. *Journal of Pharmaceutical Analysis*, 6(2), 71–79. <https://doi.org/10.1016/j.jpha.2015.11.005>
- Benabdallah, J., Setifi, Z., Setifi, F., Boughzala, H., & Titi, A. (2019). Crystal structure of tris(2,2'-bipyridine)cobalt(II) bis(1,1,3,3-tetracyano-2-ethoxypropenide). *Acta Crystallographica Section E: Crystallographic Communications*, 75(2), 142–145. doi:10.1107/s2056989018018261
- Beyene, B. B., & Wassie, G. A. (2020). Antibacterial activity of Cu(II) and Co(II) porphyrins: role of ligand modification. *BMC Chemistry* 14, 51:1-8 <https://doi.org/10.1186/s13065-020-00701-6>
- Chaudhary, R. G., Juneja, H. D., Pagadala, R., Gandhare, N. V. & Gharpure, M. P. (2015). Synthesis, characterization, and thermal degradation behavior of some coordination polymers by using TG–DTG and DTA techniques. *Journal of Saudi Chemical Society*, 19(4), 442–453. doi:10.1016/j.jscs.2014.06.002]]
- Chen, H., Xu, X.-Y., Gao, J., Yang, X.J., Lu, L. D., & Wang, X. (2006). Study on crystal structure of  $[Ni(phen)_3](ClO_4)_2$ . *Acta Physico-Chimica Sinica*, 22 (7), 856–859. DOI:10.3866/PKU.WHXB20060717
- Czakis-Sulikowska, D., & Czykowska, A. (2003). Thermal and other properties of complexes of Mn(II), Co(II) and Ni(II) with 2,2'-bipyridine and trichloroacetates. *Journal of Thermal Analysis and Calorimetry*, 74, 349–360 (2003). <https://doi.org/10.1023/A:1026371029185>
- Dalal, M. A. (2017). Textbook of Inorganic Chemistry-Volume 1 (First Edition). CHAPTER 9. *Magnetic Properties of Transition Metal Complexes*. India: Dalal Institute, pp.342-386.
- Davis, W. W., Stout, T. R.(1971). Disc plate method of microbiological antibiotic assay. I. Factors influencing variability and error. *Applied Microbiology*, 22(4), 659-65. doi:

- 10.1128/am.22.4.659-665.1971. PMID: 5002143; PMCID: PMC376382.
- Hassoon, A. A., Harrison, R. G., Nawar, N., Smith, S. J., & Mostafa, M. M. (2020). Synthesis, single crystal X-ray, spectroscopic characterization and biological activities of Mn<sup>2+</sup>, Co<sup>2+</sup>, Ni<sup>2+</sup> and Fe<sup>3+</sup> complexes. *Journal of Molecular Structure*, *1203*(3), 127240-127264. doi:10.1016/j.molstruc.2019.12724.
- Kani, I., Atlier, Ö., & Güven, K. (2016). Mn(II) complexes with bipyridine, phenanthroline and benzoic acid: Biological and catalase-like activity. *Journal of Chemical Sciences*, *128*(4), 523–536. DOI 10.1007/s12039-016-1050-z.
- Kumar, S. P., Suresh, R., Giribabu, K., Manigandan, R., Munusamy, S., Muthamizh, S., & Narayanan, V. (2014). Microwave synthesis of Tris-(1,10-phenanthroline)Manganese(II) complex and its electrochemical sensing property of catechol. *International Journal of ChemTech Research*, *6* (6), 3280-3283.
- Kusumawardani, C., Kainastiti, F., and Sugiyarto, K. H. (2018). Structural Analysis of Powder Complex of Cu(bipy)<sub>3</sub>(CF<sub>3</sub>SO<sub>3</sub>)<sub>2</sub>(H<sub>2</sub>O)<sub>x</sub> (x = 0.5, 1). *Chiang Mai Journal of Science*, *45*(4), 1944-1952. <http://epg.science.cmu.ac.th/ejournal/>
- Kusumawardani, C., Permasari, L., Fatonah, S. D., & Sugiyarto K. H. (2017). Structural Analysis of Powder Complex of Tris(1,10-phenanthroline)copper(II) Trifluoromethane Sulfonate Dihydrate, *Oriental Journal of Chemistry*, *33*(6), 2841-2847. <http://dx.doi.org/10.13005/ojc/330617>
- Lancashire, R. J. (2021). LibreTexts Chemistry: *Selection Rules for Electronic Spectra of Transition Metal Complexes*, Last updated, Jan 30, 2023. [https://chem.libretexts.org/Bookshelves/Physical\\_and\\_Theoretical\\_Chemistry\\_Textbook\\_Maps/Supplemental\\_Modules\\_\(Physical\\_and\\_Theoretical\\_Chemistry\)/Spectroscopy/Electronic\\_Spectroscopy/Selection\\_Rules\\_for\\_Electronic\\_Spectra\\_of\\_Transition\\_Metal\\_Complexes](https://chem.libretexts.org/Bookshelves/Physical_and_Theoretical_Chemistry_Textbook_Maps/Supplemental_Modules_(Physical_and_Theoretical_Chemistry)/Spectroscopy/Electronic_Spectroscopy/Selection_Rules_for_Electronic_Spectra_of_Transition_Metal_Complexes)
- Lancashire, R. J. *LibreTexts™* (2020). *Magnetic Moments of Transition Metals*. <https://chem.libretexts.org/@go/page/19707> [accessed 15 December 2021].
- Lever, A. B. P., & Mantovani, E. (2011). Isotopic Studies of the Metal–Ligand Bond. Part III. The Far Infrared Spectra of Some Tetragonal Diamine Complexes of Cobalt(II) and Nickel(II): Studies of the Metal–Nitrogen Bond, as a Function of Metal Ion and of Spin State, *Canadian Journal of Chemistry*, *51*(10):1567-1581. DOI:10.1139/v73-237
- LibreTexts™ (2020). *Magnetism*. <https://chem.libretexts.org/@go/page/263246>. [accessed 15 December 2021]
- Mihsen, H. H., & Shareef, N. K. (2018). Synthesis, Characterization of Mixed- ligand Ccomplexes Containing 2,2-Bipyridine and 3-aminopropyltriethoxysilane. *Journal of Physics: Conference Series*, *1032*, 012066. doi:10.1088/1742-6596/1032/1/012066.
- Mir, M.A., & Ashraf, M. W. (2021). TG, DTA Pyrolytic Analysis of Cobalt, Nickel, Copper, Zinc, and 5,8-Dihydroxy-1,4-Naphthoquinone Chelate Complexes, *Hindawi Journal of Chemistry*, 1-13. <https://doi.org/10.1155/2021/6691137>
- Oswole, A. A., Kolawole, G. A., & Fagade, O. E. (2008). Synthesis, characterization and biological studies on unsymmetrical Schiff-base complexes of nickel(II), copper(II) and zinc(II) and adducts with 2,2'-dipyridine and 1,10-phenanthroline, *Journal of Coordination Chemistry*, *61* (7), 1046–1055.
- Paswan, S., Anjum, A., Singh, A. P., & Dubey, R. K. (2019). Synthesis and Spectroscopic Characterization of Lanthanide Complexes Derived from 9,10-Phenanthrenequinone And Schiff Base Ligands Containing N, O Donor Atoms. *Indian Journal of Chemistry*, *58A*(4), 446-453.
- Pathshala (2021). *Inorganic Chemistry-II: Metal-Ligand Bonding, Electronic Spectra and Magnetic Properties of Transition Metal Complexes*. [http://meerutcollege.org/mcm\\_admin/upload/1588000002.pdf](http://meerutcollege.org/mcm_admin/upload/1588000002.pdf). [accessed 15 December 2021]
- Rastina, Sudarwanto, M., & Wientarsih, I. (2015). Antibacterial Activity of Ethanol Extract of Curry Leaf (*Murraya koenigii*) on *Staphylococcus aureus*, *Escherichia coli*, and *Pseudomonas Sp.* *Jurnal Kedokteran Hewan (Indonesian Journal of Veterinary Sciences)*, *9*(2), 185-188.
- Shad, H. A., Thebo, K. H., Ibupoto, Z. H., Malik, M. A., O'Brien, P., & Raftery, J. (2011). Synthesis, characterization, and crystal structure of a copper(II) complex of 1,10-phenanthroline and succinate, *Journal of Coordination Chemistry*, *64*(13), 2353-2360. DOI 10.1080/00958972.2011.595789.
- Singh, B. K., Mishra, P., Prakash, A., & Bhojak, N. (2017). Spectroscopic, electrochemical and biological studies of the metal complexes of the Schiff base derived from pyrrole-2-carbaldehyde and ethylenediamine, *Arabic Journal of Chemistry*, *10*(2), S472-S483. <http://dx.doi.org/10.1016/j.arabjc.2012.10.007>
- Skyrianou, K. C., Perdih, F., Turel, I., Kessissoglou, D. P., & Psomas, G. (2010). Nickel–quinolones interaction. Part 2 – Interaction of nickel(II) with the antibacterial drug oxolinic acid, *Journal of Inorganic Biochemistry*, *104* (2), 161–170. <https://doi.org/10.1016/j.jinorgbio.2009.10.017>

- Sondavid, N., Shweta, B., Bryan, W., Joung, C., Naresh, T., & Jun, K. H. (2020). Cobalt(II) Benzazole Derivative Complexes: Synthesis, Characterization, Antibacterial and Synergistic Activity. *ChemistrySelect*, 5, 3471-3476. DOI:10.1002/slct.202000222.
- Sugiyarto, K. H., Kusumawardani, C., & Wulandari, K. E. (2018). Synthesis and Structural Analysis of Powder Complex of Tris(bipyridine)cobalt(II) trifluoromethanesulfonate Octahydrate, *Indonesian Journal of Chemistry*, 18 (4), 696 - 701. DOI: 10.22146/ijc.26833
- Sugiyarto, K. H., Kusumawardani, C., Sutrisno, H., & Wibowo, M. W. A. (2018). Structural Analysis of Powdered Manganese(II) of 1,10-Phenanthroline (phen) as Ligand and Trifluoroacetate (TFA) as Counter Anion. *Oriental Journal of Chemistry*, 34(2), 735-742. DOI:10.13005/ojc/340216
- Sugiyarto, K. H., Louise, I. S. Y., & Wilujeng, S. S. (2020). Preparation and Powder XRD Analysis of Tris(2,2'-bipyridine)nickel(II) Trifluoroacetate. *Indonesian Journal of Chemistry*, 20(4), 833 - 841. DOI: 10.22146/ijc.46483
- Sugiyarto, K. H., Marini, D. W., Sutrisno, H., Purwaningsih, D., & Kusumawardani, C. (2023). Synthesis of Powdered  $[Mn(bipy)_3](CF_3SO_3)_2 \cdot 5.5H_2O$ : The Physical Properties and Antibacterial Activity. *Indonesian Journal of Chemistry*, 23 (1), 242 - 250. DOI: 10.22146/ijc.77565.
- Sugiyarto, K. H., Saputra, H. W., Permanasari, L., & Kusumawardani, C. (2017). Structural analysis of powder complex of  $[Mn(phen)_3](CF_3SO_3)_2 \cdot 6.5H_2O$ , *AIP Conference Proceedings* 1847, 040006-1-040006-7. DOI: 10.1063/1.4983902. <http://dx.doi.org/10.1063/1.4983902>.
- Sutrisno, H., Kusumawardani, C., Rananggana, R. Y., & Sugiyarto, K. H. (2018). Structural Analysis of Powder Tris(phenanthroline)nickel(II) Trifluoroacetate, *Chiang Mai Journal of Science*, 45(7), 2768-2778. <http://epg.science.cmu.ac.th/ejournal/>
- Suzuki, H., Takiguchi, T., & Kawasaki, Y. (1978). Synthesis and spectroscopy of acetato and dithiocarbamate complexes of bis(cyclopentadienyl) zirconium(IV), *Bulletine of the Chemical Society of Japan*, 51 (6), 1764-1767.
- Tosoniani, S., Ruiz, C. J., Rios, A., Frias, E., & Eichler, J. F. (2013). Synthesis, characterization, and stability of iron (III) complex ions possessing phenanthroline-based ligands, *Open Journal Inorganic Chemistry*, 3 (1), 7-13. DOI:10.4236/ojic.2013.31002
- Uddin, S., Hossain, Md. S., Latif, Md. A., Karim, Md. R., Mohapatra, R. K., & Zahan, Md. K-E. (2019). Antimicrobial Activity of Mn Complexes Incorporating Schiff Bases: A Short Review. *American Journal of Heterocyclic Chemistry*, 5(2), 27-36. DOI: 10.11648/j.ajhc.20190502.12.
- Yao, J. C., Ma, L. F., & Yao, F. J. (2005). Crystal structure of tris(2,2'-bipyridine)cobalt(II)diperchlorate,  $[Co(C_{10}H_8N_2)_3][ClO_4]_2$ . *Zeitschrift Für Kristallographie, New Crystal Structures*, 220(3): 483-484. doi:10.1524/ncrs.2005.220.3.483.
- Zhou, Y., Li, X., Xu, Y., Cao, R., & Hong, M. (2003). Tris(2,2'-bipyridine)nickel(II) perchlorate, *Acta Crystallography, Section E: Structure Report Online*, 59 (5), m300-m302.

# FORMULATION OF RTS FROM PINEAPPLE (ANANAS COMOSUS) AND ALOE VERA (ALOE BARBADENSIS) PULP: EVALUATION OF NUTRACEUTICAL PROFILE AND SHELF-LIFE STUDIES

Renu B. Sharma<sup>1a</sup>, Yogesh Kumar Awasthi<sup>2b\*</sup>, Sushreeta Roy<sup>3b</sup>, Shreya Deb<sup>4b</sup>, Priya Naithani<sup>5b</sup>, Deergha Gupta<sup>6b</sup>, Nishi Saini<sup>7b</sup>

**Abstract:** Pineapple and aloe vera are rich sources of nutraceutical compounds such as flavonoids, ascorbic acid, and phenolic compounds with antioxidant properties, making them highly appealing to both consumers and processors. Aloe vera's beneficial qualities are attributed to its polysaccharide content. Ready-to-serve (RTS) beverages are popular non-fermented drinks that are appreciated for their flavor and therapeutic potential. This study focused on developing RTS drinks from blends of aloe vera and pineapple pulp with varying sugar content (10 °Brix, 12 °Brix, 14 °Brix, and 16 °Brix) and evaluating their physicochemical, microbiological, and sensory properties over 45 days. Storage at 9 °C resulted in a slight increase in TSS, titratable acidity, reducing sugar, and microbial load, while significant decreases were observed in total sugar, pH, phenolic content, and DPPH content. Among the formulations, the RTS beverage with 12 O Brix exhibited superior physicochemical and sensory qualities. Combining aloe vera and pineapple in RTS beverages offers not only an appealing flavor profile but also potential health benefits, making them an ideal choice for product innovation.

**Keywords:** Ready-to-serve (RTS), TSS, nutraceutical, shelf-life, physicochemical properties.

## 1. Introduction

Ready-to-serve (RTS) drink is a result of a combination of traditional and modern elements, seamlessly blending the best of both worlds (Vilas-Boas et al., 2022). This creative process yields a balanced composition that is highly palatable, nutritious, and health-supportive. Enriched with vitamins, minerals, and antioxidants, these juices contain vital micronutrients known to confer various health advantages, including mitigating the risks of cardiovascular diseases, diabetes, and cancer (Kaur et al., 2017). As highlighted by A. Yadev et al., these beverages serve as veritable storehouses of essential nutrients that are essential for healthy growth and development (A. Yadav et al., 2013).

Aloe vera juice is renowned for its multifaceted health benefits, including improved digestion, detoxification, aiding weight loss, and regulating blood sugar levels. Extensive studies have underscored its antioxidant properties, which may reduce inflammation and help prevent the onset of chronic diseases. Notably, research published in the International Journal of Environmental Science and Technology reveals the richness of aloe vera juice in vitamins, minerals, folic acid, and other essential compounds (Añibarro-Ortega et al., 2019). Moreover, the

presence of key minerals such as calcium, iron, potassium, and sodium in aloe vera juice contributes to maintaining healthy blood pressure, muscle function, and nerve function. Furthermore, beneficial enzymes and amino acids found in aloe vera juice promote optimal digestion and facilitate nutrient absorption, as demonstrated by various studies. A finding from the American Journal of Clinical Nutrition demonstrates the lipid-lowering effects of aloe vera juice, which is particularly beneficial for individuals with high cholesterol (Alinejad-Mofrad et al., 2015). Additionally, research suggests that aloe vera juice exhibits antidiabetic properties, helping in the regulation of blood sugar and insulin levels (Rodríguez et al., 2010). Similarly, pineapple juice emerges as a nutritional powerhouse, brimming with essential vitamins, minerals, such as potassium, and antioxidants, as well as a variety of polyphenols and flavonoids (Valderrain-Rodríguez et al., 2017).

The objectives of this research were to investigate:

1. To produce a pineapple & aloe vera RTS beverage
2. To assess the effect of the storage period on total soluble solids acidity, DPPH content, total phenolic content, reducing sugar, and microbial characteristics of the beverage. Additionally, sensory evaluations were conducted over 45 days, both at 9 °C and room temperature.

### Authors information:

<sup>a</sup>Devbhoomi Uttarakhand University Dehradun - 248007, INDIA. E-mail: [shrmareubt@gmail.com](mailto:shrmareubt@gmail.com)<sup>1</sup>

<sup>b</sup>School of Applied & Life Sciences (SALS), Uttaranchal University Dehradun, Uttarakhand-248007, INDIA. E-mail: [yogeshawasthi999@gmail.com](mailto:yogeshawasthi999@gmail.com)<sup>2</sup>; [roysushreeta@gmail.com](mailto:roysushreeta@gmail.com)<sup>3</sup>; [shreyadebagri@gmail.com](mailto:shreyadebagri@gmail.com)<sup>4</sup>; [priyanaithani20@gmail.com](mailto:priyanaithani20@gmail.com)<sup>5</sup>; [deergha.gupta@gmail.com](mailto:deergha.gupta@gmail.com)<sup>6</sup>; [nishisaininishi@gmail.com](mailto:nishisaininishi@gmail.com)<sup>7</sup>

\*Corresponding Author: [yogeshawasthi999@gmail.com](mailto:yogeshawasthi999@gmail.com)

Received: January 5, 2023

Accepted: September 8, 2023

Published: June 30, 2024

## 2. Experimental Methods

The present study, titled “Studies on beverages from aloe vera (*Aloe barbanensis*) and Pineapple (*Ananas comosus* L.) blends,” was conducted at the Centre of Food Science and Technology, Banaras Hindu University, Varanasi (U.P.), India, during the academic year 2015–2016. The following sections detail the materials used in the experimental methodology employed in this study:

### Aloe Vera Pulp Preparation

Aloe vera leaves selected for this study were required to be healthy, undamaged, free of mildew and rot, and 3–4 years old to ensure the concentration of active components. Conventional hand filleting techniques were employed to remove the pulp to prevent contamination of the internal fillet with yellow sap. Portions of the rind containing a significant amount of mucilage were discarded during this process. It is imperative to complete this procedure within 36 h of procuring the leaves to preserve the integrity of the active constituents. Subsequently, the pulp was heated for 10 min at 60–65 °C to ensure sanitation. The heated pulp was then minced using a hand beater. Aloe vera juice was obtained by filtering the mashed pulp through a muslin cloth (R. Yadav et al., 2013).

### Preparation of Pineapple Pulp

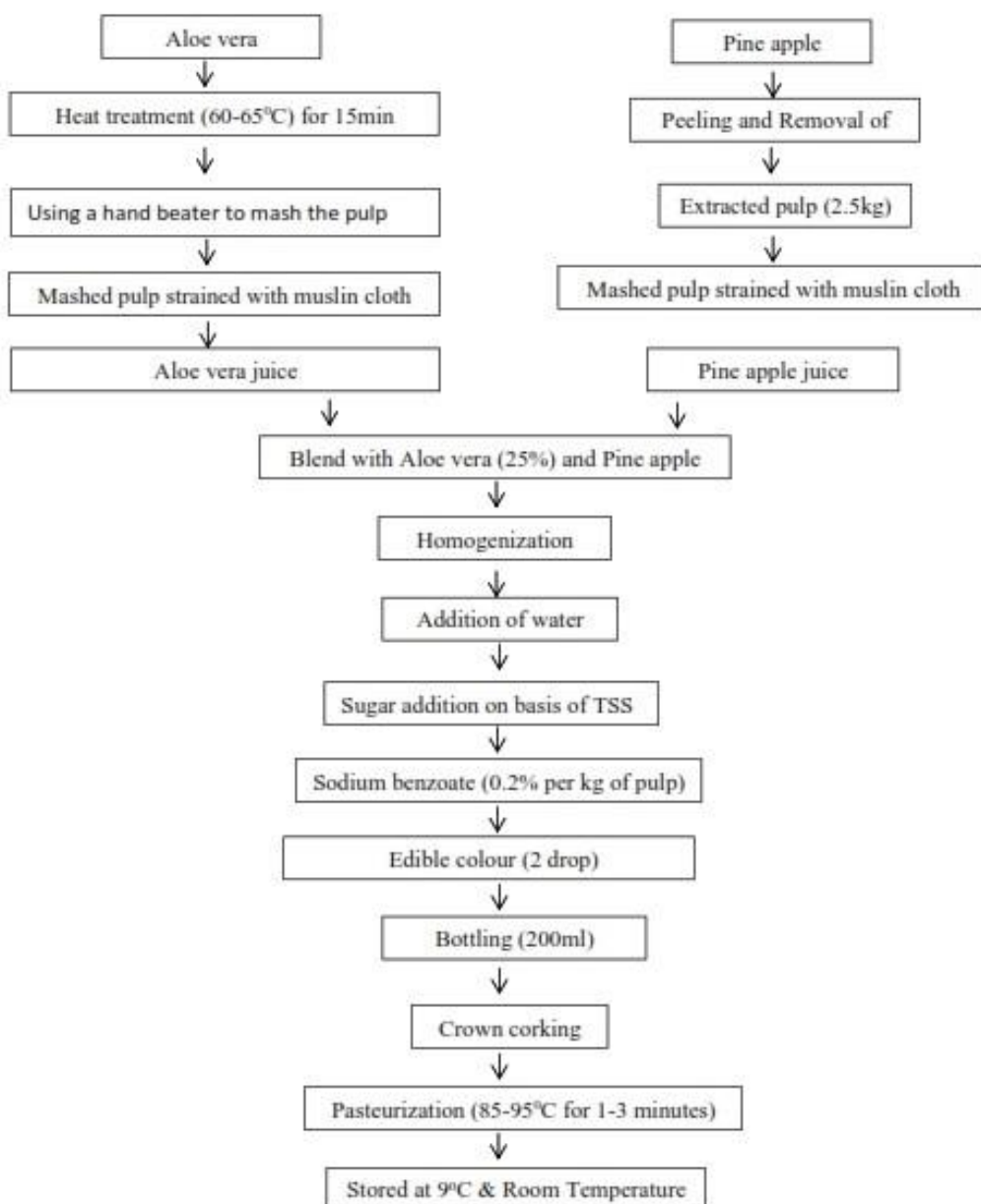
Fresh, fully matured Kew variety of pineapple was used to extract the pulp. The fruits were squashed using a pulper to obtain the pulp. Following extraction, the pulp was carefully stored in stainless steel containers.

### Preparation of RTS beverage

The RTS beverage was formulated by blending aloe vera pulp and pineapple pulp at different concentration levels, maintaining a ratio of 25% aloe vera pulp to 75% pineapple pulp. Additionally, the blended beverage included sodium benzoate at a concentration of 0.2% by weight per kilogram of pulp for preservation, as well as a suitable amount of edible color (2 drops) and water to achieve the desired consistency and visual appeal.



**Figure 1.** The pineapple aloe-vera RTS was developed in four samples (10,12,14, and 16 °Brix TSS)



The process flow chart for the production of Pineapple Aloe Vera RTS (R. Yadav et al., 2013)

**Determination of Physicochemical Quality of Pineapple Aloe Vera RTS**

**pH**

The pH of the pineapple-aloe vera RTS solution was determined by measuring the logarithm of its hydrogen ion concentration.

**pH = -log (H<sup>+</sup>)**

Where H<sup>+</sup> = hydrogen ion concentration (g/L).

An electronic pH meter was employed to measure pH readings, following the method outlined in the previous study (Ranganna,2001). Calibration of the electronic pH meter was performed using standard buffer solutions with pH values of 7 and 4. The pH function selector switch was set, and the reading was taken after allowing the digital display to stabilize.

**Total Soluble Solids (TSS) Measurement**

The total soluble solids (TSS) of the aloe vera RTS were determined using a hand refractometer, as recommended by a previous study (Srivastava et al., 2004). The degree Brix (°Brix) was calculated based on the refractometer reading using the following equation:

**TSS (°Brix) = Refractometer reading**

**Acidity Measurement**

The acidity levels of several samples were determined following the method outlined by Ranganna (Ranganna, 2001). A 5 mL sample of aloe vera RTS was dissolved in 501 mL of distilled water. Subsequently, a 20 mL aliquot of this solution was withdrawn and titrated with 0.1 N NaOH, with phenolphthalein serving as the indicator. The appearance of a pink color indicated

the endpoint of the titration. The volume of NaOH used was recorded, and the acidity was calculated as a percentage of total acids using the following equation:

$$\text{Acidity (\%)} = \frac{\text{Vol. of NaOH used (mL)} \times \text{Norm. of NaOH} \times \text{Equi. wt. of citric acid} \times 100}{\text{Vol. of sample (mL) titrated}}$$

### Reducing Sugar Measurement

#### Principle

The determination of reducing sugar in the samples was based on the principle described by Miller, employing Dinitro salicylic acid (DNS) (Miller, 1959). When a reducing sugar reacts with a basic solution, it forms an aldehyde or ketone. The reduced form of 3, 5-dinitro salicylic acid (DNS) reacts with water in the presence of the aldehyde group of glucose. It catalyzes the reaction to form 3-amino-5-nitro salicylic acid and liberate oxygen gas as a by-product.

The absorption of light at a wavelength of 540 nm is affected by the formation of 3-amino-5-nitro salicylic acid. The quantity of reducing sugar present is directly proportional to the absorbance, as determined using a spectrophotometer.

### Total Phenolic Content

#### Sample Preparation

A sample of 1 mL of fresh juice was diluted to 25 mL and then centrifuged at 4 °C for 20 min at 5000 rpm. The supernatant solution obtained was then used for further analysis.

### Determination of Total Phenolic Content

The Folin-Ciocalteu's reagent was diluted with distilled water to a 1/100 concentration, and 1.0 mL of this diluted reagent was added to the tubes. Subsequently, 0.2 mL of the diluted sample extract was transferred to the tubes. After waiting for 10 min, 0.8 mL of a 7.5% w/v sodium carbonate solution was added to the sample. The absorbance was measured at 743 nm after allowing the sample to equilibrate at room temperature for 30 min. The total phenolic content of the fruit juice was expressed in terms of milligrams of gallic acid equivalent (GAE) per 100 mL of juice. The concentration of polyphenols in the sample was calculated using a gallic acid standard curve with a range of 0.2–4 mg/L.

### Sensory Evaluation

The sensory evaluation was conducted for the freshly formulated RTS beverage and repeated at intervals of 15 days. Various sensory parameters, including taste, color, flavor, texture, and overall acceptability were assessed. A panel comprising 35 semi-trained individuals, including teachers, students, and laboratory staff, was assembled to carry out the analysis. The evaluation was conducted using a 9-point Hedonic scale, where a rating of 9 indicated "Extremely like" and a rating of 1 indicated "Extremely dislike" (Nazni & Mythili, 2013).

### Statistical Analysis

In this research analysis, experimental values were studied in triplicate and outlined as the mean value  $\pm$  standard deviation (SD). The comparison of mean ratios was conducted using one-way ANOVA, followed by Duncan's test ( $p < 0.05$ ) to assess significant differences among the groups.

### 3. Results and Discussion

Parameters	Sample	Storage period (days)								
		0		15		30		45		
		9 °C	RT	9 °C	RT	9 °C	RT	9 °C	RT	
(a) T.S.S.(°Brix)	A <sub>10</sub>	10.29	10.29	10.28	10.37	10.75	10.83	10.94	10.98	
		±0.18	±0.18	±0.06	±0.03	±0.10	±0.03	±0.05	±0.03	
	A <sub>12</sub>	12.00	12.00	12.62	12.83	12.91	13.04	13.32	13.56	
		±0.29	±0.0	±0.07	±0.03	±0.10	±0.07	±0.10	±0.08	
	A <sub>14</sub>	14.00	14.00	14.40	14.78	14.71	14.97	14.93	15.29	
		±0.1	±0.0	±0.1	±0.03	±0.1	±0.02	±0.1	±0.07	
	A <sub>16</sub>	16.00	16.00	16.35	16.70	16.85	17.42	17.04	17.93	
		±0.0	±0.0	±0.1	±0.5	±0.05	±0.21	±0.06	±0.03	
	(b) Titrable acidity (% citric acid)	A <sub>10</sub>	0.17	0.17	0.20	0.24	0.27	0.30	0.30	0.36
			±0.2	±0.2	±0.15	±0.15	±0.2	±0.2	±0.15	±0.15
		A <sub>12</sub>	0.19	0.19	0.21	0.27	0.27	0.29	0.34	0.39
			±0.2	±0.24	±0.21	±0.37	±0.21	±0.34	±0.22	±0.03
A <sub>14</sub>		0.17	0.17	0.21	0.24	0.27	0.29	0.30	0.35	
		±0.02	±0.02	±0.02	±0.02	±0.02	±0.02	±0.03	±0.02	
A <sub>16</sub>		0.19	0.19	0.22	0.24	0.29	0.31	0.37	0.39	
		±0.04	±0.02	±0.03	±0.03	±0.03	±0.03	±0.03	±0.03	
(c) pH		A <sub>10</sub>	4.4	4.4	4.2	3.9	4.0	3.8	3.7	3.4
			±0.25	±0.25	±0.2	±0.2	±0.25	±0.25	±0.25	±0.3
		A <sub>12</sub>	4.4	4.4	4.0	3.9	3.9	3.8	3.5	3.3
			±0.25	±0.25	±0.15	±0.2	±0.25	±0.25	±0.3	±0.2
	A <sub>14</sub>	4.4	4.4	4.2	4.1	3.9	3.8	3.6	3.2	
		±0.25	±0.25	±0.15	±0.2	±0.25	±0.15	±0.3	±0.25	
	A <sub>16</sub>	4.4	4.4	4.0	3.7	3.7	3.6	3.4	3.2	
		±0.25	±0.25	±0.3	±0.25	±0.25	±0.36	±0.35	±0.21	
	(d) Reducing sugar (g/100 mL)	A <sub>10</sub>	10.02	10.02	11.46	12.74	12.37	13.13	14.1	15.65
			±0.25	±0.25	±0.2	±0.2	±0.25	±0.25	±0.25	±0.3
		A <sub>12</sub>	10.41	10.41	12.94	13.69	13.36	15.03	14.79	15.26
			±0.25	±0.25	±0.15	±0.2	±0.25	±0.25	±0.25	±0.2
A <sub>14</sub>		10.72	10.72	14.38	15.55	14.79	15.95	14.9	16.25	
		±0.25	±0.25	±0.15	±0.2	±0.25	±0.15	±0.3	±0.25	
A <sub>16</sub>		11.85	13.69	14.87	15.89	16.21	17.32	16.3	17.45	
		±0.25	±0.25	±0.3	±0.25	±0.25	±0.36	±0.35	±0.25	

**Note:** Data are mean ± SD (n = 3). Similar letters in each row at p < 0.05 were not significantly different.

**Table 1.** Effect on T.S.S, acidity, and reducing sugar during the storage period

Parameters	Sample	Storage period (days)							
		0		15		30		45	
		9 °C	RT	9 °C	RT	9 °C	RT	9 °C	RT
(e)Total phenolic content (mg GAE/100 mL)	A <sub>10</sub>	49.02	46.85	43.04	37.2	39.63	36.28	37.84	32.11
		±0.21	±0.28	±0.21	±0.14	±0.12	±0.31	±0.22	±0.14
	A <sub>12</sub>	35.50	37.13	27.50	32.44	35.96	33.54	33.54	29.78
		±0.24	±0.11	±0.24	±0.11	±0.21	±0.17	±0.41	±0.48
	A <sub>14</sub>	49.65	30.25	41.90	22.97	37.66	32.08	33.21	29.17
		±0.21	±0.2	±0.17	±0.15	±0.19	±0.26	±0.36	±0.31
	A <sub>16</sub>	50.34	32.53	43.86	24.14	34.72	31.27	30.46	27.64
		±0.17	±0.21	±0.14	±0.13	±0.32	±0.37	±0.29	±0.17
(f)DPPH content	A <sub>10</sub>	52.36	52.28	50.28	42.35	47.13	32.65	41.03	25.65
		±0.06	±0.15	±0.88	±0.13	±0.64	±0.21	±0.25	±0.15
	A <sub>12</sub>	51.27	53.35	49.37	43.59	46.56	33.54	39.59	23.49
		±0.07	±0.08	±0.13	±0.26	±0.25	±0.33	±0.25	±0.45
	A <sub>14</sub>	55.05	55.25	51.97	45.72	47.37	34.39	40.69	26.96
		±0.05	±0.1	±0.34	±0.57	±0.58	±0.44	±0.2	±0.15
	A <sub>16</sub>	50.61	49.21	47.86	39.38	45.83	29.98	38.68	22.81
		±0.2	±0.09	±0.46	±0.14	±0.44	±0.15	±0.3	±0.35

**Note:** Data are mean ± SD (n = 3). Similar letters in each row at p < 0.05 were not significantly different

**Table 2.** Effect on total phenolic and DPPH content during the storage period

**Effect on Total Soluble Solids**

Table 1 presents the experimental data for illustrating the changes in TSS of the pineapple aloe vera RTS beverage during storage. Figure 2a depicts a line graph illustrating the variations in the TSS for various pineapple-aloe vera RTS samples over the storage period. The findings indicate that the RST beverage exhibited significant levels of total phenol and flavonoids.

As observed in Table 1, the total soluble solids experienced a notable increase from 0 to 45 days of storage. The TSS of the four processed ready-to-serve beverage samples were maintained at 10, 12, 14, and 16 °Brix, respectively. Notably, sample A16 (RT) exhibited the highest increase in TSS, rising from 16 °Brix to 17.93 °Brix. Conversely, sample A10 (9 °C) showed the smallest rise, increasing from 10 °Brix to 10.94 °Brix.

Additionally, Kalra et al. (1991), Sagar (1995), Murari K. and Verma R.A (1989), and Saravanan K. et al. (2000) have reported a similar increase in TSS during storage. This occurrence could be attributed to the conversion of insoluble polysaccharides to sugar.

**Effect of Titrable Acidity**

The experimental findings regarding the change in titrable acidity of the pineapple aloe vera RTS beverage during storage are presented in Table 1. Figure 2b illustrates a line chart depicting the changes in titrable acidity of various RTS samples over the 45-day storage period. The data from Table 1 indicate a significant increase in titrable acidity over the storage duration. Notably,

sample A10 (9 °C) exhibited the least increase in acidity, rising from 0.17% to 0.30%. This increase can be partly attributed to the intrinsic acid content of the beverage. Hamaran and Amuth (2007) observed similar trends in their study. They found that both ambient temperature (35–36 °C) and low temperature (3–5 °C) storage conditions led to an increase in the acidity values of banana and sapota beverages (A. Yadav et al., 2013).

**Effect of pH**

Experimental results for the change in pH of the RTS beverage during storage are presented in Table 1. Figure 2c depicts a line graph illustrating the pH variations of various RTS samples over 45 days. Sample A10 (9 °C) exhibited the least decline among the four samples, decreasing from 4.4 to 3.7. Similar trends were observed in the cases of banana and sapota beverages by Hamaran and Amuth (2007). Conversely, Bhatti (1975), Ullah (1975), and Tiwari (2000) reported an increase in pH. This gradual decline in pH is noteworthy as it acts as a preservative by inhibiting the growth of pathogenic organisms.

**Effect on Reducing Sugar**

Table 1 presents experimental data depicting the changes in reducing the sugar content of RTS beverages over time. Figure 2d illustrates the reduction in sugar content in several RTS beverages over the storage period through a line graph representation. It is apparent from Table 1 that the reduced sugar content

significantly increased over the 45-day storage period. The highest increases were observed in samples A14 (RT) and A16 (RT), rising from 10.72% to 16.25% and from 13.69% to 17.45%, respectively. Sample A10 exhibited the smallest increase, rising from 10.02% to 14.1%. This increase in reduced sugar content can be attributed to the acid in the beverage hydrolyzing sucrose to produce glucose and fructose, leading to a simultaneous decrease in non-reducing sugars (Shahanas et al., 2019).

**Effect on total phenolic content**

Experimental data regarding the changes in phenolic content of the pineapple aloe vera RTS beverage during storage are presented in Table 2. Figure 2e depicts a line graph illustrating the variations in phenolic concentration among various RTS samples over the storage period. It is evident from Table 2 that the phenolic content experienced a significant decrease from 0 to 45 days of storage. Among the four samples, sample A10 (9 °C) exhibited the least amount of phenolic content loss, dropping from 49.02% to 43.4%. In recent years, there has been increased motivation among individuals to modify their diets in order to reduce susceptibility to or better manage certain health

conditions. Consequently, research on antioxidants has increased due to concerns about improving health and the potential benefits of agricultural goods (Moore et al., 2005). Free radical damage to proteins, lipids, and nucleic acids has been linked to a variety of degenerative human diseases, including cancer, cardiovascular, and cerebrovascular diseases (Park et al., 2009).

**Effect on total DPPH content**

Compound 2,2-diphenyl-1-picrylhydrazyl (DPPH) is a stable free radical compound commonly used to assess antioxidant activity. Spectrophotometric analysis using DPPH was conducted to quantify phenolic compounds, following the methodology described by Cuendet *et al.* (1997). Table 2 presents the experimental findings regarding the variation in DPPH content of pineapple-aloe vera RTS beverage over the storage period. Figure 2f depicts the fluctuation in DPPH content across various RTS samples over time, represented through a line graph. Observing Table 2, a noticeable decline in DPPH content is evident during the storage duration of 0 to 45 days. Notably, samples A10 (9 °C) and A16 (9 °C) exhibited the most significant reductions in DPPH concentration, decreasing from 52.36% to 41.03% and 50.61 to 38.68%, respectively.

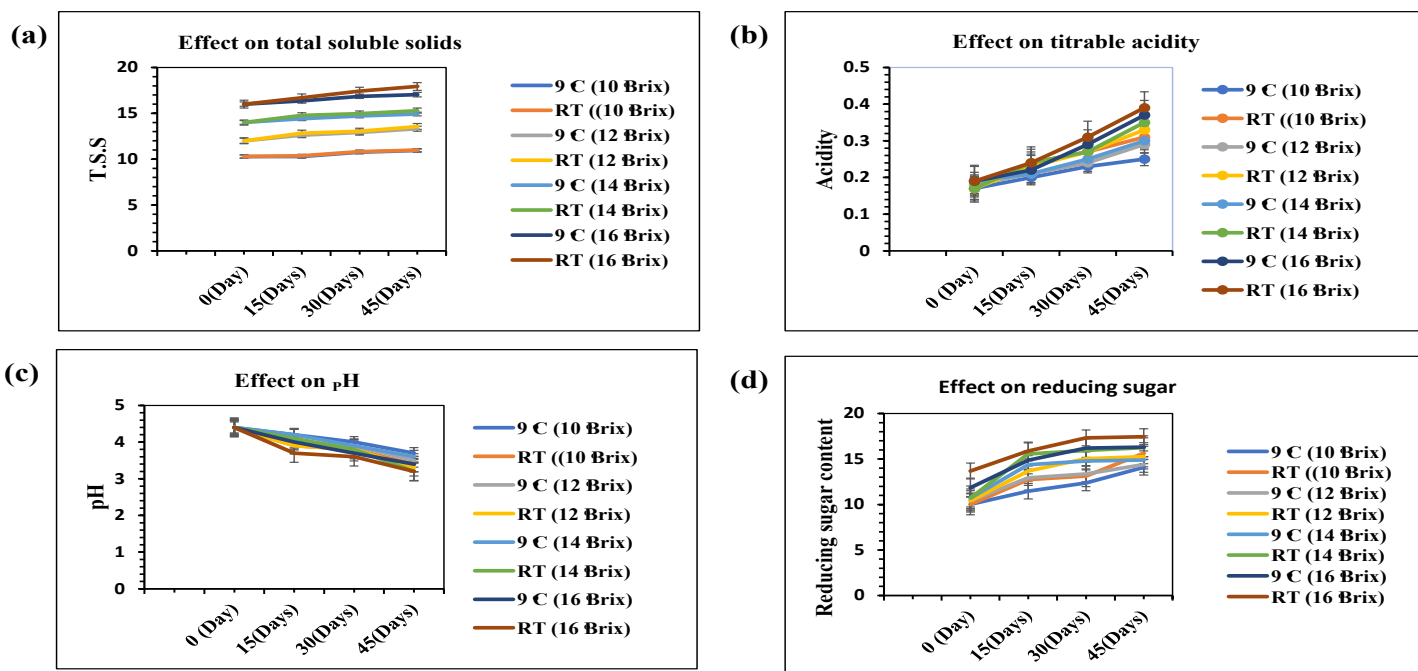


Figure 2. Graphical representation for effect on T.S.S, acidity, and reducing sugar during the storage period

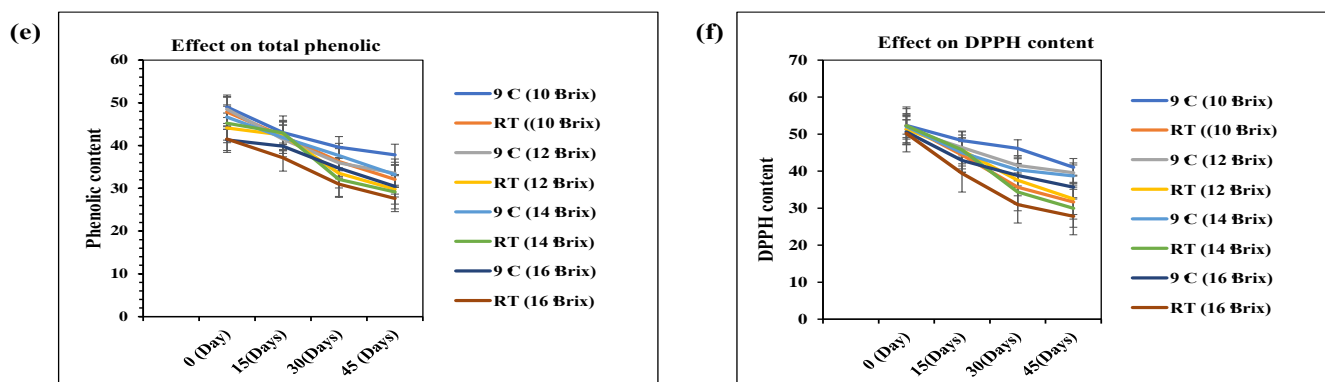


Figure 3. Graphical representation for effect on total phenolic and DPPH content during the storage period

**Variation in Microbial Load Of Pineapple Aloe-Vera RTS During Storage**

Table 4 presents experimental data tracking the microbial load changes in pineapple aloe vera RTS beverages over the storage period. Figure 5 complements this data with a line graph illustrating microbial load changes across various RTS samples during storage. Microbial analysis at a 10<sup>-3</sup> dilution was conducted after 0 to 45 days of storage. Notably, sample A12 (RT) had the highest bacterial count, escalating from 0.65 x 10<sup>-3</sup> to 1.45 x 10<sup>-3</sup>, while sample A16 (9 °C) displayed the lowest bacterial contamination, increasing from 0.97 x 10<sup>-3</sup> to 1.06 x 10<sup>-3</sup>.

Throughout the observed period, there was a slight increase in the microbial load of the ready-to-serve beverage. However, it is noteworthy that the microbiological growth was inhibited to some extent, likely due to the preservative characteristics of sugar. The presence of fruit pulp, serving as a substrate for bacterial development owing to its carbohydrate content, influenced the microbial dynamics, as indicated by both the physical and chemical results. These findings align with the observations of Dhamsaniya & Varshney (2013), confirming the effect of the storage conditions and beverage composition on microbial growth in RTS beverages.

Storage period (in days)	Sample & Storage temperature (M)							
	A <sub>10</sub>		A <sub>12</sub>		A <sub>14</sub>		A <sub>16</sub>	
	9 °C 10 <sup>-3</sup> Dilution (CFU/mL)	RT 10 <sup>-3</sup> Dilution (CFU/mL)	9 °C 10 <sup>-3</sup> Dilution (CFU/mL)	RT 10 <sup>-3</sup> Dilution (CFU/mL)	9 °C 10 <sup>-3</sup> Dilution (CFU/mL)	RT 10 <sup>-3</sup> Dilution (CFU/mL)	9 °C 10 <sup>-3</sup> Dilution (CFU/mL)	RT 10 <sup>-3</sup> Dilution (CFU/mL)
0 (Day)	0.22 ± 0.04	0.24 ± 0.04	0.18 ± 0.04	0.19 ± 0.04	0.15 ± 0.02	0.2 ± 0.04	0.17 ± 0.05	0.16 ± 0.05
30 (Days)	0.25 ± 0.05	0.37 ± 0.06	0.27 ± 0.05	0.41 ± 0.06	0.27 ± 0.08	0.32 ± 0.03	0.36 ± 0.04	0.39 ± 0.06
45 (Days)	0.31 ± 0.02	0.42 ± 0.08	0.34 ± 0.03	0.46 ± 0.4	0.333 ± 0.06	0.45 ± 0.03	0.39 ± 0.05	0.51 ± 0.07

Table 4. Changes in microbial load of pineapple aloe-vera RTS during storage.

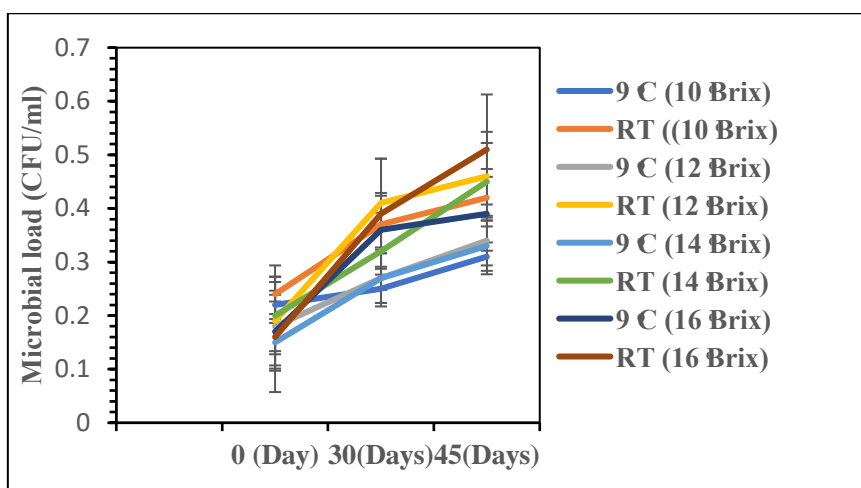


Figure 4. Microbial load of pineapple aloe-vera RTS during storage

#### 4. Conclusion

The current study highlights the positive attributes associated with *Ananas Comosus* beverages, including an enhanced phytochemical profile, improved storage stability, and improved physicochemical, sensory, and microbiological qualities of the product. The formulated beverage contains four different TSS levels and is subjected to storage conditions at both room temperature and 9 °C, revealing various compositional changes over time.

However, observations indicate that over the 45-day storage period, these beneficial compounds experience gradual degradation, particularly when stored at 9 °C and room temperature. Despite this degradation, the RTS beverage comprising *Ananas Comosus* and *Aloe Barbadosis* presents itself as a promising product for consumers, offering numerous nutraceutical and functional benefits.

#### 5. References

- Alinejad-Mofrad, S., Foadoddini, M., Saadatjoo, S. A., & Shayesteh, M. (2015). Improvement of glucose and lipid profile status with Aloe vera in pre-diabetic subjects: a randomized controlled-trial. *Journal of Diabetes & Metabolic Disorders*, 14(1), 1–7.
- Añibarro-Ortega, M., Pinela, J., Barros, L., Ćirić, A., Silva, S. P., Coelho, E., Mocan, A., Calhella, R. C., Soković, M., & Coimbra, M. A. (2019). Compositional features and bioactive properties of Aloe vera leaf (fillet, mucilage, and rind) and flower. *Antioxidants*, 8(10), 444.
- Dhamsaniya, N. K., & Varshney, A. K. (2013). Development and evaluation of whey based RTS beverage from ripe banana juice. *Journal of Food Processing and Technology*, 4(2), 1–5.
- Kaur, A., Gupta, V., Christopher, A. F., Malik, M. A., & Bansal, P. (2017). Nutraceuticals in prevention of cataract – An evidence based approach. In *Saudi Journal of Ophthalmology* (Vol. 31, Issue 1, pp. 30–37). Elsevier B.V. <https://doi.org/10.1016/j.sjopt.2016.12.001>
- Miller, G. L. (1959). Use of dinitrosalicylic acid reagent for determination of reducing sugar. *Analytical Chemistry*, 31(3), 426–428.
- Moore, J., Hao, Z., Zhou, K., Luther, M., Costa, J., & Yu, L. (2005). Carotenoid, tocopherol, phenolic acid, and antioxidant properties of Maryland-grown soft wheat. *Journal of Agricultural and Food Chemistry*, 53(17), 6649–6657.
- Nazni, P., & Mythili, A. (2013). Formulation and optimization of vitamin-C rich beverage prepared from ziziphus jujube. *International Journal of Food and Nutritional Sciences*, 2(2), 54.
- Pandhair, V., & Sekhon, B. S. (2006). Reactive oxygen species and antioxidants in plants: an overview. *Journal of Plant Biochemistry and Biotechnology*, 15(2), 71–78.
- Park, B. S., Song, D. H., Kim, H. M., Choi, B.-S., Lee, H., & Lee, J.-O. (2009). The structural basis of lipopolysaccharide recognition by the TLR4–MD-2 complex. *Nature*, 458(7242), 1191–1195.
- Rodríguez, E. R., Martín, J. D., & Romero, C. D. (2010). Aloe vera as a Functional Ingredient in Foods. *Critical Reviews in Food Science and Nutrition*, 50(4), 305–326. <https://doi.org/10.1080/10408390802544454>
- Shahanas, E., Panjikkaran, S. T., Suman, K. T., Aneena, E. R., & Sharon, C. L. (2019). Standardisation and quality evaluation of jam using tender coconut pulp and fruit pulp. *Asian Journal of Dairy and Food Research*, of. <https://doi.org/10.18805/ajdfr.dr-1427>

- Sirohi, D., Patel, S., Choudhary, P. L., & Sahu, C. (2005). Studies on preparation and storage of whey-based mango herbal Pudina (*Mentha arvensis*) beverage. *JOURNAL OF FOOD SCIENCE AND TECHNOLOGY-MYSORE*, 42(2), 157–161.
- Srivastava, S. K., Singh Rawat, A. K., & Mehrotra, S. (2004). Pharmacognostic evaluation of the root of *Berberis asiatica*. *Pharmaceutical Biology*, 42(6), 467–473.
- Valderrain-Rodríguez, G. R., de Ancos, B., Sánchez-Moreno, C., & González-Aguilar, G. A. (2017). Functional properties of pineapple. *Handbook of Pineapple Technology: Production, Postharvest Science, Processing and Nutrition*, 240–257.
- Vilas-Boas, A. A., Magalhães, D., Campos, D. A., Porretta, S., Dellapina, G., Poli, G., Istanbulu, Y., Demir, S., San Martín, Á. M., García-Gómez, P., Mohammed, R. S., Ibrahim, F. M., el Habbasha, E. S., & Pintado, M. (2022). Innovative Processing Technologies to Develop a New Segment of Functional Citrus-Based Beverages: Current and Future Trends. In *Foods* (Vol. 11, Issue 23). MDPI. <https://doi.org/10.3390/foods11233859>
- Yadav, A., Chandra, S., Singh, J., & Kumar, V. (2013). Effect of storage conditions on physico-chemical, microbial and sensory quality of ready-to-serve banana beverage. *Madras Agricultural Journal*, 100.
- Yadav, R., Tripathi, A. D., & Jha, A. (2013). Effect of storage time on Aloe vera beverage. *International Journal of Food, Nutrition and Public Health*, 6(2), 173.

# SIMPLEX OPTIMIZATION FOR THE SPECTROPHOTOMETRIC DETERMINATION OF AZITHROMYCIN DRUG VIA ION-PAIR FORMATION

Ali Khalil Mahmood<sup>1a</sup>, Hasan Mohammed Luaibi<sup>2b</sup>, Khalid Waleed S. Al-Janabi<sup>3a</sup>, and Tayser Sumer Gaaz<sup>4c\*</sup>

**Abstract:** A spectrophotometric determination of azithromycin was optimized using the simplex model. The approach proved to be accurate and sensitive. The analyte reacted with bromothymol blue (BTB) to form a colored ion pair, which was extracted in chloroform in a buffer medium of pH 4 potassium phthalate. The extracted colored product was assayed at 415 nm, exhibiting a linear quantification range of 1-20 µg/mL. The LOD was 0.671 µg/mL, with a correlation coefficient of 0.9998 and an RSD% of 0.96±0.2. The molar absorptivity was 20253.5 L/mol·cm. The excipients did not interfere with the proposed method for assaying azithromycin in curative formulations.

**Keywords:** Azithromycin, spectrophotometric, simplex, ion-pair.

## 1. Introduction

A Croatian research team made the initial discovery of azithromycin, also known as "9-deoxo-9a-aza-9a-methyl-9a-homoerythromycin" (Deming et al., 1988). This medication is effective against diverse types of bacteria, including chlamydia, legionella, and mycobacteria (Dinos, 2017). It functions as an inhibitor of bacterial protein synthesis. Azithromycin has been approved by the Food and Drug Administration (FDA) for the treatment of pneumonia (Dekate et al., 2011). It is also approved for treating several upper respiratory infections, including acute obstructive pulmonary disease flare-ups and otitis media (MJ, 2014). Its chemical composition is represented in Figure 1.

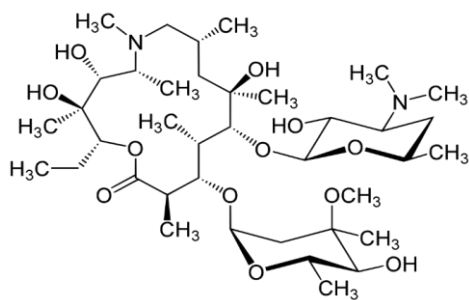


Figure 1. Molecular configuration of azithromycin.

### Authors information:

<sup>a</sup>Department of Chemistry, College of Education for Pure Sciences/ Ibn Al-Haitham, University of Baghdad, Baghdad, IRAQ. E-mail: ali.khalil.mahmood@gmail.com<sup>1</sup>; khalid.Janabi@gmail.com<sup>3</sup>

<sup>b</sup>Department of Renewable Energy, College of Energy and environment Sciences, Alkarkh University of Science, IRAQ. E-mail: hasan.luaibi@gmail.com<sup>2</sup>

<sup>c</sup>Prosthetics and Orthotics Engineering Department, College of Engineering and Technologies, Al-Mustaqbal University, Babylon, 51001, IRAQ. E-mail:

tayser.sumer.gaaz@uomus.edu.iq<sup>4</sup>

\*Corresponding Author: taysersumer@atu.edu.iq

The determination of azithromycin has been achieved through various spectrophotometric techniques (Abdullah et al., 2014; Chiluka & Raut, 2022; Devi, 2011; Doan et al., 2023; El-Yazbi et al., 2020; Gulhane et al., 2021; Ibrahim et al., 2017; Jayanna et al., 2012; Rufino et al., 2008; Sayanna et al., 2019; Suhagia et al., 2006; Walsh et al., 2007). Spendley (1962) introduced the use of simplex optimization, which was later refined by Nelder and Aberg (Åberg & Gustavsson, 1982; Nelder, 1965). This method has various applications in analytical chemistry (Michałowska-Kaczmarczyk & Michałowski, 2014; Momenbeik et al., 2005; Pulgarín et al., 2002; Tinoi et al., 2005) and is a geometric form where (n) denotes the number of variables. It relies on a statistical strategy search to determine the maximum or minimum responses by eliminating the worst point and substituting a new point.

The present work describes a modified simplex technique for spectral quantifying azithromycin (as dihydrate) using BTB as a chromogenic reagent. The optimization of chemical-dependent factors was also studied using a computer program.

## 2. Materials and Methods

### Apparatus

Shimadzu-1800 UV-vis spectrophotometer, pH meter (DW942) Philips, Sartorius balance (210S).

### Experimental

SDI provided standard powders of azithromycin (as dihydrate), The State Company for Drug Industries and Medical Appliances. A 0.1g of BTB was dissolved in 5 mL of methyl alcohol, and the remaining 95 mL were filled with distilled water to create a solution containing 0.10% (w/v) of BTB. A 0.10 M hydrochloric

Received: November 20, 2022

Accepted: August 8, 2023

Published: June 30, 2024

acid solution was prepared by combining 0.850 mL of hydrochloric acid (with a specific gravity of 1.18 and concentration of 37%) with 50 mL of distilled water.

A 0.10 M potassium hydroxide solution was prepared by dissolving 0.560 g of KOH in 100 mL of distilled water. A 0.20 M phthalate buffer was also created by dissolving 4.08 g of potassium hydrogen phthalate in 100 mL of distilled water.

**Standard Solution**

By dissolving 50 mg analyte in 5 mL methanol then diluting it to 100 mL distilled water, a standard solution of 500 µg/mL azithromycin (dehydrated) was created.

**General Procedure**

In total, 1 mL aliquots of the medication, 0.5 mL of pH 4.0 phthalate buffer, and 0.25 mL of 0.1% BTB were added to a 50 mL separating funnel. After shaking the separatory funnels for five minutes with five milliliters of chloroform, the absorbance of the colored chloroform phase was measured at 415 nm against a blank.

**Assaying Azithromycin in Medications**

Ten tablets and ten capsules were separately ground into fine powder. Then, 500 mg of the powdered tablets and 250 mg of the powdered capsules were each dissolved in 10 mL of methyl alcohol in separate volumetric flasks. The volumes were then made up to 100 mL with distilled water and filtered.

**3. Results and Discussion**

Ion-pair extractive spectrophotometry can determine many pharmaceutical formulations (Basavaiah et al., 2007; Milano & Cardoso, 2005; Siddappa et al., 2008). Azithromycin reacts in an acidic pH with Bromothymol Blue to produce a yellowish product that is soluble in chloroform. The electronic transition  $n \rightarrow \pi^*$  occurs between the nitrogen atom in the azacyclopentadecan ring and the sulfur atom in the BTB reagent, resulting in an ion-pair complex. This transition shifts the absorption from the ultraviolet region for azithromycin to the visible region, specifically at 415 nm (Figure 2). This shift permits optimal analytical conditions for the examination of the drug in its dosage form.

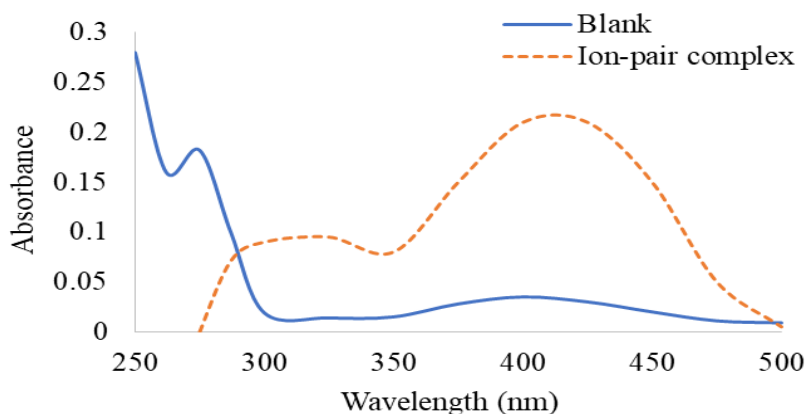


Figure 2. Absorption of the ion-pair complex of azithromycin (10 µg/mL) vs blank.

**Optimization by Simplex Method**

The simplex approach was employed to optimize the pH, reagent quantities, and mixing duration (Table 1). Initially, one of the four major parameters was selected based on its impact on the absorption signal of the colored complex. The absorbance values for these four experiments were measured, and the output of the simplex program is shown in Table 2. The least significant point was replaced with a new one, and the program continued to run. A measured signal was fed back into the computer, and the process was repeated until optimal conditions were achieved (Table 3). The variable setting was then used as a reference point in subsequent experiments.

Table 1. Boundary variables of the study.

Variable	Data Range
pH	3-6
Reagent Vol. (mL)	0. 1-0.25
Shaking time (min.)	1-5

Table 2. Simplex program of the first four experiments.

#	pH	BTB Vol. (mL)	Shaking Time (min.)	Absorbance
I	4.00	0.10	1.0	0.163
II	5.50	0.20	2.0	0.230
III	6.00	0.15	4.0	0.024
IV	3.00	0.25	3.0	0.225

**Effect of pH**

It was observed that pH 4.0 yielded the highest color intensity and stable absorbance values (Table 3). Solutions with higher or lower pH values than this optimal value exhibited decreased absorbance due to forming a new absorbing species. Given that azithromycin's pKa is 8.85 (McFarland et al., 1997), it is evident that at a pH lower than this value, the antibiotic is likely to be protonated, and at a higher pH, it will be deprotonated (Sayle, 2000). This supports the hypothesis that an ion pair would form. Consequently, all subsequent experiments were conducted at pH 4.0.

**Table 3.** Experimental Simplex program.

pH	BTB Vol. (mL)	Shaking Time (min.)	Absorbance
6.0	0.25	5	0.238
6.0	0.20	5	0.202
4.5	0.25	4	0.245
5.0	0.25	5	0.234
4.0	0.25	5	0.256
3.0	0.25	5	0.212
5.0	0.25	5	0.234
5.0	0.25	5	0.211
4.5	0.25	4	0.245
3.5	0.25	5	0.240
4.5	0.25	4	0.245
3.5	0.25	5	0.240
4.5	0.25	4	0.245
3.5	0.25	5	0.240
4.5	0.25	4	0.245
4.5	0.25	4	0.245

**Calibration Graph**

Under optimal conditions, a linear calibration curve for azithromycin spanning the concentration range of 1.0 to 20 µg/mL was established to determine the concentration of unknown azithromycin analytes (Figure 3). Table 3 presents the

data, including the regression equations, R, R<sup>2</sup>, and DL. The concentration can be calculated using Beer-Lambert's law  $A = \epsilon b c A$  under these conditions. The molar absorptivity ( $\epsilon$ ) can thus be obtained from the linear equation in Table 3.

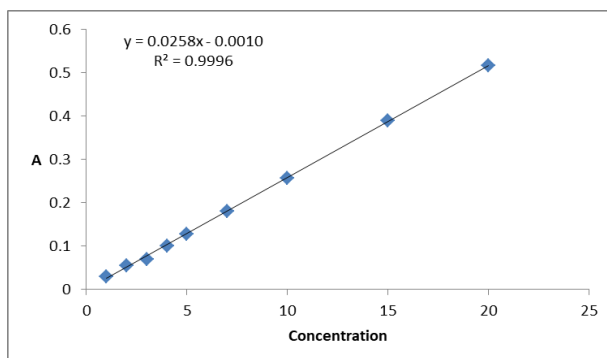


**Figure 3.** Azithromycin calibration curve under optimum conditions.

**Table 4.** Spectral parameters and statistics.

Parameter	Data
$\lambda_{max}$	415 nm
Color	Yellow
Linearity	(1.0 – 20.0) µg/mL
Molar absorptivity ( $\epsilon$ )	20253.5 (L/mol.cm)
Regression equation	$A = 0.0258x + 0.0010$
Calibration Sensitivity	0.0258
Correlation of Linearity (R <sup>2</sup> )	0.9996
Correlation coefficient (R)	0.9998
Limit of detection	0.671 µg/mL

**Validation**

The proposed method was validated by the analysis of five replicates for two different concentrations of each medication by working out the percentage of relative error and relative standard deviation (Table 5). The results indicate that the suggested method was valid and accurate.

**Table 5.** Some statistic parameters of the suggested method.

Concentration (µg/mL)	%Rel. Error	% *RSD
Taken(X)	<b>*Measured</b>	
2	2.0221	+1.105
10	9.9556	-0.444
20	19.878	-0.161

\*Average of five measurements.

**Stoichiometry of the Complexes**

Using Job's method, the formation of a 1:1 complex between protonated azithromycin and the anion of BTB was confirmed (Shah et al., 2008; Taha et al., 2002), as illustrated in Figure 4. The formation of the color complex can be represented in Scheme 1.

**Continuous Variation (Job's method)**

This procedure involved preparing several solutions with varying concentrations of azithromycin and the complexing agent (BTB) ( $3.5 \times 10^{-5}$  to  $3.5 \times 10^{-4}$  mmol) for each solution while maintaining a constant total volume and total moles of reactants in each mixture. However, the mole ratio of reactants

systematically varies (for example, 1:9, 8:2, 7:3, etc.). In the formula  $VD / (VD + VR)$ , where VD is the volume of the drug solution (azithromycin) and VR is the volume of the reagent solution, the absorbance was plotted against the volume fraction of one reactant (BTB).

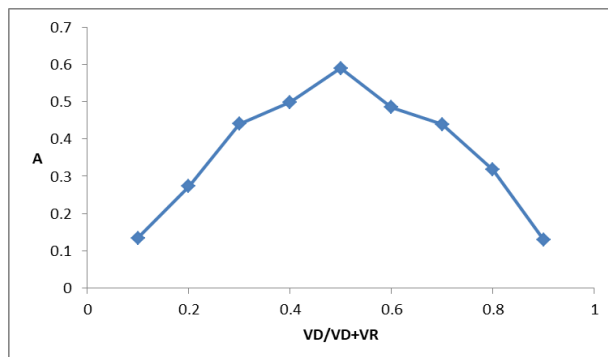
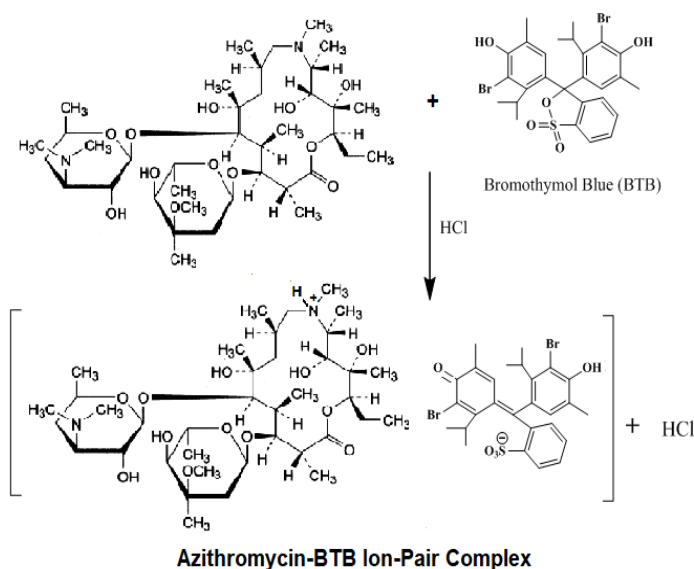


Figure 4. Continuous variation of azithromycin, BTB complex formation.



Scheme 1. The proposed reaction of the color complex.

However, there were no interferences with azithromycin determination when 250  $\mu\text{g/mL}$  of the excipients mentioned in Table 6 were present.

**Table 6.** Recoveries of interferences with 10  $\mu\text{g/mL}$  of azithromycin.

Interferences	Conc. Measured ( $\mu\text{g/mL}$ )	%Rec.
Sucrose	9.9424	99.424
lactose	9.9333	99.333
starch	10.211	102.11
Glucose	9.8881	98.881
Sodium Citrate	9.9635	99.635

**Analysis of Dosage Forms**

The relevance of the active component content of pharmaceutical dosage forms was assessed using the suggested method. The results in Table 6 met expectations, since the RSD was within the range of  $0.96 \pm 0.2\%$ , with a good recovery of (98.321%-101.72%). Therefore, this method can be applied for the routine determination of azithromycin.

**Table 7.** Spectrometric quantification of azithromycin in medicinal compounds with the Formation of Ion-Pair

Pharmaceutical compound	Conc. ( $\mu\text{g}/\text{mL}$ ) Taken(X)	*Measured	% Rel. Error	% Rec.	% *RSD
Azithromycin tablet 500mg (as dihydrate), SANDOZ, Australia	5	4.9442	-1.116	98.884	0.8871
-Zithroriv Capsule Azithromycin dihydrate 250 mg, Egypt	10	9.9464	-0.536	99.468	0.7218
ZAHA-500 tablet	5	5.0513	+1.026	101.02	1.2012
Azithromycin dihydrate 500 mg Ajanta-India	10	10.172	+1.720	101.72	1.1098
	5	4.9322	-1.356	98.644	0.8991
	10	9.8321	-1.679	98.321	0.9019

\*Average of five measurements.

#### 4. Conclusion

Simplex optimisation has been reported for the spectrophotometric measurement of azithromycin in bulk and dosage forms. This approach utilized ion-pair formation with BTB as a chromogenic reagent and proved to be straightforward, accurate, inexpensive, and sensitive (calibration sensitivity 0.0258). These findings clearly indicate that the proposed method is effective for the tested medications.

#### 5. References

- Abdullah, J. H., Yahya, T. A. A., Alkaf, A. G., Alghorafi, M. A., & Yassin, S. H. (2014). Selective spectrophotometric methods for the determination of azithromycin in pharmaceutical formulation. *Journal of Chemical and Pharmaceutical Research*, 6(12), 202–208.
- Åberg, E. R., & Gustavsson, A. G. T. (1982). Design and evaluation of modified simplex methods. *Analytica Chimica Acta*, 144, 39–53.
- Basavaiah, K., Prameela, H., & Somashekar, B. (2007). Spectrophotometric determination of pefloxacin mesylate in pharmaceuticals. *Acta Pharmaceutica*, 57(2), 221–230. <https://doi.org/10.2478/v10007-007-0018-4>
- Chiluka, R., & Raut, R. (2022). Spectrophotometric Determination of Azithromycin Dihydrate in Formulation and its Application to Dissolution Studies. *International Journal of Pharmaceutical Quality Assurance*, 13(2), 116–122. <https://doi.org/10.25258/ijpqa.13.2.4>
- Dekate, P. S., Mathew, J. L., Jayashree, M., & Singhi, S. C. (2011). Acute community acquired pneumonia in emergency room. *The Indian Journal of Pediatrics*, 78(9), 1127–1135.
- Deming, S. N., Michotte, Y., Massart, D. L., Kaufman, L., & Vandeginste, B. G. M. (1988). *Chemometrics: A textbook*. Elsevier.
- Devi, P. U. (2011). Determination of azithromycin by extractive spectrophotometry. *Asian Journal of Chemistry*, 23(2), 921.
- Dinos, G. P. (2017). The macrolide antibiotic renaissance. *British Journal of Pharmacology*, 174(18), 2967–2983. <https://doi.org/10.1111/bph.13936>
- Doan, C. S., Tong, T. T. V., & Le, D. C. (2023). Novel approach for infrared spectroscopic quantitation of azithromycin in commercial tablets employing paracetamol as matrix modifier. *Heliyon*, 9(3).
- El-Yazbi, A. F., Khamis, E. F., Youssef, R. M., El-Sayed, M. A., & Aboukhalil, F. M. (2020). Green analytical methods for simultaneous determination of compounds having relatively disparate absorbance; application to antibiotic formulation of azithromycin and levofloxacin. *Heliyon*, 6(9).
- Gulhane, C. A., Motule, A. S., Manwar, J. V., Sawarkar, H. S., Ajmire, P. V., & Bakal, R. L. (2021). UV-Visible Spectrophotometric estimation of azithromycin and cefixime from tablet formulation by area under curve method. *World Journal of Pharmaceutical Sciences*, 163–168.
- Ibrahim, F. A., Wahba, M. E. K., & Galal, G. M. (2017). Two spectrophotometric methods for the determination of azithromycin and roxithromycin in pharmaceutical preparations. *European Journal of Chemistry*, 8(3), 203–210.
- Jayanna, B. K., Nagendrappa, G., & Gowda, N. (2012). Spectrophotometric estimation of azithromycin in tablets. *Indian Journal of Pharmaceutical Sciences*, 74(4), 365.
- McFarland, J. W., Berger, C. M., Froshauer, S. A., Hayashi, S. F., Hecker, S. J., Jaynes, B. H., Jefson, M. R., Kamicker, B. J., Lipinski, C. A., & Lundy, K. M. (1997). Quantitative structure–activity relationships among macrolide antibacterial agents: in vitro and in vivo potency against *Pasteurella multocida*. *Journal of Medicinal Chemistry*, 40(9), 1340–1346.
- Michałowska-Kaczmarczyk, A. M., & Michałowski, T. (2014). Simplex optimization and its applicability for solving analytical problems. *Journal of Applied Mathematics and Physics*, 2014.
- Milano, J., & Cardoso, S. G. (2005). Spectrophotometric determination of oxiconazole in topical lotion using methyl orange. *Journal of Pharmaceutical and Biomedical Analysis*, 37(4), 639–642.
- MJ, P. (2014). Erakovic Haber V, Giamarellos-Bourboulis EJ, Perletti G, Verleden GM, Vos R. Azithromycin: mechanisms of action and their relevance for clinical applications. *Pharmacol Ther*, 143, 225–245.

- Momenbeik, F., Momeni, Z., & Khorasani, J. H. (2005). Separation and determination of Vitamins E and A in multivitamin syrup using micellar liquid chromatography and simplex optimization. *Journal of Pharmaceutical and Biomedical Analysis*, 37(2), 383–387.
- Nelder, J. (1965). A. & Mead, R. (1965). *Computer J*, 7, 308–313.
- Pulgarín, J. A. M., Molina, A. A., & Pardo, M. T. A. (2002). The use of modified simplex method to optimize the room temperature phosphorescence variables in the determination of an antihypertensive drug. *Talanta*, 57(4), 795–805.
- Rufino, J. L., Pezza, H. R., & Pezza, L. (2008). Flow-injection spectrophotometric determination of azithromycin in pharmaceutical formulations using p-chloranil in the presence of hydrogen peroxide. *Analytical Sciences*, 24(7), 871–876.
- Sayanna, V. S., Veeraiah, T., & Venkata, C. R. R. (2019). Simultaneous spectrophotometric determination of levofloxacin and azithromycin using  $\Pi$ -acceptors as analytical reagents. *IOSR J. Pharm.*, 9, 50–61.
- Sayle, R. (2000). Physiological ionization and pKa prediction. *Euro MUG*, 19–20.
- Shah, J., Jan, M. R., & Manzoor, S. (2008). Extractive spectrophotometric methods for determination of clarithromycin in pharmaceutical formulations using bromothymol blue and cresol red. *Journal of the Chinese Chemical Society*, 55(5), 1107–1112.
- Siddappa, K., Mallikarjun, M., Reddy, T., & Tambe, M. (2008). Simple and sensitive extractive spectrophotometric method for the assay of Mebeverine Hydrochloride in pure and pharmaceutical formulations. *Journal of the Chinese Chemical Society*, 55(5), 1062–1068.
- Spendley, W. (1962). G. R. Hext, and FR Himsworth. *Technometrics*, 4, 441.
- Suhagia, B. N., Shah, S. A., Rathod, I. S., Patel, H. M., & Doshi, K. R. (2006). Determination of azithromycin in pharmaceutical dosage forms by spectrophotometric method. *Indian Journal of Pharmaceutical Sciences*, 68(2), 242–245.
- Taha, E. A., Soliman, S. M., Abdellatef, H. E., & Ayad, M. M. (2002). Colorimetric methods for the determination of some tricyclic antidepressant drugs in their pure and dosage forms. *Mikrochimica Acta*, 140(3–4), 175–182. <https://doi.org/10.1007/s00604-002-0904-x>
- Tinoi, J., Rakariyatham, N., & Deming, R. L. (2005). Simplex optimization of carotenoid production by *Rhodotorula glutinis* using hydrolyzed mung bean waste flour as substrate. *Process Biochemistry*, 40(7), 2551–2557.
- Walash, M. I., Rizk, M. S., Eid, M. I., & Fathy, M. E. (2007). Spectrophotometric determination of four macrolide antibiotics in pharmaceutical formulations and biological fluids via binary complex formation with eosin and spectrophotometry. *Journal of AOAC International*, 90(6), 1579–1587.

# ANALYSIS OF PLANT GROWTH DYNAMICS UNDER THE EFFECT OF TOXICITY: A DELAY DIFFERENTIAL EQUATION MODEL

Pankaj Kumar<sup>1a</sup>, Davneet Kaur<sup>2a\*</sup>

**Abstract:** A mathematical model is designed to examine plant growth under stress in the presence of toxicity with a delay. It is observed that toxic substances change the soil's structure and activity, which has a negative impact on the concentration of nutrients there. The deficiency of soil nutrients and the presence of toxicity are significant elements affecting total biomass. It has been noted that the presence of toxicity changes the physiology and growth of the plant, which ultimately reduces crop growth and production. This adverse effect of toxicity is only seen after an incubation period and is demonstrated by considering the delay in the state variable. Additionally, Hopf bifurcation is observed for the crucial value of the delay parameter. Utilising explicit techniques, the direction and stability of bifurcating periodic solutions are found. Sensitivity analysis is used to determine the sensitivity of solutions of the model when the values of parameters are varied. MATLAB is used for simulation.

**Keywords:** *Nutrients, plant biomass, toxicity, delay, sensitivity, hopf bifurcation.*

## 1. Introduction

Plants uptake nutrients from the soil for proper growth as part of the plant-soil interaction process. Macronutrients and micronutrients are the two major types of nutrients found in soil. The macronutrients found in soil, including phosphorus, potassium, nitrogen, calcium, hydrogen and carbon, are advantageous resources that support plant growth. Nickel, zinc and copper are often present in soil at extremely low concentrations and play important roles in plant growth. However, some heavy metals, including chromium, cadmium, lead, mercury, nickel, etc., have a negative impact on soil quality [1] [2]. Excessive levels of heavy metals poison the soil and gradually affect plant growth [3]. Numerous factors, including geological, social, economic and biological ones, contribute to the rise in toxic heavy elements in the soil. Additionally, nutrients play a significant role in discrete plant growth, which has an impact on nonlinear population growth dynamics and, ultimately, on the yield of standing crops [4]. Metals or toxicity cause an imbalance in the soil's nutrition levels. The presence of toxicity affects both the biomass of trees and plants. Thornley was the first to experiment with mathematical modelling in plant physiology by considering various climatic change factors, such as humidity, temperature, rainfall, transpiration, respiration, rate of photosynthesis and guard cells of stomata, among others. However, these models were limited to specific plant species and conditions [5][6]. A mathematical model is proposed to justify the

fact that toxic metals have a negative impact on tree biomass [7]. Biomass is negatively affected by the primary and secondary toxicity domains [8]. Also, nutrients have a crucial role in discrete plant growth, influencing the dynamics of nonlinear population increase and, ultimately, the yield of standing crops. Another factor affecting crop yield and crop growth is geographical location [9]. According to a mathematical model, a plant's growth rate is a dynamic process that depends on factors like plant size, decreased growth rate and nutrient mortality rate [10]. Delay was utilised to learn the combined impact of acid and toxic metals on plant populations [11]. The distribution of exponential polynomial roots is explained by Rouches's Theorem (1960). Ruan and Wei (2001) used Rouches' theorem for their consideration of the distribution of exponential polynomial roots [12]. As plant biomass decreases under the influence of toxicity, the variable oscillates for the delay value [13]. Delay was utilised to study the global stability in the collection of non-linear differential equations [14] [15]. It is possible to establish the direction of Hopf bifurcation as well as various numerical simulations using Hassard et al.'s manifold and normal form [16] [17]. The delay differential equations are used to construct the direct and adjoint approaches for sensitivity analysis in bioscience numerical modelling [18]. The sensitivity analysis for a system of nonlinear differential equations with time lags is performed using the 'Direct method' [19]. A generalised method for sensitivity analysis of the delay differential equation is suggested [20] [21]. In relation to the delays, theoretical conclusions for sensitivity are presented. The periodic responses to delay differential equations are studied using a parametric sensitivity analysis [22].

### Authors information:

<sup>a</sup>Department of Mathematics, Lovely Professional University, Phagwara, Punjab, INDIA. E-mail: [pankaj.kumar1@lpu.co.in](mailto:pankaj.kumar1@lpu.co.in); [davneet02@gmail.com](mailto:davneet02@gmail.com)<sup>2</sup>

\*Corresponding Author: [davneet02@gmail.com](mailto:davneet02@gmail.com)

Received: November 22, 2022

Accepted: April 12, 2023

Published: June 30, 2024

## 2. Mathematical Model

Assume that  $N$  is the plant nutrient concentration,  $B$  is the quantity of plant biomass and  $T$  is the amount of toxicity concentration in the plant, all of which serve as three state variables. These are used to model the dynamics of plant growth. The formulation of the model is as follows:

$$\frac{dN}{dt} = N_0 - \alpha_1 N(t - \tau)B - \alpha_2 N - \alpha_3 NT \tag{1}$$

$$\frac{dB}{dt} = rB \left(1 - \frac{B}{K}\right) + \beta_1 N(t - \tau)B - \beta_2 B \tag{2}$$

$$\frac{dT}{dt} = T_0 - \gamma_1 NT - \gamma_2 T \tag{3}$$

Initially:  $N(0) > 0, B(0) > 0, T(0) > 0 \forall t$  and  $N(t - \tau) = \text{constant}$  for  $t \in [-\tau, 0]$ .

The parameters are as follows:  $N_0$  represents the fixed amount of nutrients that are available;  $T_0$  denotes the fixed amount of toxicity that are available in soil because of the presence of toxic metals;  $r$  represents the growth rate of the plant;  $K$  represents the carrying capacity;  $\alpha_1$  is the rate of consumption of nutrients by biomass;  $\alpha_3$  is the rate of decay of nutrients due to its interaction with toxicity;  $\beta_1$  is the utilisation coefficient of nutrients; and  $\gamma_1$  is the rate of toxicity decay due to interaction with nutrients. The rates of natural decay for  $N, B$  and  $T$  are  $\alpha_2, \beta_2$  and  $\gamma_2$ , respectively. Here, it is assumed that all parameters  $\alpha_1, \alpha_2, \alpha_3, \beta_1, \beta_2, \gamma_1, \gamma_2, N, B$  and  $T$  are positive.

### Boundedness

**Lemma 1:** Consider the function,  $W = N + B + T$

such that,  $\frac{dW}{dt} = \frac{dN}{dt} + \frac{dB}{dt} + \frac{dT}{dt}$

Using equations (1)–(3),  $\frac{dW(t)}{dt} = N_0 - \alpha_1 NB - \alpha_2 N - \alpha_3 NT + r \left(1 - \frac{B}{K}\right) + \beta_1 NB - \beta_2 B + T_0 - \gamma_1 NT - \gamma_2 T$  and  $\min(\alpha_1, \alpha_2, \alpha_3, \beta_1, \beta_2, \gamma_1, \gamma_2) = \delta$  and assuming  $N \approx N(t - \tau)$  as  $t \rightarrow \infty$ ,  $\frac{dW(t)}{dt} \leq (N_0 + T_0)$

By Comparison theorem as  $t \rightarrow \infty, W \leq \frac{N_0 + T_0}{\delta}$ , so  $0 \leq (N + B + T) \leq \frac{N_0 + T_0}{\delta}$

### Positivity of Solutions

Positivity of system defines that model's solution, with initial data, will eventually be positive for all  $\forall t$  exceeding some finite value. It is crucial to demonstrate that every solution provided by the equations is a positive solution. Considering equations (1)–(3), where initial condition is  $N(0) > 0, B(0) > 0, T(0) > 0 \forall t$  and  $N(t - \tau) = \text{constant}$  for  $t \in [-\tau, 0]$ , the model solution  $(N, B, T)$  remains positive  $\forall$  for all time  $t > 0$ .

Using equation (3),  $\frac{dT}{dt} \geq -\delta(N + 1)T$  i.e.  $\frac{dT}{dt} \geq -((N_0 + T_0) + \delta)T, T \geq c_1 e^{-((N_0 + T_0) + \delta)t}$ , here  $c_1$  is constant of integration. So,  $T > 0 \forall t$ . For  $N$  and  $B$ , the same argument is valid.

### Interior Equilibrium Point

A mathematical model under consideration has an equilibrium point that defines a constant solution. We identify the internal equilibrium  $E^*$  of the model. For the set of equations (1)–(3), there is only one possible equilibrium at  $E^*(N^*, B^*, T^*)$ .

$$N^* = \frac{-b \mp \sqrt{b^2 - 4ac}}{2a}$$

$$T^* = \frac{T_0}{\gamma_1 N^* - \gamma_2}$$

$$B^* = \frac{K}{r} (r - \beta_1 N^* - \beta_2)$$

Where  $a = \alpha_1 K \beta_1 \gamma_1, b = \alpha_1 \gamma_1 K r - \alpha_1 K \beta_2 \gamma_1 - \alpha_1 K \beta_1 \gamma_2 + \alpha_2 \gamma_1 r, c = \alpha_1 K r + \alpha_1 K \beta_2 \gamma_1 - \alpha_2 \gamma_2 r + \alpha_3 T_0$

### Analysis of Hopf bifurcation

This section analyses the dynamical internal equilibrium point behaviour  $E^*(N^*, B^*, T^*)$  of model (1)–(3). In relation to the equilibrium  $E^*$ , the exponential characteristic equation is provided by

$$\lambda^3 + P_1 \lambda^2 + P_2 \lambda + P_3 + (Q_1 \lambda^2 + Q_2 \lambda + Q_3) e^{-\lambda \tau} = 0 \tag{4}$$

where  $P_1 = \alpha_2 + \alpha_3 T + \frac{r}{k} + \beta_2 + \gamma_1 N + \gamma_2$ ,

$$P_2 = \frac{r}{k} \alpha_2 + \frac{r}{k} \alpha_3 T + \beta_2 \alpha_2 + \beta_2 \alpha_3 T + \frac{r}{k} \gamma_1 N + \frac{r}{k} \gamma_2 + \beta_2 \gamma_1 N + \beta_2 N_2 + \alpha_2 \gamma_1 N + \gamma_1 N \alpha_3 + \gamma_2 \alpha_2 + \gamma_2 \alpha_3 T,$$

$$P_3 = \frac{r}{k} \alpha_2 \gamma_1 N + \frac{r}{k} \alpha_2 \gamma_2 + \alpha_2 \beta_2 \gamma_1 N + \alpha_2 \beta_2 \gamma_2 + \frac{r}{k} \alpha_3 \gamma_1 NT + \frac{r}{k} \alpha_3 \gamma_2 T + \alpha_3 \beta_2 \gamma_1 NT + \alpha_3 \beta_2 \gamma_2 T - \gamma_1 \alpha_3 TN,$$

$$Q_1 = \alpha_1 B,$$

$$Q_2 = \frac{r}{k} \alpha_1 B + \beta_2 \alpha_1 B + \gamma_1 \alpha_1 N + \gamma_2 \alpha_1 B,$$

$$Q_3 = \frac{r}{k} \alpha_1 \gamma_1 BN + \frac{r}{k} \alpha_1 \gamma_2 B + \alpha_2 \beta_2 \gamma_1 BN + \alpha_1 B_2 \gamma_2 B$$

Clearly,  $P_1, P_2, P_3, Q_1, Q_2, Q_3$  all are positive.

Equation (4) can only be solved if and only if  $\lambda = i\omega$  is true.

$$(i\omega)^3 + P_1(i\omega)^2 + P_2(i\omega) + P_3 + (Q_1(i\omega)^2 + Q_2(i\omega) + Q_3)e^{-i\omega\tau} = 0 \tag{5}$$

Separating the real and imaginary parts, we get the following equations:

$$P_3 - P\omega^2 + (Q_3 - Q_1\omega^2)\cos \omega\tau + Q_2\omega \sin \omega\tau = 0 \tag{6}$$

$$P_2\omega - \omega^3 + Q_2\omega \cos \omega\tau - (Q_3 - Q_1\omega^2) \sin \omega\tau = 0 \tag{7}$$

This further gives:

$$\omega^6 + (P_1^2 - Q_1^2 - 2P_2)\omega^4 + (P_2^2 - Q_2^2 + 2Q_1Q_3 - 2P_1P_3)\omega^2 + (P_3^2 - Q_3^2) = 0 \tag{8}$$

Let

$$u = (P_1^2 - Q_1^2 - 2P_2), v = (P_2^2 - Q_2^2 + 2Q_1Q_3 - 2P_1P_3), z = (P_3^2 - Q_3^2).$$

Let  $\omega^2 = x$ , then equation (8) becomes  $x^3 + ux^2 + vx + z = 0$ . [9]

Claim 1: If  $z < 0$ , equation (9) has one real positive zero.

Proof: Consider  $s(x) = x^3 + ux^2 + vx + z$ .

Here,  $s(0) = z < 0$  and  $\lim_{x \rightarrow \infty} s(x) = \infty$ . So,  $\exists z_0 \in (0, \infty)$  such that  $s(x_0) = 0$ .

Claim 2: If  $z \geq 0, D = u^2 - 3v \geq 0$  is a necessary condition for the existence of positive real roots in equation (9).

Proof: Since  $s(x) = x^3 + ux^2 + vx + z$ , therefore  $s'(x) = 3x^2 + 2ux + v$ .

$$s'(x) = 0 \text{ implies } 3x^2 + 2ux + v = 0. \tag{10}$$

The roots of equation (10) can be written as  $x_{1,2} = \frac{-2u \mp \sqrt{4u^2 - 12v}}{6} = \frac{-u \mp \sqrt{D}}{3}$  [11]

There are no real roots in equation (10) if  $D < 0$ . Consequently, the function  $s(x)$  is an increasing monotone function in  $x$ . Since  $k(0) = z \geq 0$ , therefore positive real roots cannot exist in equation (9). It has been proven.

Clearly if  $D \geq 0$ , then  $x_1 = \frac{-u + \sqrt{D}}{3}$  is the local minima of  $s(x)$ . Hence, the following assertion.

Claim 3: If  $z \geq 0$ , and only if  $x_1 > 0$  and  $s(x_1) \leq 0$ , equation (9) has positive real.

Proof: It is clear that there is enough. There is only one requirement: necessity. If not, assume that  $s(x) > 0$  and either  $x_1 \leq 0$  or  $x_1 > 0$ .

Consequently,  $s(x)$  has no positive real zeros if  $x_1 \leq 0$  since  $s(x)$  is rising for  $x \geq x_1$  and  $s(0) = c \geq 0$ . Since  $x_2 = \frac{-u - \sqrt{D}}{3}$  is the local maximum value if  $x_1 > 0$  and  $s(x_1) > 0$ , it follows that  $s(x_1) \leq s(x_2)$ . Because  $s(x)$  lacks positive real roots,  $s(0) = c \geq 0$ . Proof is now complete.

**Lemma 2:** Assume that equation (11) defines  $x_1$ .

- (I) If  $z < 0$ , at least a positive real zero exists in equation (9).
- (II) If  $z \geq 0$  and  $D = u^2 - 3v < 0$ , no positive zeros can be found for equation (9).
- (III) If  $z \geq 0$ , there are positive zeros in equation (9) if  $x_1 > 0$  and  $s(x_1) \leq 0$ .

Proof: Assume that equation (9) has roots that are positive. Suppose it has three constructive roots without losing generality, signified by  $x_1, x_2$ , and  $x_3$ . Then equation (8) has three positive roots, denoted by  $\omega_1 = \sqrt{x_1}, \omega_2 = \sqrt{x_2}$ , and  $\omega_3 = \sqrt{x_3}$ .

Using equation (7),  $\sin \omega\tau = \frac{P_2\omega - \omega^3}{d}$

Which gives  $\tau = \frac{1}{\omega} \left[ \sin^{-1} \left( \frac{P_2\omega - \omega^3}{d} \right) + 2(j - 1)\pi \right]; j = 1, 2, 3, -$

Let  $\tau_k^{(j)} = \frac{1}{\omega_k} \left[ \sin^{-1} \left( \frac{P_2\omega_k - \omega_k^3}{d} \right) + 2(j - 1)\pi \right]; k = 1, 2, 3.; j = 0, 1, 2, - - -$

Then  $\mp i\omega_k$  form a pair of equation (8) roots that are entirely imaginary.

Where  $\tau = \tau_k^{(j)}, k = 1, 2, 3.; j = 0, 1, 2, 3, - - -$ ,  $\lim_{j \rightarrow \infty} \tau_k^{(j)} = \infty$  where  $k = 1, 2, 3$ .

Thus, we define  $\tau_0 = \tau_{k_0}^{(j_0)} = \min_{1 \leq k \leq 3, j \geq 1} [\tau_k^{(j)}], \omega_0 = \omega_{k_0}, x_0 = x_{k_0}$  [12]

**Lemma 3:** Assume that  $P_1 > 0, (P_3 + d) > 0$ , and  $P_1P_2 - (P_3 + d) > 0$ .

- (I) The real part of every root of equation (4) is negative  $\forall \tau \geq 0$  if  $z \geq 0$  and  $D = u^2 - 3v < 0$ .
- (II) The real part of every root of equation (4) is negative  $\forall \tau \in [0, \tau_0)$  if  $z < 0$  or  $z \geq 0, x_1 > 0$  and  $s(x_1) \leq 0$ .

Proof: When  $\tau = 0$ , equation (4) changes to:

$$\lambda^3 + (P_1 + Q_1)\lambda^2 + (P_2 + Q_2)\lambda + (P_3 + Q_3) = 0. \tag{13}$$

Using Routh-Hurwitz's criteria, (H1): if  $(P_3 + Q_3) > 0, (P_1 + Q_1)(P_2 + Q_2) - (P_3 + Q_3) > 0$ , then all the roots in equation (4) have negative real parts.

If  $z \geq 0$  and  $D = u^2 - 3v < 0$ , equation (4) does not have any roots with a real part of zero  $\forall \tau \geq 0$  according to Lemma 2 (II). When  $z < 0$  or  $z \geq 0, x > 0$  and  $s(x_1) \leq 0$ , Lemma 2 (I) and (III) implies that when  $\tau \neq \tau_k^{(j)}, k = 1, 2, 3; j \geq 1$ , Since  $\tau_0$  is the smallest value of  $\tau$  and equation (4) only has imaginary roots, it does not have any real roots with any real parts. The result is obtained using the theorem 1.

$$\text{Suppose } \lambda(\tau) = \psi(\tau) + i\omega(\tau) \tag{14}$$

being the roots of the equation (4) holds:  $\psi(\tau_0) = 0, \omega(\tau_0) = \omega_0$ .

Assume that  $s'(x_0) \neq 0$  to ensure that  $\mp \omega_0$  are simple and purely imaginary roots of equation (4), as  $\tau = \tau_0$  and  $\lambda(\tau)$  satisfies the transversality requirement.

**Lemma 4:** Assume that  $x_0 = \omega_0^2$ . If  $\tau = \tau_0$ , then  $\text{Sign} [\psi'(\tau_0)] = \text{Sign} [s'(x_0)]$ .

Proof: Differentiating with respect to  $\tau$  and inserting  $\lambda(\tau)$  into equation (4) results in the following:

$$\frac{d\lambda}{d\tau} [3\lambda^2 + 2P_1\lambda + Q_2 + ((Q_1\lambda^2 + Q_2\lambda + Q_3)(-\tau) + (2Q_1\lambda + Q_2))e^{-\lambda\tau}] = \lambda(Q_1\lambda^2 + Q_2\lambda + Q_3)e^{-\lambda\tau}$$

$$\text{Then } \left(\frac{d\lambda}{d\tau}\right)^{-1} = \frac{(3\lambda^2 + 2P_1\lambda + P_2)e^{\lambda\tau}}{\lambda(Q_1\lambda^2 + Q_2\lambda + Q_3)} + \frac{(2Q_1\lambda + Q_2)}{\lambda(Q_1\lambda^2 + Q_2\lambda + Q)} - \frac{\tau}{\lambda}$$

From equations (6) - (8):

$$\mu'(\tau_0) = \text{Re} \left[ \frac{(3\lambda^2 + 2P_1\lambda + P_2)e^{\lambda\tau}}{\lambda(Q_1\lambda^2 + Q_2\lambda + Q_3)} \right] + \text{Re} \left[ \frac{(2Q_1\lambda + Q_2)}{\lambda(Q_1\lambda^2 + Q_2\lambda + Q_3)} \right] = \frac{1}{\Delta} [3\omega_0^6 + 2u\omega_0^4 + v\omega_0^2]$$

Where  $\Delta = [(Q_3 - Q\omega^2)^2 + (Q_2\omega)^2]$ . In this case,  $\Delta > 0$  and  $\omega_0 > 0$ .

Consequently, it is proved that  $\text{Sign} [\psi'(\tau_0)] = \text{Sign} [s'(x_0)]$ .

### 3. Direction Analysis and Stability Analysis of The Hopf Bifurcation Solution

Assuming that  $y_1 = N - N^*, y_2 = B - B^*, y_3 = T - T^*$  and time scaling as well as normalising the delay  $\tau, t \rightarrow \frac{t}{\tau}$ , equation (1)–(3) become:

$$\frac{dy_1}{dt} = -\alpha_2 y_1 - \alpha_1 B^* y_1(t-1) - \alpha_1 y_1(t-1) y_2 - \alpha_3 T^* y_1 - \alpha_3 N^* y_3 - \alpha_3 y_1 y_3 \tag{15}$$

$$\frac{dy_2}{dt} = \frac{r}{k} y_2 - \beta_2 y_2 + \beta_1 N^* y_1(t-1) + \beta_1 y_1(t-1) y_2 \tag{16}$$

$$\frac{dy_3}{dt} = -\gamma_1 T^* y_1 - \gamma_1 N^* y_3 - \gamma_2 y_3 - \gamma_1 y_1 y_3 \tag{17}$$

Thus, work can be done in the phase  $C = C((-1, 0), R_+^3)$ . Without loss of generality, denote the critical value  $\tau_j$  by  $\tau_0$ . Let  $\tau = \tau_0 + \mu$ , then  $\mu = 0$  is a Hopf bifurcation value of the system given by equations (15)–(17). Rewrite this system as follows for notational simplicity:

$$y'(t) = L_\mu(y_t) + F(\mu, y_t) \tag{18}$$

Where  $y(t) = (y_1(t), y_2(t), y_3(t))^T \in R^3, y_t(\theta) \in C$  is defined by  $y_t(\theta) = y_t(t + \theta)$ , and

$L_\mu: C \rightarrow R, F: R \times C \rightarrow R$  are provided, respectively by

$$L_\mu \delta = (\tau_0 + \mu) \begin{bmatrix} -(\alpha_2 + \alpha_3 T^*) & 0 & -\alpha_3 N^* \\ 0 & -\left(\frac{r}{k} + \beta_2\right) & 0 \\ -\gamma_1 T^* & 0 & -(\gamma_1 N^* + \gamma_2) \end{bmatrix} \begin{bmatrix} \delta_1(0) \\ \delta_2(0) \\ \delta_3(0) \end{bmatrix} + (\tau_0 + \mu) \begin{bmatrix} -\alpha_1 B^* & 0 & 0 \\ -\beta_1 B^* & 0 & 0 \\ 0 & 0 & 0 \end{bmatrix} \begin{bmatrix} \delta(-1) \\ \delta(-2) \\ \delta(-3) \end{bmatrix}$$

and  $F(\mu, \delta) = (\tau_0 + \mu) \begin{bmatrix} F_1 \\ F_2 \\ F_3 \end{bmatrix}$  respectively where  $F_1 = -\alpha_1 \delta_1(-1) \delta_2(0)$ ,

$$F_2 = \beta_1 \delta_1(-1) \delta_2(0), F_3 = -\gamma_1 \delta_1(0) \delta_3(0),$$

$$\delta(\theta) = (\delta_1(\theta), \delta_2(\theta), \delta_3(\theta))^T \in C((-1, 0), R).$$

According to the Riesz theorem, a function  $\eta(\theta, \mu)$  is constrained variation for  $\theta \in [-1, 0]$ , such that  $L_\mu \delta = \int_{-1}^0 d\eta(\theta, 0) \delta(\theta)$  for  $\delta \in C$ .

Choose in reality.

$$\eta(\theta, \mu) = (\tau_0 + \mu) \begin{bmatrix} -(\alpha_2 + \alpha_3 T^*) & 0 & -\alpha_3 N^* \\ 0 & -\left(\frac{r}{k} + \beta_2\right) & 0 \\ -\gamma_1 T^* & 0 & -(\gamma_1 N^* + \gamma_2) \end{bmatrix} \delta(\theta) + (\tau_0 + \mu) \begin{bmatrix} -\alpha_1 B^* & 0 & 0 \\ -\beta_1 B^* & 0 & 0 \\ 0 & 0 & 0 \end{bmatrix} \delta(\theta + 1)$$

Here,  $\delta \in C([-1, 0], R_+^3)$  define

$$A(\mu) \delta = \begin{cases} \frac{d\delta(\theta)}{d\theta}, & \theta \in [-1, 0) \\ \int_{-1}^0 d\eta(\theta, 0) \delta(\theta), & \theta = 0. \end{cases} \quad \text{And} \quad R(\mu) \delta = \begin{cases} 0, & \theta \in [-1, 0) \\ F(\mu, \delta), & \theta = 0. \end{cases}$$

The equation (18) then corresponds to:

$$y'(t) = A(\mu) \delta + R(\mu) y_t \tag{19}$$

For  $\psi \in C^1([-1,0], R_+^3)$ , state

$$A^*\psi(h) = \begin{cases} -\frac{d\psi(h)}{ds}, & h \in [-1,0) \\ \int_{-1}^0 d\eta^T(-t,0)\psi(-t), & h = 0. \end{cases}$$

And bilinear inner product

$$\langle \psi(h), \delta(\theta) \rangle = \overline{\psi(0)}\delta(0) - \int_{-1}^0 \int_{\xi=\theta}^{\theta} \overline{\psi(\xi - \theta)}d\eta(\theta)\delta(\xi) d\xi \tag{20}$$

Since  $A^*$  and  $A = A(0)$  are adjoint operators, and  $i\omega_0$  are eigen values of  $A(0)$ , they are also eigen values of  $A^*$ . Assuming that  $q(\theta) = q(0)e^{i\omega_0\theta}$  is an eigen vector of  $A(0)$  corresponding to the eigen value  $i\omega_0$ . Then  $A(0) = i\omega_0 q(\theta)$ . When  $\theta = 0$ ,

$$[i\omega_0 I - \int_{-1}^0 d\eta(\theta)e^{i\omega_0\theta}] q(0) = 0, \text{ the outcome is } q(0) = (1, \sigma_1, \rho_1)^T$$

$$\sigma_1 = \frac{(\alpha_1 B^* + (\alpha_2 + \alpha_3 T^*) - i\omega_0)}{\alpha_3 N^*} \text{ and } \rho_1 = \frac{\beta_1 B^* \left( \frac{r}{k} + \beta_2 \right) - i\omega_0}{\left( \frac{r}{k} + \beta_2 \right)^2 + \omega_0^2}$$

Similarly, it can be confirmed that  $q^*(s) = D(1, \sigma_2, \rho_2)e^{i\omega_0\tau_0 s}$  is the eigen value of  $A^*$  that corresponds to  $-i\omega_0$ , where:

$$\sigma_1 = \frac{(\alpha_1 B^* + (\alpha_2 + \alpha_3 T^*) - i\omega_0)}{\alpha_3 N^*} \text{ and } \rho_1 = \frac{\beta_1 B^* \left( \frac{r}{k} + \beta_2 \right) - i\omega_0}{\left( \frac{r}{k} + \beta_2 \right)^2 + \omega_0^2}$$

To ensure  $\langle q^*(s), q(\theta) \rangle = 1$ , it is necessary to calculate the value of  $D$ .

From equation (22),  $\langle q^*(s), q(\theta) \rangle$

$$\begin{aligned} &= \overline{D}(1, \overline{\sigma_2}, \overline{\rho_2})(1, \sigma_1, \rho_1)^T - \int_{-1}^0 \int_{\xi=\theta}^{\theta} \overline{D}(1, \overline{\sigma_2}, \overline{\rho_2})e^{-i\omega_0\tau_0(\xi-\theta)}d\eta(\theta)(1, \sigma_1, \rho_1)^T e^{i\omega_0\tau_0\xi} d\xi \\ &= \overline{D} \left\{ 1 + \sigma_1 \overline{\sigma_2} + \rho_1 \overline{\rho_2} - \int_{-1}^0 (1, \overline{\sigma_2}, \overline{\rho_2}) \theta e^{i\omega_0\tau_0\theta} (1, \sigma_1, \rho_1)^T \right\} \\ &= \overline{D} \{ 1 + \sigma_1 \overline{\sigma_2} + \rho_1 \overline{\rho_2} + \tau_0 \overline{\sigma_2} W^* (\beta_1 \rho_1 - \alpha_1 \sigma_1) e^{i\omega_0\tau_0} \} \end{aligned}$$

$$\text{Hence, select } \overline{D} = \frac{1}{(1 + \sigma_1 \overline{\sigma_2} + \rho_1 \overline{\rho_2} + \tau_0 \overline{\sigma_2} W^* (\beta_1 \rho_1 - \alpha_1 \sigma_1) e^{i\omega_0\tau_0})}$$

This ensures that  $\langle q^*(s), q(\theta) \rangle = 1, \langle q^*(s), \overline{q(\theta)} \rangle = 0$ .

The coordinates characterising the centre manifold  $C_0$  at  $\mu = 0$  are computed by applying the algorithm described in [16] and using their notations. Assume  $y_t$  as a solution of equation (18) at  $\mu = 0$ . Therefore:

$$z(t) = \langle q^*(s), y_t(\theta) \rangle, W(t, \theta) = y_t(\theta) - 2Re(z(t)q(\theta)) \tag{21}$$

On the centre manifold  $C_0$ ,  $W(t, \theta) = W(z(t), \overline{z(t)}, \theta)$

$$\text{Where } W(z, \overline{z}, \theta) = W_{20}(\theta) \frac{z^2}{2} + W_{11}(\theta) z\overline{z} + W_{02}(\theta) \frac{\overline{z}^2}{2} + \dots$$

Local coordinates for the centre of the manifold  $C_0$  are  $z$  and  $\overline{z}$  towards  $q^*$  and  $\overline{q^*}$ . Consider that  $W$  is real if  $y_t$  is real. Only real solutions should be taken into consideration. For the solution  $y_t \in C_0$  of equation (20), since  $\mu = 0$ ,

$$\begin{aligned} z'(t) &= i\omega_0\tau_0 z + \langle \overline{q^*}(\theta), F(0, B(z, \overline{z}, \theta) + 2Re(z(t)q(\theta))) \rangle \\ &= i\omega_0\tau_0 z + \overline{q^*}(0) F(0, W(z, \overline{z}, 0) + 2Re(z(t)q(\theta))) \\ &\equiv i\omega_0\tau_0 z + \overline{q^*}(0) F_0(z, \overline{z}) \end{aligned}$$

Rewrite this equation as:

$$z'(t) = i\omega_0\tau_0 z(t) + g(z, \overline{z}) \tag{22}$$

$$\text{Where } g(z, \overline{z}) = \overline{q^*}(0) F_0(z, \overline{z}) = g_{20}(\theta) \frac{z^2}{2} + g_{11}(\theta) z\overline{z} + g_{02}(\theta) \frac{\overline{z}^2}{2} + g_{21}(\theta) \frac{z^2\overline{z}}{2} + \dots \tag{23}$$

As  $y_t(\theta) = (y_{1t}, y_{2t}, y_{3t}) = W(t, \theta) + z q(\theta) + \overline{z} \overline{q(\theta)}$  and  $q(0) = (1, \sigma_1, \rho_1)^T e^{i\omega_0\tau_0\theta}$ , so

$$\begin{aligned} y_{1t}(0) &= z + \overline{z} + W_{20}^{(1)}(0) \frac{z^2}{2} + W_{11}^{(1)}(0) z\overline{z} + W_{02}^{(1)}(0) \frac{\overline{z}^2}{2} + \dots, \\ y_{2t}(0) &= \sigma_1 z + \overline{\sigma_1} \overline{z} + W_{20}^{(2)}(0) \frac{z^2}{2} + W_{11}^{(2)}(0) z\overline{z} + W_{02}^{(2)}(0) \frac{\overline{z}^2}{2} + \dots, \\ y_{3t}(0) &= \rho_1 z + \overline{\rho_1} \overline{z} + W_{20}^{(3)}(0) \frac{z^2}{2} + W_{11}^{(3)}(0) z\overline{z} + W_{02}^{(3)}(0) \frac{\overline{z}^2}{2} + \dots, \end{aligned}$$

$$y_{1t}(-1) = ze^{-i\omega_0\tau_0} + \bar{z}e^{i\omega_0\tau_0} + W_{20}^{(1)}(-1)\frac{z^2}{2} + W_{11}^{(1)}(-1)z\bar{z} + W_{02}^{(1)}(-1)\frac{\bar{z}^2}{2} + \dots,$$

$$y_{2t}(-1) = \sigma_1 e^{-i\omega_0\tau_0 z} + \bar{\sigma}_1 e^{i\omega_0\tau_0 \bar{z}} + W_{20}^{(2)}(-1)\frac{z^2}{2} + W_{11}^{(2)}(-1)z\bar{z} + W_{02}^{(2)}(-1)\frac{\bar{z}^2}{2} + \dots,$$

Thus, comparing coefficients to equation (23) provides:

$$g_{20} = \bar{D}(1, \sigma_1, \rho_1)f_{z^2}, g_{02} = \bar{D}(1, \bar{\sigma}_1, \bar{\rho}_2)f_{\bar{z}^2},$$

$$g_{11} = \bar{D}(1, \bar{\sigma}_1, \bar{\rho}_2)f_{z\bar{z}}, g_{21} = \bar{D}(1, \bar{\sigma}_1, \bar{\rho}_2)f_{z^2\bar{z}}.$$

For clarification of  $g_{21}$ , computation must be the main focus of  $W_{20}(\theta)$  and  $W_{11}(\theta)$ . From equations (19) and (21):

$$W' = u_t' - z'q - \bar{z}'q = \begin{cases} AW - 2Re[\bar{q}^*(0)F_0q(\theta)], & \theta \in [-1, 0) \\ AW - 2Re[\bar{q}^*(0)F_0q(0)] + F_0, & \theta = 0 \end{cases}$$

Let  $W' = AW + H(z, \bar{z}, \theta)$  [24]

Where  $H(z, \bar{z}, \theta) = H_{20}(\theta)\frac{z^2}{2} + H_{11}(\theta)z\bar{z} + H_{02}(\theta)\frac{\bar{z}^2}{2} + H_{21}(\theta)\frac{z^2\bar{z}}{2} + \dots$  [25]

As opposed to that, on  $C_0$  at the origin  $W' = W_z z' + W_{\bar{z}} \bar{z}'$ .

The above series is expanded, the coefficients are calculated and the result is:

$$[A - 2i\omega_0 I]W_{20}(\theta) = -H_{20}(\theta), AW_{11}(\theta) = -H_{11}(\theta)$$
 [26]

By equation (22), for  $\theta \in [-1, 0]$ :

$$H(z, \bar{z}, \theta) = -\bar{q}^*(0)F_0q(\theta) - \bar{q}^*(0)F_0\bar{q}(\theta) = -gq(\theta) - \bar{g}\bar{q}(\theta)$$

Comparing the coefficients with (23) for  $\theta \in [-1, 0]$ :

$$H_{20}(\theta) = -g_{20}q(\theta) - \bar{g}_{02}\bar{q}(\theta), H_{11}(\theta) = -g_{11}q(\theta) - \bar{g}_{11}\bar{q}(\theta).$$

From equation (22), (25) and the definition of  $A$ , we obtained:

$$W_{20}(\theta) = 2i\omega_0\tau_0 W_{20}(\theta) + g_{20}q(\theta) + \bar{g}_{02}\bar{q}(\theta)$$

Solving for  $W_{20}(\theta)$ :

$$W_{20}(\theta) = \frac{ig_{20}}{\omega_0\tau_0}q(0)e^{i\omega_0\tau_0\theta} + \frac{i\bar{g}_{02}}{3\omega_0\tau_0}\bar{q}(0)e^{-i\omega_0\tau_0\theta} + E_1 e^{2i\omega_0\tau_0\theta},$$

and similarly

$$W_{11}(\theta) = \frac{-ig_{11}}{\omega_0\tau_0}q(0)e^{i\omega_0\tau_0\theta} + \frac{i\bar{g}_{11}}{\omega_0\tau_0}\bar{q}(0)e^{-i\omega_0\tau_0\theta} + E_2,$$

where  $E_1$  and  $E_2$  are both three dimensional vectors and can be determined by setting  $\theta = 0$  in  $H$ . In fact since  $H(z, \bar{z}, \theta) = -2Re[\bar{q}^*(0)F_0q(0)] + F_0$ , So

$$H_{20}(\theta) = -g_{20}q(\theta) - \bar{g}_{02}\bar{q}(\theta) + F_{z^2},$$

$$H_{11}(\theta) = -g_{11}q(\theta) - \bar{g}_{11}\bar{q}(\theta) + F_{z\bar{z}}$$

Where  $F_0 = F_{z^2}\frac{z^2}{2} + F_{z\bar{z}}z\bar{z} + F_{\bar{z}^2}\frac{\bar{z}^2}{2} + \dots$

Hence combining the definition of  $A$ ,

$$\int_{-1}^0 d\eta(\theta)W_{20}(\theta) = 2i\omega_0\tau_0 W_{20}(0) + g_{20}q(0) + \bar{g}_{02}\bar{q}(0) - F_{z^2} \text{ and}$$

$$\int_{-1}^0 d\eta(\theta)W_{11}(\theta) = g_{11}q(0) - \bar{g}_{11}\bar{q}(0) - F_{z\bar{z}}$$

Notice that

$$\left[ i\omega_0\tau_0 I - \int_{-1}^0 e^{i\omega_0\tau_0\theta} d\eta(\theta) \right] q(0) = 0 \text{ and } \left[ -i\omega_0\tau_0 I - \int_{-1}^0 e^{-i\omega_0\tau_0\theta} d\eta(\theta) \right] \bar{q}(0) = 0,$$

which implies

$$\left[ 2i\omega_0\tau_0 I - \int_{-1}^0 e^{2i\omega_0\tau_0\theta} d\eta(\theta) \right] E_1 = F_{z^2} \text{ and } - \left[ \int_{-1}^0 d\eta(\theta) \right] E_2 = F_{z\bar{z}}$$

Hence,

$$\begin{bmatrix} (2i\omega_0 + \alpha_2 + \alpha_3 T^* + \alpha_1 B^* e^{-2i\omega_0\tau_0}) & 0 & -\alpha_3 N^* \\ -\beta_1 W^* e^{-2i\omega_0\tau_0} & (2i\omega_0 + \frac{r}{K} + \beta_2) & 0 \\ \gamma_1 T^* & 0 & (2i\omega_0 + \gamma_1 N^* + \gamma_2) \end{bmatrix} E_1 = -2 \begin{bmatrix} \alpha_1 \sigma_1 e^{-i\omega_0\tau_0\theta} \\ \beta_1 \sigma_1 e^{-i\omega_0\tau_0\theta} \\ -\gamma_1 \rho_1 \end{bmatrix} \text{ and}$$

$$\begin{bmatrix} (\alpha_2 + \alpha_3 T^* + \alpha_1 B^*) & 0 & -\alpha_3 N^* \\ -\beta_1 W^* & (\frac{r}{K} + \beta_2) & 0 \\ \gamma_1 T^* & 0 & (\gamma_1 N^* + \gamma_2) \end{bmatrix} E_2 = -2 \begin{bmatrix} \alpha_1 Re\{\sigma_1\} e^{i\omega_0\tau_0\theta} \\ -\beta_1 Re\{\sigma_1\} e^{i\omega_0\tau_0\theta} \\ -\gamma_1 Re\{\rho_1\} \end{bmatrix}$$

Consequently, the parameters can express  $g_{21}$ .

Using the parameters, each  $g_{ij}$  can be determined based on the study mentioned above. Consequently, the following values can be calculated:

$$C_1(0) = \frac{i}{2\omega_0\tau_0} (g_{11}g_{20} - 2|g_{11}|^2 - \frac{|g_{02}|^2}{3}) + \frac{g_{21}}{2}, \mu_2 = -\frac{Re\{C_1(0)\}}{Re\{\lambda'(\tau_0)\}}, \beta_2 = 2Re\{C_1(0)\},$$

$$T_2 = -\frac{Im\{C_1(0)\} + \mu_2 Im\{\lambda'(\tau_0)\}}{\omega_0\tau_0}$$
 [27]

Theorem 2: The value of  $\mu_2$  can be determined by the direction of the Hopf bifurcation: if  $\mu_2 > 0$  ( $\mu_2 < 0$ ), then the Hopf bifurcation is supercritical (subcritical) and the bifurcating periodic solutions exists for  $\tau > \tau_0$  ( $\tau < \tau_0$ ). The value of  $\beta_2$  can determine the stability of bifurcating solutions: the bifurcating periodic solutions are orbitally asymptotically stable (unstable) if  $\beta_2 < 0$  ( $\beta_2 > 0$ ). The bifurcating periodic solutions is determined by the value of  $T_2$ : the period increases (decreases) if  $T_2 > 0$  ( $T_2 < 0$ ).

### 4. Numerical Stimulation

MATLAB simulation is used to numerically consolidate the analytical findings. The system behaves as follows:

$$N_o = 3.17, \alpha_1 = 0.22, \alpha_2 = 0.001, \alpha_3 = 0.0009, r = 1.89, \beta_1 = 0.2, \beta_2 = 0.001, T_o = 2.06, \gamma_1 = 0.06, \gamma_2 = 0.001$$

Figure 1 shows that when there is no delay parameter  $\tau$ , the system is stable. Plant nutrients concentration ( $N$ ), plant biomass ( $B$ ) and toxicity ( $T$ ) show no fluctuation in their natural growth. Figures 2 and 3 show that when the delay parameter  $\tau$  increased from 0 to 1.24, the system shows limit cycles or perturbation early on but finally stabilises; this is called asymptotically behaviour. Figures 4 and 5 show that when the delay parameter  $\tau$  crosses the critical value of 1.25, the limit cycle of same period and same direction continue together and Hopf bifurcation occurs.

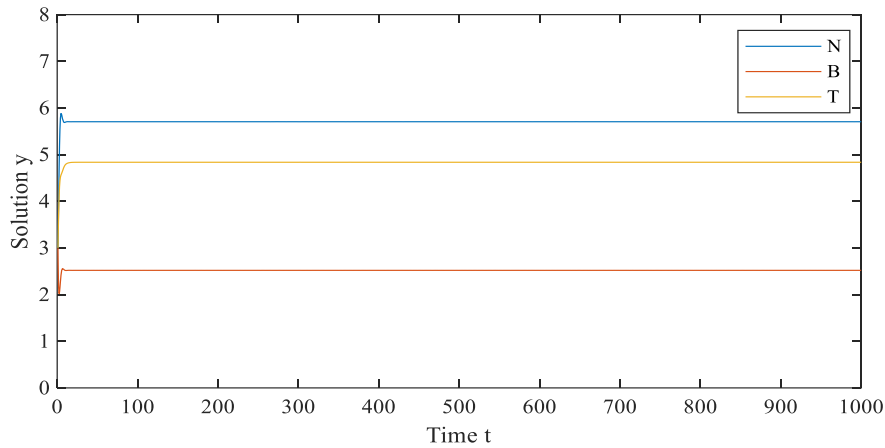


**Figure 1.** When there is absence of delay, i.e.  $\tau = 0$ , the system interior equilibrium point  $E_1$  is stable.

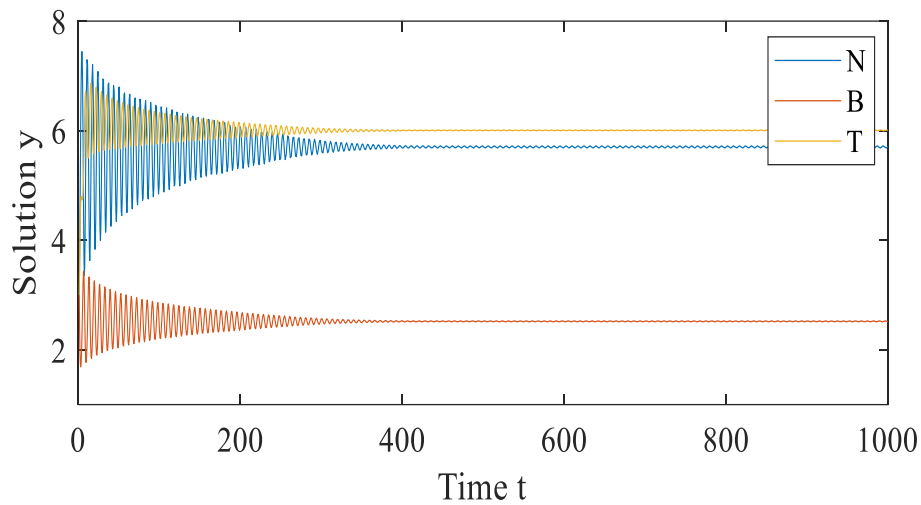


**Figure 2.** When there is delay, i.e.  $\tau < 1.25$ , the system interior equilibrium point  $E_1$  is asymptotically stable.

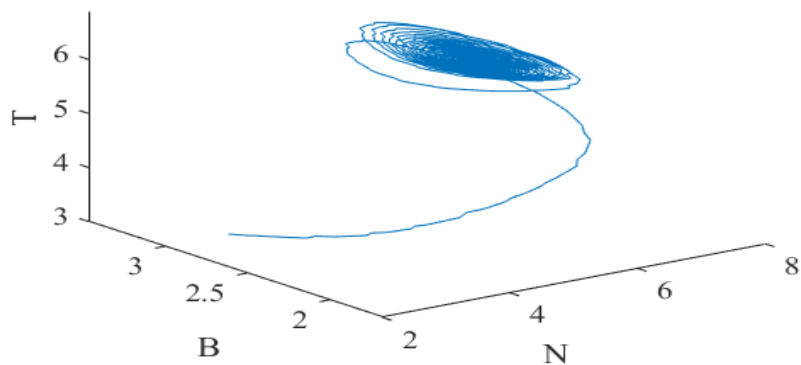


Figure 3. The phase space representation of toxicity ( $T$ ), plant biomass ( $B$ ) and nutrients ( $N$ ) with a delay of  $\tau < 1.25$ .

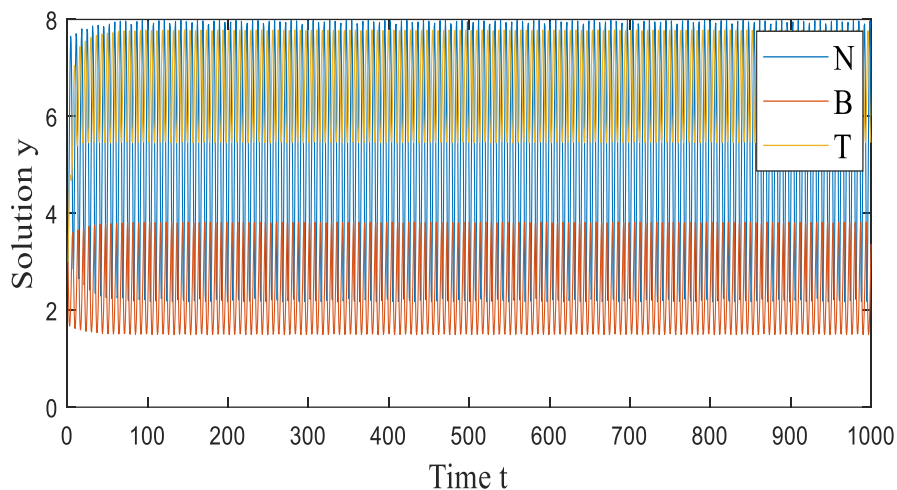


Figure 4. When there is delay, i.e.  $\tau > 1.25$ , the system's interior equilibrium point  $E_1$  loses its stability and shows Hopf bifurcation.

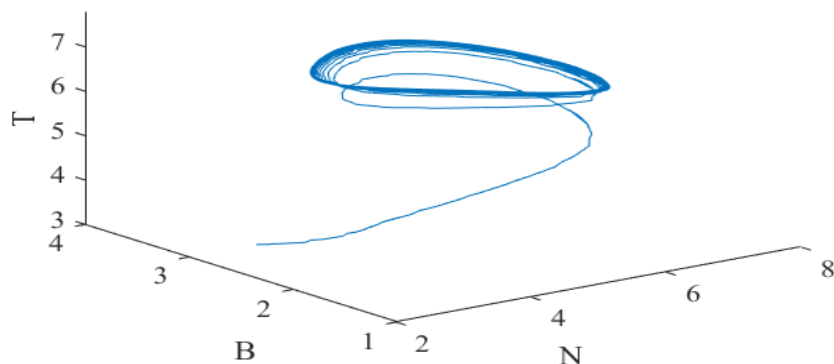


Figure 5. The phase space representation of toxicity ( $T$ ), plant biomass ( $B$ ) and nutrients ( $N$ ) with a delay of  $\tau > 1.25$ . Asymptotically and orbitally stable is the bifurcating periodic solution.

**Sensitivity Analysis**

The model has constant parameters in this study. To calculate the global sensitivity coefficient, the 'Direct Method' is utilised. For each parameter the partial derivatives of the solution can be found, may be all that is required for sensitivity analysis in this situation if all of the parameters ( $\alpha_1, \alpha_2, \alpha_3, \beta_1, \beta_2, \gamma_1, \gamma_2$ ) present in the system (1)–(3) are assumed to be constants. Taking derivative partially of the solution ( $N, B$  and  $T$ ) in relation to the  $\beta_1$ , the set of sensitivity equations shown below are produced.

$$\frac{dS_1}{dt} = -\alpha_1 N(t - \tau)S_2 - \alpha_1 BS_1(t - \tau) - \alpha_2 S_1 + \alpha_3 NS_3 - \alpha_3 TS_1 \tag{28}$$

$$\frac{dS_2}{dt} = -\frac{r}{k} S_2 + \beta_1 N(t - \tau)S_2 - \beta_1 BS_1(t - \tau) - \beta_2 S_2 \tag{29}$$

$$\frac{dS_3}{dt} = -\gamma_1 NS_3 - \gamma_1 TS_1 - \gamma_2 S_3 \tag{30}$$

Here  $S_1 = \frac{\partial N}{\partial \beta_1}, S_2 = \frac{\partial B}{\partial \beta_1}, S_3 = \frac{\partial T}{\partial \beta_1}$

The nutrient concentration becomes unstable when  $\beta_1 = 0.2$  and Hopf bifurcation occurs. But when the utilisation coefficient declines from  $\beta_1 = 0.2$  to  $\beta_1 = 0.18$ , the graph becomes asymptotically stable, and it exhibits stability at  $\beta_1 = 0.12$  as shown in Figure 6. Similarly, as  $\beta_1$  drops from  $\beta_1 = 0.2$  to  $\beta_1 = 0.12$ , as shown in Figures 8 and 9, the amount of plant biomass produced and the toxicity decreases respectively.

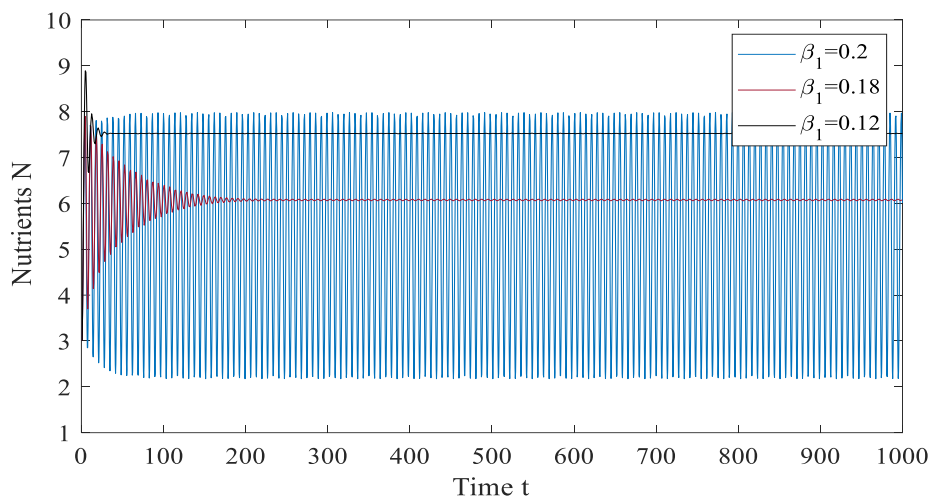


**Figure 6.** For various values of the utilisation coefficient  $\beta_1$ , a time series graph shows the relationship between small variations in nutrients concentration  $N$ .

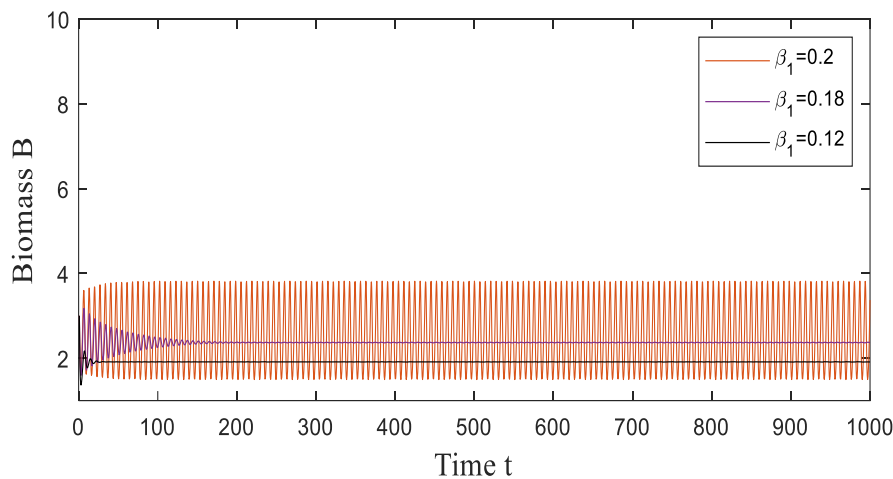


**Figure 7.** For various values of the utilisation coefficient  $\beta_1$ , time series graph shows the relationship between small variations in biomass  $B$

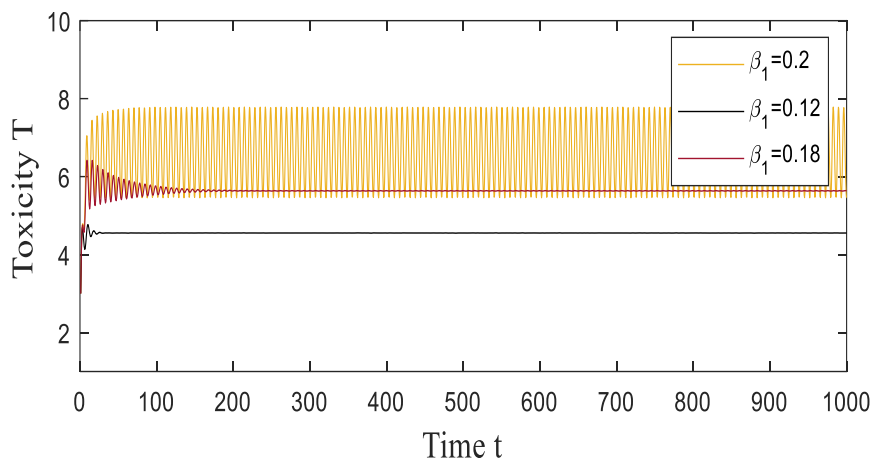


**Figure 8.** For various values of the utilisation coefficient  $\beta_1$ , a time series graph shows the relationship between small variations in toxic metal  $T$ .

## 5. Conclusion

In this paper, we investigated the impact of delay on the dynamics of plant growth when toxic metals are present. Stable equilibrium, Hopf bifurcation, periodic oscillations, sensitivity analysis, directional analysis and other dynamic phenomena are all seen. Based on some numerical simulations, we draw the conclusion that for some parameter values, the stability and Hopf bifurcation about interior equilibrium  $E^*$  can occur. It has been verified that interior equilibrium  $E^*$  is stable in the absence of a delay (Figure 1). For a critical value below ( $\tau \leq 1.25$ ) of the parameter delay, the system was asymptotically stable (Figures 2 and 3). The proposed model became unstable and showed oscillations when  $\tau \geq 1.25$  (Figures 4 and 5). It was concluded that after taking time lag into account, limit cycles are observed for interior equilibrium points when time delay exceeds a certain critical value. For state variables at the interior equilibrium with respect to the system parameters, sensitivity indices were calculated in the mathematical model (1)–(3). The 'direct method' was used to evaluate sensitivity of state variables by changing the parameter  $\beta_1$  included in delay differential systems (28)–(30). Analysis of sensitivity demonstrate that the state variable  $N, B$  and  $T$  significantly change their rate of oscillations for various values of the parameter  $\beta_1$ . Figures 6–8 depict this phenomenon of sensitivity graphically.

## 6. References

- A. Lacointe, "Carbon allocation among tree organs: A review of basic processes and representation in functional-structural tree models," 2000.
- A. Overman, "A memoir on mathematical models of crop growth and yield: Effect of geographic location," *Univ. Florida*.
- A. R. Watkinson, "Density-dependence in single-species populations of plants," *J. Theor. Biol.*, vol. 83, no. 2, 1980, doi: 10.1016/0022-5193(80)90297-0.
- B. Ingalls, M. Mincheva, and M. R. Roussel, "Parametric Sensitivity Analysis of Oscillatory Delay Systems with an Application to Gene Regulation," *Bull. Math. Biol.*, vol. 79, no. 7, 2017, doi: 10.1007/s11538-017-0298-x.
- C. Sun, M. Han, and Y. Lin, "Analysis of stability and Hopf bifurcation for a delayed logistic equation," *Chaos, Solitons and Fractals*, vol. 31, no. 3, 2007, doi: 10.1016/j.chaos.2005.10.019.
- D. H. Hardy, J. Myers and C. Stokes, *Heavy metals in North Carolina soils : occurrence & significance*. N.C. Department of Agriculture and Consumer Services, Agronomic Division.
- D. Kaur and P. Kumar, "Bifurcation induced by delay parameter in plant growth dynamics," *J. Phys. Conf. Ser.*, vol. 2267, 2022.
- D. Sharsma, S. Sundar and R. Naresh, "Modelling the effect of toxicant on plant biomass with time delay," *Int. J. non linear Sci.*, vol. 17, pp. 254–267, 2014.
- Dipesh and P. Kumar, "Effect of time delay on dynamic of plant competition under allelopathy," *Math. Method Appl. Sci.*, vol. 45, pp.9308–9321, 2022.
- F. A. Rihan, "Sensitivity analysis for dynamics systems with time-lags," *J. Comput. Appl. Math.*, vol. 151, no. 2, 2003, doi: 10.1016/S0377-0427(02)00659-3.
- G. A. Bocharov and F. A. Rihan, "Numerical modelling in biosciences using delay differential equations," *J. Comput. Appl. Math.*, vol. 125, no. 1–2, 2000, doi: 10.1016/S0377-0427(00)00468-4.

- G. Deleo, L. Delfuria, and M. Gatto, "The interaction between soil acidity and forest dynamics: A simple-model exhibiting catastrophic behavior," *Theor. Popul. Biol.*, vol. 43, no. 1, 1993, doi: 10.1006/tpbi.1993.1002.
- G. Ladas and C. Qian, "Oscillation and global stability in a delay logistic equation," *Dyn. Stab. Syst.*, vol. 9, no. 2, 1994, doi: 10.1080/02681119408806174.
- H. T. Banks, D. Robbins, and K. L. Sutton, "Generalized sensitivity analysis for delay differential equations," in *International Series of Numerical Mathematics*, vol. 164, 2013. doi: 10.1007/978-3-0348-0631-2\_2.
- J. B. Shukla, A. Agarwal, P. Sinha and B. Dubey, "Modelling Effects of Primary and Secondary Toxicant on Renewable Resources," *Nat. Resour. Model.*, vol. 16, pp. 99–120, 2008.
- K. R. Schneider, "Hassard, B. D. / Kazarinoff, N. D. / Wan, Y.-H., Theory and Applications of Hopf Bifurcation. London Mathematical Society Lecture Note Series 41. Cambridge, Cambridge University Press 1981. 320 S., £ 15.00 A P/B. ISBN 0-521-23158-2," *ZAMM - Zeitschrift für Angew. Math. und Mech.*, vol. 62, no. 12, 1982, doi: 10.1002/zamm.19820621221.
- O. P. Misra and P. Kalra, "Effect of toxic metal on the structural dry weight of a plant: A Model," *Int. J. Biomath.*, vol. 6, no. 5, 2013, doi: 10.1142/S1793524513500289.
- O. P. Misra and P. Kalra, "Modelling Effect of Toxic Metal on the Individual Plant Growth: A Two Compartment Model," *Am. J. Comput. Appl. Math.*, vol. 2, no. 6, 2013, doi: 10.5923/j.ajcam.20120206.06.
- S. Trvedi and L. Erdei, "Effects of cadmium and lead on the accumulation of Ca<sup>2+</sup> and K<sup>+</sup> and on the influx and translocation of K<sup>+</sup> in wheat of low and high K<sup>+</sup> status," *Physiol. Plant.*, vol. 84, no. 1, 1992, doi: 10.1111/j.1399-3054.1992.tb08770.x.
- S. Ruan and J. Wei, "IMA Journal of Mathematics Applications in Medical Biology," *IMA J. Math. Appl. Med. Biol.* 1841-52 (2001)., vol. 18, pp. 41–52, 2001.
- S. H. Saker and I. Kubiacyk, "Oscillation and stability in nonlinear delay differential equations of population dynamics," *Math. Comput. Model.*, vol 35, pp. 298–301, 2002.
- T. J. H. M, "Mathematical Models in Plant Physiology. A Quantitative Approach to Problems in Plant and Crop Physiology.," *Acad. Press. London*, 1976.

# A COMPARATIVE STUDY OF A CLASS OF LINEAR AND NONLINEAR PANTOGRAPH DIFFERENTIAL EQUATIONS VIA DIFFERENT ORTHOGONAL POLYNOMIAL WAVELETS

Ashish Rayal<sup>1a\*</sup>, Prerak A Patel<sup>2b</sup>, Shailendra Giri<sup>3c</sup>, Pawan Joshi<sup>4d</sup>

**Abstract:** We propose a wavelet approach on different orthogonal polynomials for solving linear and nonlinear pantograph equations with stretch kind. The pantograph differential equation is a unique proportional delay functional differential equation class. It has been used to deal with numerous physics, mathematics, and engineering applications, such as quantum mechanics, control systems, electrodynamics, and number theory. This scheme is based on constructing the operational matrix for integration via different wavelets with their collocation nodes. This study aims to examine the numerical dynamics of the pantograph equation under stretch kind through different orthogonal polynomial wavelets. Illustrative examples are presented to highlight the flexibility of this scheme, and comparisons are made between the mentioned scheme and other existing schemes using tables and graphs. These numerical results correctly predict the applicability and effectiveness of the mentioned scheme.

**Keywords:** Pantograph differential equation, muntz wavelets, chebyshev wavelets of different kinds, operational matrix, collocation nodes.

## 1. Introduction

In variant mathematical modeling, delay differential equations (DEs) are key in solving various problems. Moreover, delay DEs are also used extensively in a distinct range of real-world situations such as economy, physiological and pharmaceutical kinetics, population dynamics, infectious diseases, chemical kinetics, epidemiology, ship navigational control, hydraulic network, etc. (Fox, 1971; Driver, 1977; Baker et al., 1995). Pantograph equation is a unique and special time delay DE that arises in several branches of applied and pure mathematics like number theory, quantum mechanics, dynamic systems, electrodynamics, control system, probability, and many more (Drfel and Iserles, 1997; Saadatmandi and Dehghan, 2009; Yusufoglu, 2010). In particular, Ockendon and Tayler (1971) and Tayler (1986) formulated this equation to describe how electricity is gathered through the pantograph of electrical locomotive. Figure 1 shows the pantograph model.

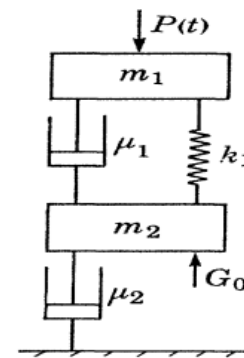


Figure 1. Pantograph Model (Ockendon and Tayler, 1971)

In this manuscript, we handle pantograph differential equation of stretch kind (PDESK) of the following form:

$$\frac{d}{dt}y(t) = g(y(\lambda t), y(t), t), \quad 0 < \lambda \in \mathbb{R} < 1, \quad t \in [0,1],$$

with the condition

$$y(0) = r_0,$$

where  $r_0$  is the real constant, and  $\lambda$  is a stretched argument. The given problem is an initial value problem. In general form, we can write the above problem as

$$G\left(\frac{d}{dt}y(t), y(\lambda t), y(t), t\right) = 0, \quad (1)$$

with the condition

$$y(0) = r_0, \quad (2)$$

### Authors information:

<sup>a</sup>Department of Mathematics, School of Applied and Life Sciences, Uttarakhand University, Dehradun, 248007, Uttarakhand, INDIA. E-mail: ashish1989rayal@gmail.com<sup>1</sup>

<sup>b</sup>Gujarat Power Engineering & Research Institute, Gujarat Technological University, Mehsana, Gujarat, INDIA. E-mail: patelprerak111@gmail.com<sup>2</sup>

<sup>c</sup>Department of Mathematics, Education Department, Govt of Uttarakhand, Pauri Garhwal-246001, INDIA. E-mail: shailly7777@gmail.com<sup>3</sup>

<sup>d</sup>Department of Applied Sciences, Shivalik college of Engineering, Dehradun-248197, INDIA. E-mail: pawan.joshi@sce.org.in<sup>4</sup>

\*Corresponding Author: ashish1989rayal@gmail.com

Received: January 16, 2023

Accepted: July 13, 2023

Published: June 30, 2024

Various numerical approaches are based on existing orthogonal functions to solve the pantograph DEs. An overview of these approaches can be analyzed in the following studies: Sezer and Dascioglu (2007), Alomari et al. (2009), Yalcinbas et al. (2011), Sedaghat et al. (2012), Anakira et al. (2013), Tohidi et al. (2013), Yalcinbas et al. (2013), Bahsi and Cevik (2015), Jayadi et al. (2016), Yang (2018), Wang et al. (2019), Jafari et al. (2021), and Asma et al. (2022). In this study, we are interested in solving the PDESK defined in Eqs. (1-2) using wavelets based on different orthogonal functions.

In recent years, wavelets have become a growing and new area in physics, engineering, and mathematics. Wavelet analysis is a robust mathematical concept broadly used in image processing, signal processing, quantum field theory, numerical analysis, and several others (Daubechies, 1988; Mallat, 2018). Today, most physics models are analyzed through wavelet approaches. Due to the better precision of wavelets over other techniques, many researchers in different fields are interested in wavelets-based approaches (Raya and Verma, 2020a; Raya and Verma, 2020b; Raya and Verma, 2020c; Raya and Verma, 2022; Raya et al., 2022; Raya, 2023a; Raya et al., 2023b). The most popular related techniques are the Legendre wavelets method (Hafshejani et al., 2011), Laguerre wavelets method (Shiralashetti et al., 2016), Hermite wavelets scheme (Saeed and Rehman,

2014), Bernoulli wavelets scheme (Rahimkhani et al., 2016), Gegenbauer wavelets method (Muhammad et al., 2017), Mamadu-Njoseh wavelets scheme (Raya et al., 202, and Muntz wavelets scheme (Raya, 2023d).

This study aims to compute the continuous approximate solutions of the PDESK defined in Eq. (1) using different orthogonal polynomial wavelets. An approximation scheme is introduced based on different orthogonal polynomial wavelets with integral operational matrix (IOM) and collocation grids to solve PDESK. The scheme converts the problems into simultaneous algebraic equations by expressing an unknown function  $y(t)$  in a truncated wavelet series. The wavelet characteristics, collocation technique, and integral operational matrix are utilized to evaluate  $y(t)$  in the given problem.

This manuscript is framed as follows: Section 2 introduces different orthogonal polynomial wavelets. Section 3 describes the function approximation through wavelets series. Section 4 explains the IOM for different wavelets. Section 5 proposes an approximate scheme for solving the problem. Section 6 estimates the errors to check the accuracy of the mentioned scheme. Section 7 contains examples of predicting the efficiency and precision of the proposed technique. Section 8 summarizes this study.

## 2. Orthogonal Polynomial Wavelets

This section defines the wavelets based on different orthogonal polynomials.

### Muntz Wavelets

The definition of Muntz wavelets (MWs) on  $[0,1]$  for  $\gamma \in (0,1)$  is as follows (Bahmanpour, 2018):

$$\psi_{n,m}(t) = \begin{cases} \sqrt{\frac{1}{2} + m\gamma} 2^{\frac{k}{2}} P_m(2^{k-1}t - (n-1), \gamma), & \frac{n-1}{2^{k-1}} \leq t < \frac{n}{2^{k-1}}, \\ 0, & \text{elsewhere} \end{cases}$$

where  $n = 0,1,2,3, \dots, M-1$ ,  $n = 1,2,3, \dots, 2^{k-1}$ ,  $k, M$  are natural numbers. The term  $\sqrt{\frac{1}{2} + m\gamma}$  is employed for normality and  $P_m(t)$  represents the Muntz functions of degree  $m$  that are orthogonal, corresponding to the unit weighted function  $w(t)$  on  $[0,1]$  and is represented in the following form:

$$P_m(t, \gamma) = \sum_{k=0}^m c_{m,k} t^{\gamma k},$$

where

$$c_{m,k} = \frac{(-1)^{m-k}}{\gamma^m k! (m-k)!} \prod_{i=0}^{m-1} ((k+i)\gamma + 1).$$

The MWs set is orthogonal under the weighted function,  $w_n(t) = w(2^{k-1}t - n + 1)$ .

### Chebyshev Wavelets of The First Kind

The first kind of Chebyshev wavelets (CWs) have the arguments  $\psi(n, m, k, t)$ , in which  $n = 1,2,3, \dots, 2^k$ ,  $m = 0,1,2, \dots, M-1$  is the order for first Chebyshev functions,  $k \in \mathbb{N}$  and  $t$  represents the normalized time.

The definition of the CWs on  $[0,1]$  is provided as (Tavassoli, 2009):

$$\psi_{n,m}(t) = \begin{cases} \frac{\alpha_m}{\sqrt{\pi}} 2^{\frac{k}{2}} T_m(2^{k+1}t - (2n - 1)), & \frac{n-1}{2^k} \leq t < \frac{n}{2^k}, \\ 0, & \text{elsewhere} \end{cases}$$

where

$$\alpha_m = \begin{cases} \sqrt{2} & m = 0 \\ 2 & m = 1, 2, 3, \dots \end{cases}$$

Here, coefficient  $\alpha_m/\sqrt{\pi}$  is employed for orthonormality and  $T_m(t)$  is the first kind of Chebyshev function of degree  $m$  that is orthogonal under the weighted function  $w(t) = 1/\sqrt{1-t^2}$  on  $[-1,1]$  and has the following iterative relation:

$$\begin{aligned} T_0(t) &= 1, \\ T_1(t) &= t, \\ T_{m+1}(t) &= 2t T_m(t) - T_{m-1}(t), \quad m = 1, 2, \dots \end{aligned}$$

The set of CWs is orthogonal under the weighted function,  $w_n(t) = w(2^{k+1}t - 2n + 1)$ .

### Chebyshev Wavelets of the Second Kind

The second kind of Chebyshev wavelets (SCWs) have the arguments  $\psi(n, m, k, t)$  in which  $n = 1, 2, 3, \dots, 2^{k-1}$ ,  $m = 0, 1, 2, 3, \dots, M - 1$  is the order for the second Chebyshev functions,  $k \in \mathbb{N}$  and  $t$  represents the normalized time.

The definition of SCWs on  $[0,1]$  is provided as (Zhu and Wang, 2013):

$$\psi_{n,m}(t) = \begin{cases} \frac{2}{\sqrt{\pi}} 2^{\frac{k}{2}} U_m(2^k t - 2n + 1), & \frac{n-1}{2^{k-1}} \leq t < \frac{n}{2^{k-1}}, \\ 0, & \text{elsewhere} \end{cases}$$

Here, the term  $\sqrt{2/\pi}$  is employed for normality and  $U_m(t)$  is the second kind of Chebyshev function of degree  $m$  that is orthogonal under the weighted function  $w(t) = \sqrt{1-t^2}$  on  $[-1,1]$  and has the following iterative relation:

$$\begin{aligned} U_0(t) &= 1, \\ U_1(t) &= 2t, \\ U_{m+1}(t) &= 2t U_m(t) - U_{m-1}(t), \quad m = 1, 2, 3, \dots \end{aligned}$$

The set of SCWs is orthogonal under the weighted function.  $w_n(t) = w(2^k t - 2n + 1)$ .

### Chebyshev Wavelets of the Third Kind

The third kind of Chebyshev wavelets (TCWs) have the arguments  $\psi(n, m, k, t)$  in which  $n = 1, 2, 3, \dots, 2^{k-1}$ ,  $m = 0, 1, 2, 3, \dots, M - 1$  is the order for the third kind Chebyshev functions,  $k \in \mathbb{N}$  and  $t$  represents the normalized time.

The definition of TCWs on  $[0,1]$  is provided as (Polat, 2019):

$$\psi_{n,m}(t) = \begin{cases} \frac{1}{\sqrt{\pi}} 2^{\frac{k}{2}} V_m(2^k t - 2n + 1), & \frac{n-1}{2^{k-1}} \leq t < \frac{n}{2^{k-1}}, \\ 0, & \text{elsewhere} \end{cases}$$

Here, the coefficient  $\sqrt{1/\pi}$  is used for normality and  $V_m(t)$  is the third Chebyshev function of degree  $m$  that is orthogonal under the weighted function  $w(t) = \frac{\sqrt{1+t}}{\sqrt{1-t}}$  on  $[-1,1]$  and has the following iterative relation:

$$\begin{aligned} V_0(t) &= 1, \\ V_1(t) &= 2t - 1, \\ V_{m+1}(t) &= 2t V_m(t) - V_{m-1}(t), \quad m = 1, 2, 3, \dots \end{aligned}$$

The set of TCWs is orthogonal under the weighted function,  $w_n(t) = w(2^k t - 2n + 1)$ .

### Chebyshev Wavelets of the Fourth Kind

The fourth kind of Chebyshev wavelets (FCWs) have the arguments  $\psi(n, m, k, t)$  in which  $n = 1, 2, 3, \dots, 2^{k-1}$ ,  $m = 0, 1, 2, 3, \dots, M - 1$  is the order for the fourth kind Chebyshev functions,  $k \in \mathbb{N}$  and  $t$  represents the normalized time.

The definition of FCWs on  $[0,1]$  is as follows (Azodi and Yaghouti, 2018):

$$\psi_{n,m}(t) = \begin{cases} \frac{1}{\sqrt{\pi}} 2^{\frac{k}{2}} W_m(2^k t - (2n - 1)), & \frac{n-1}{2^{k-1}} \leq t < \frac{n}{2^{k-1}}, \\ 0, & \text{elsewhere} \end{cases}$$

Here, the coefficient  $1/\sqrt{\pi}$  is used for normality and  $W_m(t)$  is the fourth Chebyshev function of degree  $m$  that is orthogonal under the weighted function  $w(t) = \sqrt{\frac{1-t}{1+t}}$  on  $[-1,1]$  and has the following iterative relation:

$$\begin{aligned} W_0(t) &= 1, \\ W_1(t) &= 2t + 1, \\ W_{m+1}(t) &= 2t W_m(t) - W_{m-1}(t), \quad m = 1, 2, 3, \dots \end{aligned}$$

The set of CWs is orthogonal under the weighted function,  $w_n(t) = w(2^k t - 2n + 1)$ .

Now, the wavelet function approximation is described in the successive sections using the considered wavelet basis functions.

### 3. Function Approximation

A function  $h(t)$  on  $[0,1]$  can be approximated via considered wavelets as

$$h(t) \approx \sum_{n=1}^{\infty} \sum_{m=0}^{\infty} e_{n,m} \psi_{n,m}(t), \tag{3}$$

where  $e_{n,m}$  are computed by

$$e_{n,m} = \langle h(t), \psi_{n,m} \rangle_{w_n(t)} = \int_0^1 h(t) \psi_{n,m}(t) w_n(t) dt$$

Here, the notation  $\langle \cdot, \cdot \rangle$  describes the inner product in  $L^2[0,1]$  with the weighted function  $w_n(t)$ . The truncated form of Eq. (3) is rewritten as:

$$h(t) \approx \sum_{n=1}^{2^{k-1}} \sum_{m=0}^{M-1} e_{n,m} \psi_{n,m}(t) = E^T \Psi(t) = \Psi^T(t) E, \tag{4}$$

where  $E$  and  $\Psi(t)$  are provided by

$$\begin{aligned} E &= [e_{1,0}, \dots, e_{1,(M-1)}, e_{2,0}, \dots, e_{2,(M-1)}, \dots, e_{2^{k-1},0}, \dots, e_{2^{k-1},(M-1)}]^T \\ &= [e_1, e_2, \dots, e_{\hat{m}}]^T, \end{aligned} \tag{5}$$

$$\begin{aligned} \Psi(t) &= \begin{bmatrix} \psi_{1,0}(t), \dots, \psi_{1,(M-1)}(t), \psi_{2,0}(t), \dots, \psi_{2,(M-1)}(t), \dots, \\ \psi_{2^{k-1},0}(t), \dots, \psi_{2^{k-1},(M-1)}(t) \end{bmatrix}^T \\ &= [\psi_1, \psi_2, \dots, \psi_{\hat{m}}]^T. \end{aligned} \tag{6}$$

Here,  $\hat{m} = 2^{k-1}M$  denotes the total considered wavelets basis, but in the case of the first kind of Chebyshev wavelets  $\hat{m} = 2^k M$ .

### 4. Integral Operational Matrix for Orthogonal Polynomial Wavelets

This section provides the IOM  $P_{\hat{m} \times \hat{m}}$  for different wavelets that play an important part in the PDESK solution. This operational matrix is employed to transform the given model to the algebraic system of equations in terms of wavelet coefficient. By applying the IOM, a large unknown coefficient vector does not occur when computing the numerical approximation of a linear and nonlinear PDESK class. Consequently, the calculations are made simple, resulting in better solution accuracy. In general,

$$\int_0^t \Psi(t) dt \approx P_{\hat{m} \times \hat{m}} \Psi(t), \tag{7}$$

where  $\Psi(t)$  is provided in Eq. (6) and  $P_{\hat{m} \times \hat{m}}$  is the IOM determined by

$$P_{\hat{m} \times \hat{m}} = \langle g_{\hat{m} \times 1}(t), \Psi_{\hat{m} \times 1}^T(t) \rangle_{w_n(t)},$$

where

$$g_{\hat{m} \times 1}(t) = \int_0^t \Psi(t) dt$$

and the notation  $\langle . . \rangle$  represents the inner product in  $L^2[0,1]$  under the weighted function  $w_n(t)$ .

Using Eq. (7), construct the following IOM for different wavelets:

- (a) The IOM of the Muntz wavelets ( $\gamma = 0.5, k = 1, M = 8$ ):

$$(P_{8 \times 8})_{MWS} = \begin{bmatrix} \frac{1}{2} & \frac{\sqrt{2}}{5} & \frac{1}{10\sqrt{3}} & 0 & 0 & 0 & 0 & 0 \\ -\frac{\sqrt{2}}{5} & 0 & \frac{\sqrt{2}}{7\sqrt{3}} & \frac{\sqrt{2}}{35} & 0 & 0 & 0 & 0 \\ -\frac{1}{10\sqrt{3}} & -\frac{\sqrt{2}}{7\sqrt{3}} & 0 & \frac{2}{15\sqrt{3}} & \frac{\sqrt{5}}{42\sqrt{3}} & 0 & 0 & 0 \\ 0 & -\frac{\sqrt{2}}{35} & -\frac{2}{15\sqrt{3}} & 0 & \frac{2\sqrt{5}}{77} & \frac{\sqrt{2}}{33\sqrt{3}} & 0 & 0 \\ 0 & 0 & -\frac{\sqrt{5}}{42\sqrt{3}} & -\frac{2\sqrt{5}}{77} & 0 & \frac{\sqrt{10}}{39\sqrt{3}} & \frac{\sqrt{35}}{286} & 0 \\ 0 & 0 & 0 & -\frac{\sqrt{2}}{33\sqrt{3}} & -\frac{\sqrt{10}}{39\sqrt{3}} & 0 & \frac{\sqrt{14}}{55\sqrt{3}} & \frac{2}{65\sqrt{3}} \\ 0 & 0 & 0 & 0 & -\frac{\sqrt{35}}{286} & -\frac{\sqrt{14}}{55\sqrt{3}} & 0 & \frac{2\sqrt{14}}{221} \\ 0 & 0 & 0 & 0 & 0 & -\frac{2}{65\sqrt{3}} & -\frac{2\sqrt{14}}{221} & 0 \end{bmatrix};$$

(b) The IOM of the first kind of Chebyshev wavelets ( $k = 0, M = 8$ ):

$$(\mathbf{P}_{8 \times 8})_{\text{CWS}} = \begin{bmatrix} \frac{1}{2} & \frac{1}{2\sqrt{2}} & 0 & 0 & 0 & 0 & 0 & 0 \\ -\frac{1}{4\sqrt{2}} & 0 & \frac{1}{8} & 0 & 0 & 0 & 0 & 0 \\ -\frac{1}{3\sqrt{2}} & -\frac{1}{4} & 0 & \frac{1}{12} & 0 & 0 & 0 & 0 \\ \frac{1}{8\sqrt{2}} & 0 & -\frac{1}{8} & 0 & \frac{1}{16} & 0 & 0 & 0 \\ -\frac{1}{15\sqrt{2}} & 0 & 0 & -\frac{1}{12} & 0 & \frac{1}{20} & 0 & 0 \\ \frac{1}{24\sqrt{2}} & 0 & 0 & 0 & -\frac{1}{16} & 0 & \frac{1}{24} & 0 \\ -\frac{1}{35\sqrt{2}} & 0 & 0 & 0 & 0 & -\frac{1}{20} & 0 & \frac{1}{28} \\ \frac{1}{48\sqrt{2}} & 0 & 0 & 0 & 0 & 0 & -\frac{1}{24} & 0 \end{bmatrix};$$

(c) The IOM of second kind Chebyshev wavelets ( $k = 1, M = 8$ ):

$$(\mathbf{P}_{8 \times 8})_{\text{SCWS}} = \begin{bmatrix} \frac{1}{2} & \frac{1}{4} & 0 & 0 & 0 & 0 & 0 & 0 \\ -\frac{3}{8} & 0 & \frac{1}{8} & 0 & 0 & 0 & 0 & 0 \\ \frac{1}{6} & -\frac{1}{12} & 0 & \frac{1}{12} & 0 & 0 & 0 & 0 \\ -\frac{1}{8} & 0 & -\frac{1}{16} & 0 & \frac{1}{16} & 0 & 0 & 0 \\ \frac{1}{10} & 0 & 0 & -\frac{1}{20} & 0 & \frac{1}{20} & 0 & 0 \\ -\frac{1}{12} & 0 & 0 & 0 & -\frac{1}{24} & 0 & \frac{1}{24} & 0 \\ \frac{1}{14} & 0 & 0 & 0 & 0 & -\frac{1}{28} & 0 & \frac{1}{28} \\ -\frac{1}{16} & 0 & 0 & 0 & 0 & 0 & -\frac{1}{32} & 0 \end{bmatrix};$$

(d) The IOM of third kind Chebyshev wavelets ( $k = 1, M = 8$ ):

$$(\mathbf{P}_{8 \times 8})_{\text{TCWs}} = \begin{bmatrix} \frac{3}{4} & \frac{1}{4} & 0 & 0 & 0 & 0 & 0 & 0 \\ -1 & -\frac{1}{8} & \frac{1}{8} & 0 & 0 & 0 & 0 & 0 \\ \frac{5}{12} & -\frac{1}{8} & -\frac{1}{24} & \frac{1}{12} & 0 & 0 & 0 & 0 \\ -\frac{7}{24} & 0 & -\frac{1}{12} & -\frac{1}{48} & \frac{1}{16} & 0 & 0 & 0 \\ \frac{9}{10} & 0 & 0 & -\frac{1}{16} & -\frac{1}{80} & \frac{1}{20} & 0 & 0 \\ -\frac{11}{60} & 0 & 0 & 0 & -\frac{1}{20} & -\frac{1}{120} & \frac{1}{24} & 0 \\ \frac{13}{84} & 0 & 0 & 0 & 0 & -\frac{1}{24} & -\frac{1}{168} & \frac{1}{28} \\ -\frac{15}{112} & 0 & 0 & 0 & 0 & 0 & -\frac{1}{28} & -\frac{1}{224} \end{bmatrix};$$

(e) The IOM of fourth kind Chebyshev wavelets ( $k = 1, M = 8$ ):

$$(\mathbf{P}_{8 \times 8})_{\text{FCWs}} = \begin{bmatrix} \frac{1}{4} & \frac{1}{4} & 0 & 0 & 0 & 0 & 0 & 0 \\ 0 & \frac{1}{8} & \frac{1}{8} & 0 & 0 & 0 & 0 & 0 \\ -\frac{1}{12} & -\frac{1}{8} & \frac{1}{24} & \frac{1}{12} & 0 & 0 & 0 & 0 \\ \frac{1}{24} & 0 & -\frac{1}{12} & \frac{1}{48} & \frac{1}{16} & 0 & 0 & 0 \\ -\frac{1}{40} & 0 & 0 & -\frac{1}{16} & \frac{1}{80} & \frac{1}{20} & 0 & 0 \\ \frac{1}{60} & 0 & 0 & 0 & -\frac{1}{20} & \frac{1}{120} & \frac{1}{24} & 0 \\ -\frac{1}{84} & 0 & 0 & 0 & 0 & -\frac{1}{24} & \frac{1}{168} & \frac{1}{28} \\ \frac{1}{112} & 0 & 0 & 0 & 0 & 0 & -\frac{1}{28} & \frac{1}{224} \end{bmatrix};$$

The next section explores the numerical PDESK solutions.

### 5. Formulation of the Method

This section presents an approximate method based on orthogonal polynomial wavelets. The procedure of applying the method to a given problem is as follows.

Take the model equation from Eqs. (1-2) and expand the function,  $\frac{d}{dt}y(t)$  via truncated series of wavelets over the interval [0,1] as

$$\frac{d}{dt}y(t) \approx E^T \Psi(t), \tag{8}$$

where  $E$  and  $\Psi(t)$  are provided in Eqs. (5) and (6) respectively. By integrating Eq. (8) from 0 to  $t$ , we get

$$y(t) \approx E^T \int_0^t \Psi(t) dt + y(0) = E^T P_{\hat{m} \times \hat{m}} \Psi(t),$$

where  $P_{\hat{m} \times \hat{m}}$  is the IOM of wavelets given in Eq. (7). After simplification, we obtain

$$\begin{aligned} y(t) &\approx E^T P_{\hat{m} \times \hat{m}} \Psi(t) + y(0) \\ &= E^T P_{\hat{m} \times \hat{m}} \Psi(t) + r_0 \\ &= E^T P_{\hat{m} \times \hat{m}} \Psi(t) + d^T \Psi(t) \\ &= (E^T P_{\hat{m} \times \hat{m}} + d^T) \Psi(t) = y_{\hat{m}}(t), \end{aligned} \tag{9}$$

where vector  $d$  is chosen as:

$$d^T \Psi(t) = r_0. \tag{10}$$

By using an approximation form of function  $y(t)$  given in Eq. (9), we obtain  $y(\lambda t)$  as

$$y(\lambda t) \approx (E^T P_{\hat{m} \times \hat{m}} + d^T) \Psi(\lambda t), \tag{11}$$

where  $\Psi(\lambda t)$  is a stretched wavelets function. Using Eqs. (8-10) into Eq. (1), we obtain:

$$G(E^T \Psi(t), (E^T P_{\hat{m} \times \hat{m}} + d^T) \Psi(\lambda t), (E^T P_{\hat{m} \times \hat{m}} + d^T) \Psi(t), t) = 0. \tag{12}$$

Now, collocating the obtained system at the appropriate grids  $t_i$ :

$$G(E^T \Psi(t_i), (E^T P_{\hat{m} \times \hat{m}} + d^T) \Psi(\lambda t_i), (E^T P_{\hat{m} \times \hat{m}} + d^T) \Psi(t_i), t_i) = 0, \tag{13}$$

where

$$t_i = \frac{2i - 1}{2^k M}, \quad i = 1, 2, \dots, 2^{k-1} M. \tag{14}$$

The resultant algebraic set in Eq. (13) can be evaluated properly for wavelet coefficients  $E$ . Finally, the solution  $y_{\hat{m}}(t)$  of the given problem is achieved through the inclusion of estimated coefficient  $E$  into Eq. (9) as  $y_{\hat{m}}(t) = (E^T P_{\hat{m} \times \hat{m}} + d^T) \Psi(t)$ .

Figure 2 displays the flowchart for implementing the constructed scheme.

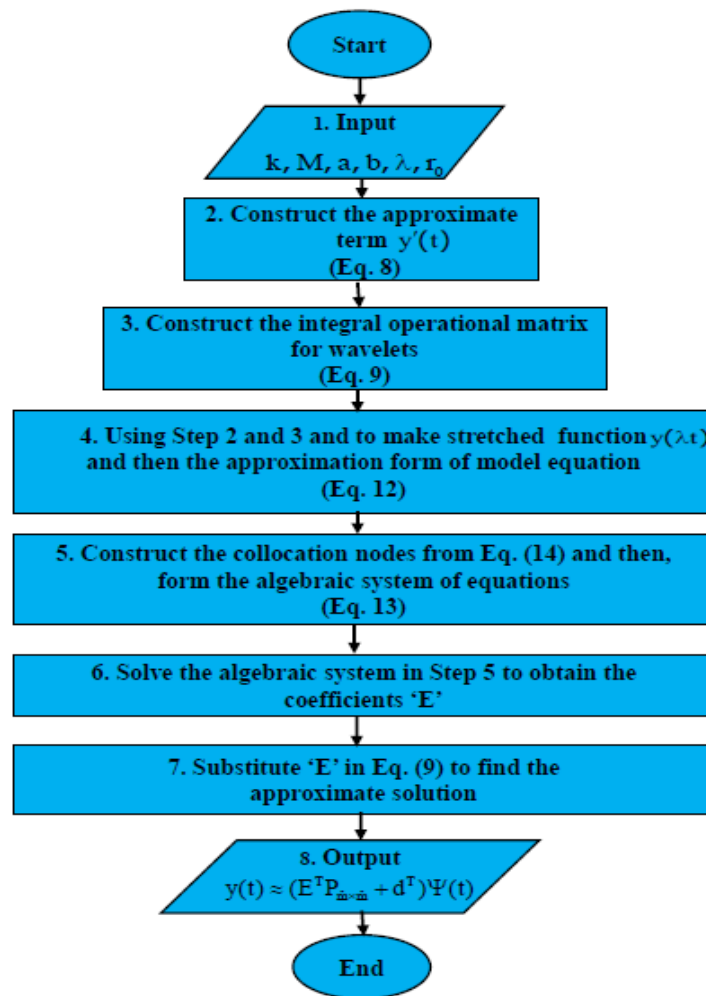


Figure 2. Flowchart for implementing the constructed scheme

### 6. Error Estimation of Solution

This section provides the convergence formulae to analyze the errors in the computation results. To investigate the accuracy of the proposed method, we define the error formulae as:

(a) Let  $y_{\hat{m}}(t)$  be the estimate solution to  $y(t)$  of Eqs. (1-2). Then  $E_{Abs}(t)$  at  $t \in [0,1]$  is calculated as

$$E_{Abs}(t) = |y(t) - y_{\hat{m}}(t)|,$$

where  $y(t)$  is the analytical solution of the considered model.

(b)  $L_{\infty}$ , the maximum absolute error is computed by

$$L_{\infty} = \max_{t \in [0,1]} |E_{Abs}(t)|$$

(c) The  $L^2$  norm consecutive error ( $\mathcal{C}. \mathcal{E}$ ) is computed by

$$\mathcal{C}. \mathcal{E} = \|y_{\hat{m}+1}(t) - y_{\hat{m}}(t)\|_2, \quad t \in [0,1]. \tag{15}$$

(d) The reliability of the results and accuracy of the scheme can be checked through residual error function in the absence of an exact solution of the proposed model as:

$$E_{\hat{m}}(t) = \left| \frac{d}{dt} y_{\hat{m}}(t) - g(y_{\hat{m}}(\lambda t), y_{\hat{m}}(t), t) \right|, \quad t \in [0,1]$$

If  $E_{\hat{m}}(t) \rightarrow 0$  for  $\hat{m}$ , then the error decreases.

### 7. Method Implementation

This section implements the constructed scheme with MWs, CWs, SCWs, TCWs, and FCWs to solve PDESK, and the approximated outputs obtained are compared with the corresponding available analytical solution. The  $L^2$  norm consecutive errors and absolute errors demonstrate the accuracy of the constructed scheme. The proposed method is easy to implement, but the computational cost may be complex. All numerical outputs are computed using Mathematica.

**Example 1.**

Consider the PDESK (Bellen & Zennaro, 2003) as:

$$\frac{d}{dt}y(t) = y(0.5t), \quad 0 \leq t \leq 1,$$

with the condition

$$y(0) = 1$$

The closed-form solution of the considered example is provided (Bellen & Zennaro, 2003):

$$y(t) = \sum_{j=0}^{\infty} \frac{1}{j!} (2)^{\frac{j(1-j)}{2}} t^j.$$

We solve the above example for  $\hat{m} = 8$  using the scheme introduced in Section 5. The wavelet coefficient vector of  $y(t)$  can be determined as:

$$\begin{aligned}
 y_{MWs}(t) &= 1.0 + 0.0000109285\sqrt{t} + 0.99986t + 0.000833015t^{1.5} + 0.24731t^2 \\
 &\quad + 0.0049748t^{2.5} + 0.0155824t^3 + 0.00292117t^{3.5}. \\
 y_{CWs}(t) &= 1.0 + t + 0.25t^2 + 0.0208333t^3 + 0.000651042t^4 + 8.13802 \times 10^{-6}t^5 \\
 &\quad + 4.23849 \times 10^{-8}t^6 + 9.49902 \times 10^{-11}t^7. \\
 y_{SCWs}(t) &= 1.0 + t + 0.25t^2 + 0.0208333t^3 + 0.000651042t^4 + 8.13802 \times 10^{-6}t^5 \\
 &\quad + 4.2385 \times 10^{-8}t^6 + 9.4948 \times 10^{-11}t^7. \\
 y_{TCWs}(t) &= 1.0 + t + 0.25t^2 + 0.0208333t^3 + 0.000651042t^4 + 8.13802 \times 10^{-6}t^5 \\
 &\quad + 4.23847 \times 10^{-8}t^6 + 9.50405 \times 10^{-11}t^7. \\
 y_{FCWs}(t) &= 1.0 + t + 0.25t^2 + 0.0208333t^3 + 0.000651042t^4 + 8.13802 \times 10^{-6}t^5 \\
 &\quad + 4.23854 \times 10^{-8}t^6 + 9.48487 \times 10^{-11}t^7.
 \end{aligned}$$

Figures 3 and 4 display the achieved solutions and corresponding errors via different wavelets. Tables 1 and 2 present the approximate wavelet solutions through different wavelets with an exact solution and the Legendre wavelets method (LWM) (Hafshejani et al., 2011). One may observe from the tables and figures that the wavelet solutions converge faster to the analytical result. The error decreases more rapidly when the number of basic functions increases. Table 3 shows the  $L^2$  norm consecutive error for the order of approximation  $\hat{m} = 7,8$ . Table 3 confirms that the error decreases with the increase of the order of approximation  $\hat{m}$ , which shows the accuracy of the described scheme. The  $L^2$  norm consecutive error is calculated for the first time in this study using Eq. (15).

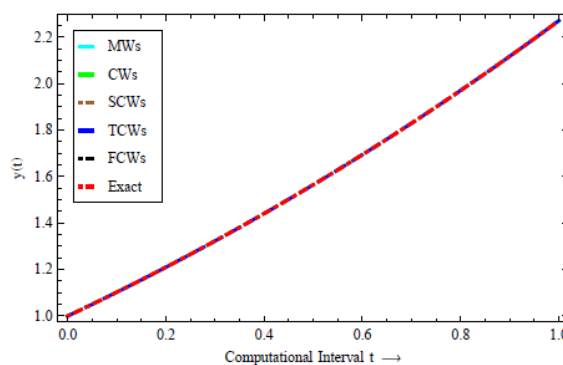


**Figure 3.** The behavior of the estimated solutions for different wavelets with  $\hat{m} = 8$  in Example 1

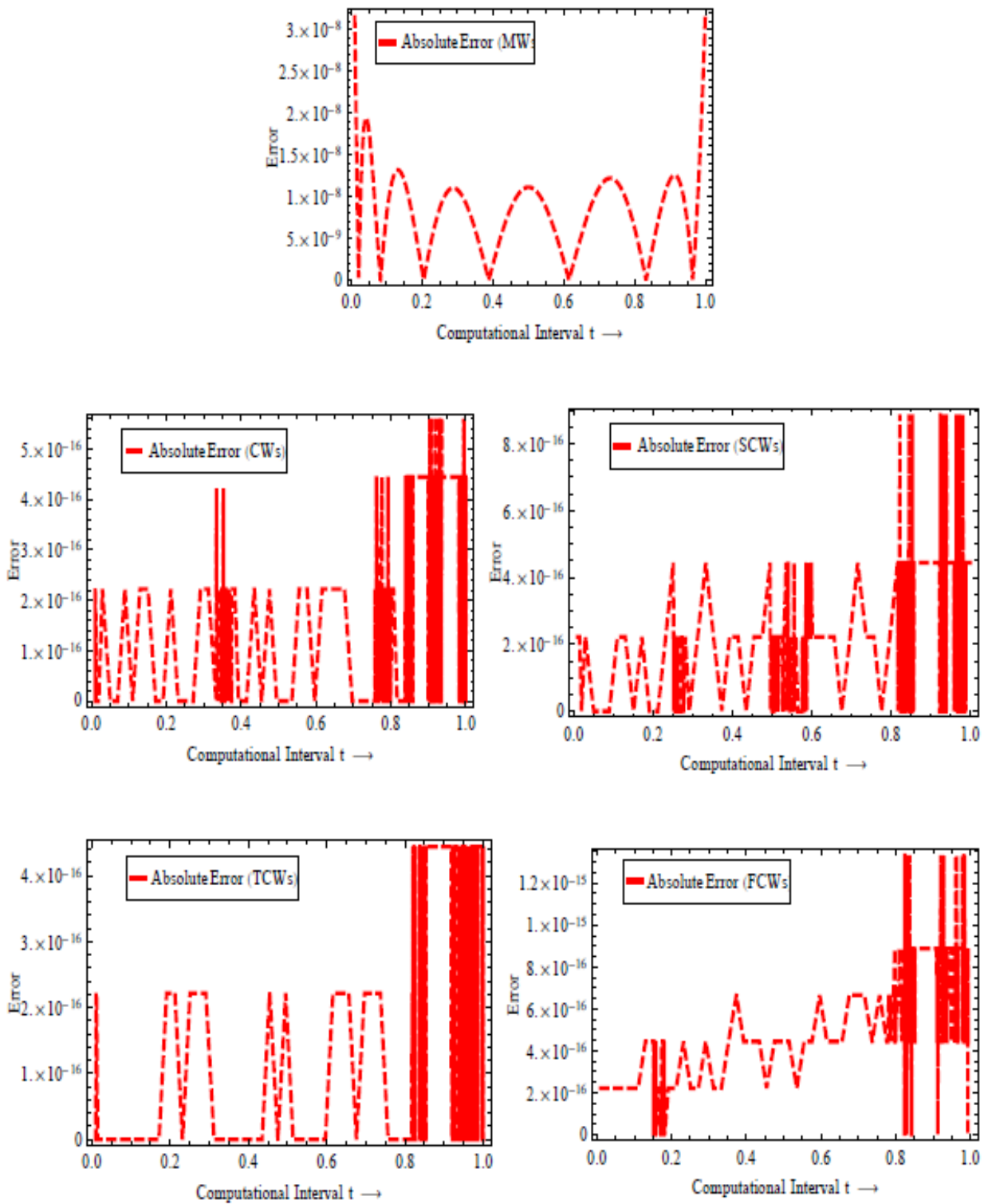


Figure 4. Absolute errors of the solutions via different wavelets with  $\hat{m} = 8$  in Example 1

**Table 1.** Computed values of  $y(t)$  via the constructed approach compared to Example 1

t	LWs (Hafshejani et al., 2011), $\hat{m} = 18$	Present Method (MWs), $\hat{m} = 8$	Exact Solution
0.000	0.999999999999999	0.999999725312605	1.000000000000000
0.125	1.12894709929840	1.128947112205302	1.1289470992984005
0.250	1.26595307192248	1.265953063336836	1.2659530719224836
0.375	1.41126781788344	1.411267815667616	1.4112678178834435
0.500	1.56514511174700	1.565145122864885	1.5651451117469977
0.625	1.72784263272750	1.727842631181262	1.7278426327275054
0.750	1.89962199489918	1.899621983149178	1.8996219948991855
0.875	2.08074877752466	2.080748786130356	2.0807487775246620
1.000	2.27149255550106	2.271492523809371	2.2714925555010614

**Table 2.** Approximated values of  $y(t)$  via constructed scheme in Example 1

t	Present method (CWs), $\hat{m} = 8$	Present method (SCWs), $\hat{m} = 8$	Present method (TCWs), $\hat{m} = 8$	Present method (FCWs), $\hat{m} = 8$
0.000	1.000000000000000	1.000000000000000	0.999999999999999	1.000000000000000
0.125	1.1289470992984003	1.1289470992984005	1.1289470992984005	1.1289470992984003
0.250	1.2659530719224834	1.2659530719224836	1.2659530719224836	1.2659530719224834
0.375	1.4112678178834435	1.4112678178834437	1.4112678178834435	1.4112678178834432
0.500	1.5651451117469974	1.5651451117469979	1.5651451117469979	1.5651451117469972
0.625	1.7278426327275052	1.7278426327275054	1.7278426327275054	1.7278426327275047
0.750	1.8996219948991855	1.8996219948991860	1.8996219948991855	1.8996219948991848
0.875	2.0807487775246620	2.0807487775246620	2.0807487775246620	2.0807487775246614
1.000	2.2714925555010614	2.2714925555010620	2.2714925555010614	2.2714925555010610

**Table 3.** Efficiency of the constructed method in the terms of  $L^2$  norm consecutive error via different wavelets in Example 1

$\hat{m}$	MWs	CWs	SCWs	TCWs	FCWs
7	$5.86 \times 10^{-6}$	$1.49 \times 10^{-11}$	$1.50 \times 10^{-11}$	$2.12 \times 10^{-11}$	$2.03 \times 10^{-11}$
8	$1.61 \times 10^{-7}$	$8.25 \times 10^{-15}$	$8.30 \times 10^{-15}$	$1.18 \times 10^{-14}$	$1.16 \times 10^{-14}$

**Example 2**

Consider the linear PDESK (Yalcinbas, 2011; Bahsi & Cevik, 2015) as:

$$\frac{d}{dt}y(t) = -y(0.8t) - y(t), \quad 0 \leq t \leq 1,$$

with the condition

$$y(0) = 1.$$

There is no analytical solution to this problem. We treat this example for  $\hat{m} = 8$  by using the scheme introduced in Section 5 and the wavelets series solution of  $y(t)$  can be achieved as:

$$y_{MWS}(t) = 1.00007 - 0.0028539\sqrt{t} - 1.96514t - 0.193559t^{1.5} + 2.3507t^2 - 0.78919t^{2.5} - 0.59084t^3 + 0.29353t^{3.5}.$$

$$y_{CWS}(t) = 1 - 2t + 1.79997t^2 - 0.983756t^3 + 0.370964t^4 - 0.10267t^5 + 0.0204596t^6 - 0.00229864t^7.$$

$$y_{SCWS}(t) = 1 - 2t + 1.79996t^2 - 0.983709t^3 + 0.370873t^4 - 0.102583t^5 + 0.0204227t^6 - 0.00229449t^7.$$

$$y_{TCWS}(t) = 1 - 2t + 1.79994t^2 - 0.9836t^3 + 0.370581t^4 - 0.102167t^5 + 0.0201234t^6 - 0.00220884t^7.$$

$$y_{FCWS}(t) = 1 - 2t + 1.79998t^2 - 0.983827t^3 + 0.371189t^4 - 0.103032t^5 + 0.0207461t^6 - 0.00238706t^7.$$

As mentioned above, we do not know the analytical solution to the given problem. Therefore, we estimate the solutions in Table 4 and observe a convergence. A comparison of Table 4 with the solutions achieved through several schemes is displayed in Table 5 (Tohidi et al., 2013; Yalcinbas et al., 2015; Yang, 2018; Yuzbas et al., 2014; Bahsi & Cevik, 2015; Yalcinbas et al., 2011; Sezer & Akyuz-Dascioglu, 2007). The calculated approximate solutions and corresponding absolute errors are displayed in Figures 5 and 6, respectively. Table 6 shows the  $L^2$  norm consecutive error for the order of approximation  $\hat{m} = 7,8$ , which clearly shows the accuracy of the constructed approach. The numerical results of the suggested method are consistent.

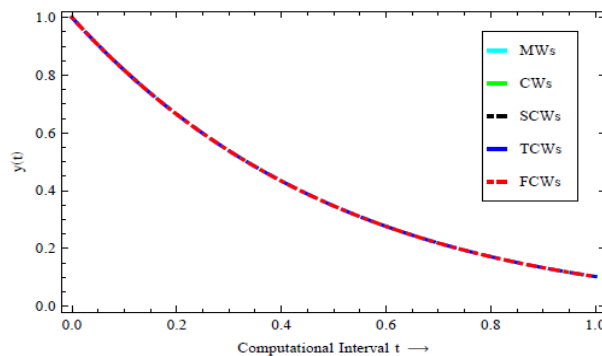


Figure 5. The behavior of the approximate wavelet solutions for different wavelets with  $\hat{m} = 8$  in Example 2

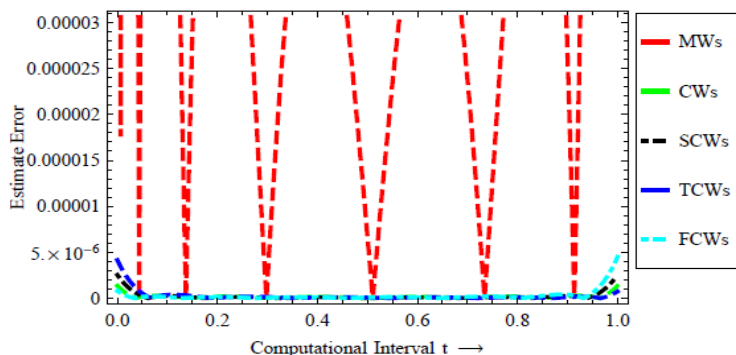


Figure 6. Estimate absolute errors of the solutions through different wavelets with  $\hat{m} = 8$  in Example 2

Table 4. Approximated values of  $y(t)$  with  $\hat{m} = 8$  using the proposed scheme in Example 2

t	Present Method (MWs)	Present method (FCWs)	Present method (TCWs)	Present method (SCWs)	Present method (CWs)
0.0	1.0000737941	0.9999999944	0.9999999133	0.9999999523	0.9999999893
0.2	0.6646904337	0.6646910015	0.6646909898	0.6646909954	0.6646909970
0.4	0.4335604608	0.4335607737	0.4335607859	0.4335607800	0.4335607781
0.6	0.2764814550	0.2764823377	0.2764823264	0.2764823318	0.2764823311
0.8	0.1714859287	0.1714840995	0.1714841125	0.1714841063	0.1714841076
1.0	0.1026802165	0.1026700336	0.1026701212	0.1026700791	0.1026701151

**Table 5.** Approximated values of  $y(t)$  using different schemes for comparison in Example 2

t	Bernoulli method (Tohidi et al., 2013), $\hat{m} = 7$	Bernstein method (Yalcinbas et al. 2015), $\hat{m} = 11$	Chebyshev method (Yang, 2018), $\hat{m} = 7$	Laguerre method (Yuzbas et al., 2014), $\hat{m} = 9$	PIA (1,1) (Bahsi, & Cevik, 2015)	Hermite method (Yalcinbas et al., 2011), $\hat{m} = 9$	Taylor method (Sezer & Akyuz-Dascioglu, 2007), $\hat{m} = 12$
0.0	1.0000000	1.00000000	1.00000000	1.0000000	1.0000000	1.000000	1.000000
0.2	0.6646905	0.66469100	0.66469101	0.6646910	0.6646910	0.664691	0.664691
0.4	0.4335605	0.43356077	0.43356077	0.4335607	0.4335607	0.433561	0.433561
0.6	0.2764822	0.27648233	0.27648233	0.2764831	0.2764823	0.276482	0.276482
0.8	0.1714836	0.17148411	0.17148412	0.1714942	0.1714841	0.171484	0.171484
1.0	0.1026832	0.10267012	0.10267013	0.1027437	0.1026701	0.102670	0.102670

**Table 6.** Efficiency of the constructed method in terms of  $L^2$  norm consecutive error using different wavelets in Example 2

$\hat{m}$	MWs	CWs	SCWs	TCWs	FCWs
7	$1.10 \times 10^{-4}$	$4.39 \times 10^{-6}$	$4.13 \times 10^{-6}$	$5.33 \times 10^{-6}$	$6.31 \times 10^{-6}$
8	$1.61 \times 10^{-5}$	$2.01 \times 10^{-7}$	$1.95 \times 10^{-7}$	$2.56 \times 10^{-7}$	$2.93 \times 10^{-7}$

**Example 3**

Consider the PDESK as

$$\frac{d}{dt}y(t) = 0.95y(t) - y(0.99t), \quad 0 \leq t \leq 1,$$

with the initial condition

$$y(0) = 1.$$

There is no analytical solution to this problem. We solve it by considering the example for  $\hat{m} = 8$  using the scheme introduced in Section 5. Because we do not know the analytical solution to the given problem, we show the accuracy of the described scheme by evaluating the residual error function. Table 7 shows the estimated numerical solutions via different wavelets, showing smooth convergence. Figure 7 plots the approximated solutions obtained for  $\hat{m} = 8$ . Figure 8 shows the graphical representation of the estimated errors in terms of residual function via different wavelets. Figure 7 shows that the approximated solution of the considered example decreases as  $t$  increases from 0 to 1. Table 8 exhibits the  $L^2$  norm consecutive error for  $\hat{m} = 7,8$ . Table 8 confirms that the error decreases rapidly with increasing order of approximation,  $\hat{m}$ , which clearly shows the effectiveness of the constructed scheme.

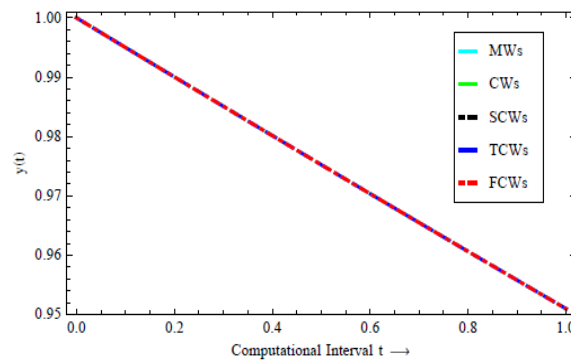


**Figure 7.** The behavior of the approximate solutions for different wavelets with  $\hat{m} = 8$  in Example 3

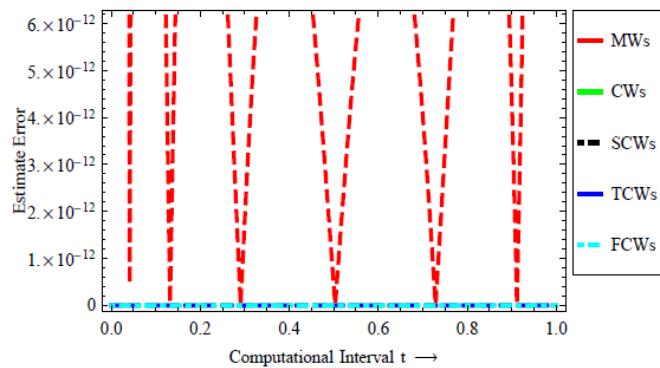


**Figure 8.** Error functions of the solutions using different wavelets with  $\hat{m} = 8$  in Example 3

**Table 7.** Approximated values of  $y(t)$  using the proposed scheme in Example 3

t	Present Method (MWs), $\hat{m} = 8$	Present method (CWs), $\hat{m} = 8$	Present method (SCWs), $\hat{m} = 8$	Present method (TCWs), $\hat{m} = 8$	Present method (FCWs), $\hat{m} = 8$
0.0	0.9999999999816	0.9999999999999	1.0000000000000	1.0000000000000	0.9999999999999
0.2	0.9900399198148	0.9900399198147	0.9900399198147	0.9900399198147	0.9900399198147
0.4	0.9801593591690	0.9801593591690	0.9801593591690	0.9801593591690	0.9801593591690
0.6	0.9703578393905	0.9703578393904	0.9703578393904	0.9703578393904	0.9703578393904
0.8	0.9606348837531	0.9606348837534	0.9606348837534	0.9606348837534	0.9606348837534
1.0	0.9509900174734	0.9509900174754	0.9509900174754	0.9509900174754	0.9509900174754

**Table 8.** Efficiency of the constructed method in terms of  $L^2$ , norm consecutive error using different wavelets in Example 3.

$\hat{m}$	MWs	CWs	SCWs	TCWs	FCWs
7	$2.11 \times 10^{-9}$	$2.62 \times 10^{-16}$	$2.36 \times 10^{-17}$	$2.73 \times 10^{-17}$	$1.60 \times 10^{-16}$
8	$1.17 \times 10^{-11}$	$2.16 \times 10^{-16}$	$3.30 \times 10^{-18}$	$1.33 \times 10^{-17}$	$3.11 \times 10^{-18}$

**Example 4.**

Consider the nonlinear PDESK (Hafshejani et al., 2011; Anakira et al., 2013) as

$$\frac{d}{dt}y(t) = 1 - 2y^2\left(\frac{t}{2}\right), \quad 0 \leq t \leq 1,$$

with the condition

$$y(0) = 0.$$

The analytical solution to the example is provided as follows:

$$y(t) = \sin(t).$$

We treat this example for  $\hat{m} = 8$  using the procedure given in Section 5. Figure 9 plots the approximate solutions obtained using different wavelets for  $\hat{m} = 8$ . Table 9 displays the estimated absolute errors using different wavelets to compare the method (Hafshejani et al., 2011). Table 10 gives the maximum absolute error for  $\hat{m} = 6, 7, 8$ . The maximum absolute errors to the same problem are  $1.2 \times 10^{-6}$ ,  $4.0 \times 10^{-8}$ ,  $9.99 \times 10^{-10}$ , and  $1.2 \times 10^{-7}$  (for 3 iteration), respectively (Alomari et al., 2009; Anakira et al., 2013; Hafshejani et al., 2011; Bahsi & Cevik, 2015). Table 11 exhibits the  $L^2$  norm consecutive error for  $\hat{m} = 7, 8$ , which confirms that the error decreases rapidly as the order of approximation  $\hat{m}$  increases.

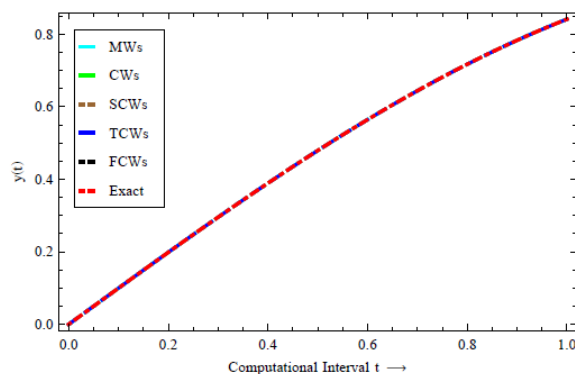


**Figure 9.** The behavior of the approximate solutions for different wavelets with  $\hat{m} = 8$  in Example 4

**Table 9.** Absolute errors of  $y(t)$  using the current scheme at  $\hat{m} = 8$  compared to Example 4

t	MWs	CWs	SCWs	TCWs	FCWs	LWM (Hafshejani et al., 2011) $\hat{m} = 18$
0.125	$9.7 \times 10^{-6}$	$5.1 \times 10^{-10}$	$2.5 \times 10^{-10}$	$1.1 \times 10^{-10}$	$3.8 \times 10^{-10}$	$1.9 \times 10^{-9}$
0.250	$6.6 \times 10^{-6}$	$1.4 \times 10^{-11}$	$1.7 \times 10^{-10}$	$3.6 \times 10^{-10}$	$1.6 \times 10^{-11}$	$1.9 \times 10^{-9}$
0.375	$6.4 \times 10^{-6}$	$2.8 \times 10^{-11}$	$2.8 \times 10^{-11}$	$1.3 \times 10^{-10}$	$1.8 \times 10^{-10}$	$1.9 \times 10^{-9}$
0.500	$7.3 \times 10^{-6}$	$4.7 \times 10^{-10}$	$2.9 \times 10^{-10}$	$2.8 \times 10^{-10}$	$3.1 \times 10^{-10}$	$9.9 \times 10^{-10}$
0.625	$5.1 \times 10^{-6}$	$2.8 \times 10^{-11}$	$1.3 \times 10^{-11}$	$1.2 \times 10^{-10}$	$1.5 \times 10^{-10}$	$9.9 \times 10^{-10}$
0.750	$2.9 \times 10^{-6}$	$2.6 \times 10^{-11}$	$1.1 \times 10^{-10}$	$8.3 \times 10^{-11}$	$3.0 \times 10^{-10}$	$9.9 \times 10^{-10}$
0.875	$4.0 \times 10^{-6}$	$4.3 \times 10^{-10}$	$1.3 \times 10^{-10}$	$2.8 \times 10^{-10}$	$1.4 \times 10^{-11}$	$9.9 \times 10^{-10}$
1.000	$2.7 \times 10^{-6}$	$5.6 \times 10^{-10}$	$1.8 \times 10^{-9}$	$4.1 \times 10^{-10}$	$3.2 \times 10^{-9}$	$9.9 \times 10^{-10}$

**Table 10.** Maximum absolute error using different wavelets in Example 4

$\hat{m}$	MWs	CWs	SCWs	TCWs	FCWs
6	$1.97 \times 10^{-4}$	$2.96 \times 10^{-7}$	$2.02 \times 10^{-7}$	$1.36 \times 10^{-7}$	$3.09 \times 10^{-7}$
7	$2.59 \times 10^{-5}$	$1.66 \times 10^{-8}$	$7.53 \times 10^{-9}$	$8.36 \times 10^{-9}$	$1.30 \times 10^{-8}$
8	$7.42 \times 10^{-6}$	$2.20 \times 10^{-10}$	$8.63 \times 10^{-11}$	$3.35 \times 10^{-10}$	$1.64 \times 10^{-10}$

**Table 11.** Efficiency of the proposed method in terms of  $L^2$  norm consecutive error using different wavelets in Example 4

$\hat{m}$	MWs	CWs	SCWs	TCWs	FCWs
7	$1.50 \times 10^{-4}$	$2.34 \times 10^{-7}$	$2.43 \times 10^{-7}$	$3.46 \times 10^{-7}$	$3.21 \times 10^{-7}$
8	$1.22 \times 10^{-5}$	$1.53 \times 10^{-8}$	$1.50 \times 10^{-8}$	$2.12 \times 10^{-8}$	$2.11 \times 10^{-8}$

### 8. Conclusion

This paper proposes an approximation scheme using five orthogonal polynomial wavelets to solve PDESK. This method is examined using four problems. The error graphs and tables show the Chebyshev wavelets family, especially SCWs, is good for an approximate PDESK solution. Since most elements of derived matrices in the scheme are zeros, the computing time is short. The key advantage of the constructed scheme is that it can obtain results with high accuracy using fewer collocation nodes. The approximated PDESK solutions are provided in the form of graphs and tables. The obtained solution for the given examples shows that this scheme perfectly approximates the existing exact solution. The developed scheme is simple to implement.

### 9. Acknowledgement

The authors are very grateful to the editor and reviewer for carefully reading the manuscript and giving valuable suggestions, which significantly contributed to the presentation of the manuscript.

### 10. References

Alomari, A.K., Noorani, M.S., & Nazar, R. (2009). Solution of delay differential equation by means of homotopy analysis method. *Acta Applicandae Mathematicae*, 108(2), 395-412.

Anakira, N.R., Alomari, A.K., & Hashim, I. (2013). Optimal homotopy asymptotic method for solving delay differential equations. *Mathematical Problems in Engineering*, Article ID 498902.

Asma, Rahman, G.u., & Gómez-Aguilar, J.F. et al. (2022). Study of Multi-Term Pantograph Differential Equations of Arbitrary Order. *Few-Body Syst* 63, 71. <https://doi.org/10.1007/s00601-022-01770-0>

Azodi, H.D., & Yaghouti, M.R. (2018). A new method based on fourth kind Chebyshev wavelets to a fractional order model of HIV infection of CD4<sup>+</sup>T cells. *Computational Methods for Differential Equations*, 6(3), 353-371.

Bahmanpour, M., Tavassoli Kajani M., & Maleki, M. (2018). A Muntz wavelets collocation method for solving fractional differential equations. *Comp. Appl Math*, 37, 5514-5526.

Bahsi, M.M., & Cevik, M. (2015). Numerical Solution of Pantograph-Type Delay Differential Equations Using Perturbation-Iteration Algorithms. *Journal of Applied Mathematics*, Article ID 139821, 10 pages. <http://dx.doi.org/10.1155/2015/139821>.

Baker, C.T.H., Paul, C.A.H., & Wille, D.R. (1995). Issues in the numerical solution of evolutionary delay differential equations. *Advances in Computational Mathematics*, 3, 171-196.

Bellen, A., & Zennaro, M. (2003). *Numerical Methods for Delay Differential Equations*. Numerical Mathematics and Scientific Computations Series, Oxford University Press, Oxford.

Daubechies, I. (1988). Orthonormal bases of compactly supported wavelets. *Comm. Pure Appl Math*, 41, 909-996.

Drfel, G., & Iserles, A. (1997). The pantograph equation in the complex plane. *J Math Anal Appl*, 213, 117-132.

Driver, RD (1977). *Ordinary and Delay Differential Equations*. Applied Mathematics Series, Springer, New York.

Fox, L., Mayers, D.F., Ockendon, J.R., & Tayler, A.B. (1971). On a functional differential equation. *IMA Journal of Applied Mathematics*, 8(3), 271-307.

- Hafshejani, M.S., Vanani, S.K., & Hafshejani, J.S. (2011). Numerical solution of Delay Differential Equations Using Legendre Wavelet Method. *World Applied Sciences Journal*, 13, 27-33.
- Jafari, H., Mahmoudi, M. & Noori Skandari, M.H. (2021). A new numerical method to solve pantograph delay differential equations with convergence analysis. *Adv Differ Equ*, 129. <https://doi.org/10.1186/s13662-021-03293-0>
- Javadi, S., Babolian, E., & Taheri, Z. (2016). Solving generalized pantograph equations by shifted orthonormal Bernstein polynomials. *Journal of Computational and Applied Mathematics*, 303, 1-14.
- Kajani, M.T., HadiVencheh, A., & Ghasemi, M. (2009). The Chebyshev wavelets operational matrix of integration and product operation matrix. *International Journal of Computer Mathematics*, 86(7), 1118-1125.
- KarimiVanani, S., & Aminataei, A. (2010). On the numerical solution of delay differential equations using multiquadric approximation scheme. *J Functional Differential Equations*, 17, 391-399.
- Mallat, S. (2008). *A wavelet tour of signal processing: the sparse way*, Academic press, 3rd edition.
- Muhammad, A.I., Muhammad, S., Syed, T.M.D., & Muhammad, R. (2017). Modified wavelets-based algorithm for nonlinear delay differential equations of fractional order. *Advances in Mechanical Engineering*, 9, 1-8. DOI: 10.1177/1687814017696223.
- Ockendon, J.R., & Tayler, A.B. (1971). The dynamics of a current collection system for an electric locomotive. *Proc Roy Soc Lond A*, 322, 447-468.
- Rahimkhani, P., Ordokhani, Y., & Babolian, E. (2016). Numerical solution of fractional pantograph differential equations by using generalized fractional-order Bernoulli wavelet. *Journal of Computational and Applied Mathematics*, 309, 493-510.
- Rayal, A., Tamta, S., Rawat, S., & Kashif, M., (2022). Numerical view of Lucas-Lehmer polynomials with its characteristics. *Uttaranchal Journal of Applied and Life Sciences*, Uttaranchal University, 3(1), 66-75.
- Rayal, A., & Verma, S.R. (2020a). An approximate wavelets solution to the class of variational problems with fractional order. *Journal of Applied Mathematics and Computing*, 65, 735-769.
- Rayal, A., & Verma, S.R. (2020b). Numerical analysis of pantograph differential equation of the stretched type associated with fractal-fractional derivatives via fractional order Legendre wavelets. *Chaos, Solitons Fractals*, 139(1), 110076.
- Rayal, A., & Verma, S.R. (2020c). Numerical study of variational problems of moving or fixed boundary conditions by Muntz wavelets. *Journal of Vibration and Control*, 28, 1-16.
- Rayal, A., & Verma, S.R. (2022). Two-dimensional Gegenbauer wavelets for the numerical solution of tempered fractional model of the nonlinear Klein-Gordon equation. *Applied Numerical Mathematics*, 174, 191-220.
- Rayal, A., (2023a). An effective Taylor wavelets basis for the evaluation of numerical differentiations. *Palestine Journal of Mathematics*, 12(1), 551-568.
- Rayal, A., Joshi, B.P., Pandey, M., & Torres, D.F.M. (2023b). Numerical Investigation of the Fractional Oscillation Equations under the Context of Variable Order Caputo Fractional Derivative via Fractional Order Bernstein Wavelets. *Mathematics*, 11(11), 2503; <https://doi.org/10.3390/math11112503>
- Rayal, A., Anand, M., Chauhan, K., & Prinsa (2023c). An Overview of Mamadu-Njoseh wavelets and its properties for numerical computations. *Uttaranchal Journal of Applied and Life Sciences*, Uttaranchal University, 4(1), 1-8.
- Rayal, A. (2023d) Muntz Wavelets Solution for the Polytropic Lane–Emden Differential Equation Involved with Conformable Type Fractional Derivative. *Int. J. Appl. Comput. Math* 9, 50; <https://doi.org/10.1007/s40819-023-01528-0>
- Saadatmandi, A., & Dehghan, M. (2009). Variational iteration method for solving a generalized pantograph equation. *Computers and Mathematics with Applications*, 58, 2190-2196.
- Saeed, U., & Rehman, M.U. (2014). Hermite Wavelet Method for Fractional Delay Differential Equations. *Journal of Difference Equations*, Article ID 359093, 1-8.
- Sedaghat, S., Ordokhani, Y., & Dehghan, M. (2012). Numerical solution of the delay differential equations of pantograph type via Chebyshev polynomials. *Communications in Nonlinear Science and Numerical Simulation*, 17, 4815-4830.
- Sezer, M., & Akyuz-Dascioglu, A. (2007). A Taylor method for numerical solution of generalized pantograph equations with linear functional argument. *Journal of Computational and Applied Mathematics*, 200, 217-225.
- Shiralashetti, S.C., Kumbinaraiah, S., Mundewadi, R.A., & Hoogar, B.S. (2016). Series solutions of pantograph equations using wavelets. *Open Journal of Applied & Theoretical Mathematics*, 2(4), 505-518.
- Tayler, A.B. (1986). *Mathematical Models in Applied Mathematics*. Clarendon Pres, Oxford, 40-53.

Tohidi, E., Bhrawy, A.H., & Erfani, K. (2013). A collocation method based on Bernoulli operational matrix for numerical solution of generalized pantograph equation. *Applied Mathematical Modelling*, 37, 4283-4294.

Tural-Polat, S.N. (2019). Third-kind Chebyshev Wavelet Method for the Solution of Fractional Order Riccati Differential Equations. *Journal of Circuits, Systems and Computers*, 28(14), 1950247.

Wang, L.P., Chen, Y.M., Liu, D.Y., & Boutat, D. (2019). Numerical algorithm to solve generalized fractional pantograph equations with variable coefficients based on shifted Chebyshev polynomials. *International Journal of Computer Mathematics*, 96, 2487-2510.

Yalcinbas, S., Aynigul, M., & Sezer, M. (2011). A collocation method using Hermite polynomials for approximate solution of pantograph equations. *Journal of the Franklin Institute*, 348, 1128-1139.

Yalcinbas, S., Sorkun, H.H., & Sezer, M. (2015). A numerical method for solutions of pantograph type differential equations with variable coefficients using Bernstein polynomials. *New Trends in Mathematical Sciences*, 3(4), 179-195.

Yang, C., (2018). Modified Chebyshev collocation method for pantograph-type differential equations. *Appl Numer Math*, 134, 132-144.

Yusufoglu, E. (2010). An efficient algorithm for solving generalized pantograph equations with linear functional argument. *Applied Mathematics and Computation*, 217, 3591-3595.

Yuzbas, S., Gok, E., & Sezer, M. (2014). Laguerre matrix method with the residual error estimation for solutions of a class of delay differential equations. *Mathematical Methods in the Applied Sciences*, 37(4), 453-463.

Zhu, L., & Wang, Y. (2013). Second Chebyshev wavelet operational matrix of integration and its application in the calculus of variations. *International Journal of Computer Mathematics*, 90(11), 2338-2352.

# COMPLEX OF Co(II) WITH LIGAND 2,2'-BIPYRIDINE AND ANIONIC TRIFLUOROACETATE: SYNTHESIS, PHYSICAL PROPERTY, STRUCTURAL ANALYSIS AND ITS ANTIBACTERIAL ACTIVITY

Haidar J. Mohamad<sup>1a\*</sup>, Shaymaa H. Kafi<sup>2a</sup>, Farah J. Kadhum<sup>3a</sup>

**Abstract:** The increasing demand for optical sensors is driven by their wide applications, making surface plasmon resonance (SPR) play a crucial role in this field. In this study, a multilayered thin film consisting of tantalum pentoxide (Ta<sub>2</sub>O<sub>5</sub>) and silver (Ag) deposited on a glass prism was used to study SPR. The Ag layer thickness was fixed at 50 nm, while the Ta<sub>2</sub>O<sub>5</sub> layer thickness varied from 0 to 70 nm. The Kretschmann configuration was employed to assess the sensitivity of air and gases with different refractive indices. Therefore, different layer thicknesses along with different wavelengths and angles were investigated. MATLAB software was employed to simulate and analyze SPR with a half-sphere prism to extend the incident angle. The simulation conditions with Fresnel equations were used to calculate the reflectivity and transmittance coefficients for the studied sample. The results revealed that the best output was at a Ta<sub>2</sub>O<sub>5</sub> thickness of 50 nm to get optimal full width at half maximum of 2.4 and sensitivity factor of 162.5. This device works in the visible and infrared regions.

**Keywords:** Thin film, modeling, optical sensor, sensor sensitivity.

## 1. Introduction

Tantalum pentoxide (Ta<sub>2</sub>O<sub>5</sub>) thin films have remarkable properties, including a high dielectric constant. In the visible region, these films have a high refractive index as well as high transmittance and high-temperature resistance [1]. Surface plasmon resonance (SPR), used for sensor applications, has emerged as a branch of modern technology. It has a fast response, can work with small-volume materials, and is highly sensitive to changes in the refractive index of the medium located near the thin metal film. SPR-based sensors are used extensively in optical devices and sensing applications, including biomolecular detection [2], medical diagnosis [3], biological analyses [4], antibody-antigen interaction [5], organic chemical sensing [6], bioimaging [7], environmental safety [8], and water testing [9]. It has been employed in optoelectronic devices, such as SPR imaging and film thickness monitoring [10].

All materials interact with light in a certain manner. This interaction of photons with a crystal or electronic structure of matter leads to several phenomena, such as reflection, refraction, transmission, and absorption [11]. The value of reflectivity depends on the angle of incidence. Materials with a higher refractive index have a higher reflectivity than those with a lower refractive index [12]. The optical properties of a material are related to its interaction with electromagnetic radiation. Generally, plasmonic devices require metallic components with an abundance of free electrons. Free electrons display negative

permittivity, which is considered an essential property of any plasmonic material. These electrons are affected by any electromagnetic wave, resulting in oscillation and the surface plasmon phenomenon [13].

SPR sensor devices have a complex optical system design and may have expensive components [14]. Therefore, simulation analytics are crucial in constructing SPR sensors, optimizing optical parameters, and reducing operational costs [15]. Several studies concentrated on simulations to demonstrate the advantages and disadvantages of SPR. Wen *et al.* (2020) presented the kinetics of the plasmon model and explained how they depended on the particle simulation method. The modeling of a single electron in plasmon excitation included two steps to locate electron movement and reveal electron spill-out effects [16]. However, they did not explore this field altogether, leaving room for further investigation.

Costa *et al.* (2019) analyzed multilayer reflectance using Otto's configuration. The incident light angle range starts from 30° to 40°, which is small compared with our work [17]. Hassan *et al.* (2020) proposed a photonic crystal fiber sensor whose output analysis depends on its refractive index. They performed simulations using the finite element method. They suggested a design with airholes in hexagonal shapes, and the center airhole was benzene coated with gold to generate the plasmon effect. The high performance was in the refractive index from 1.45 to 1.49 only [18]. Kumar *et al.* (2021) investigated the hybrid structure of BP-Ti3C2Tx with Cu-Ni layers for biochemical sensor applications. They noticed that by changing the thickness of the Cu-Ni layers, the sensitivity was enhanced and could be optimized [18]. Farah *et al.* (2021) simulated multilayer samples

### Authors information:

<sup>a</sup>Mustansiriyah University - College of Science- Physics Dept., Baghdad, IRAQ. Email:

haidar.mohamad@uomustansiriyah.edu.iq<sup>1</sup>;  
iraqshaymaa.h.kafi@uomustansiriyah.edu.iq<sup>2</sup>;  
farahjawadalnuaimi@uomustansiriyah.edu.iq<sup>3</sup>

\*Corresponding

Author:

haidar.mohamad@uomustansiriyah.edu.iq

Received: February 17, 2023

Accepted: May 31, 2023

Published: June 30, 2024

of Au–Si3N4 at different thicknesses deposited on the N-LASF9 glass. They studied different wavelengths and incident angles to plot the resonance angle of SPR with reflection. The sensor had a range of 600–700 nm and 900–1000 nm [19].

In this study, the primary reason behind using silver/tantalum pentoxide (Ag/ Ta2O5) is to modify the absorption capacity of incident light and enhance the interface effect between layers. An SPR system was simulated to detect the benzene medium. This system consists of a Ta2O5 layer used as a waveguide medium and a silver (Ag) layer deposited on the glass prism in the Kretschmann configuration. The behavior of the SPR curve was examined by changing the sample thickness and the incident angle for different wavelengths. It gives the sensing range of wavelengths and optimal angles to attain resonant surface plasmon.

## 2. Methodology

When light interferes with a medium, the electrons oscillate harmonically with the incident light. In the case of SPR, oscillation and propagation occur along the interface between the dielectric and metal mediums. SPR depends on observing the reflected light spectrum obtained by angular or wavelength interrogation [20]. Therefore, the angular change resolution is preferred when investigating SPR. Measuring the change in resonant angle allows the extraction from the spectrum the reflectance curve as a function of incident angle for the same wavelength. This spectrum gives two significant factors to describe the SPR curve: minimum reflectance and full width at half maximum (FWHM). Noble metals such as Au and Ag have been used to propagate polarizing waves in surface plasma at a specific wavelength [21].

The Kretschmann configuration was used in the simulation of the SPR sensor system in this work (Figure 1). The sensor consists of a LaSF9 glass prism, Ag thin film with a thickness of 50 nm, a Ta2O5 layer of varying thicknesses ( $d = 0, 25, 50,$  and  $75$  nm), and

a sensing medium considered to be benzene (C6H6) with the refractive index changed by  $\Delta n = 0$  and  $0.04$ .

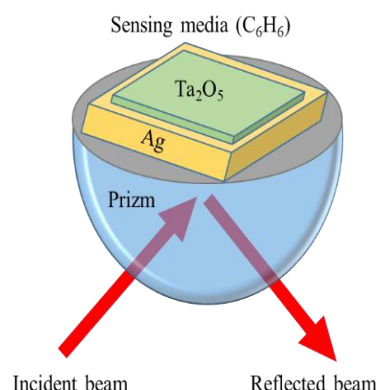


**Figure 1.** The schematic diagram of the SPR system based on the Kretschmann configuration.

The complex refractive index ( $n_m$ ) can be calculated due to the reaction of light with the semi-transparent matter as follows [22]:

$$n_m = n_r + in_k \tag{1}$$

Where  $n_r$  represents the real part of the refractive index. The imaginary part,  $n_k$ , is called the extinction coefficient, which also refers to the amount of attenuation coefficient along the  $z$ -direction. The complex refractive index ( $n$ ) is related to the wave number ( $k$ ) by  $k = 2\pi n/\lambda$ . The electromagnetic wave plane component for any wavelength in the vacuum can be expressed as follows [22]:

$$E_{(z,t)} = E_o e^{i(kz - \omega t)} = E_o e^{\frac{i(2\pi(n_r + in_k)z - \omega t)}{\lambda}} = e^{-\frac{2\pi n_k z}{\lambda}} \left[ E_o e^{i\left(\frac{2\pi n_r z}{\lambda} - \omega t\right)} \right] n_m = n_r + in_k \tag{2}$$

The electromagnetic wave exponentially decays with ( $z$ ) by the factor  $e^{-\left(\frac{2\pi n_k z}{\lambda}\right)}$ ; thus, the attenuation coefficient becomes  $\alpha = \frac{4\pi k}{\lambda}$ .  $n_r$  and  $n_k$  are frequency dependent, and  $n_k$  has two conditions, namely,  $n_k > 0$  and  $n_k = 0$ , meaning that the light is absorbed by media and travels without loss, respectively.

Dielectrics have greater absorption capacity compared with metals. Dielectric-like glass has very low DC conductivity and negligible loss at low frequencies, leading to small absorption values. Although the absorption increases dramatically at high frequencies, it can be reduced by the transparent material properties. The Kramers–Kronig relations determine the complex refractive index of real and imaginary components,  $n_r$  and  $n_k$ , respectively. These components are measured indirectly by calculating the reflectance and transmittance of the sample [23].

Ag is considered one of the most favorable materials used as a sensing metal because of its high electric field conductivity and low imaginary component of its refractive index [24]. Ta2O5 also has favorable properties such as a high refractive index (2.05–2.30) within the visible band, a large energy gap of 4.2 eV, and no absorption within the range of 10 to 400 nm [25]. Therefore, it is necessary to plot the behavior of the refractive index as a function of wavelength for all the substrates (glass prism), an Ag layer, Ta2O5, and C6H6. The data in Figure 2 were collected online [26].

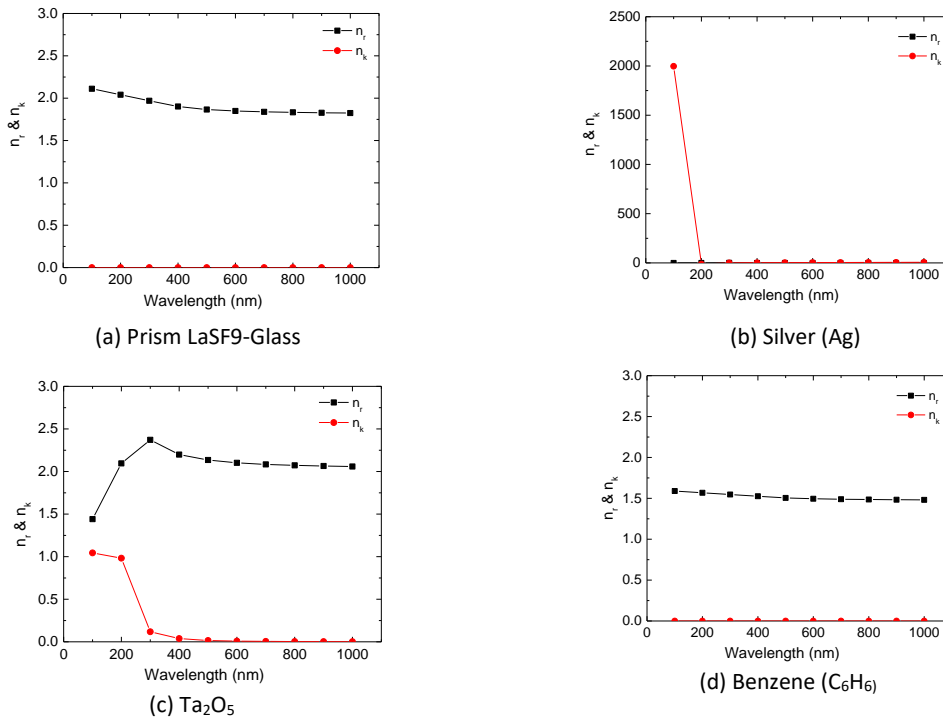


Figure 2. Real (n) and Imaginary (k) parts the with the wavelength ( $\lambda$ ) for (a) prism, (b) Ag layer, (c) Ta2O5, and (d) C6H6.

The change in the refractive index due to the interaction between light and the sample’s surface led to the shift in the SPR curve. Therefore, the details of the SPR curve are significant as the indicator for the sensing tool [27]. We used the Kretschmann configuration for the studied sample to understand the SPR curve. The reflectivity of the multilayer sample is presented by Fresnel’s equations: the first layer boundary ( $E_a$  and  $H_a$ ) and the last layer boundary ( $E_N$  and  $H_N$ ) for the electric and magnetic field component amplitudes, respectively. It can be represented by the total matrix [28]:

$$\begin{aligned}
 [E_a \ H_a] &= \left[ \prod_{m=1}^N M_m \right] [E_N \ H_N] \\
 &= [M_{11} \ M_{12} \ M_{21} \ M_{22}] [E_N \ H_N]
 \end{aligned}
 \tag{3}$$

The transfer matrix method was used to investigate the optical properties of the suggested SPR sensor. The light interaction matrix  $M_m$  of the  $m$ th layer ( $m = 1$  to  $N$ ) can be expressed by [29]:

$$M_m = \begin{bmatrix} \cos \beta_m & \frac{i}{q_m} \\ \sin \beta_m & \cos \beta_m \\ iq_m \sin \beta_m & \cos \beta_m \end{bmatrix}
 \tag{4}$$

Where  $\beta_m$  and  $q_m$  are defined as  $\left(\frac{2\pi}{\lambda}\right) n_m d_m \cos \theta_m$  and  $n_m \cos \theta_m$ , respectively.  $n_m$  is the complex refractive index,  $\theta_m$  is the incidence angle of  $m^{th}$  layer. This equation is important to model the electric and magnetic component field interfaced of  $m^{th}$  layer.

The description of the single field that passes through layer  $m$  can be given by

$$\beta_m = \left(\frac{2\pi}{\lambda}\right) n_m d_m \cos \theta_m
 \tag{5}$$

The p-polarization field for any layer ( $q_m$ ) is represented by [30]:

$$q_m = \frac{n_m \sqrt{\epsilon_o \mu_o}}{\cos \theta_m}
 \tag{6}$$

where  $\epsilon_o$  and  $\mu_o$  are the vacuum permittivity and the permeability, respectively.

From the preceding matrix, Fresnel’s reflection coefficient ( $r$ ) and transmission coefficient ( $t$ ) within the sample are obtained as follows [29]:

$$r = \frac{[q_N M_{11} + q_o q_N M_{12}] - [M_{21} + q_o M_{22}]}{[q_N M_{11} + q_o q_N M_{12}] + [M_{21} + q_N M_{22}]}
 \tag{7}$$

$$t = \frac{2q_o \left(\frac{n_N}{n_o}\right)}{[q_N M_{11} + q_o q_N M_{12}] + [M_{21} + q_N M_{22}]}
 \tag{8}$$

The total reflectance (R) and the total transmittance (T) are given by [29]:

$$R = |r|^2 \quad (9)$$

$$T = |t|^2 \quad (10)$$

The most significant parameter of any SPR sensor is its sensitivity. Sensitivity can be explained in terms of the marked change in the resonance angle ( $\Delta\theta_{SPR}$ ). This change is caused by the changes in the refractive index ( $n_m$ ) of the sensing medium. Therefore, the parameters of the sensing medium are vital, for instance, sample thickness, number of layers, material specifications, and shape or design. The sensitivity equation is written as [31]:

$$S = \left( \frac{\Delta\theta_{SPR}}{\Delta n} \right) \quad (11)$$

where  $\Delta\theta_{SPR}$  is the resonance angle change,  $\Delta n_m$  is the change in the refractive index.  $\Delta\theta_{SPR}$  is related to the minimum reflectance ( $R_{min}$ ) and its value is extracted from the R- $\theta$  curve.

In terms of sensing performance, the resonance is dependent on the Ta2O5 layer thickness. In this study, the performance characteristics of the noble metal Ag/dielectric Ta2O5 sensor were studied by carefully carrying out a sophisticated MATLAB algorithm of SPR simulation followed by determining SPR curve characteristics. Reflectance (R) was simulated as a function of the incident angle for the Ag/Ta2O5 structure. Ag thickness was fixed

at 50 nm, whereas the thickness of the dielectric slab Ta2O5 was varied ( $d = 0, 25, 50,$  and  $75$  nm). Here, the dielectric Ta2O5 acts as a waveguide medium, supporting the propagation of waveguide modes within the selected sample.

The simulation of the experimental data was achieved using the following algorithm:

#### Compute FWHM and $L_d$ algorithm

The dip data are represented by  $y=f(x)$ , where  $x$  represents the incident angle ( $0^\circ$  to  $90^\circ$ ).

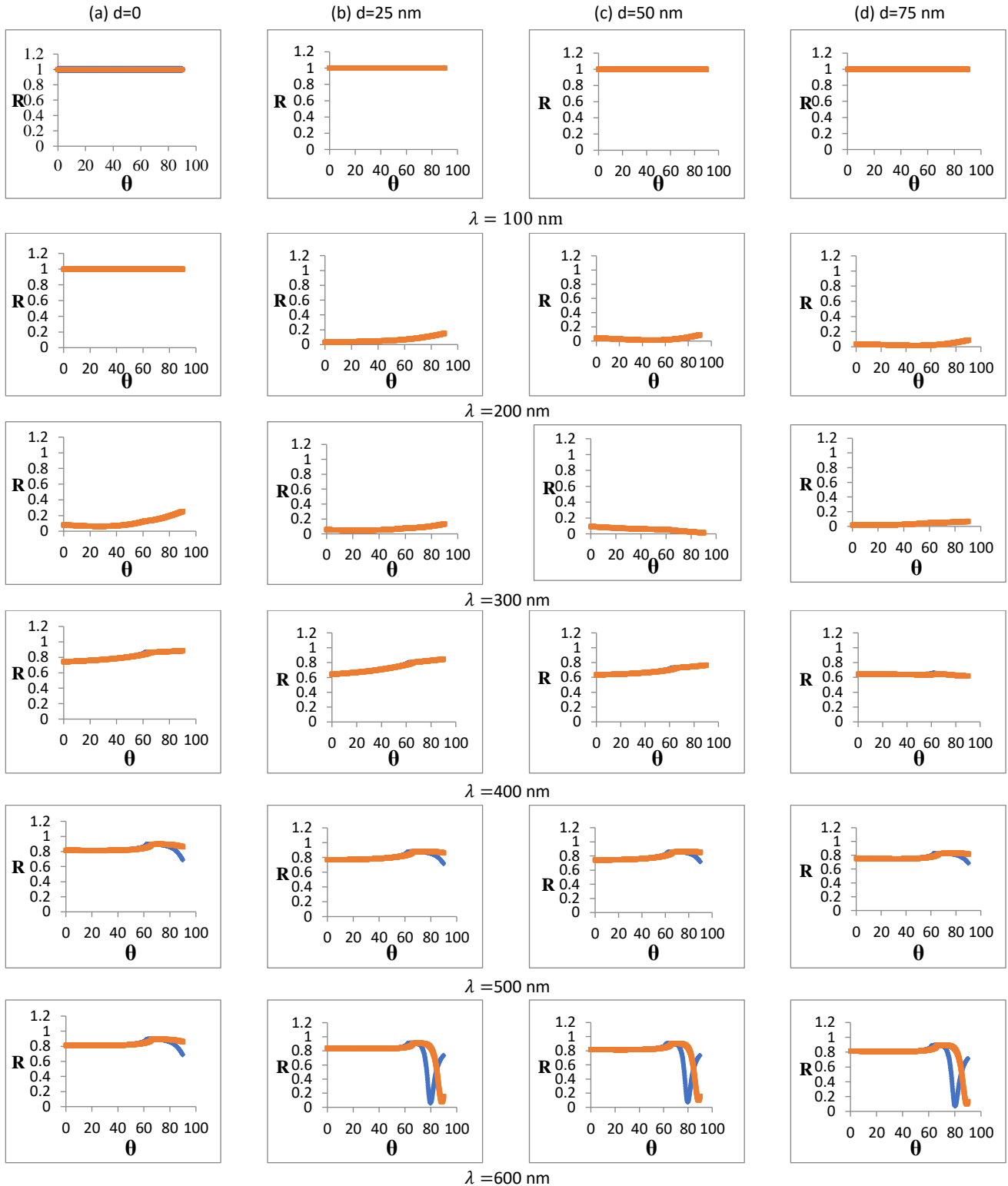
#### Start algorithm

1. Extract maximum SPR peak curve ( $L_d$ ) at SPR angle (SPR\_Theta) using  $[L_d \text{ SPR\_Theta}] = \min(y)$
2. Extract the half max value for the SPR peak curve: **halfMax** =  $(\min(y) + \max(y)) / 2$ ;
3. Extract data at curve decay below **halfMax** value and save it in *halfmax1*.
4. Extract data at curve above **halfMax** value and save it in *halfmax2*.
5. Compute FWHM using  $\text{FWMH} = \text{halfmax2} - \text{halfmax1}$

#### End algorithm

### 3. Results and Discussion

In this study, we investigated the direct effect of the change in Ta2O5 layer thickness on the sensitivity of the suggested SPR sensor. Therefore, the Ag layer thickness was precisely fixed at 50 nm, while the Ta2O5 layer thickness was varied from 0 to 70 nm. Figure 3 depicts the reflectance curves as a function of light incident angles ( $\theta$ ) for a different Ta2O5 layer thickness and different wavelengths ( $\lambda$ ) from 100 to 1000 nm, with a step size of 100 nm.



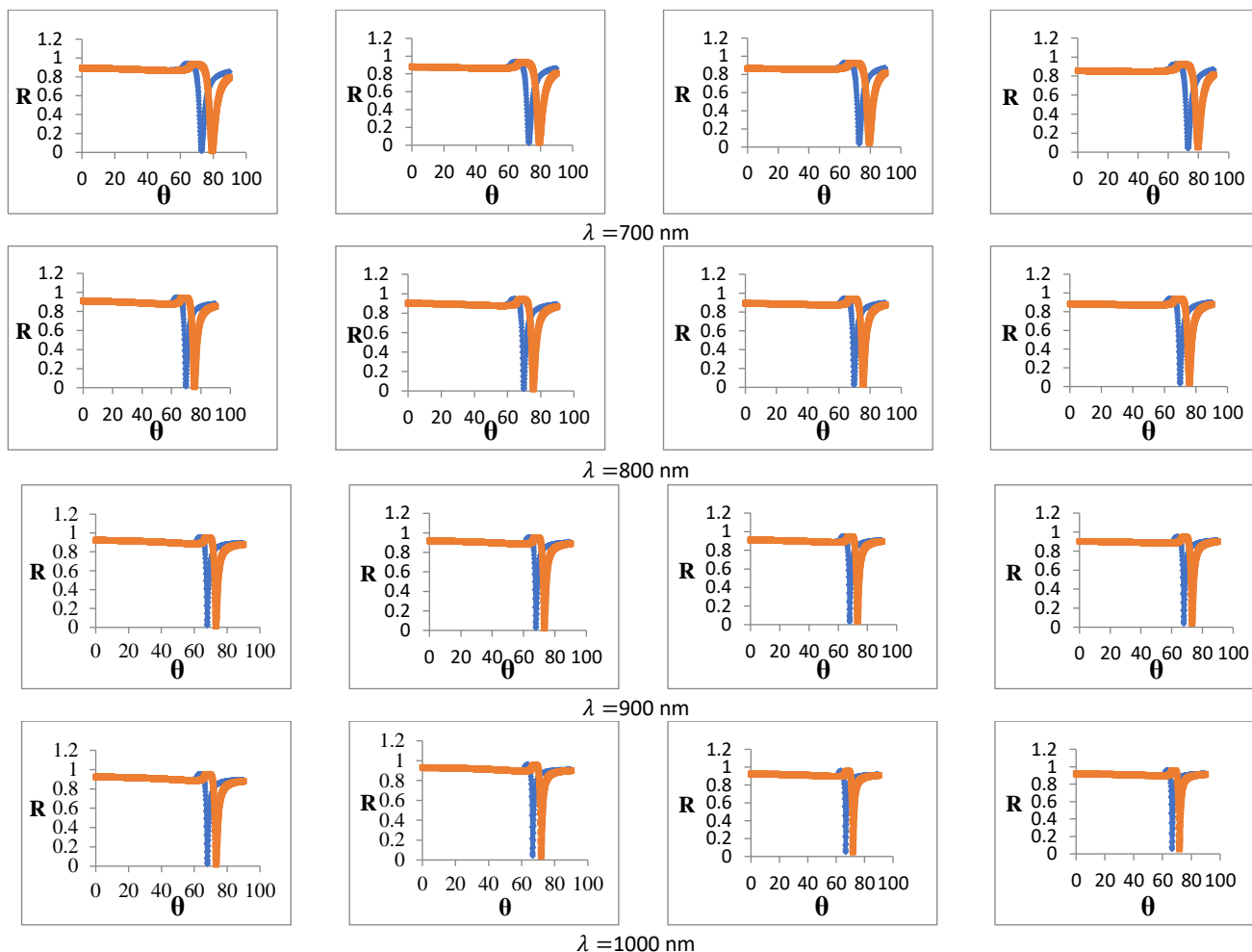


**Figure 3.** Reflectance of the suggested sample with incidence light angle for different wavelengths ( $\lambda=100-1000$  nm) and different  $Ta_2O_5$  layer thicknesses (a)  $d=0$  nm, (b)  $d=25$  nm, (c)  $d=50$  nm, and (d)  $d=75$  nm. The blue line is  $\Delta n_m = 0$ , and red line  $\Delta n_m = 0.04$

Figure 3 demonstrates that there is no effect of resonance from wavelength 100 to 600 nm, and the effect becomes discernible at wavelength 700 nm. Evidently, the shift between the blue and red curves, caused by the change in the refractive index, is significant for SPR sensor performance. The shape of the dip, like its width and height, is also significant.

The results of  $R-\theta$  curve analysis data are presented in Tables 1–4, showing FWHM, dip length ( $L_d$ ), and  $S$  values with change in the refractive index of C6H6 ( $\Delta n_m$ ) with  $d = 0$  to 75 nm. The numerical results of Ag–Pt bimetallic films were used to simulate the SPR within a small range due to the prism diagram [32]. They show that the FWHM changed with the layer thickness. Our system works with a wide range of angles and is sensitive to the visible and IR range, which offers a wide range of applications.

**Table 1.** Data corresponding to wavelengths 700–1000 nm at thickness 0.

$\lambda(nm)$	$\Delta n$	$\theta_{SPR}$	FWHM	$L_d$	$S$
700	0	72.9	3.7	0.9191	160.0
	0.04	79.3	4.6	0.9169	
800	0	69.8	2.5	0.9321	142.5
	0.04	75.5	3.0	0.9325	
900	0	76.9	1.7	0.9329	132.0
	0.04	73.2	2.1	0.9350	
1000	0	66.7	1.3	0.9214	125.0
	0.04	71.7	1.6	0.9260	

**Table 2.** Data corresponding to wavelengths 700–1000 nm of the  $R-\theta$  curve at thickness 25 nm.

$\lambda(nm)$	$\Delta n$	$\theta_{SPR}$	FWHM	$L_d$	$S$
700	0	72.9	3.5	0.9044	160.0
	0.04	79.3	4.4	0.8983	
800	0	69.8	2.4	0.9233	142.5
	0.04	75.5	2.9	0.9220	
900	0	67.9	1.6	0.9257	132.0
	0.04	73.2	2.0	0.9262	
1000	0	66.7	1.2	0.9144	125.0
	0.04	71.7	1.5	0.9181	

**Table 3.** Data corresponding to wavelengths 700–1000 nm of the R– $\theta$  curve at thickness 50 nm

$\lambda$ (nm)	$\Delta n$	$\theta_{SPR}$	FWHM	$L_d$	S
700	0	69.9	2.4	0.9138	162.5
	0.04	75.6	2.9	0.9104	
800	0	69.8	2.4	0.9233	142.5
	0.04	75.5	2.9	0.9220	
900	0	67.9	1.6	0.9175	132.5
	0.04	73.2	2.0	0.9163	
1000	0	66.7	1.2	0.9068	125.0
	0.04	71.7	1.5	0.9086	

**Table 4.** Data corresponding to wavelengths 700–1000 nm of the R– $\theta$  curve at thickness 75 nm.

$\lambda$ (nm)	$\Delta n$	$\theta_{SPR}$	FWHM	$L_d$	S
700	0	73.0	3.5	0.8803	162.5
	0.04	79.5	4.4	0.8685	
800	0	69.9	2.3	0.9067	142.5
	0.04	75.6	2.8	0.9011	
900	0	67.9	1.6	0.9097	132.5
	0.04	73.2	2.0	0.9068	
1000	0	66.7	1.2	0.8997	125.0
	0.04	71.7	1.5	0.8989	

The summary Figure 3 shows that SPR does not appear at wavelengths from 100 to 500 nm. SPR begins to appear at the wavelength of 600 nm and has an incomplete dip. At wavelengths 700, 800, 900, and 1000 nm, SPR appears at all oxide layer thicknesses. The minimum reflectivity ( $R_{min}$ ) in the R– $\theta$  curve is 0.061. This value was recorded at wavelength 900 nm with  $\theta_{SPR}$  = 73.2°. The sensor resolution changed as the wavelength varied, causing a broadening of the reflectance dip. The shape dip and its width determine the accuracy of the sensor. The highest dip length is (0.935°) at  $\lambda$  = 900 nm and thickness  $d$  = 25 nm. The higher sensitivity (S) for the proposed SPR sensor obtained with sharper shapes is 162.5.

The FWHM plays a critical role because the resonance angle in the R– $\theta$  curve should be small to be distinguished with small changes compared with different wavelengths. The sharper and narrower dip shape of SPR and the smaller value of FWHM result in high detection accuracy. Furthermore, it is worth noting that when  $L_d$  value approaches 1, a good SPR is achieved. Therefore, controlling the sample thickness is vital to get a low FWHM value and a  $L_d$  value approaching 1. The presented algorithm gives accurate details to calculate FWHM, and equation 5 gives the value of the sensitivity of the suggested sensor.

#### 4. Conclusions

The suggested sample for the optical sensor has many positive and important points. The sensitivity (S) increases significantly with the appearance of the Ta<sub>2</sub>O<sub>5</sub> layer because it works as a waveguide and increases the resonance signal. The relationship between the change in the Ta<sub>2</sub>O<sub>5</sub> layer thickness and the refractive index of the sensing medium has a minor influence. The R– $\theta$  curve dip shifted in this case due to the changes in the refractive index. Therefore, the SPR dip width should be smaller

to distinguish the small shift at  $\Delta n$  reaching zero. The suggested SPR sensor detects a small variation in the refractive index (0.04) of the proposed sensing medium. The suggested device works in the visible and IR regions of the electromagnetic spectrum, as shown in the R– $\theta$  curve. It is important to increase the step size in modeling to get the behavior of the resonance dip because it is sensitive to a small angle value.

#### 5. Acknowledgement

The authors would like to thank the Department of Physics/College of Science/Mustansiriyah University (www.uomustansiriyah.edu.iq) in Baghdad, Iraq, for their support in the present work.

#### 6. References

- Abdul-Hussain, M. A., and Mohamad, H. J. (2021). "Thermal Effect in a 3-D Simulation within Multilayer Thin Film of Ultrafast-Pulsed Laser". *Al-Mustansiriyah Journal of Science*, 32(4), 104-109; : <http://doi.org/10.23851/mjs.v32i4.1039>
- Abdul-Hussain, M. A., Mohamad, H. J., and Al-Haddad, A. (2022). "1-D Simulation of Ultrafast-Pulsed Laser into Nano-Sized Multilayered Structure (Ni81Fe19/Cu/YIG/GGG) for Memory Device Applications". *Iraqi Journal of Science*, 63(3), 1045-1054; <https://doi.org/10.24996/ij.s.2022.63.3.14>
- Ali, M. Z. (2021). "Plasmon-polariton gap and associated phenomenon of optical bistability in photonic hypercrystals". *Physics Letters A*, 387(n/a), 127026; <https://doi.org/10.1016/j.physleta.2020.127026>
- Alias, R., Mahmoodian, R., and Abd Shukur, M. H. (2019). "Development and characterization of a multilayer silver/silver-tantalum oxide thin film coating on stainless steel for biomedical applications". *International Journal of Adhesion and Adhesives*, 92(n/a), 89-98; <https://doi.org/10.1016/j.ijadhadh.2019.04.010>
- Anand, U., Chandel, A. K. S., Oleksak, P., Mishra, A., Krejcar, O., Raval, I. H., and Kuca, K. (2022). "Recent advances in the potential applications of luminescence-based, SPR-based, and carbon-based biosensors". *Applied Microbiology and Biotechnology*, 106(8), 2827-2853; <https://doi.org/10.1007/s00253-022-11901-6>
- Balaur, E., Sadatnajafi, C., and Abbey, B. (2022); "Optical barcoding using polarisation sensitive plasmonic biosensors for the detection of self-assembled monolayers". *Scientific Reports*, 12(1), 13081; : <https://doi.org/10.21203/rs.3.rs-1360592/v1>
- Bereli, N., Bakhshpour, M., Topçu, A. A., and Denizli, A. (2021). "Surface Plasmon Resonance-Based Immunosensor for IgM Detection with Gold Nanoparticles. *Micromachines*", 12(9), 1092; <https://doi.org/10.3390/mi12091092>
- Berguiga, L., Ferrier, L., Jamois, C., Benyattou, T., Letartre, X., and Cuffe, S. (2021). Ultimate phase sensitivity in surface plasmon resonance sensors by tuning critical coupling with phase change materials. *Optics Express*, 29(25), 42162-42175; <https://doi.org/10.1364/OE.439869>

- Böer, K. W., and Pohl, U. W. (2018). "Interaction of Light with Solids". In K. W. Böer and U. W. Pohl (Eds.), *Semiconductor Physics* (pp. 333-388). Cham: Springer International Publishing. [https://link.springer.com/referenceworkentry/10.1007/978-3-319-69150-3\\_10](https://link.springer.com/referenceworkentry/10.1007/978-3-319-69150-3_10)
- Costa, E. B., Rodrigues, E. P., and Pereira, H. A. (2019). "Sim-SPR: an Open-Source Surface Plasmon Resonance Simulator for Academic and Industrial Purposes". *Plasmonics*, 14(6), 1699-1709, <https://doi.org/10.1007/s11468-019-00970-5>
- Ding, Wen J., Lim, Jeremy Zhen J., Do Hue Thi Bich, Xiong Xiao, Mahfoud Zackaria, Png Ching Eng, Bosman Michel, Ang Lay Kee, and Wu Lin (2020). "Particle simulation of plasmons". *Nanophotonics* 9(10), 3303-3313; <https://doi.org/10.1515/nanoph-2020-0067>
- Ding, Wen J., Lim, Jeremy Zhen J., Do Hue Thi Bich, Xiong Xiao, Mahfoud Zackaria, Png Ching Eng, Bosman Michel, Ang Lay Kee, and Wu Lin (2020). "Particle simulation of plasmons". *Nanophotonics* 9(10), 3303-3313; <https://doi.org/10.1515/nanoph-2020-0067>
- Divya, J., Selvendran, S., Raja, A. S., and Sivasubramanian, A. (2022). "Surface plasmon based plasmonic sensors: A review on their past, present and future". *Biosensors and Bioelectronics*: X, 11(n/a), 100175; <https://doi.org/10.1016/j.biosx.2022.100175>
- Duan, Q., Liu, Y., Chang, S., Chen, H., and Chen, J.H. (2021). "Surface Plasmonic Sensors: Sensing Mechanism and Recent Applications". *Sensors (Basel, Switzerland)*, 21(16), 5262; <https://doi.org/10.3390/s21165262>
- Farah, J. K., Shaymaa, H. K., Asrar, A. S., Ali, A. D. Z., and Anwar, H. S. (2021). "Simulation of Surface Plasmon Resonance (SPR) of Silver with Titanium Oxide as a BiLayer Biosensor". *The Scientific Journal of King Faisal University*, 22(2), (n/a); <https://doi.org/10.37575/b/sci/210046>
- Ferrari, J. L., Lima, K. d. O., and Gonçalves, R. R. (2021). "Refractive Indexes and Spectroscopic Properties to Design Er<sup>3+</sup>-Doped SiO<sub>2</sub>-Ta<sub>2</sub>O<sub>5</sub> Films as Multifunctional Planar Waveguide Platforms for Optical Sensors and Amplifiers". *ACS Omega*, 6(13), 8784-8796; <https://doi.org/10.1021/acsomega.0c05351>
- Harumi, A., Endo, K., and Suzuki, T. (2021). "Reflectionless metasurface with high refractive index in the terahertz waveband". *Optics Express*, 29(10), 14513-14524; <https://doi.org/10.1364/OE.420827>
- Kumar, R., Pal, S., Pal, N., Mishra, V., and Prajapati, Y. K. (2021). "High-performance bimetallic surface plasmon resonance biochemical sensor using a black phosphorus-MXene hybrid structure". *Applied Physics A*, 127(n/a), 1-12; <https://doi.org/10.1007/s00339-021-04408-w>
- Lee, H.T., Ji, G.S., Oh, J.Y., Seo, C.W., Kang, B.W., Kim, K.W., and Park, H.R. (2021). "Measuring Complex Refractive Indices of a Nanometer-Thick Superconducting Film Using Terahertz Time-Domain Spectroscopy with a 10 Femtoseconds Pulse Laser". *Crystals*, 11(6), 651; <https://doi.org/10.3390/cryst11060651>
- Li, J., Han, D., Zeng, J., Deng, J., Hu, N., and Yang, J. (2020). "Multi-channel surface plasmon resonance biosensor using prism-based wavelength interrogation". *Optics Express*, 28(9), 14007-14017; <https://doi.org/10.1364/OE.389226>
- Mishra, S. K., Verma, R. K., and Mishra, A. K. (2021). "Versatile Sensing Structure: GaP/Au/Graphene/Silicon". *Photonics*, 8(12), 547. <https://doi.org/10.3390/photonics8120547>
- Mohamad, H. J., Shelford, L. R., Aziz, M., Al-Jarah, U. A. S., Al-Saigh, R., Valkass, R. A. J., and Hicken, R. J. (2017). "Thermally induced magnetization dynamics of optically excited YIG/Cu/Ni<sub>81</sub>Fe<sub>19</sub> trilayers". *Physical Review B*, 96(13), 134431; <https://doi.org/10.1103/PhysRevB.96.134431>
- Mulyanti, B., Nugroho, H. S., Wulandari, C., Rahmawati, Y., Hasanah, L., Hamidah, I., and Majlis, B. Y. (2022). "SPR-Based Sensor for the Early Detection or Monitoring of Kidney Problems". *International Journal of Biomaterials*, 2022(n/a), 9135172; <https://doi.org/10.1155/2022/9135172>
- Pandaram, M., Santhanakumar, S., Veeran, R., Balasundaram, R. K., Jha, R., and Jaroszewicz, Z. (2022). "Platinum Layers Sandwiched Between Black Phosphorous and Graphene for Enhanced SPR Sensor Performance". *Plasmonics*, 17(1), 213-222; <https://doi.org/10.1007/s11468-021-01507-5>
- Polyanskiy, M. N. (2022). Refractive index database. <https://refractiveindex.info>
- Proposito, P., Burratti, L., and Venditti, I. (2020). "Silver Nanoparticles as Colorimetric Sensors for Water Pollutants". *Chemosensors*, 8(2), 26; <https://doi.org/10.3390/chemosensors8020026>
- Sai, T., Saba, M., Dufresne, E. R., Steiner, U., and Wilts, B. D. (2020). "Designing refractive index fluids using the Kramers-Kronig relations". *Faraday Discussions*, 223(0), 136-144; [10.1039/D0FD00027B](https://doi.org/10.1039/D0FD00027B)
- Shpacovitch, V., and Hergenröder, R. (2020). "Surface Plasmon Resonance (SPR)-Based Biosensors as Instruments with High Versatility and Sensitivity". *Sensors (Basel, Switzerland)*, 20(11), 3010; <https://doi.org/10.3390/s20113010>
- Singh, G. P., and Sardana, N. (2022). "Smartphone-based Surface Plasmon Resonance Sensors: a Review". *Plasmonics*, 17 (n/a), 1869-1888; <https://doi.org/10.1007/s11468-022-01672-1>
- Steglich, P., Giulia, L., and Andreas, M. (2022). "Surface Plasmon Resonance (SPR) Spectroscopy and Photonic Integrated Circuit (PIC) Biosensors: A Comparative Review". *Sensors*, 22(8). [doi:10.3390/s22082901](https://doi.org/10.3390/s22082901); <https://doi.org/10.3390/s22082901>
- Uddin, S. M. A., Chowdhury, S. S., and Kabir, E. (2021). "Numerical Analysis of a Highly Sensitive Surface Plasmon Resonance Sensor for SARS-CoV-2 Detection". *Plasmonics*, 16(6), 2025-2037; <https://doi.org/10.1007/s11468-021-01455-0>
- Wang, X., Deng, H., and Yuan, L. (2021). "Highly Sensitive Flexible Surface Plasmon Resonance Sensor Based on Side-Polishing Helical-Core Fiber: Theoretical Analysis and Experimental Demonstration". *Advanced Photonics Research*, 2(2), 2000054; <https://doi.org/10.1002/adpr.202000054>